CFD Simulation of Highly Transient Flows

A thesis submitted to University College London for the degree of Doctor of Philosophy

By

GARFIELD SYLVESTER DENTON

Department of Chemical Engineering
University College London
Torrington Place
London WC1E 7JE

July 2009

List of Contents

CHAPTER 3

BACKGROUND THEORY FOR MODELLING TRANSIENT FLOW IN PIPELINES

CHAPTER 4

APPLICATION OF THE METHOD OF CHARACTERISTICS (MOC)

CHAPTER 5

APPLICATION OF MOC FOR SIMULATING PUNCTURE/FULL-BORE RUPTURE OF MULTI-SEGMENT PIPELINE NETWORKS

CHAPTER 6

VALIDATION OF THE MULTI-SEGMENT PIPELINE OUTFLOW MODEL

ABSTRACT

This thesis describes the fundamental extension and extensive testing of a robust CFD model for predicting outflow following the failure of pressurised hydrocarbon pipelines. The main thrust of the study involves the extension of the basic outflow model to account for complex pipeline systems, improvements of the theoretical basis and numerical stability.

The basic model, based on the numerical solution of conservation equations using the method of characteristics, incorporates a suitable equation of state to deal with pipelines containing pressurised multi-component hydrocarbon mixtures. It utilises the homogeneous equilibrium flow (HEM) assumption, where the constituent phases in a two-phase mixture are assumed to be at thermal and mechanical equilibrium.

The first part of the study focuses on the development of an outflow model to simulate the failure of multi-segment pipelines incorporating valves and fittings passing through terrains of different inclinations. In the absence of real data, the numerical accuracy of the model is assessed based on the calculation of a mass conservation index. The results of a case study involving the comparison of the simulated outflow data based on the failure of a multi-segment pipeline as opposed to an equivalent single segment pipeline containing gas, liquid or two-phase inventories are used to highlight the impact of pipeline complexity on the simulated data.

The development and extensive testing of two models, namely the Hybrid Model and the Modified Homogeneous Equilibrium Model (MHEM) each addressing a principal limitation of the HEM are presented next. The Hybrid Model deals with the failure of the HEM in predicting post-depressurisation outflow for inclined pipelines containing two-phase mixtures or liquids through its coupling with a hydraulic flow model. The MHEM on the other hand addresses the failure of the HEM to accurately predict the discharge rates of flashing/ two-phase fluids discharging through an orifice.

Finally, the dilemma of the appropriate choice of the size and duration of the numerical discritisation steps expressed in terms of the Courant, Friedrichs and Lewy

(CFL) criterion on the stability and computational workload of the pipeline failure model is investigated for different classes of hydrocarbon inventories. These include gas, liquid (flashing and incompressible) and two-phase mixtures.

DEDICATION

I would like to dedicate this PhD thesis to my loving wife Mrs. Audian Denton. I love you more than words can ever express……..

ACKNOWLEDGEMENTS

I wish to thank the following people and organisations who have contributed so much in many ways to facilitate the completion of this thesis.

To God Almighty, the giver of life and the source of all wisdom. Thank you for everything.

My supervisor, Prof. Haroun Mahgerefteh for the opportunity given me to study in this field, your excellent supervision, and for ensuring my well-being.

To the ORS and the graduate school for the financial assistance. Thank you very much. I couldn't have done it without you.

To my family: Thank you for your love, prayers, support and guidance.

To my darling wife Mrs. Audian Denton, you are the love of my life, my strength and inspiration. Thank you for your understanding, patience and support throughout my studies.

Mr and Mrs. Dameon Miller: Thank you for your friendship and support.

My office mates Solomon, Navid, Shirin, Maria, Aisha, Peng and Emanuel it has truly been a pleasure meeting and working with you all.

The technical and admin. staff of the Department of Chemical engineering, UCL.

Finally, to Dr. Femi Atti and Dr. Umar Abbasi: Thank you for your friendship and guidance throughout my studies at UCL.

God bless you all in Jesus name, Amen and Amen.

CHAPTER 1: INTRODUCTION

The global demand for energy is projected to increase by 60 percent from 2002 to 2030 (International Energy Agency, 2009) due to economic growth and expanding populations in the world's developing countries such as India and China. Despite fossil fuels being non-renewable, the growing energy demand is expected to be met with increased oil and gas production. This has resulted in a significant increase in the use of pressurised pipelines, already by far the most widely used method for transporting oil and gas across the globe. In the US alone, almost 40% of its energy demand is supplied through such means. In some other countries this figure approaches 100%.

Given that such pipelines can be several hundreds of kilometres long conveying millions of tonnes of inventory at pressures as high as 150 bara, their accidental rupture can lead to catastrophic consequences (Mahgerefteh et al., 2008). According to data published by the US Department of Transportation for the period January 2000 to December 2008 (Office of Pipeline Safety, 2009), incidents involving pipelines transporting Natural Gas resulted in 24 fatalities and a total property damage of over $972,000,000.

In many developing countries it is now a statuary requirement to quantitatively assess all the major safety hazards associated with pressurised pipelines prior to their commissioning. In the United Kingdom, the Offshore Installations (Safety Case) Regulations 2005 (Health and Safety Executive, 2009) which came into force on April 6, 2006 require the operators of offshore platforms to identify all hazards with the potential to cause a major accident. The regulations also require the evaluation of all major accident risks and the measures used to control those risks to ensure that the relevant statutory provisions will be complied with. The assessment of fire and explosion risks are the essential first step in the effective management of such risks throughout the life-cycle of an installation. It lays the foundation for pipeline operators and safety authorities to determine minimum safe distances to populated areas and formulate emergency response planning.

Consequently, an essential part of the Safety Assessment Case for all pipelines transporting an appreciable amount of pressurised hydrocarbons is the prediction of the amount of inventory released and its variation with time following pipeline failure. These remain the two critical pieces of information required in assessing and quantifying the consequences associated with such failures which include, fire, explosion and environmental pollution. In the offshore industry, for example, such information has a direct impact on almost every safety aspect of the platform including the survival time of the temporary safe refuge.

However, the modelling of the outflow following pipeline rupture represents a set of unique challenges. Pipeline rupture results in an expansion wave that propagates from the rupture plane towards the intact end of the pipeline at the speed of sound. This wave imparts a drop in pressure which in turn results in a series of expansion waves which propagate into the disturbed fluid with an increasing negative velocity, -u and decreasing speed of sound, a. These waves result in the acceleration of the fluid particles in the opposite direction at a velocity u-a and hence outflow.

The development of a rigorous transient outflow model therefore requires the precise tracking of these expansion waves and their propagation as a function of time and distance along the pipeline length. This involves detailed consideration of several competing and often interacting factors including heat and mass transfer, unsteady flow and thermodynamics. The fact that the speed of sound is markedly affected by the state of the fluid (Mahgerefteh et al., 2000) which may in turn vary with time and distance along the pipeline, the model must also incorporate an accurate equation of state. Due consideration must also be given to the effects of heat transfer and friction both of which are flow and phase dependent. Finally, given that the constituent equations can only be solved using a numerical technique, the solution algorithm must be computationally efficient and capable of avoiding instabilities.

During the past decade, researchers at University College London (UCL) (see for example Atti, 2006) have developed a numerical model for simulating the fluid dynamics following the rupture of pressurised pipelines. The model accounts for the important processes taking place during depressurisation, including real fluid

behaviour, frictional effects, radial and axial flow in the proximity of puncture as well as the accompanying rapid pressure and thermal transients. The model utilises the homogeneous equilibrium model (HEM) where the constituent phases in a two-phase mixture are assumed to be in thermal and mechanical equilibrium. This assumption simplifies the analysis of two-phase discharge from a pipeline as a single set of conservation equations can be used to describe the behaviour of the fluid. Significant reduction in computational run times have been achieved through the development of fast numerical solution techniques (see Atti, 2006). The comparative results between the model and real data show very good agreement.

However, the model is limited to the release from single isolated or un-isolated pipelines. Additionally, long pipeline networks transporting hydrocarbons over varying topography are modelled as 'equivalent' single pipelines. Consequently, the pressure losses due to flanges, bends and elbows used to connect pipeline segments in long pipeline networks are not accounted for in the model. Neglecting these pressure losses can result in an over-prediction of the discharge rate and hence expensive mitigation to meet the statuary safety requirements.

This thesis describes the fundamental extension and testing of a single pipeline rupture model. The main thrust of the study involves the extension of this basic model to account for complex pipeline systems and improvements of the theoretical basis and numerical stability.

This thesis is divided into 10 chapters.

Chapter 2 is a review of the mathematical models available in the open literature for simulating pipeline failures. This includes the evaluation of their strengths and weaknesses in terms of robustness, computational efficiency and accuracy.

In chapter 3, the theoretical basis for the pipeline outflow model presented in this thesis together with its assumptions and justifications are presented. The chapter presents the basic equations governing flow, i.e. the conservation equations for mass,

momentum and energy. The energy balance model employed for estimating transient heat transfer across the pipeline wall and the isothermal steady state flow model are presented.

Chapter 4 presents a review of the methods used for the resolution of the conservative equations, including the method of characteristics (MOC) adopted in this study. The solution of the compatibility equations (obtained from the resolution of the conservation equations) by employing the Method of Specified Time intervals and the Euler predictor-corrector technique to enhance accuracy of the numerical results are also presented. Additionally, the nested grid system (NGS) of discritisation of the space-time domain is presented as a means of reducing the computational run time of the outflow model.

In chapter 5, the boundary conditions required to simulate the outflow from a multiple segment pipeline following failure are presented. These boundary conditions represent the source of upstream or downstream disturbances which are propagated along the length of the pipeline. The boundary conditions presented include boundary formed by a closed valve or dead-ended pipe (intact end point), full-bore rupture/orifice at pipeline end, puncture on the walls of a pipeline and junction of two pipelines (bends or connector) in a multi-segment pipeline network.

Chapter 6 presents the validation of the multi-segment pipeline outflow model. The outflow behaviour following rupture in straight pipelines as compared to rupture in pipeline networks are presented and discussed. For cases where experimental data are not available a mass conservation index is used to obtain a measure of the numerical accuracy.

Chapter 7 presents the formulation and validation of two models developed to address the limitations of the Homogeneous Equilibrium Model (HEM). The first model presented is the post-depressurisation hydraulic discharge model (termed the Hybrid Model) which accounts for the post depressurisation outflow from an inclined pipeline through coupling the HEM with a hydraulic flow model. The second model presented is the Modified HEM which addresses the failure of the HEM to accurately predict the

discharge rate of two-phase mixtures containing low quantities of gas through an orifice.

Chapter 8 presents the results of a sensitivity analysis to determine the impact of the Courant-Friedrichs-Lewy (CFL) criterion (Courant et al.,1926; Zucrow and Hoffman, 1976) on outflow predictions and computational run times following the puncture of a pressurised pipeline.

Chapter 9 presents the formulation and testing of a centrifugal pump boundary condition. The boundary condition utilises the steady-state pump curve of the centrifugal pump being modelled to predict the variation of pump discharge rate with pump head for un-isolated discharge from a pipeline following its failure (i.e. pumping continues despite pipeline failure).

Chapter 10 deals with general conclusions and suggestions for future work.

CHAPTER 2: LITERATURE REVIEW

2.1 Introduction

Interest in the modelling of accidents involving failure of pressurised pipelines started as a result of research carried out in the nuclear power industry (Offshore Technology Report, 1998) evaluating the critical scenarios of loss of coolant accidents (LOCAs) in Pressurised Water Reactors (PWRs).

In recent years however, there have been numerous pipeline rupture accidents in the oil and gas industry. Consequently, there have been subsequent stricter safety design regulations and heavy financial penalties. With easy access to relatively fast and inexpensive computational resources, strong interest has been stimulated in understating and modelling of pipeline failures.

In this chapter, various methods for modelling unsteady state flow following pipeline rupture are reviewed. Particular emphasis is paid to describing the Method of Characteristics as the solution technique for the resulting partial differential equations governing the flow as this methodology is employed in this study. Where possible, results relating to the validation of the models in comparison with available real data are presented.

2.2 Review of Mathematical Models

In 1998, the Health and Safety Executive UK (HSE) published a review on engineering software, which can be used to model release following full-bore rupture of offshore pipelines conveying fluids at high pressure (see Offshore Technology Report, 1998).

Since then, numerous publications relating to different aspects of pipeline failure/blowdown and its mathematical simulation have been published. Six of these models have found widespread use in industry and academia for simulating outflow following pipeline failures. These include:

1. APIGEC Models
2. British Gas Model
3. OLGA
4. PLAC
5. Imperial College London Models
6. University College London Models

2.3 APIGEC Models (TRANSFLOW and Exponential Equation)

In 1978, a study was conducted by the Alberta Petroleum Industry Government Environmental Committee (APIGEC, 1978) to evaluate and improve H_2S isopleth prediction techniques. Three stages involved in gas release including blowdown, atmospheric dispersion and plume rise from a pipeline following failure were considered. The last two stages are not of interest in this study, hence only the blowdown stage is herein discussed. Two blowdown models were employed to create the common blowdown curves, which were later used for dispersion calculations. These models were the TRANSFLOW blowdown model, and a simplified exponential blowdown model.

The TRANSFLOW model, based on mass, momentum, and energy balances employs a numerical simulator to calculate the time curve defining the rate of gas blowdown from the pipeline. The model accounts for valve closure, frictional effects and gas flow rate in the line before rupture. No further information about the model's theoretical basis including the thermodynamics, fluid flow dynamics and how the numerical simulator solves the conservation equations are supplied. It is therefore difficult to comment on the validity and the range of applicability of the model.

The second APIGEC blowdown model employed for calculating the discharge rate was a simplified exponential equation given by:

$$Q = A.e^{(-B.t)} \qquad (2.1)$$

Where Q and t are the gas flowrate in m^3/s and time in seconds respectively. A and B are constants depending on pipeline dimension, fluid inventory, initial pressure, and temperature.

The above equation however lacks theoretical basis and does not allow for valve closure, or gas flow or the associated pressure drop within the pipeline.

Figure 2.1 shows the variation of mass flow rate with time obtained by comparing the results of the TRANSFLOW model with field data. The data was obtained during the blowdown of a 168 mm diameter pipeline at an initial pressure of 69 bara. No information regarding the inventory composition or pipeline length was given. From the figure, it may be observed that the model underestimates the blowdown rate, with the total mass released being approximately 12 % lower than experimental results.

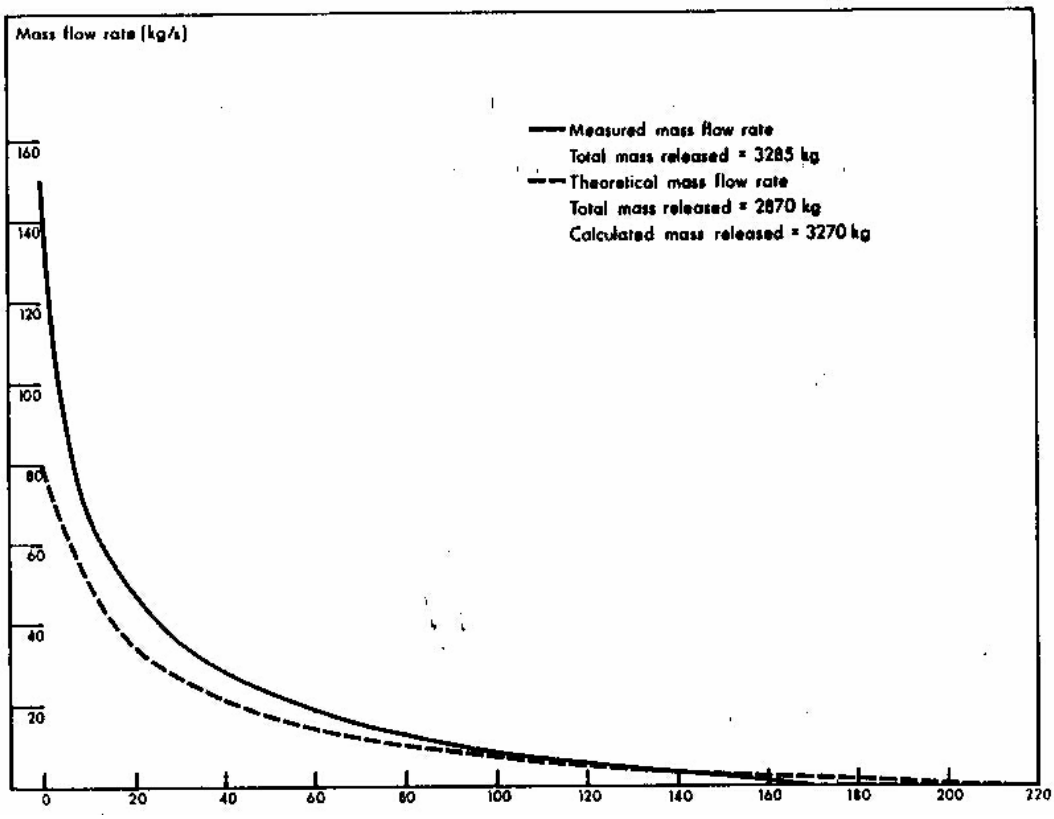

Figure 2.1: Mass flow rate from a 168.3 mm ruptured pipe at an initial pressure of 69 bar and gas temperature 10^{O}C (APIGEC, 1979).

By applying the TRANSFLOW blowdown model to various hypothetical cases, the authors observed that the pipeline length strongly affects the overall shape of the blowdown curve. However, this has no effect on the release rate during the early stages (ca 0 – 10 s) of blowdown. It was also observed that the initial release portion of the curve was strongly influenced by line pressure. However, gas temperature and initial fluid velocity have little effect on the blowdown behaviour.

The authors compared the results generated by the two blowdown models (TRANSFLOW and the exponential equation (2.1)) and concluded that they compared reasonably well considering the simplicity of the exponential model.

The main drawbacks of the APIGEC models are that they have been developed solely for gaseous flows, and hence cannot be applied to a two-phase or liquid discharge. In addition, the exponential model is incapable of simulating the fluid properties such as temperature and pressure both within the pipeline as well as at the rupture plane. Such data are essential for simulating other important consequences of pipeline rupture including brittle fracture, wax or hydrate formation.

2.4 British Gas Model (DECAY)

Jones et al. (1981) reported on a model named DECAY for analysing high-pressure natural gas decompression behaviour following pipeline rupture. The model is based on isentropic and homogeneous equilibrium fluid flow, limited to horizontal pipelines. It accounts for wave propagation along the length of the pipeline and uses the Soave-Redlich-Kwong equation of state (SRK EoS) to obtain fluid property data.

In order to validate their model, Jones et al. (1981) conducted a series of shock tube experiments using different fluid compositions. An instrumented 36.6 m long, 0.1 m diameter tube, was used for this purpose. Depressurisation was initiated by detonating an explosive charge located at the end of the tube resulting in a full-bore rupture.

Based on the variations of pressure with time along the tube length as shown in figures 2.2 and 2.3 respectively, the authors reported good agreement between the simulated results and experimental data.

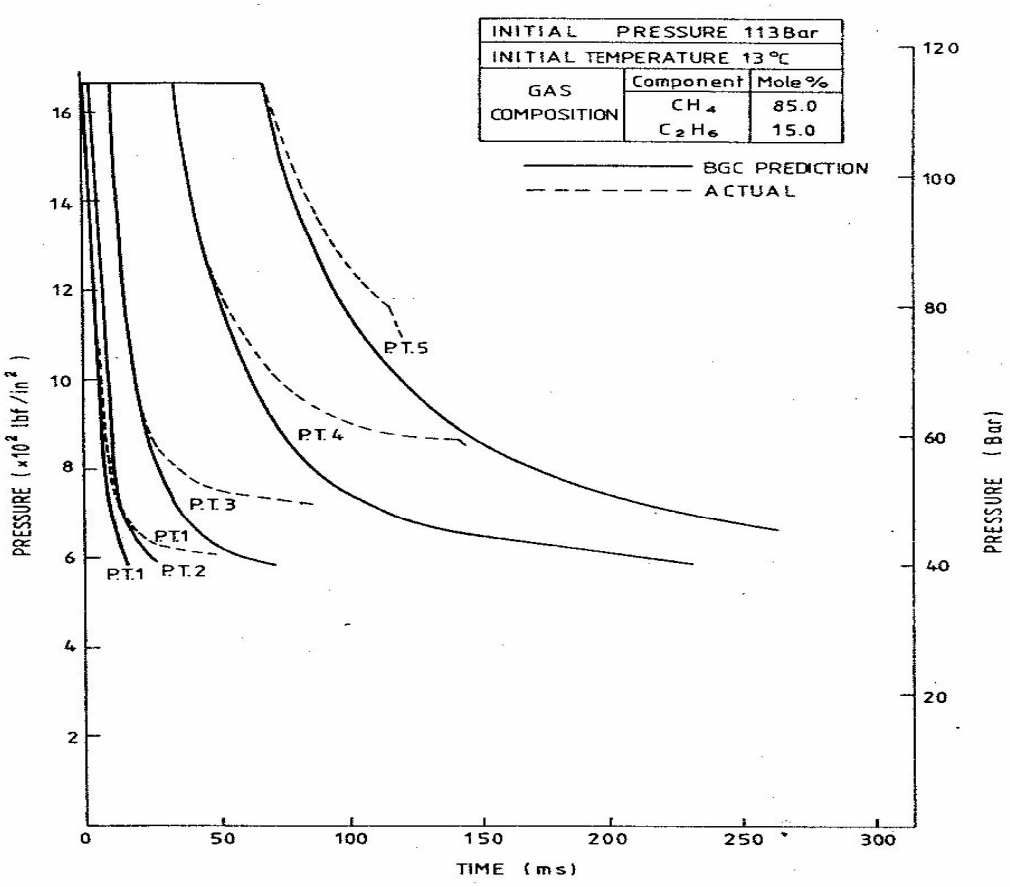

BGC SHOCK TUBE TEST
METHANE / ETHANE

Figure 2.2: Comparison between British Gas model [DECAY] and experimental data (Jones et al., 1981).

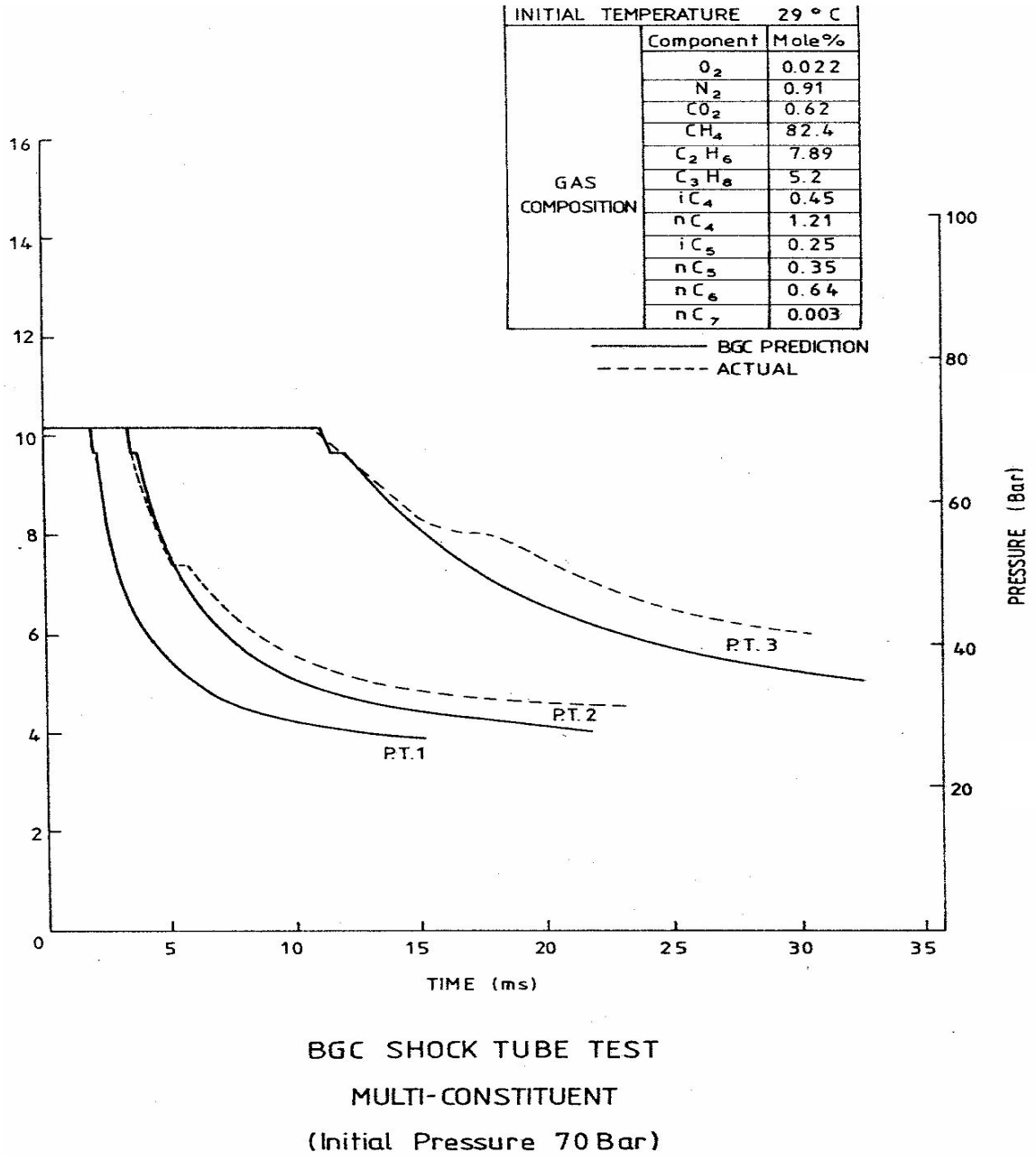

Figure 2.3: Comparison between British Gas model [DECAY] and experimental data (Jones et al., 1981).

Although good agreement was obtained with experimental data, the performance of the model is uncertain with respect to the blowdown of long pipelines, including those conveying flashing fluids. More so, neglecting the effects of friction and heat transfer

irrespective of the depressurising fluid and pipeline length can result in errors in simulated results (Kimambo et al., 1995).

2.5 OLGA (Scandpower)

The first version of OLGA was developed for the hydrocarbon industry by Statoil in 1983 to simulate slow transients associated with terrain-induced slugging, pipeline start-up, shut-in and variable production rates. Its physical model was initially based on small diameter data for low-pressure air/water flow. Initially, OLGA could successfully simulate bubble/slug flow regime but it was incapable of modelling stratified/annular flow regime. Bendiksen et al. (1991) addressed this problem as well as extending the model to deal with hydrocarbon mixtures.

In OLGA, separate conservation equations are applied for gas, liquid bulk and liquid droplets, which may be coupled through interfacial mass transfer. Two momentum equations are used:

1. A combined equation for the gas and possible liquid droplets
2. An equation for the liquid film

Heat transfer through the pipe walls is accounted for by a user specified heat transfer coefficient. Different frictional factors are used for the various flow regimes. The pertinent conservation equations are solved using an implicit finite difference numerical scheme which gives rise to numerical diffusion of sharp slug fronts and tails thus failing to predict correct slug sizes (Nordsveen et al., 1997). This problem was then addressed in a later version (Nordsveen et al., 1997) by introducing a Langrangian type front tracking scheme.

Due to inherent limitations in the numerical methods and two phase models in OLGA (Chen et al., 1993), proper phase behaviour is not incorporated.

2.5.1 Computational Runtime

No information is available publicly on OLGA's computational run time.

2.5.2 Validation of OLGA

Rygg et al. (1991) modelled a 92 kilometres long 0.36 m diameter pipeline linking two platforms using OLGA. The operational pressure ranged from 50 to 85 bara with an average temperature ranging between 10 ^{o} and 65 ^{o}C.

Figures 2.4 and 2.5 show the variation of cumulative gas and liquid mass released respectively with blowdown time when employing the slip (non-homogeneous) and no-slip (homogeneous equilibrium) assumptions.

The authors noted that the graphs illustrate that constraining the vapour and liquid phases to travel at the same velocity (i.e., homogeneous equilibrium or no slip assumption) could result in significant underestimation of the outflow rate for the vapour phase. The result of such an underestimate of the vapour outflow, when using the homogeneous flow assumption causes an initial underestimate of the outflow of the liquid phase and its subsequent overestimate at the latter stages of fluid discharge. The authors also noted that such gross inaccuracy in predicted outflow would be inadmissible in risk-assessment situations.

Similar findings were highlighted by Richardson et al. (2006) regarding the limitations of the homogeneous flow assumption for simulating two-pahse discharge through an orifice (See section 2.7.4).

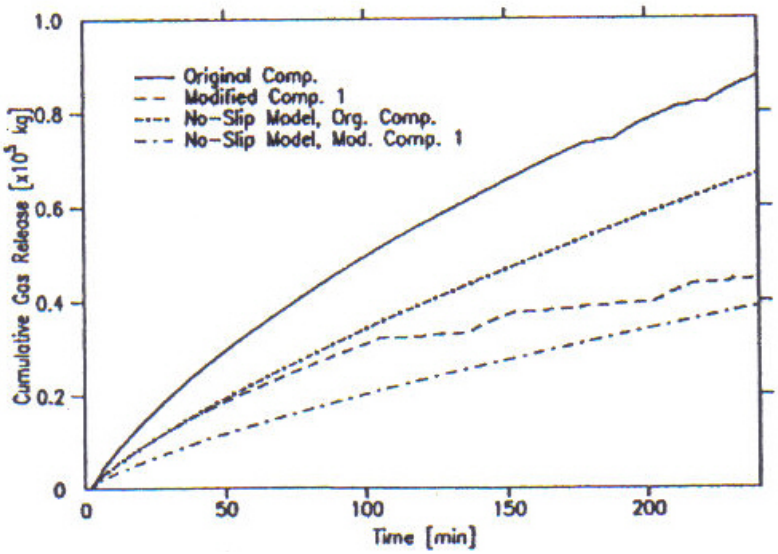

Figure 2.4: Cumulative gas mass release from the rupture point – four hours simulation (Rygg et al., 1991)

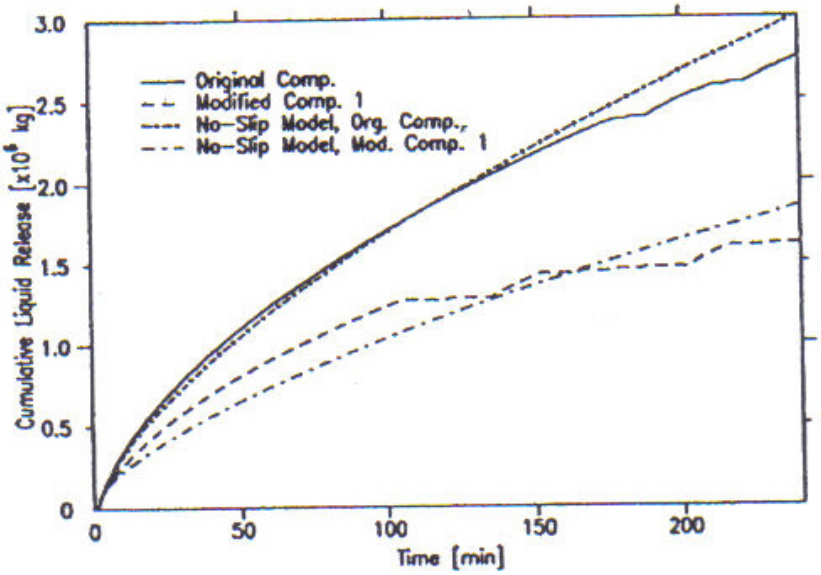

Figure 2.5: Cumulative liquid mass release from the rupture point – four hours simulation (Rygg et al., 1991)

OLGA was also validated under transient conditions by Shoup et al. (1998). The simulation results were compared with field data obtained by Deepstar for 'slow' and 'rapid' blowdown of a 5.28 km, 0.102 m diameter onshore gas condensate pipeline at

4.8 MPa (700 psi) discharging through 1.27 cm (slow blowdown) and 2.54 cm (rapid blowdown) choke openings. The precise mixture composition used was not given.

Figures 2.6 – 2.7 show the variations of pressure with time. The graphs show that reasonable agreement is obtained during slow blowdown, but the model performs relatively poorly when simulating rapid blowdown. The simulation assumes that blowdown occurs through a valve situated at the end of the pipeline; this makes the model unsuitable for modelling punctures or valves located on the walls of the pipeline, where flow is in both the axial and radial directions.

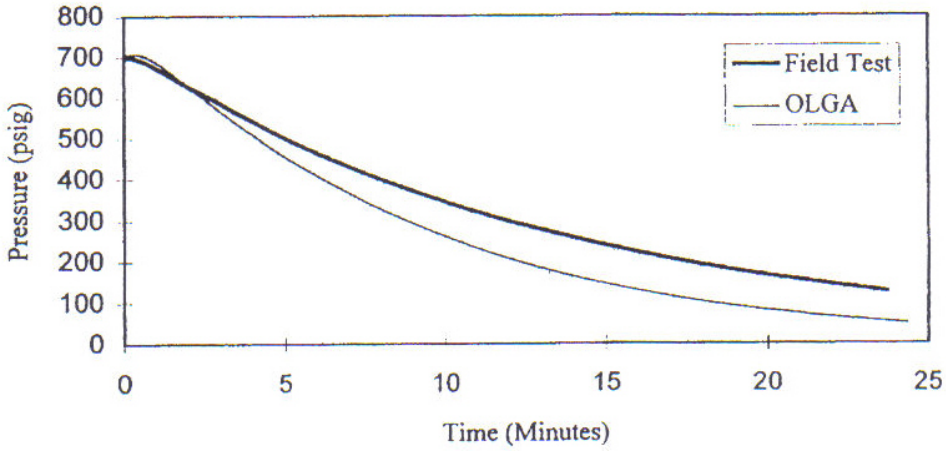

Figure 2.6: Rapid Blowdown – Pressure at Site 3. OLGA Simulations versus Field Test (Shoup et al., 1998)

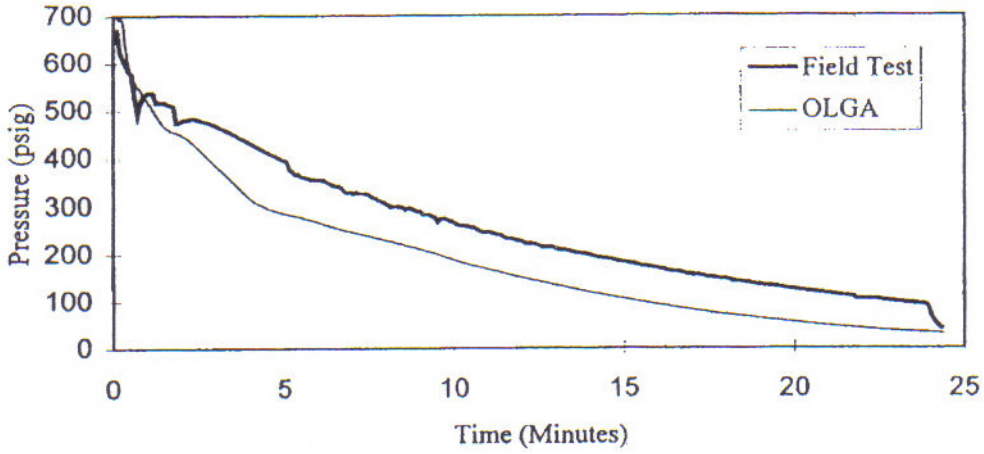

Figure 2.7: Rapid Blowdown – Pressure at Site 6. OLGA Simulations versus Field Test (Shoup et al., 1998)

2.6 PLAC (Pipe Line Analysis Code); PROFES (Produced Fluids Engineering Software)

PLAC (Pipe Line Analysis Code) was initially developed for the nuclear industry to simulate rapid transients within the cooling system pipe-work following prescribed failure scenarios (Peterson et al., 1985). PLAC can be regarded as a general transient two-phase model whose original purpose was the modelling of terrain-induced slugging in transportation pipelines. Furthermore, it is claimed (Hall et al., 1993; see also Philbin et al., 1990; Philbin, 1991) that PLAC has the capacity to simulate transients resulting from start-up, shutdown, ruptures and severe slugging.

A recent upgrade of PLAC, PROFES Transient (Hyprotech, 2001) is said to be capable of simulating transients resulting from terrain-induced slugging, emergency shutdown, initial flow-line start-up, depressurisation, coupled with leaks and pipe ruptures. However, no publicly available literature has been discovered on the pertaining theory or validation of PROFES.

PLAC is formulated as a three-dimensional, two-fluid representation allowing for friction and other dynamic interactions between phases. However, it is used as a one-dimensional approximation. The PLAC code, as presented in available literature, employs six conservation equations (two each for mass, momentum and energy) plus an equation of state and 2(n-1) species equations, where n is the number of components. These equations distinguish the gas and liquid temperatures and so explicitly characterising the inter-phase thermodynamics. Also, both mechanical and thermal non-equilibrium are taken into account with the corresponding conservation equations being similar to the two-fluid model proposed by Wallis (Wallis, 1969).

At the rupture plane, PLAC makes use of the homogeneous frozen flow model as the critical flow boundary condition. Chen (Chen et al., 1995a, 1995b) refers to this assumption as being empirical or physically unrealistic critical flow boundary condition, which is capable of contributing significantly to the poor performance of PLAC as a predictive tool for simulating outflow following FBR of pipelines.

PLAC's thermodynamic formulation for multi-component phase interaction is very elementary. The thermodynamics used are implemented by means of the package EQUIPHASE, which is based on the Peng-Robinson equation of state (Walas, 1987). A recent improvement allows a user defined equation of state. EQUIPHASE generates PVT look-up tables from which interpolations are used to characterise the phase behaviour and fluid properties (Hall et al., 1993). This interpolation approach may introduce errors in the fluid property predictions. Also, the thermodynamic package is not capable of determining the phase boundaries and fluid states accurately (Chen et al., 1995b). These limitations are considered as the main contributing factors for PLAC's poor performance in simulating real data during FBR (see section 2.62).

2.6.1 Computational Runtime

PLAC's fully optimised code has a typical runtime of 0.25 s per time step for a model using 100 cells on a SUN Sparc2 workstation.

2.6.2 Validation of PLAC

Philbin (1991) compared PLAC's predictions with experimental data obtained by Cunliffe (1978) for the production rate change in the Marlin gas condensate trunk line near Melbourne. The line was subjected to an increase in flow from 2.14 kmol/s to 3.57 kmol/s. The composition of the fluid in the line is not given. Figure 2.8 shows a comparison between the observed and calculated condensate outflow, while figure 2.9 represents the topography of the line.

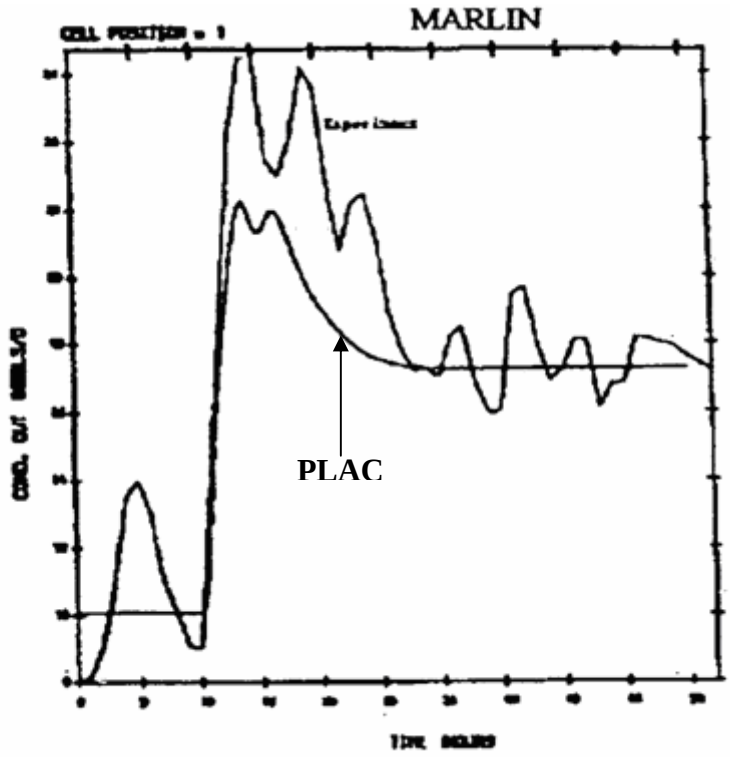

Figure 2.8: Condensate flow rate out versus Time for the Marlin Gas-condensate Trunk line (Philbin, 1991)

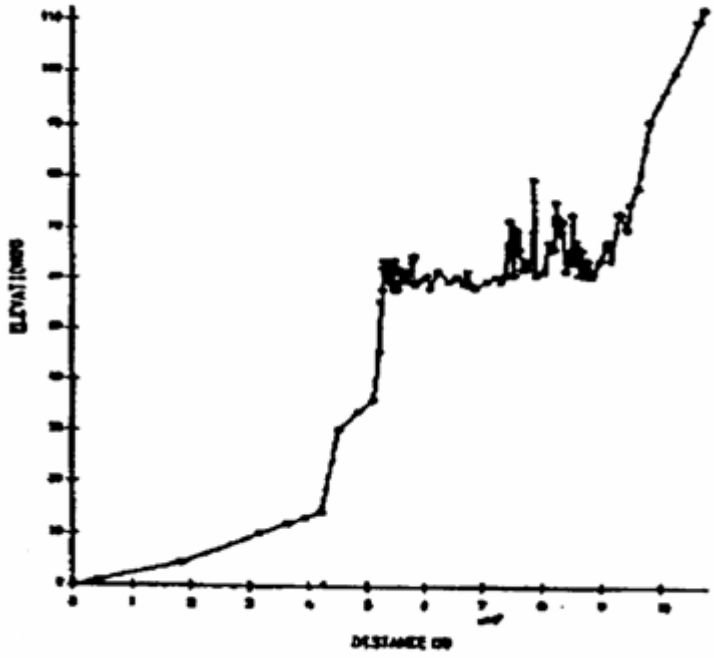

Figure 2.9: Topology of the Marlin Gas-condensate Trunk line (Philbin and Govan, 1990)

It can be seen from figure 2.8 that PLAC underestimates the initial surge following the change in flow rate. Philbin (1991) attributed this to a correlation (Andritsos, 1986) used for internal friction which over predicts at high pressures. However, the final condensate outflow is accurately predicted which is to be expected if the overall mass balance is to be satisfied. Nevertheless, the simulation overestimates the final approach to the final flow rate, although this is difficult to assess due to large variations in the experimental data. PLAC's failure to simulate such fluctuations is surprising because its perceived strength (Philbin et al., 1990) is that it can successfully simulate such terrain induced dynamic behaviour.

2.7 Imperial College London Models

2.7.1 BLOWDOWN

The computer simulation, BLOWDOWN was developed at Imperial College for modelling the quasi-adiabatic expansion process following the blowdown of pressure vessels. The model allows the evaluation of the risk of brittle vessel fracture due to low temperatures by simulating the fluid and hence the vessel wall temperatures during blowdown. BLOWDOWN remains the most comprehensive method for depressurisation of vessels. Mahgerefteh and Wong (1999) introduced a modification of this model which incorporates different equations of state.

BLOWDOWN accounts for non-equilibrium effects between the constituent phases, heat transfer between each fluid phase and their corresponding sections of vessel wall, interphase fluxes due to evaporation and condensation and the effect of sonic flow at the orifice. The outputs from BLOWDOWN simulations include the pressure, variations of discharge rate, and wall and fluid temperatures with time. The depressurisation process is approximated by a series of variable pressure increments. Critical flow is modelled by carrying out an energy balance across the release orifice.

Richardson et al. (1991, 1996a, b) extended BLOWDOWN to simulate depressurisation of pipelines by accounting for the frictional pressure drops along the pipeline. In this version of the model, the pipeline is discretised axially into many

elements. The elements are sized such that changes in physical properties along the element may be neglected. Single/two-phase flow is assumed to be quasi-steady (mass flow-rate is assumed to be the same in every element at a given time) and, for two phase flow the gas and liquid in an element move at the same velocity (homogeneous). The heat transfer between the fluid and pipe wall is assumed to be by forced convection, the heat transfer across the pipe wall (including any insulation) through conduction and the heat transfer between the pipe wall and ambient, forced/natural convection. For each element in the pipeline, the mass, energy and momentum balances are calculated and linked by an iterative scheme to satisfy the boundary condition of ambient or choking pressure at the open end of the line or exit of the orifice. The iterative variable is the mass flow rate through the line.

2.7.1.1 Validation

The extended 'pipeline version' of BLOWDOWN was validated with a reasonable degree of success by comparison with the data from a series of LPG blowdown tests. This was conducted jointly by Shell Oil and BP on the Isle of Grain (Tam et al., 1988). These tests (FBR and orifice discharge) involved the blowdown of a number of 100 m pipelines with diameters of 0.15 m and 0.5 m. The pipelines were made of carbon steel and instrumented to record the pressure, temperature and fluid inventory. The inventory comprised primarily of LPG (ca. 95 mole % Propane and 5 mole % Butane) in a pressure range of 8 - 21 bar. The results obtained for one of the experiments (test P42) is presented here for the purpose of this review.

Figures 2.10a-c respectively show the variations of the release pressure, temperature and inventory with time. As may be observed, reasonable agreement is obtained between the measured and experimental data although relatively large discrepancies in temperature profiles are observed towards the end of the blowdown. In addition, the predicted inventory remaining in the pipeline is consistently greater than the measured value. This, according to the authors, may be as a result of the quasi-steady and homogeneous flow assumption made in BLOWDOWN.

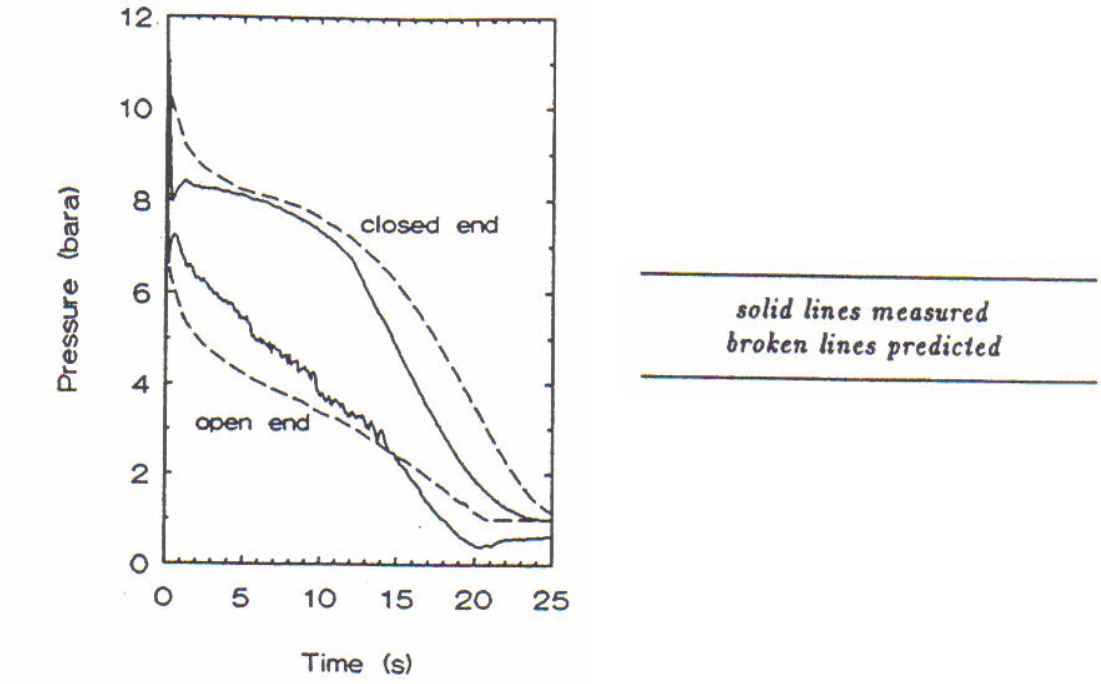

Figure 2.10a: variation of release pressure with time, Isle of Grain P42 Test (Richardson et al., 1996a)

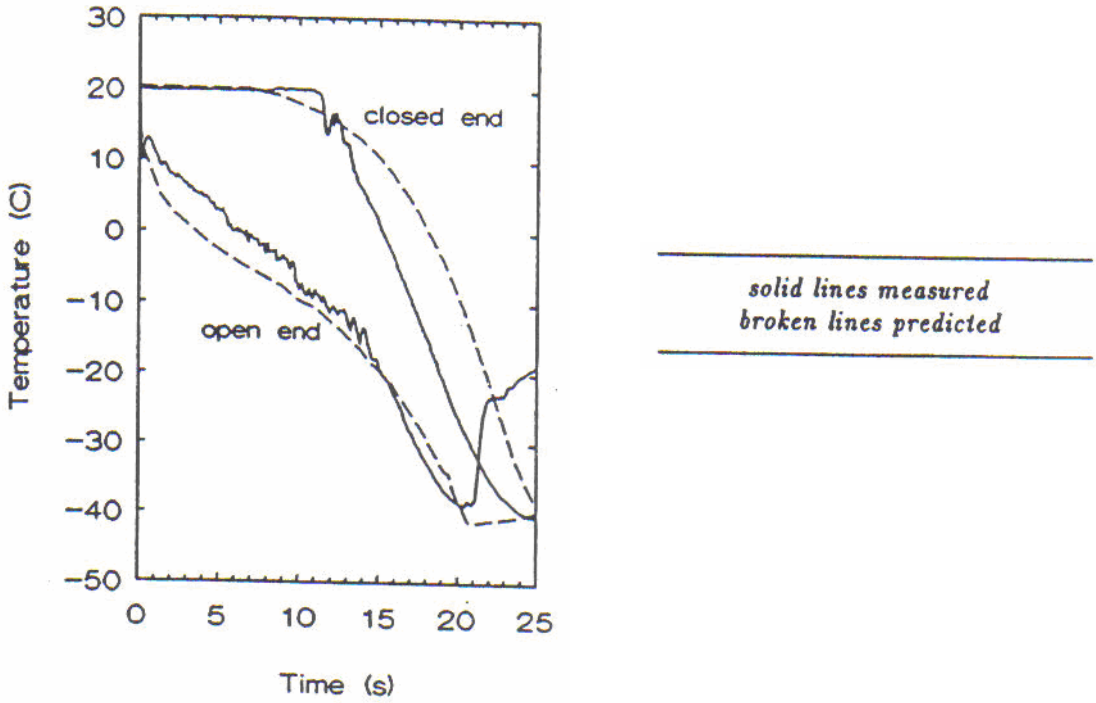

Figure 2.10b: variation of release temperature with time, Isle of Grain P42 Test (Richardson et al., 1996a)

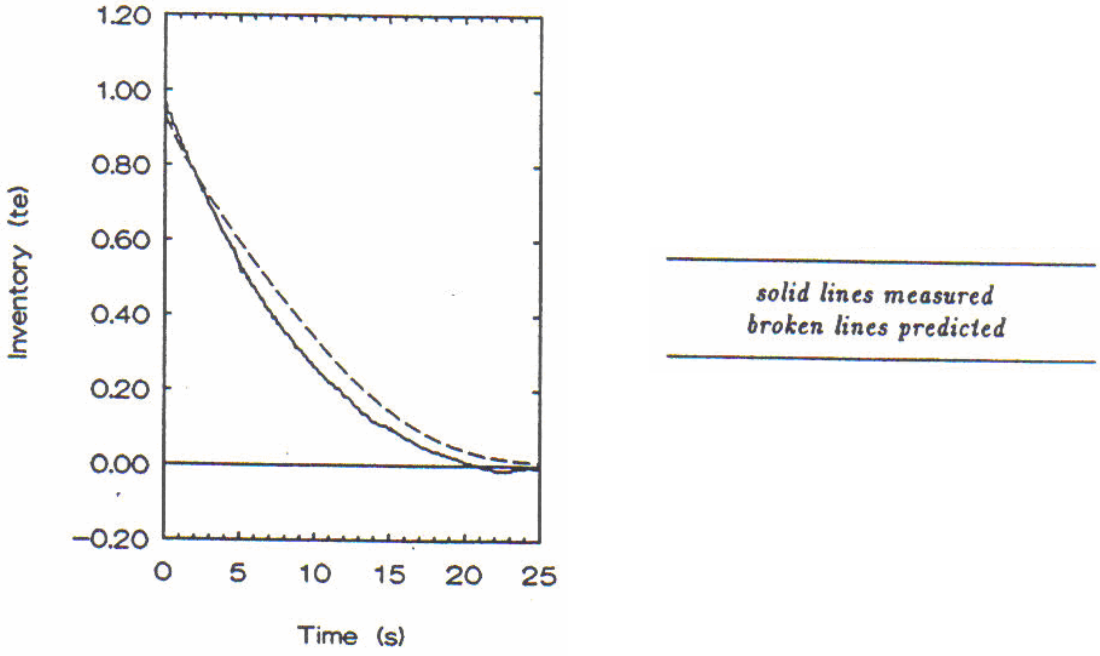

Figure 2.10c: Variation of cumulative mass with time, Isle of Grain P42 Test (Richardson et al., 1996a)

Although BLOWDOWN produces reasonable agreement with field data, the model does not account for the rupture induced expansion wave propagation. Such phenomena have a significant effect on the discharge process especially in case of the blowdown of long pipelines (see section 2.8).

2.7.1.2 Computational Runtime

BLOWDOWN typically requires a 'few' hours to simulate an Isle of Grain test, while the more refined model in which the quasi-steady state assumption is relaxed takes a 'few' days. The above CPU run times reported are based on the simulations performed on a 386 computer fitted with an 860 co-processor.

2.7.2 Chen et al., (1995a, b)

Picard et al. (1988) were the first investigators to emphasise the importance of accounting for real fluid behaviour in modelling of transient outflow in pressurised pipelines. As well as accounting for the above, in two further publications, Chen et al., (1995a, b) investigated the effects of assuming homogenous equilibrium as compared to heterogeneous equilibrium between the constituent phases on the accuracy of their simulations. In comparison to heterogeneous equilibrium, homogenous equilibrium assumes that all phases are at thermal and mechanical equilibrium, and travel at the same velocity. This assumption ensures the maximum possible mass transfer rate during any phase process, significantly simplifying the requirement of modelling the interfacial heat/mass transfer processes into a simple phase equilibrium calculation. In a further attempt to reduce complexity and hence the computational work load in Chen et al's (1995a, b) equilibrium model, it is assumed that the fluid phases are fully dispersed, thereby ignoring the concentration stratification effects accounted for in OLGA and PLAC when formulating the conservation equations.

2.7.2.1 Background Theory

The homogenous and heterogeneous equilibrium models are based on the solution of the mass, momentum and energy conservation equations. Pseudo thermo-physical properties are ascribed to the bulk fluid by assuming average values equal to the sum of the product of the mass fractions of the vapour and liquid and their associated property.

By including an explicit form of flow, non-homogeneity or Reynolds' stress in the kinetic energy of the two-phase system, Chen et al., (1995a) were able to show that the departure from equilibrium can be explicitly expressed in terms of the velocity difference between the liquid and the vapour phases. In such cases, hyperbolicity of the system is achieved by forcing the flow to be marginally stable. Under such conditions, all the information related to the structure of the flow that is not considered under the framework of non-dissipative, inviscid flow is found to be embedded in the inertial coupling constant.

In their second paper (Chen et al., 1995b), the simplified finite difference method developed earlier by the authors (Chen et al., 1993) for equilibrium two-phase models was extended and applied to the marginal stability model for multi-component mixtures. In this method, the flow channel is discretised using staggered meshes where the flow velocity is defined at the cell edge and all other variables defined at cell centre. Following the guidelines of the Fourier stability analysis, the scheme treats the momentum convection term explicitly and the flow velocity is expressed in terms of pressure. The density in the mass conservation equation is further eliminated using a locally linearised equation of state so that the discretised conservation laws can be reduced to two difference equations in terms of mixture enthalpy and pressure only. As there is no analytical solution for the speed of sound in real mixtures, its velocity at the rupture plane is calculated numerically.

Interfacial viscous drag and viscous drag at the fluid-wall interface are modelled as a linear combination of unsteady and steady drag or friction (Chen, 1993). Both of these parameters are flow regime dependent and different correlations are used for dispersed-bubbled flow (Ishii et al., 1979), intermittent flow (Schwellnus et al., 1991) and annular dispersed flow (Ishii et al., 1984).

The phase equilibrium relations and thermophysical properties of the fluids are provided by an in-house computer programme, PREPROP. This incorporates a Corresponding States Principle (CSP) based on an accurate equation of state for Methane (Saville et al., 1982) coupled with the Peng-Robinson (Peng et al., 1976) equation of state (PR). PR is considered to be generally more efficient than CSP while CSP predicts more accurate properties for 'Methane like mixtures' (Saville et al., 1982).

2.7.2.2 Validation and Discussion of Results

Figures 2.11a-d show the results of the heterogeneous equilibrium model, hereby referred to as META-MSM (META Marginal Stability Model, with META referring to the name of the main computer program) as well as homogenous equilibrium model (HEM) as compared against pipeline depressurisation test results obtained using a 'short' pipeline. The analogous data for a 'long' pipeline are shown in figures 2.12a-d.

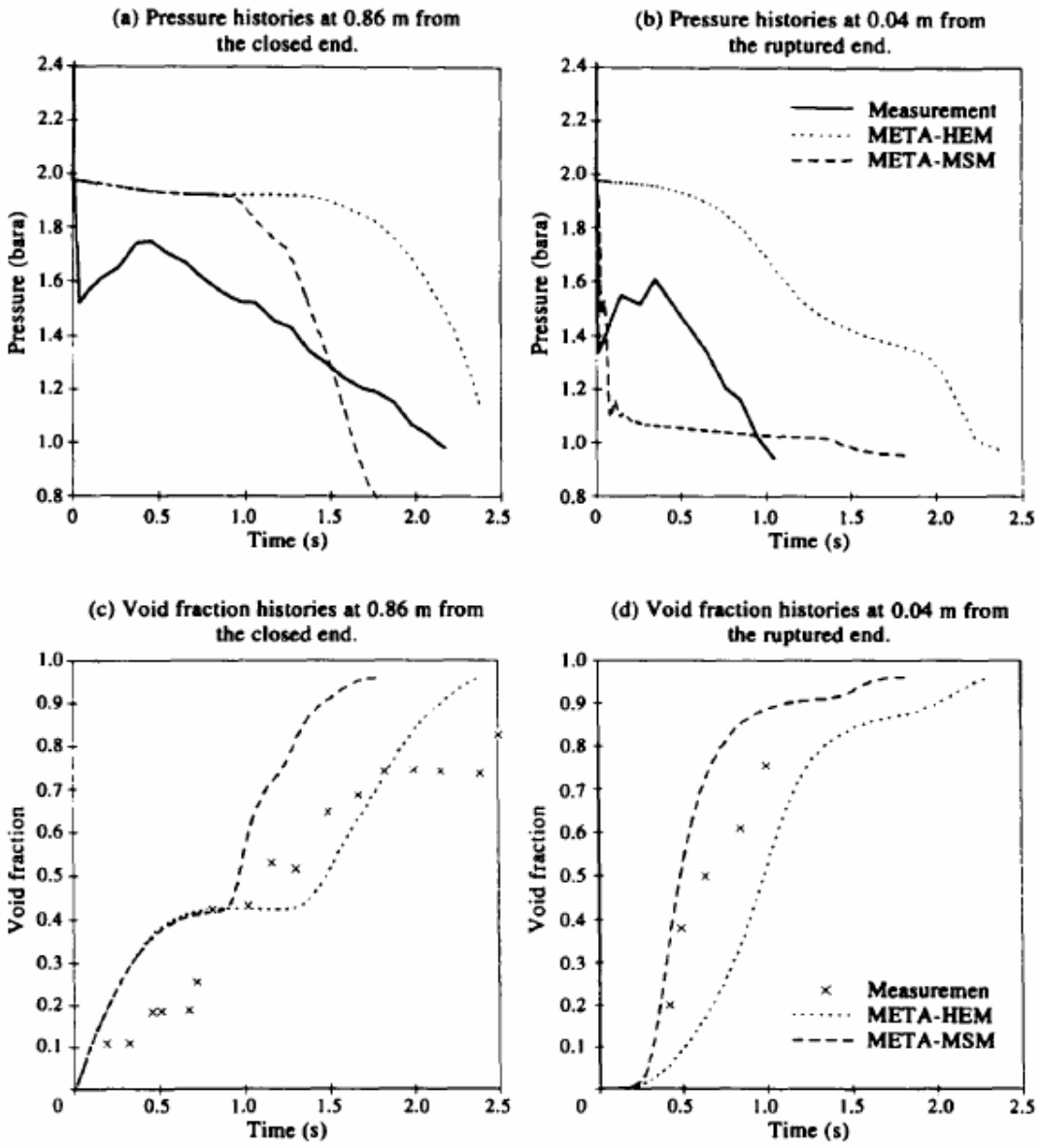

Figure 2.11 (a-d): Results of one-component systems for a 'short' pipeline (Chen et al., 1995a).

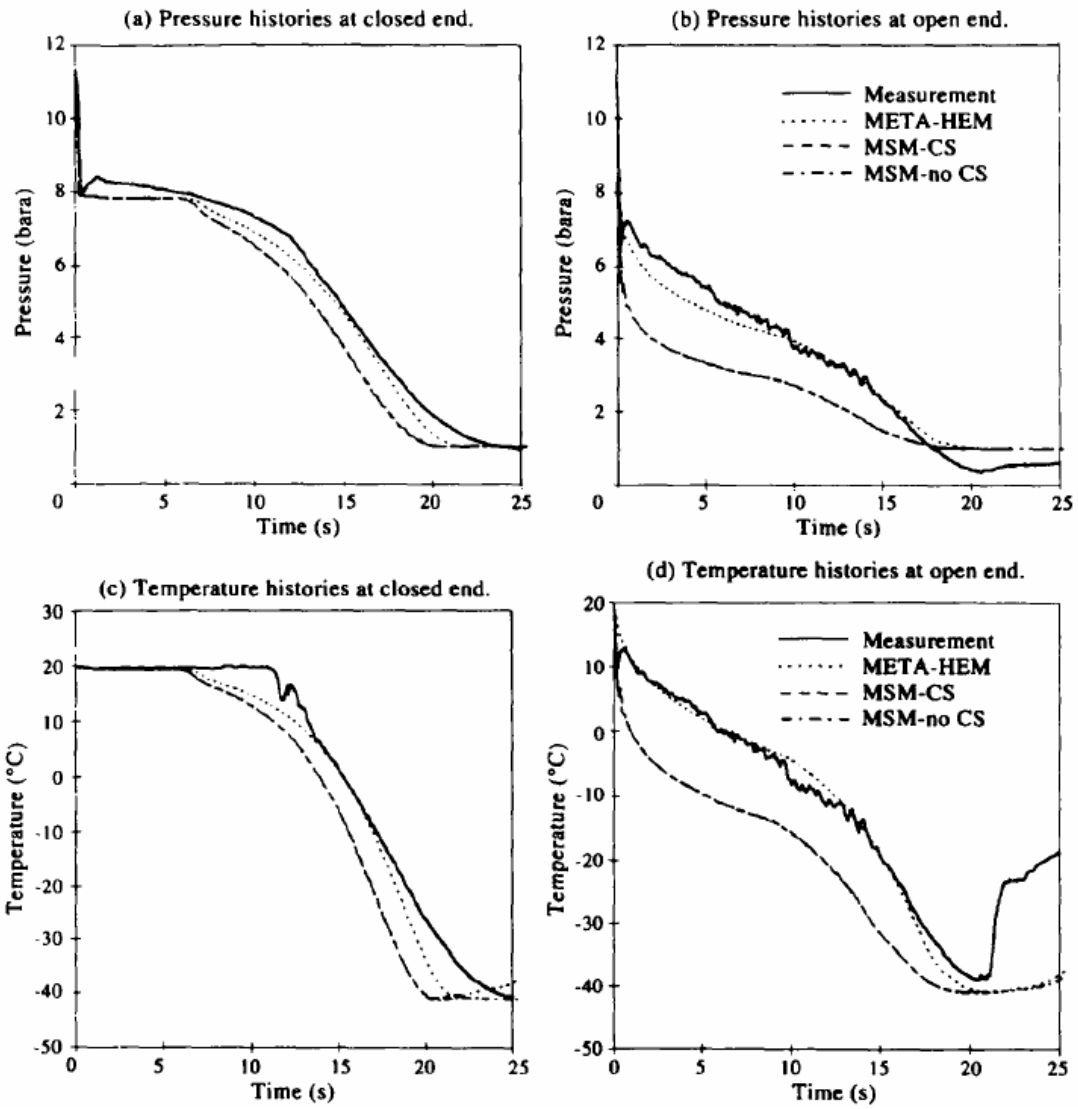

Figures 2.12 (a - d): Results of two-component systems (Chen et al., 1995a).

The long pipeline (100 m long, 0.15 m id) test results are those obtained from the Isle of Grain depressurisation experiments (Richardson et al., 1996a). These tests involved both blowdown through a discharge orifice as well as FBR of two 15.24 cm and 5.1 cm diameter 100 m long carbon steel instrumented pipelines. Inventory comprised primarily of LPG (ca. 95 mole % Propane and 5 mole % Butane) in the pressure range 8 - 21 bar. The pipe roughness was characterised by a length scale of 0.05 mm. A large number of experiments were carried out during these tests. Only a few were selected by Chen et al. (1995a) for illustration purposes.

In the case of the short pipeline (Figure 2.11a-d) (Necmi et al., 1978), it is clear that, META-MSM provides better agreement with field data as compared to META-HEM, although the performance of neither model can be considered as being good. In the case of the long pipeline depressurisation tests on the other hand, a surprisingly good agreement between META- HEM and field data is obtained. The agreement is in fact better than the non-equilibrium based models (MSM-CS and MSM-no CS). The poor performance of the latter is probably primarily a consequence in the uncertainties associated with a large amount of empirical correlations used for the generation of the hydrodynamic data for the various flow regimes. Nevertheless, based on the data presented, it can be concluded that the homogenous equilibrium assumption is applicable in the case of depressurisation of the long straight pipeline.

Figures 2.11a-d also show the predicted results of MSM with (MSM-CS) and without concentration stratification (MSM-no CS). The agreement between these results is tantamount to suggesting that in transient blowdown processes in simple geometry pipelines containing multi-component mixtures such effects can be generally ignored.

2.7.2.3 Computational Run Time

25 uniform meshes of 0.16 m and 4 m long were used in the numerical simulation of the short and long pipelines respectively. The time step was in the range 0.0004 - 0.04 s. Each calculation for the short pipeline takes about 40 min on a DEC 5000/240 station. The corresponding computation time for the long pipeline is about 20 h for META-MSM and 8 h for META-HEM.

2.7.3 Richardson et al. (2006)

Richardson et al. (2006) conducted a series of extensive experiments on highly volatile mixtures of hydrocarbons (Natural gas (mainly Methane)), commercial Propane and condensate mixtures (C_5 and C_9)) at pressures up to 100 bar and flow rates of up to 4 kgs^{-1} in order to test the applicability of the Homogenous Equilibrium model (HEM) for predicting outflow of pressurised hydrocarbons through an orifice. The experiments were conducted at a test site owned by British Gas (BG) in Spadeadam Cumbria, United Kingdom.

2.7.3.1 Background Theory

Richardson et al. (2006) stated that single-phase incompressible liquids are known to exhibit the phenomenon usually referred to as vena contracta which requires corrections to be made for the Bernoulli's equations. Neglecting kinetic energy upstream, the mass flow rate through an orifice is given by:

$$M = C_d A[2(P_u - P_d)\rho]^{1/2} \qquad (2.2)$$

Where,

C_d = Discharge coefficient. $= \dfrac{actual\ \ flow\ rate}{theoretical\ \ flow\ rate}$

A = Cross-sectional area of the orifice.

P_u and P_d are the pressures, upstream and downstream of the orifice respectively.

ρ = Specific density of the liquid.

It was observed that C_d usually has a value of 0.60 for the discharge of a liquid through an orifice.

For the flow of single-phase gases, which do not undergo phase change while flowing through an orifice, two situations namely – choked and non-choked flow are possible. In choked flow, there is a marked difference between the upstream and downstream pressures. In non-choked flow, the pressure difference is not high enough and choking does not take place.

The values of the discharge coefficient, C_d, are expected to differ for these flow regimes. Although this situation is more or less defined for single phase flows, it is very complex for two-phase gas-liquid mixtures. This is because the possibility of the phases moving at different speeds. As mentioned previously, this phenomenon is known as 'slip' or 'non-slip' flow.

Richardson et al. (2006) also stated that for a compressed volatile liquid, if the fluid upstream of the orifice is single phase liquid, the HEM assumption may be inapplicable due to the slowness of the gas nucleation processes. This is because the slow gas nucleation may inhibit the establishment of phase equilibrium as the fluid passes through the restriction. Consequently, the authors assume the change in density of the fluid is negligibly small and hence the fluid is considered to be incompressible.

2.7.3.2 Experimental Arrangement

The experimental arrangement used by Richardson et al. (2006) is shown in Figure 2.13. Figure 2.14 shows the mixer that was used in the experiment with an orifice plate. The natural gas feed enters via the 50.8 mm inlet, the accumulator feed via the 25.4 mm axial inlet and the feed from the tank via the 25.4 mm inlet. Table 2.1 gives the compositions of the natural gas, propane and condensate used in the experiments.

The majority of the experiments were conducted using sharp-edged orifice plates as the restriction element. The set up in figure 2.14 is used for mixing a feed of natural gas with a feed from the accumulators. By spraying the feed from the accumulator into the gas as an annular jet, well mixed two-phase mixtures are obtained. In order to produce very poorly-mixed mixtures, the spray head was replaced by a long 25.4 mm pipe which extended from the entry flange of the mixer to well into the nozzle at the downstream end. This ensured that the feed from the accumulators was introduced into the stream of natural gas as close to the orifice as possible and thus good mixing was not achieved.

Measurements of pressure, temperature and flow rate were logged every 3 s.

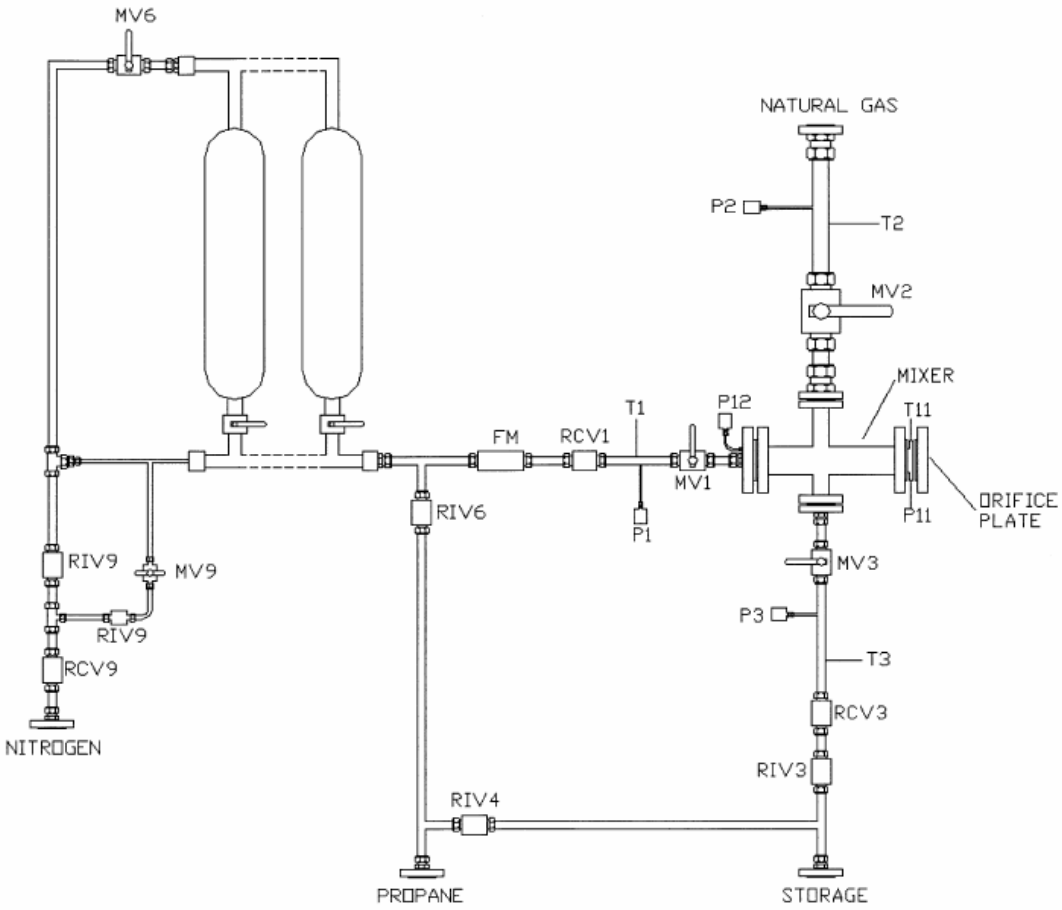

Figure 2.13: Experimental arrangement: RIV, remotely operated isolation valve; RCV, remotely operated control valve; MV, manual valve; FM, flow meter; P, pressure transducer; T, thermocouple (Richardson et al. (2006)).

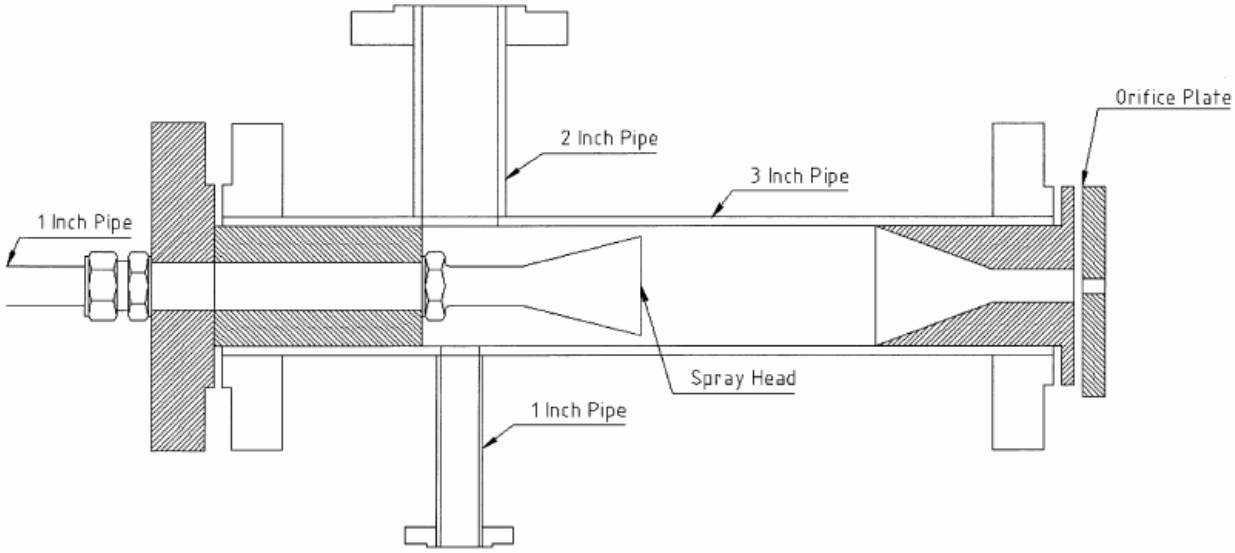

Figure 2.14: Mixer section, showing the three fluid inlets, the spray head and the orifice plate under test (Richardson et al. (2006)).

Table 2.1: Composition of natural gas, Propane and condensate used in the experiments (Richardson et al. (2006)).

	Mass fraction		
Component	Natural gas	Propane	Condensate
C1	0.897		
C2	0.089	0.003	
C3	0.011	0.963	0.002
C4	0.003	0.033	0.029
C5		0.001	0.104
C6			0.193
C7			0.262
C8			0.222
C9			0.110
C10			0.052
C11			0.014
C12 +			0.012

2.7.3.3 Results

The American Petroleum Institute (API) (American Petroleum Institute, 2000) produced a revised edition of API 520 recommended practice in January 2000 in which the HEM model was first introduced for the sizing of relief valves for two-phase flow. It replaced an earlier procedure (American Petroleum Institute, 1993) in which relief areas were calculated separately for the gas and liquid components and the two added together. Although API 520 is specifically concerned with relief valves, the same equations are frequently used for sizing orifices in, for example, emergency blowdown systems (Richardson et al., 2006). In view of the fact that many installed relief valves and restriction orifices were still sized according to the older document, Richardson et al. (2006) compared both the older and the newer API recommendations to the measured data and the HEM model PREPROP. However, for flows of compressed volatile liquid (the fluid is in the liquid phase upstream of the orifice), comparisons were made with an incompressible flow model.

Figures 2.15 - 2.18 show the variation of discharge coefficient with liquid mass fraction (upstream and within the throat of the orifice) obtained for mixtures of natural gas, Propane and condensate. Figure 2.19 shows the variation of discharge coefficient as a function of flow rate for natural gas.

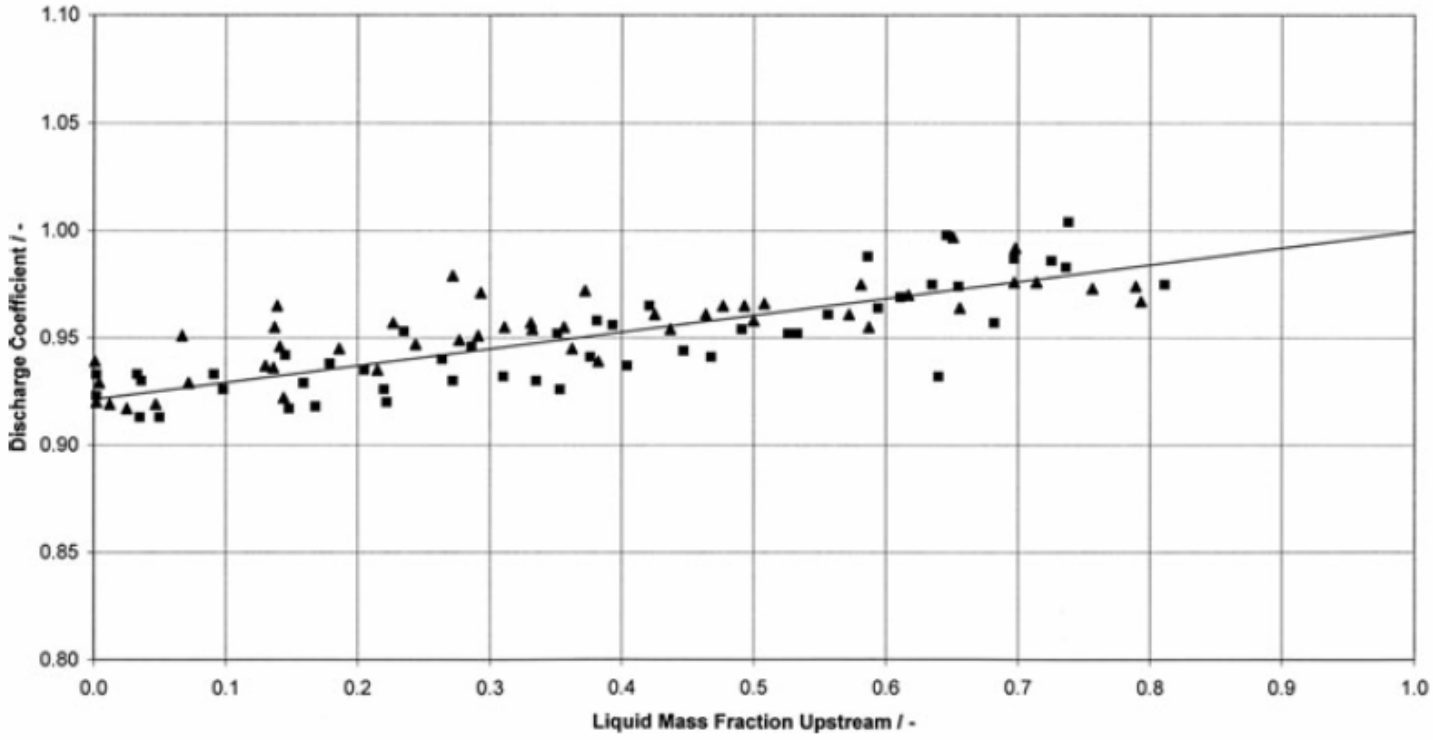

Figure 2.15: Discharge coefficient as a function of liquid mass fraction upstream of the orifice for natural gas plus Propane mixtures: squares, well-mixed mixtures; triangles, poorly-mixed mixtures (Richardson et al., 2006).

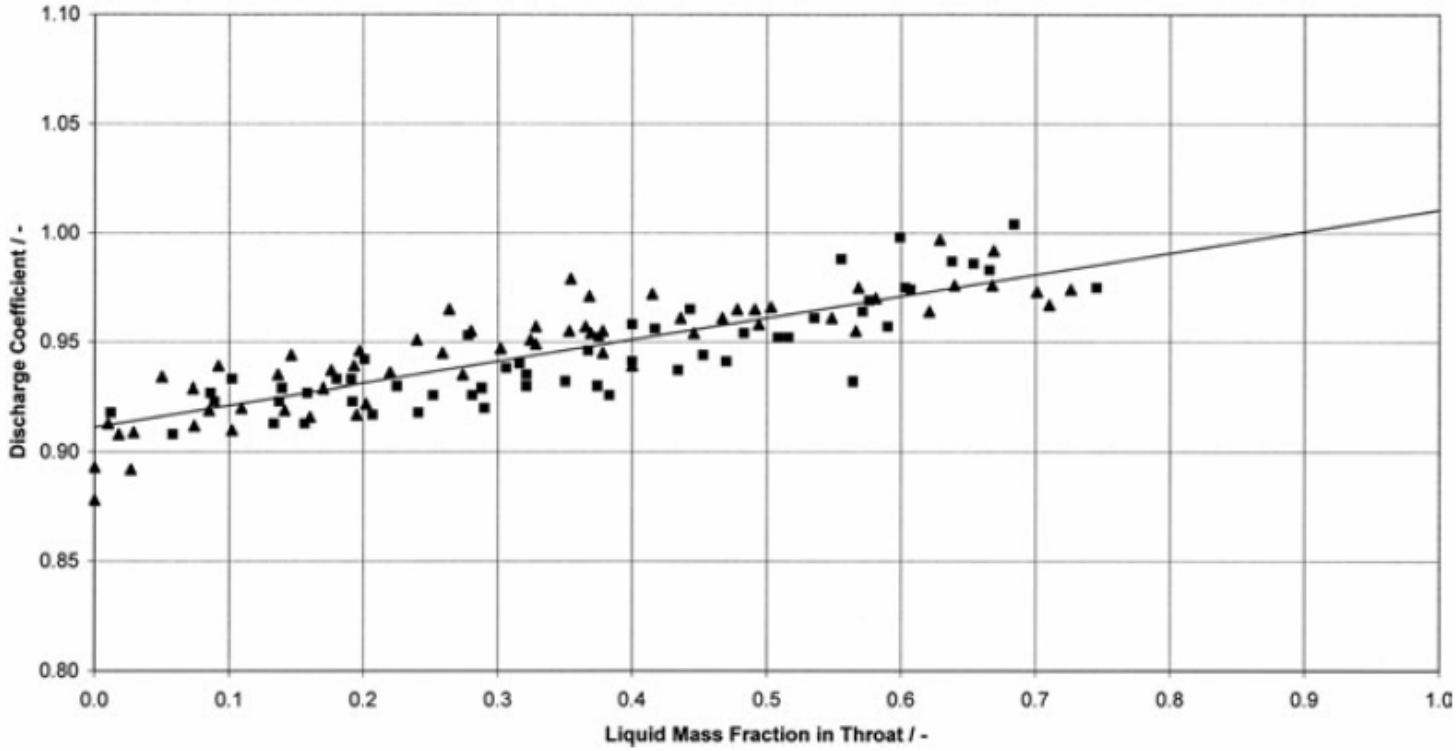

Figure 2.16: Discharge coefficient as a function of liquid mass fraction within the throat of the orifice for natural gas plus Propane mixtures: squares, well-mixed mixtures; triangles, poorly-mixed mixtures (Richardson et al., 2006).

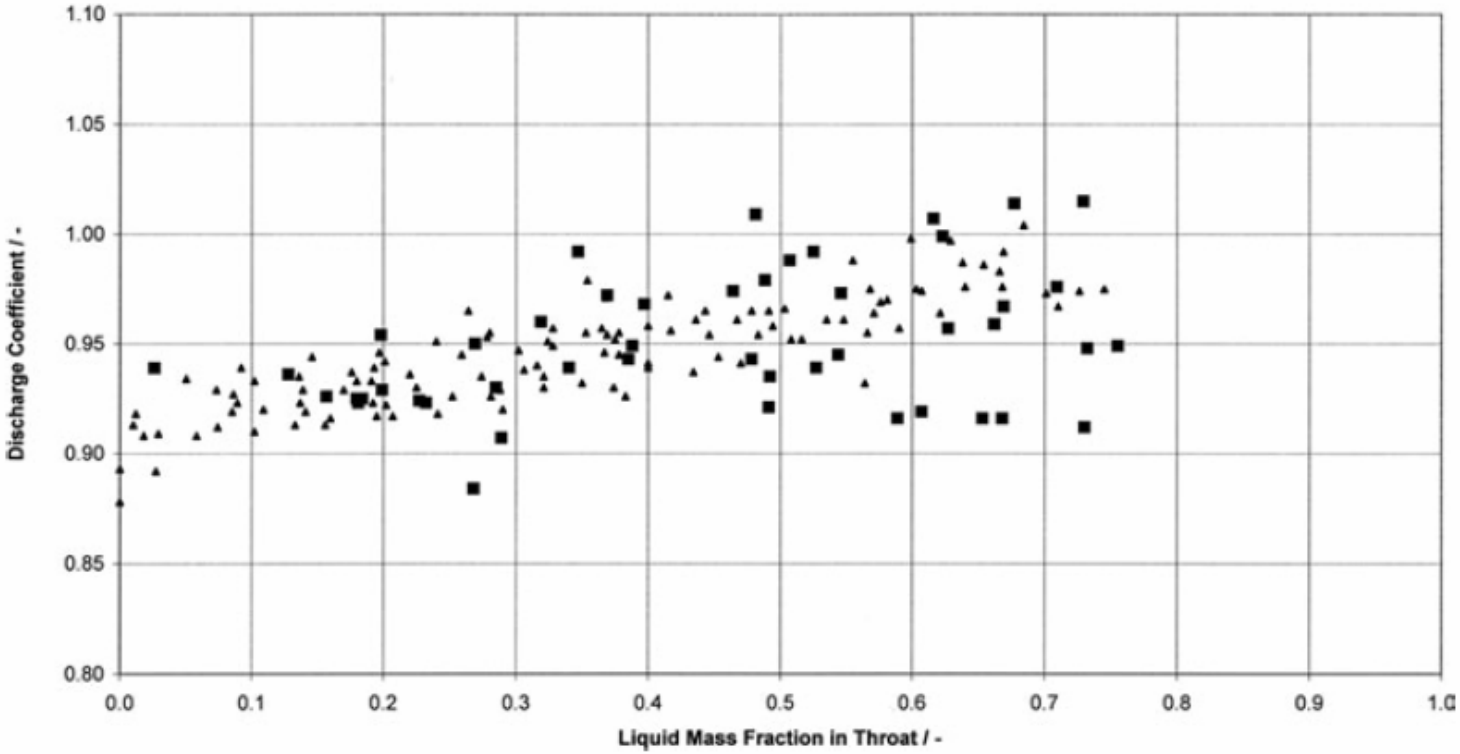

Figure 2.17: Discharge coefficient as a function of liquid mass fraction within the throat of the orifice; squares: pre-prepared mixtures containing natural gas plus Propane plus condensate; small triangles: natural gas plus Propane (Richardson et al., 2006).

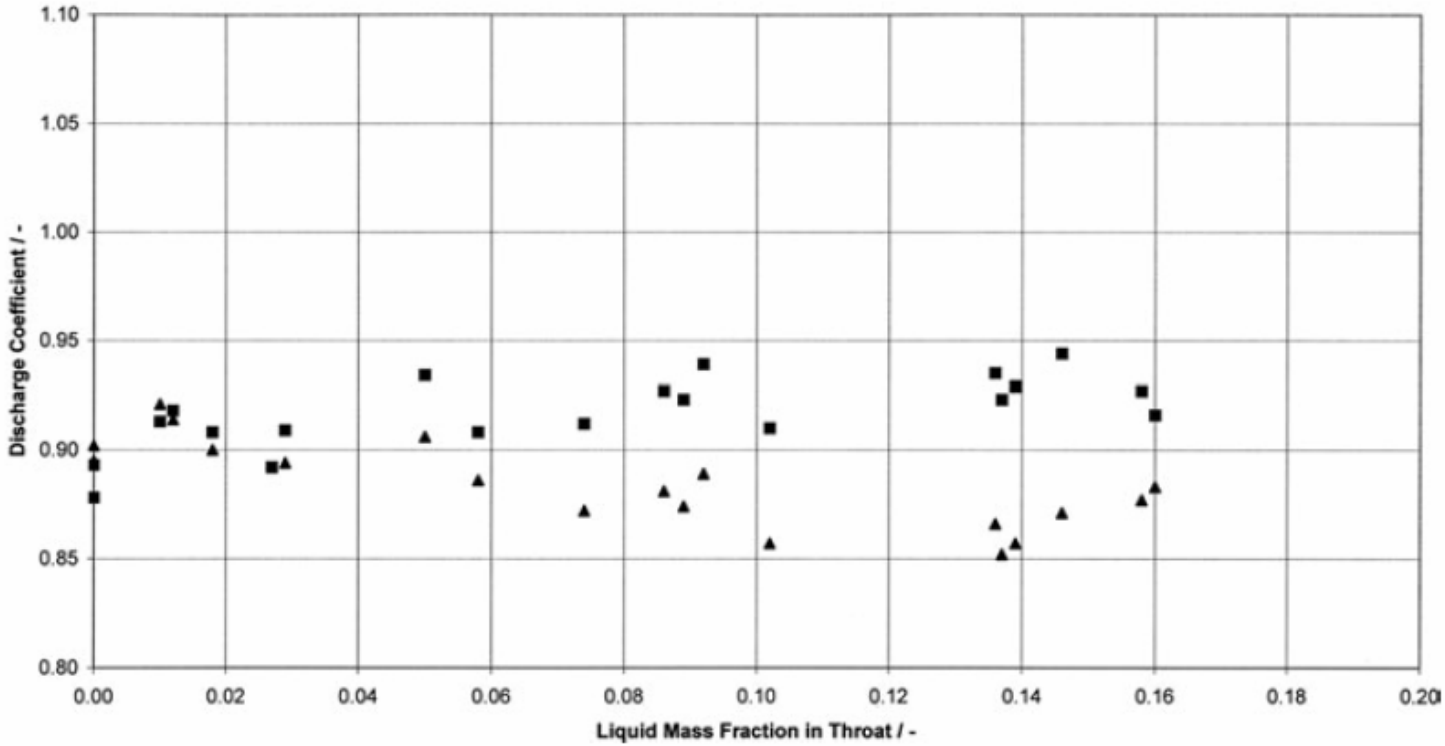

Figure 2.18: Discharge coefficient as a function of liquid mass fraction within the throat of the orifice for mixtures of natural gas plus Propane that are single-phase gas upstream of the orifice: squares, calculated according to the HEM model; triangles, calculated according to the API model (Richardson et al., 2006).

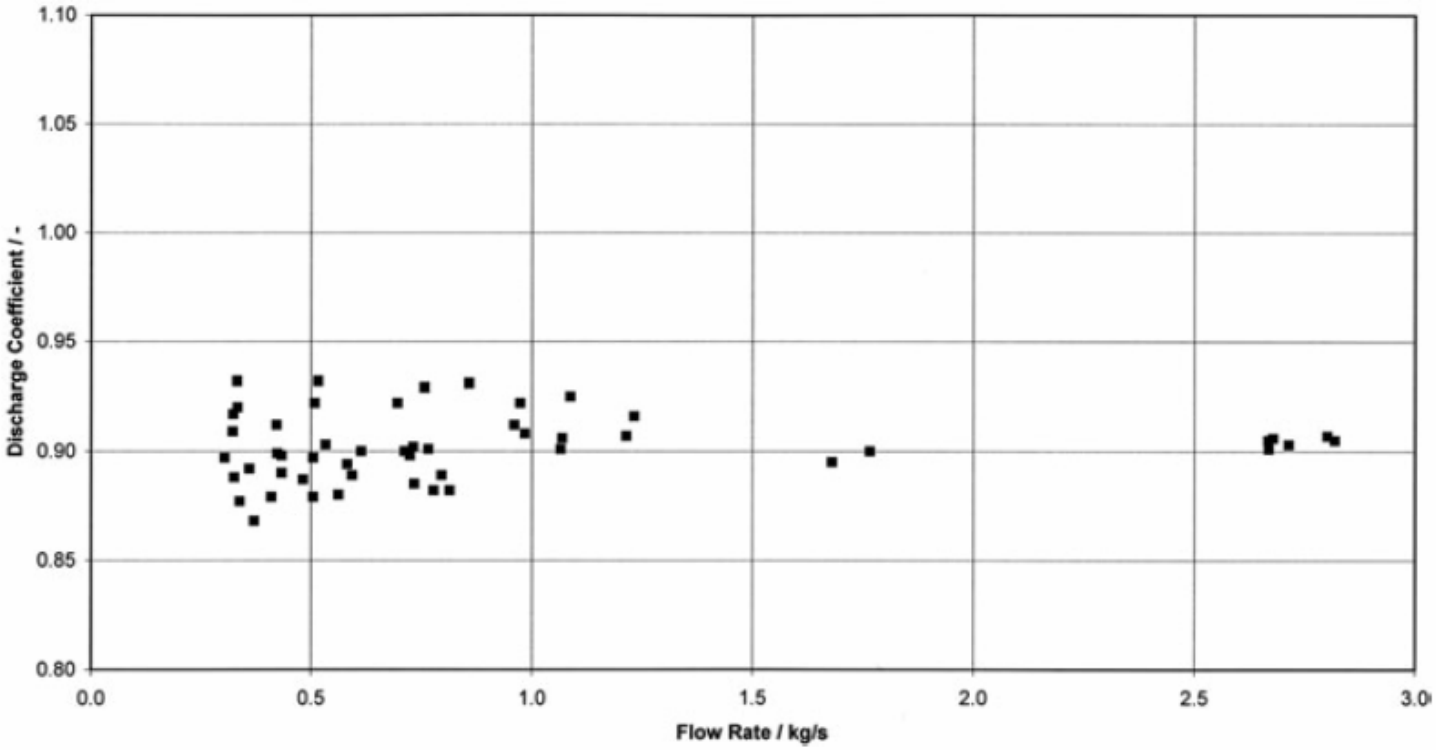

Figure 2.19: Discharge coefficient as a function of flow rate for natural gas (Richardson et al., 2006).

From the results obtained during the experiment, Richardson et al. (2006) concluded that for mixtures which contained below 0.8 liquid mass fraction, the HEM provided a good approximation. The discharge coefficient varied from 0.90 for pure single-phase gas flow to about 0.98 when the upstream liquid fraction is 0.8. For flows of compressed volatile liquids, the incompressible-flow model performs fairly accurately with a discharge coefficient of about 0.60.

Richardson et al. (2006) stated that for two-phase mixtures where the upstream liquid mass fraction is > 0.8 but < 0.97, these mixtures fall into a 'grey area' where neither the HEM nor the incompressible flow model is applicable. No experimental data was presented by Richardson et al. (2006) for this region. Additionally, the comparisons with the API recommendations revealed that in a number of circumstances the API predictions significantly over or under-predict the flow rates through restrictions.

2.8 University College London Models

2.8.1 Mahgerefteh et al., (1997-2008)

Between 1997 and 2008, Mahgerefteh et al. published a number of papers relating to transient modelling of outflow following pipeline rupture based on the solution of conservation equations for one-dimensional flow using the classical inverse marching method of Characteristics (Zucrow et al., 1976).

The dynamic response of both check and ball valves during emergency isolation were simulated by Mahgerefteh et al. (1997) where the inventory was treated as an ideal gas in order to illustrate the various dynamic effects in gas transmission pipelines.

Check valve closure is modelled by introducing closed end boundary conditions at the required time and space co-ordinates while for the ball valve, the authors account for the variation of flow rate as a function of time during valve closure.

Valve response following emergency isolation was modelled in conjunction with a real North Sea pipeline containing Methane of length and diameter 145 km and 0.87 m respectively. The initial flow velocity is 10 m/s and the line pressure and temperature are 133 bar and 283 K respectively. Under such conditions, the inventory will remain in the gas phase. The pipeline is partially insulated with an assumed heat transfer coefficient of 5 W/m^2K.

The authors investigated the effect of valve proximity to the rupture plane on the total amount of inventory released. Figure 2.20 shows the data for a ball valve and a check valve. For the sake of an example, the ball valve is designed to activate closure at a pressure of 10 bar below the normal working pressure and close at a rate of 2.54 cm/s. The check valve on the other hand is assumed to close instantaneously, upon the detection of flow reversal. The data indicates that for valves positioned in close proximity (up to 5 km) to the rupture plane, a check valve offers a much better degree of protection in terms of limiting the total amount of inventory released. For valves

positioned at larger distances, the difference in performance becomes progressively unremarkable.

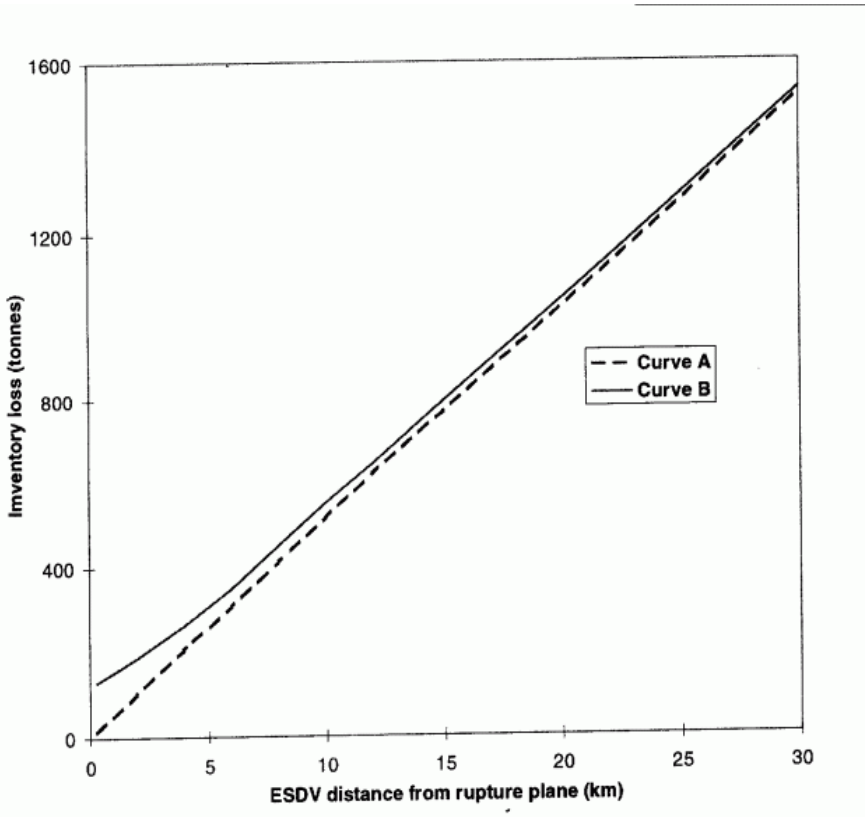

Figure 2.20: The variation of inventory loss as a function of ESDV proximity to the rupture plane: Curve A: Check valve; Curve B: Ball valve (Mahgerefteh et al., 1997).

In their second paper Mahgerefteh et al. (1999) account for real fluid behaviour using the PR-EoS and incorporating the pertinent hydrodynamic equations for two-phase flows. In addition, curved characteristics are employed in which the characteristics lines are replaced by arcs of parabolas. These are claimed to overcome the errors introduced as a result of using linear characteristics, which essentially assume a linear variation of thermo-physical properties between the various discretisation grid points. Based on earlier observations (Chen et al., 1995a, b), the homogeneous equilibrium model (HEM) in which all phases are assumed to be at thermal and mechanical equilibrium is assumed.

The problem of long CPU times associated with the numerical solution was largely addressed by using a compound nested grid system (CNGS) in which the penultimate, and the last grid next to the rupture plane are subdivided further.

The model presented in the 1999 publication (Mahgerefteh et al., 1999) was validated against intact end pressure data for the Piper Alpha riser as well as two sets of test results (P40 and P42) obtained from the Isle of Grain depressurisation tests. The results of the Piper Alpha simulation and test P40 are reviewed herewith.

Figure 2.21 shows the measured intact end pressure-time history following the FBR of the Piper Alpha to MCP-01 sub sea line. Curve A shows measured data whereas curve B shows the predictions using Compound Nested Grid System Method of Characteristics (CNGS-MOC). Curve C shows the corresponding data (CNGS-ideal) generated using linear characteristics in conjunction with the ideal gas assumption, as reported in a previous publication (Mahgerefteh et al., 1997). As it may be observed, the inclusion of real fluid behaviour results in good agreement with field data.

Comparing the CPU run times for the Piper Alpha simulation as shown in figure 2.21, it is difficult to rationalise the significantly shorter CPU run time for the CNGS-MOC ideal gas model as compared to CNGS-MOC real gas model (c.f 1.5 minutes with 6 days). This is more so considering the Chen et al. (1992) MOC based ideal gas model, similar to CNGS-ideal, took 16 hrs to execute.

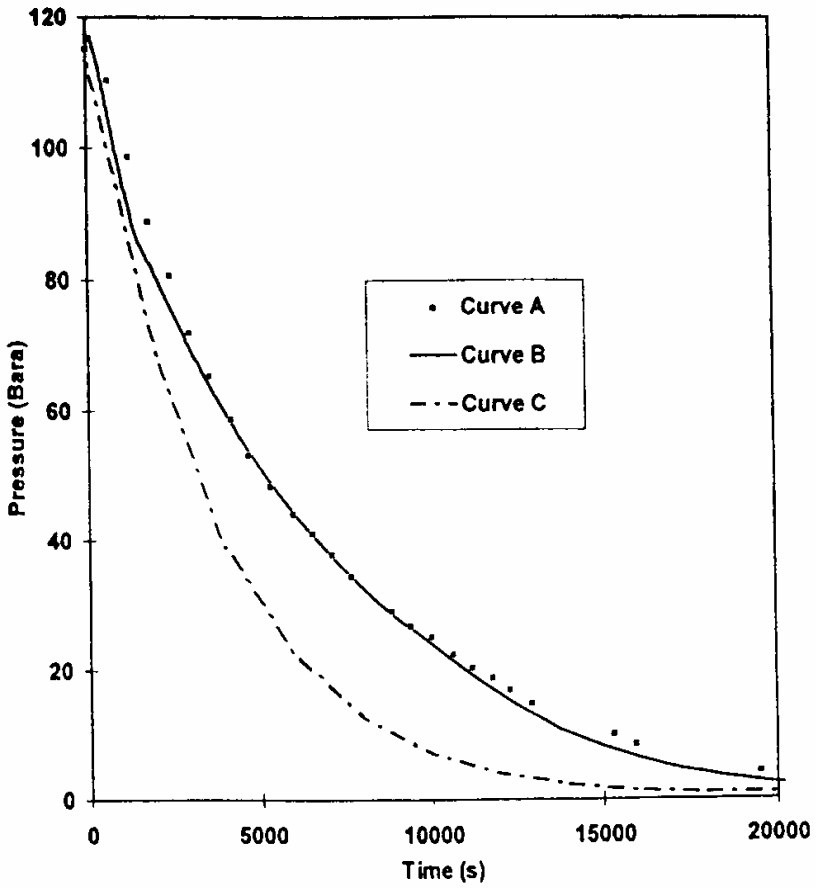

Figure 2.21: Intact end pressure vs. time profiles for the Piper Alpha-MCP pipeline (Mahgerefteh et al., 1999).

Curve A: Field Data

Curve B: CNGS-MOC, CPU time = 6 days

Curve C: CNGS-MOC ideal gas, CPU time = 1.5 min.

Figures 2.22 and 2.23 respectively show predictions for the open and closed end temperature-time and pressure-time histories for the LPG mixture test P40 as compared to experimental data. Curves A and B show the measured data whereas curves C and D represent the corresponding simulated data using CNGS-MOC. These show relatively good agreement with the experimental data. It may be observed from the temperature profile data in figure 2.22 that there is a large discrepancy towards the end of the blowdown process. This is most likely due to the use of a constant heat transfer coefficient. Mahgerefteh et al. (1999) attribute the remaining discrepancies between theory and experiment to the uncertainties associated with the measurement

data, the inaccuracies associated with the prediction of VLE data, as well as the lack of accurate information on the pipeline inventory composition.

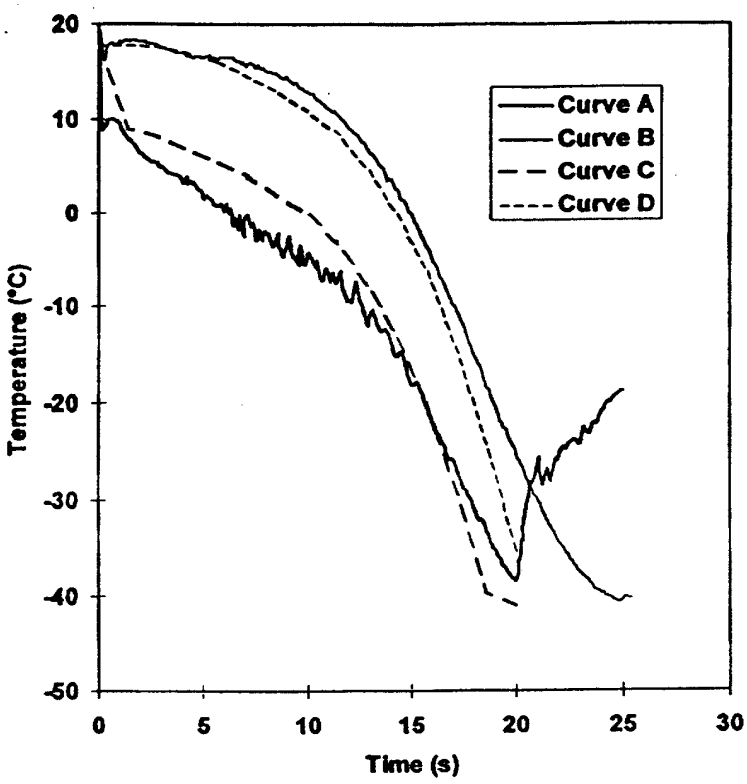

Figure 2.22: Temperature-time profiles at the open and closed ends for the P40 (LPG) test (Magerefteh et al., 1999).

Curve A: Field data (open end)

Curve B: Field data (closed end)

Curve C: CNGS-MOC (open end)

Curve D: CNGS-MOC (closed end).

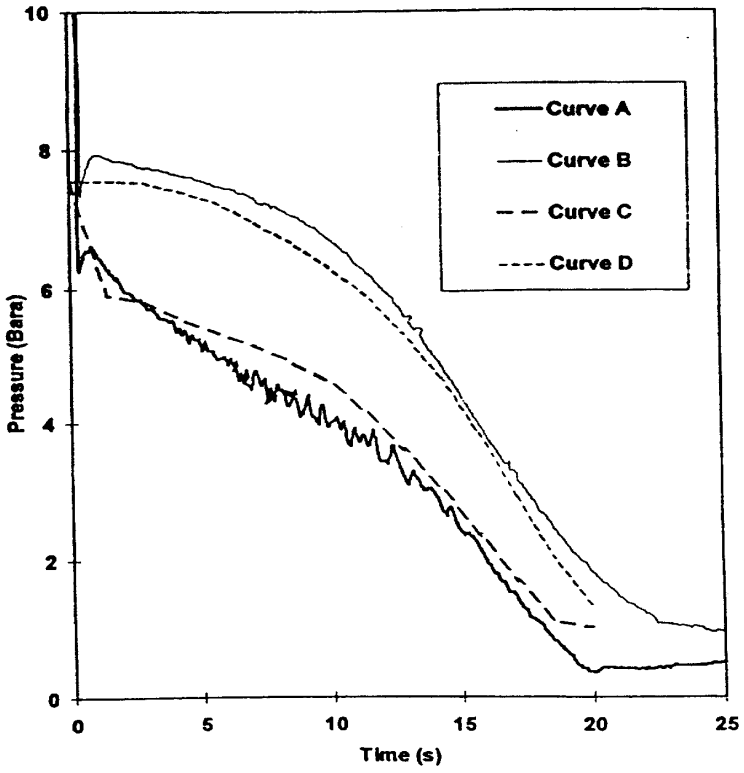

Figure 2.23: Pressure-time profiles at the open and closed ends for the P40 (LPG) test (Magerefteh et al., 1999).

Curve A: Field data (open end)

Curve B: Field data (closed end)

Curve C: CNGS-MOC (open end)

Curve D: CNGS-MOC (closed end).

Using MOC, Mahgerefteh et al. (2000) employed a real fluid model to predict the effect of phase transition on the dynamic behaviour of emergency shut down valves.

The authors concluded that a transition from gas to two-phase flow during blowdown results in a delay in valve activation. This is turn leads to more inventory loss following pipeline failure as compared to a permanent gaseous inventory. The

pressure surge upstream of the closed valve was simulated using the Joukowsky equation (Joukowsky, 1900) and the results reported.

2.8.2 Vahedi, 2003

Vahedi (2003) extended the Mahgerefteh et al. (1999) model to determine the effects of inclination and pipeline enlargement (non-uniform pipe diameter) on outflow following pipeline failure. Comparisons were also made between the results generated using linear as opposed to curved characteristics as well as a study of the effect of using different friction factor correlations on the simulated results. Fluid thermodynamic properties were calculated with the aid of the Peng-Robinson equation of state.

Simulation results were validated against the Isle of Grain experimental data and those recorded during the Piper Alpha tragedy. Good agreement between field and experimental data was obtained with the degree of agreement being similar to that obtained by Mahgerefteh et al. (1999) (see figure 2.22, curve B).

A hypothetical scenario involving the rupture of an enlarged pipeline, containing Methane at an initial pressure of 50 bara was also investigated. Figure 2.24 gives a schematic representation of the pipeline and the rupture location.

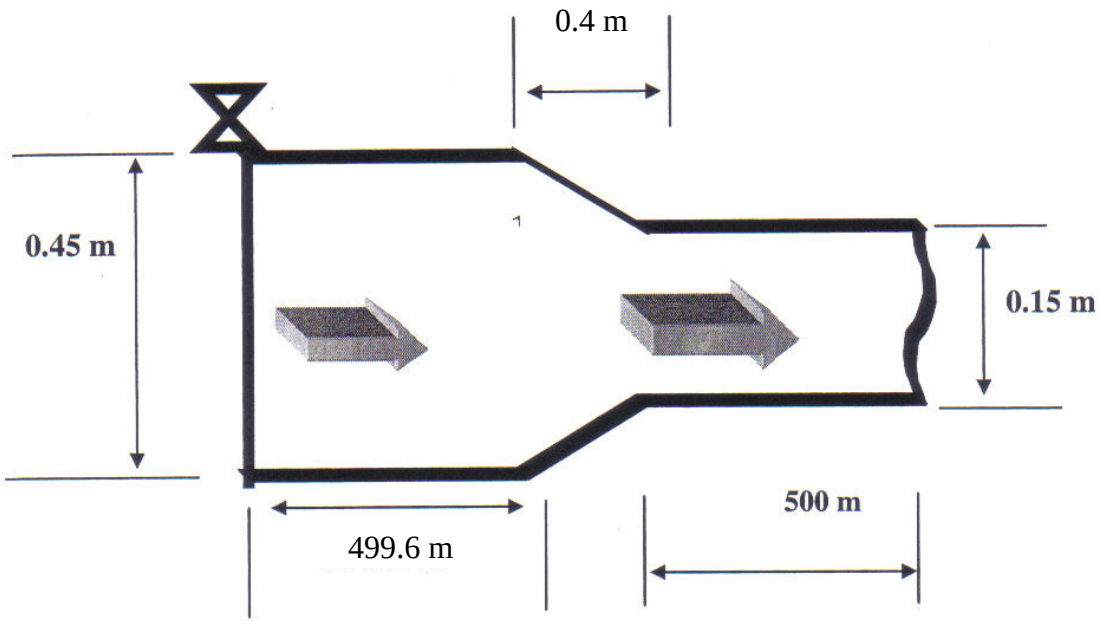

Figure 2.24: Schematic representation of enlarged pipeline simulation (Vahedi, 2003).

The simulation results for the above configuration were then compared with those obtained using a uniform diameter pipeline of the same length, containing the same amount of inventory.

Figure 2.25 shows the variation of pipeline inventory with time following the rupture of the uniform and the enlarged pipelines. As it may be observed from figure 2.25, the enlarged pipeline (curve A) depressurises at a significantly slower rate compared to the uniform diameter pipeline (curve B). The author hence concluded that reducing the pipeline diameter or 'bottlenecking' may be used as an effective way of reducing hazards following FBR by reducing the discharge rate.

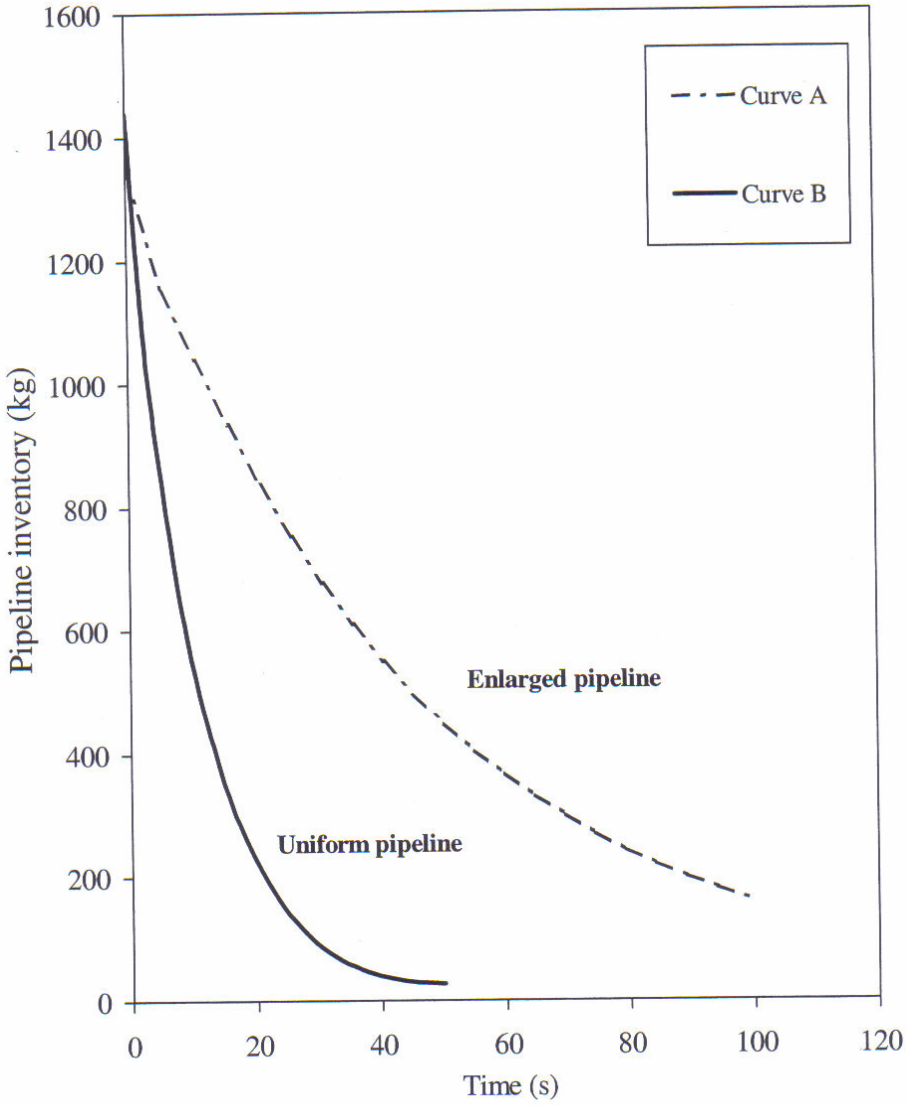

Figure 2.25: Pipeline inventory variation with time for methane following FBR (Vahedi, 2003).

Curve A: Enlarged pipeline.

Curve B: Uniform pipeline.

Other investigations made by Vahedi (2003) include the use of curved as opposed to linear characteristics on the simulation accuracy and CPU run times. It was observed that for two-phase flows, the linear characteristics provide consistently better predictions and executed faster in comparison to curved characteristics. However, for gaseous media either methodology yields practically the same result with similar computational run times.

On the study of the effect of pipeline inclination, the author concludes that the pressure wave propagation during top end rupture is slower in inclined pipelines as compared to horizontal pipelines, with the converse holding for bottom end rupture.

2.8.3 Oke et al., 2003; Oke, 2004

Oke et al. (2003) and Oke (2004) dealt with modelling outflow characteristics following the puncture and/or rupture of pipeline networks. The modelling is also based on the MOC and assumes homogenous equilibrium between phases. However, in order to investigate the impact on simulation accuracy and computational run time, the conservation equations were posed in terms of pressure, enthalpy and velocity (PHU) AND pressure, entropy, velocity (PSU) as opposed to the conventional pressure, density and velocity (PDU) formulation used by previous workers (Zucrow et al., 1976; Tiley, 1989; Chen et al., 1992; Mahgerefteh et al., 1997). In addition, the effect of adopting quadratic as opposed to linear interpolations along the space co-ordinate was examined.

Oke's (2004) model was validated against the Isle of Grain and Piper Alpha pipeline rupture data. The PDU, PHU and PSU based conservation equations were used to simulate the Isle of Grain depressurisation tests in order to investigate the effect of the choice of primitive variables on model accuracy and computational run time. Figure 2.26 shows the variation of discharge pressure with time for the Isle of Grain test P40 as compared to the simulation results. As it may be observed, in general, the PHU model performs best in terms of accuracy, respectively followed by the PSU and PDU models. The PHU model also requires the least CPU run time; 12 minutes to execute, while the PSU and PDU models required 13 minutes and 86 minutes respectively on an IBM Pentium IV 2400 MHz PC. Based on these results, the PHU model was thus used for all the subsequent simulations presented. The use of quadratic as opposed to linear interpolations although very marginally improving the model predictions resulted in longer simulation run time.

Good agreement between field and experimental data was obtained for the Piper Alpha simulation, with the accuracy similar to that obtained by other workers (Mahgerefteh et al., 1999; Vahedi, 2003). The execution time using the PHU model was ca 28 hrs.

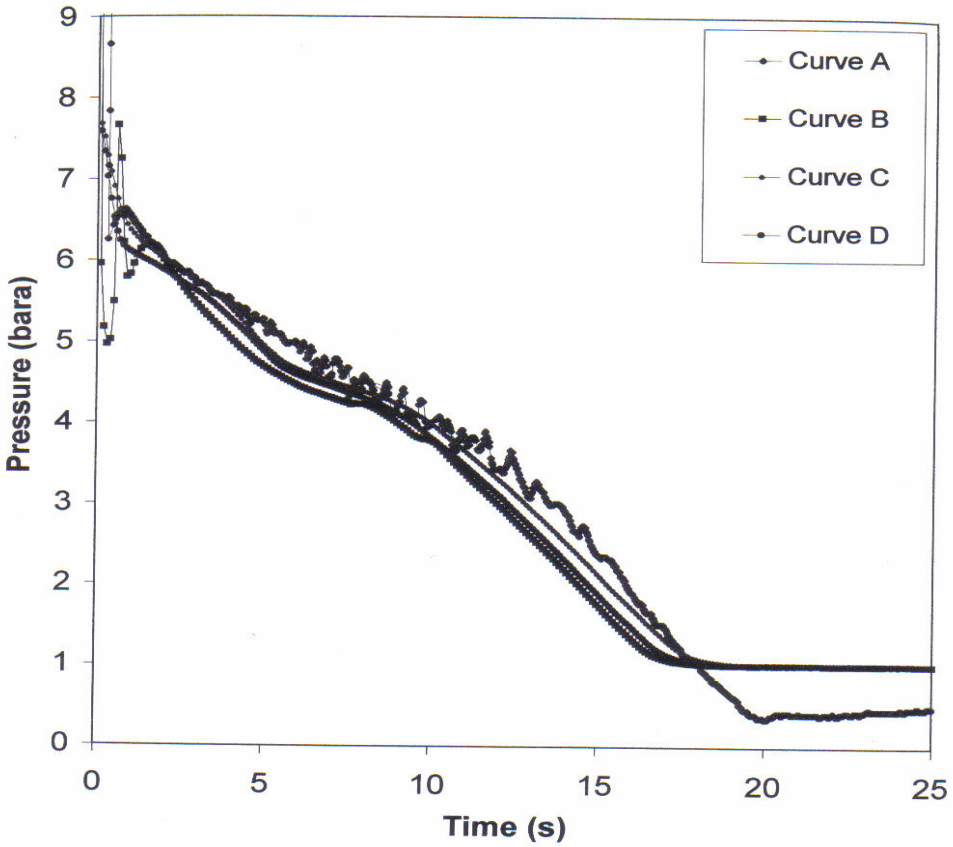

Figure 2.26: FBR pressure-time profiles at open end for test P40 (LPG) showing the effect of primitive variables on simulated results (Oke, 2004).

Curve A: Open end measurement.

Curve B: Open end simulation results using the PDU model.

Curve C: Open end simulation results using the PHU model.

Curve D: Open end simulation results using the PSU model.

Oke's model (2004) was employed to simulate the blowdown of three configurations (A – C) of pipeline networks having the same total length of 25 km as shown in figures 2.27 - 2.29. Pipe-network A consisted of a single 25 km pipeline, while pipe-network B consisted of 5 pipelines, each 5 km in length, and connected via couplers to form a 25 km long chain. Pipe-network C consisted of 5 pipelines, each 5 km in

length, but with a branch at the end of pipeline 3 as shown in figure 2.29. All the pipelines were partially insulated (heat transfer coefficient of 5 W/m^2K) and contained pressurised natural gas (90-mole % Methane, and 10-mole% Ethane).

From the simulations, Oke, 2004 concluded that that the depressurisation of a pipeline network is strongly influenced by the overall distance travelled by the expansion waves from the rupture plane to the intact end. The shorter the distance travelled, the faster the depressurisation. This implies that where two different network configurations of equal total length are concerned, the configuration with the higher number of branches is more likely to depressurise faster. Thus in terms of industrial safety, following pipeline failure, the greater the number of branches possessed by a pipeline network, the quicker emergency facilities must respond, the higher the risk of widespread secondary escalation (such as fires and environmental pollution), and the shorter the personnel safe evacuation time.

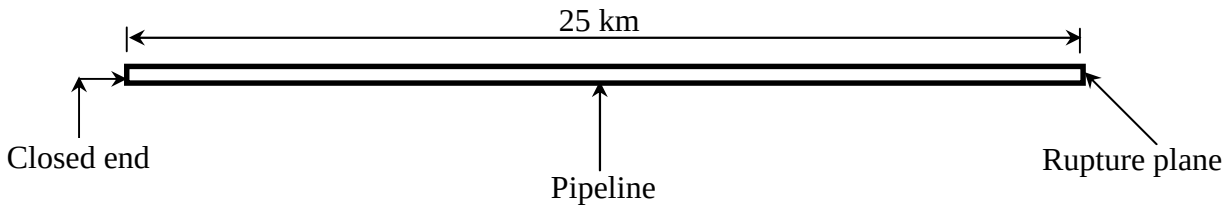

Figure 2.27: Schematic representation of pipeline-network A (Oke, 2004).

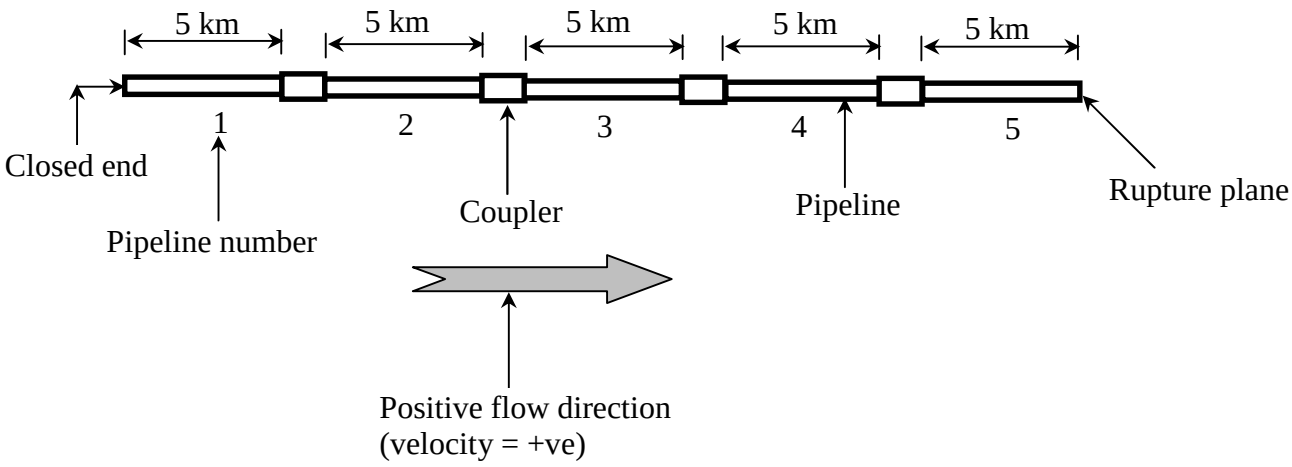

Figure 2.28: Schematic representation of pipeline-network B (Oke, 2004).

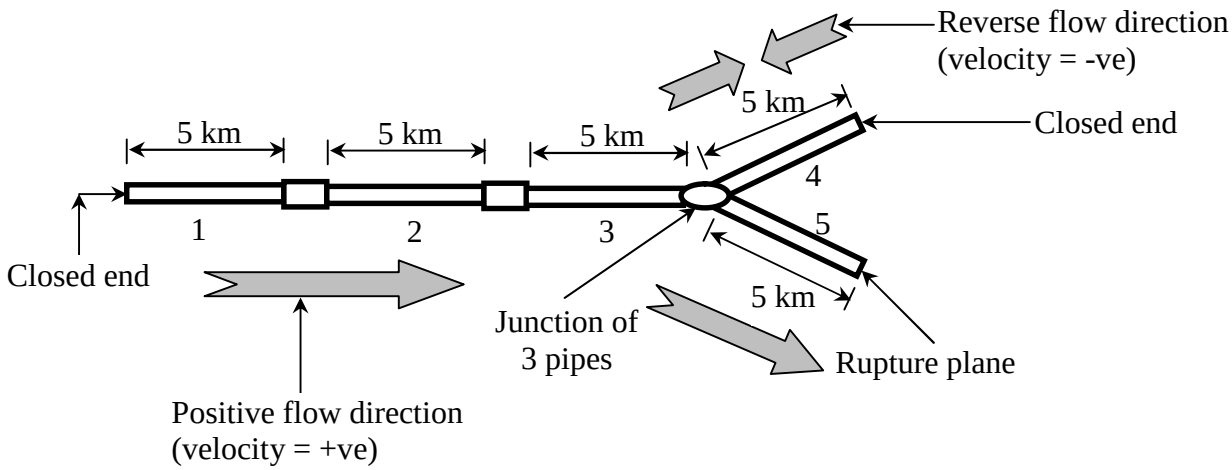

Figure 2.29: Schematic representation of pipeline-network C (Oke, 2004).

The fluid dynamics following the puncture of a hypothetical pipeline was discussed using the model presented by Oke et al. (2003). The pipeline was assumed to be 16 km long, conveying a condensable hydrocarbon mixture with an initial flow rate of 0.3 m^3/s which was sustained for 90 seconds after rupture using a centrifugal pump. The PHU model was used in the simulation with the pipeline assumed to be isolated downstream upon puncture. Figure 2.30 shows a pictorial timeline simulation of the fluid flow pattern following puncture as presented by Oke et al. (2003).

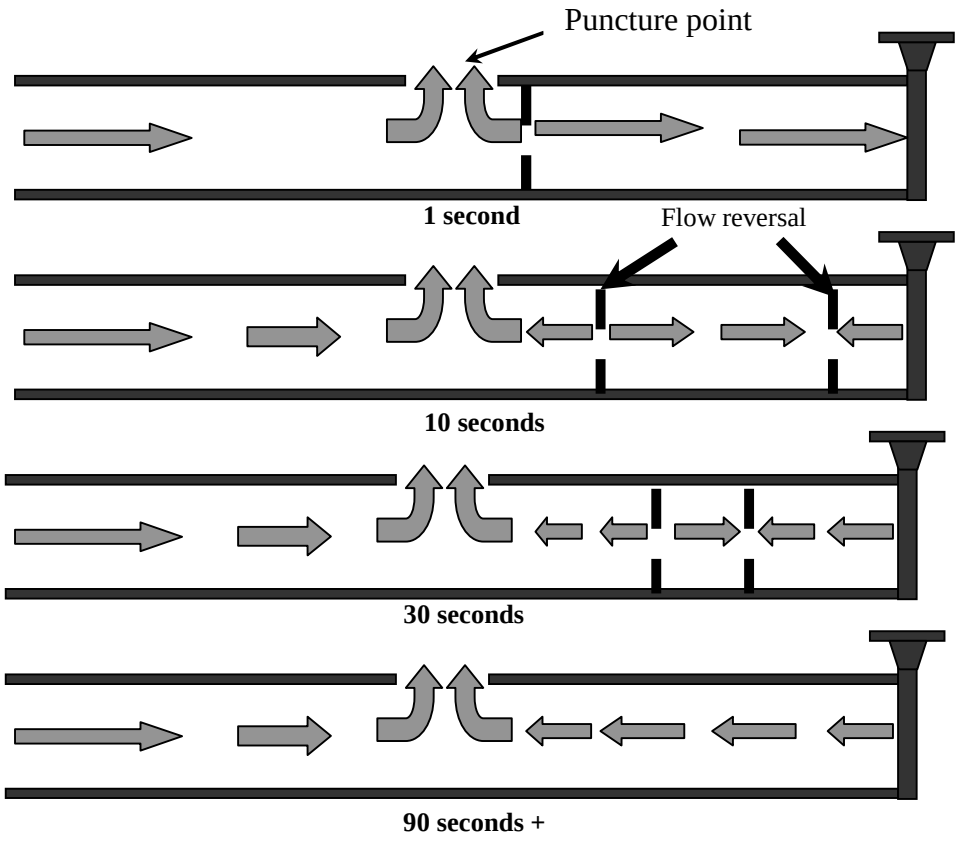

Figure 2.30: Schematic representation of flow patterns in the pipeline following puncture (Oke et al., 2003).

Although the models presented above are in principle capable of simulating outflow from punctures and pipeline networks, the boundary conditions and their solutions as presented by the authors (Oke et al., 2003; Oke, 2004) required modification. The modifications were made by Atti (2006) which highlighted and corrected the errors in the formulation of the boundary conditions.

2.8.4 Atti, 2006

Atti (2006) developed an interpolation technique for reducing Mahgerefteh et al. (2000) HEM model's computational runtime. The conservation equations were posed in terms of pressure, enthalpy and velocity (PHU) (Oke (2004)). The values of pressure (P), speed of sound (a), enthalpy (h), density (r) and velocity (u) as functions of time and distance along the pipeline were obtained by the inverse marching method of characteristics. This involved dividing the pipeline into a large number of distance (Δx) and time elements (Δt) and expressing the compatibility equations in finite difference form paying due regard to the Courant stability criterion (Courant et al., 1952; Zucrow and Hoffman, 1976) regarding the maximum allowable distance and time elements. These finite difference equations were solved at the intersection of the linear characteristic lines with the spatial axis using iteration and interpolation in conjunction with P–h (pressure–enthalpy) flash calculations.

The reduction in the computation workload was obtained by first determining the maximum and minimum fluid enthalpies (h_{max}, h_{min}) at the likely fluid pressure (P_{max}, P_{min}) and temperature (T_{max}, T_{min}) ranges. P_{max} and P_{min} were taken as the inlet and ambient pressures respectively. T_{max} was the greater of the feed and the ambient temperatures, and T_{min} was determined by ignoring pipe wall/ambient heat transfer and performing an isentropic flash from P_{max} and T_{max} to P_{min}.

Figure 2.31 shows the corresponding interpolation space domain.

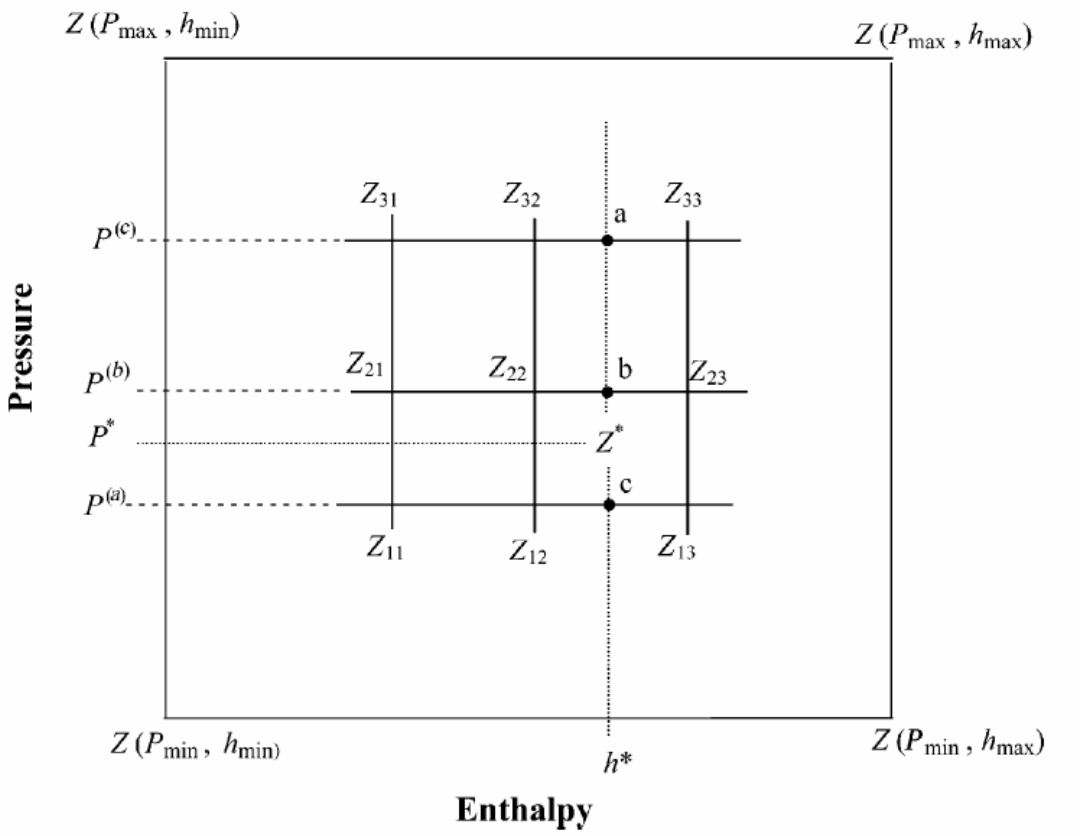

Figure 2.31: Schematic representation of the depressurizing fluid pressure/enthalpy interpolation domain (Atti, 2006).

The interpolation scheme was performed in two stages. The initial sweep involved determining the intermediate values of Z at points a, b and c corresponding to the enthalpy, h* by interpolating between points Z_{11}–Z_{13}, Z_{21}–Z_{23} and Z_{31}–Z_{33}, respectively. The second step involved determining Z* by interpolating between Z(a), Z(b) and Z(c) along the pressure axis.

Atti (2006) stated that the application of the interpolation scheme to a range of representative fluids such as permanent gases, two-phase mixtures, flashing liquids and permanent liquids produces a maximum 0.01% difference between the predicted fluid properties based on interpolation as compared to direct flash calculations. This finite difference was found to have negligible effect on the predicted fluid flow profiles such as the time variant pressure, discharge velocity, mass flow rate and discharge temperature data following pipeline rupture.

Atti (2006) validated the model by comparison against the results of the pipeline rupture tests conducted by BP and Shell Oil on the Isle of Grain as well as intact end pressure data relating to the MCP-01 riser rupture recorded during the Piper Alpha tragedy. Figures 2.32 - 2.34 respectively show the variations of fluid pressure, temperature and discharged mass with time at the rupture plane for the Isle of Grain test, P40. The measured data is represented by curve A. Curves B and C on the other hand respectively represent the simulation results with and without the interpolation scheme.

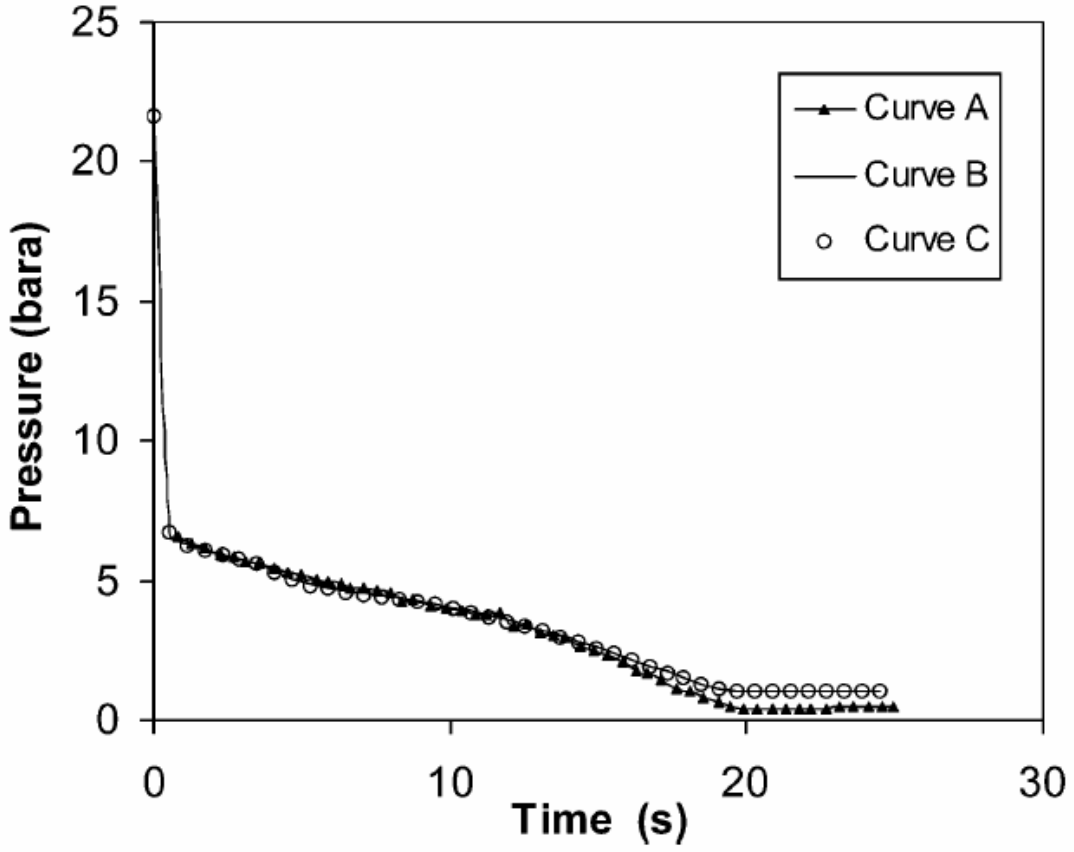

Figure 2.32: Pressure versus time profiles at open end for test P40 (LPG) (Atti, 2006).

Curve A: measurement (Richardson et al., 1996a, b).

Curve B: simulation data without the interpolation scheme: CPU runtime, 12 min.

Curve C: simulation data employing the interpolation scheme: CPU runtime, 3.5 min.

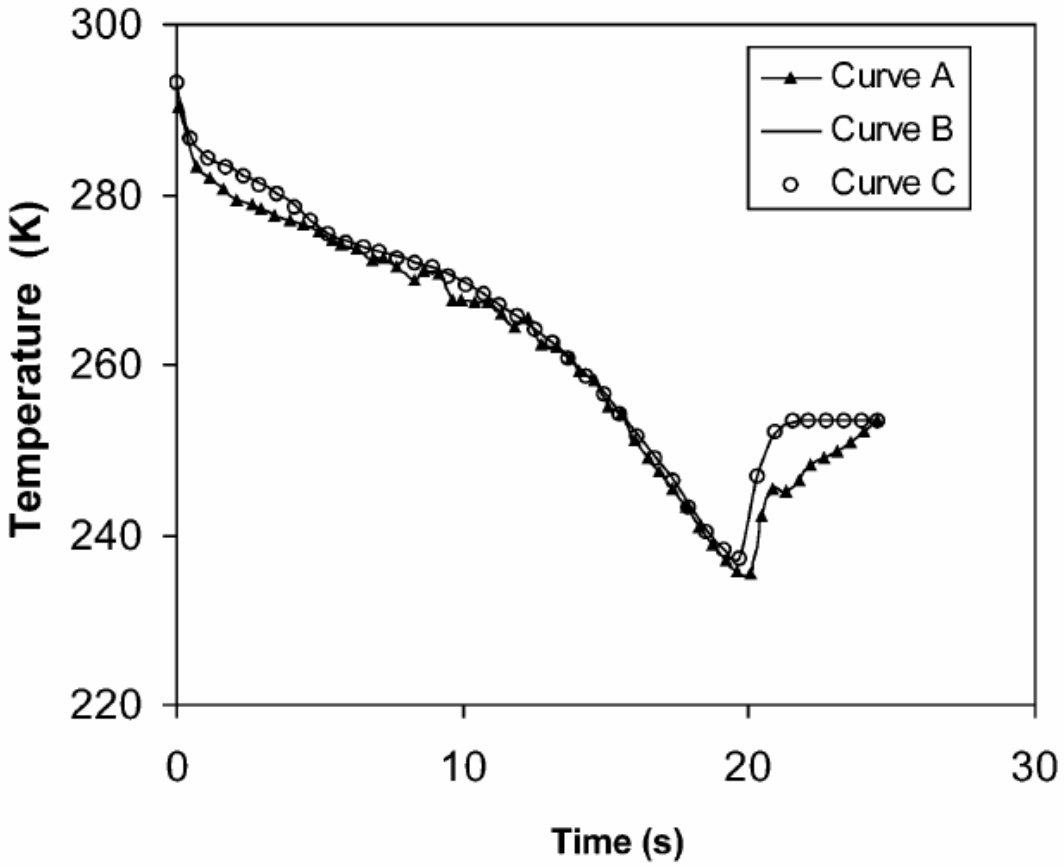

Figure 2.33: Temperature versus time profiles at rupture plane for test P40 (LPG) (Atti, 2006).

Curve A: measurement (Richardson and Saville, 1996a, b).

Curve B: simulation data without the interpolation scheme: CPU runtime, 12 min.

Curve C: simulation data employing the interpolation scheme: CPU runtime, 3.5 min.

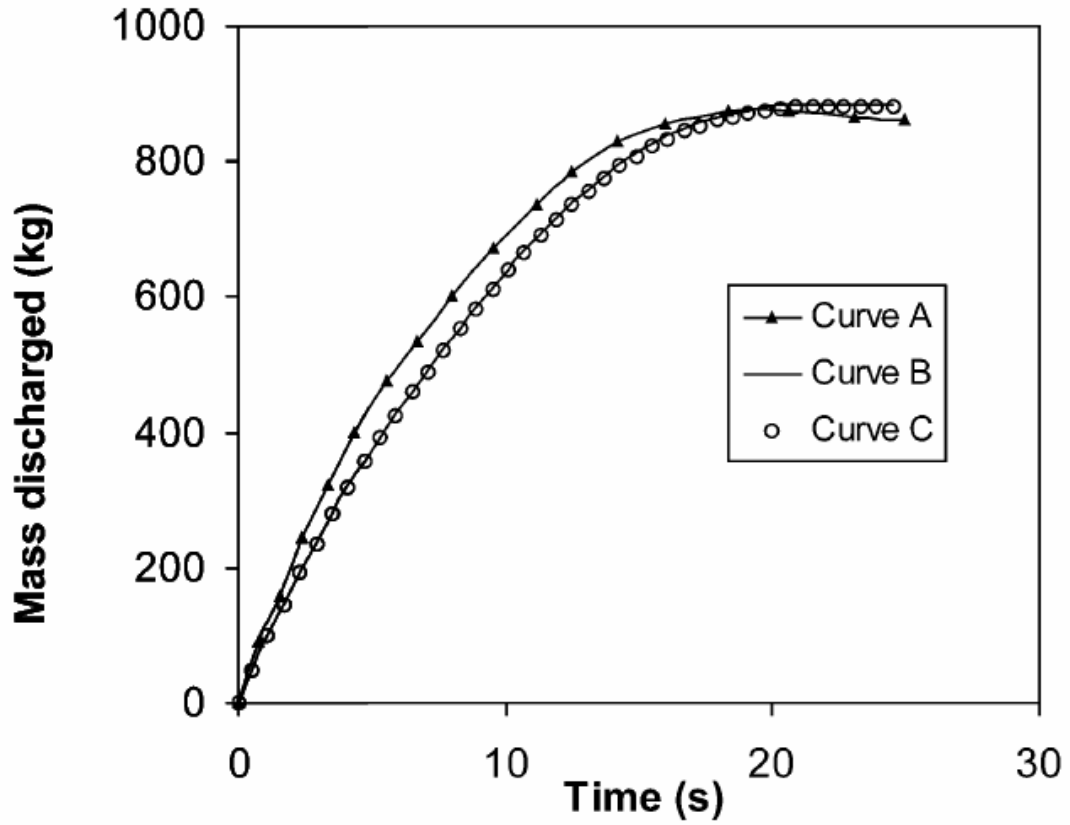

Figure 2.34: Cumulative mass discharged versus time profiles for test P40 (LPG) (Atti, 2006).

Curve A: measurement (Richardson and Saville, 1996a, b).

Curve B: simulation data without the interpolation scheme: CPU runtime, 12 min.

Curve C: simulation data employing the interpolation scheme: CPU runtime, 3.5 min.

As it may be observed from figures 2.32 - 2.34, the simulated data (curves B and C) are identical and in good accord with the test data. Furthermore, the use of the interpolation scheme (curve B) results in approximately 70% reduction in the computational run time (c.f. 12 min versus 3.5 min).

2.9 Concluding Remarks

Based on the above review, it is clear that significant progress has been made to improve both the accuracy and reduce the computation runtime in simulating outflow following the rupture or puncture of pressurised pipelines. However, there is still significant scope for improving the pipeline failure models reported in the open literature.

For example, of the models presented, the homogenous equilibrium based models by Mahgerefteh et al. (1999), Chen et al. (1995a, b) and Atti (2006) are the most robust with the latter performing best in terms of accuracy and computational run time when compared to experimental data (Atti, 2006). Nonetheless, when simulating the complete blowdown of long pipelines (>100 km), the computational run time associated with all of these models are rather long. Hence, ways of further reducing the computational run time needs to be investigated.

Additionally, Richardson et al. (2006) highlighted the limitations of using the HEM assumption for modelling the discharge of two-phase mixtures containing > 80% liquid through an orifice. This limitation has a significant impact on the efficacy of all puncture HEM based models presented in the review.

The review also showed that most models dealing with pipeline rupture have been limited to modelling straight pipelines or pipeline networks containing horizontal pipelines of uniform diameter and pipe thickness. In practice however, long pipelines conveying hydrocarbons over a varying topography usually consist of a multiple pipeline segments with varying internal diameter and wall thickness. These pipeline segments are normally connected using flanges, elbows and bends which introduce a greater degree of complexity to modelling of pipeline failures. Neglecting the corresponding pressure losses can result in an over-prediction of the discharge rate and hence expensive mitigation.

CHAPTER 3: BACKGROUND THEORY FOR MODELLING TRANSIENT FLOW IN PIPELINES

3.1 Introduction

The development of a transient outflow model consists of three main steps:

1. Formulation of the basic equations governing the flow, the thermodynamics, and the initial and boundary conditions.
2. Selection and implementation of an efficient and accurate method that resolves or simplifies these equations into easily solvable forms.
3. Where possible, the validation of the model against field or experimental data.

An essential precursor to the above is the formulation of the conservation equations relating to mass, momentum and energy in conjunction with a suitable equation of state. The Navier-Stokes conservation equations represent the most complete formulation that describes any fluid flow situation. These equations allow for the variation of fluid property in four dimensions, i.e. the three dimensions of space, x, y, and z, and also time, t. Due to the difficulty in solving the full system of equations, it is always necessary to resolve every term in the Navier-Stokes conservation equations resulting in substantial computational resource requirement. Depending on the type of flow, certain terms in the equations will have a negligible effect on the final solution and may therefore effectively be ignored without any serious loss of accuracy.

The final form of the Navier-Stokes equations, depending on the assumptions and simplifications made, may be linear, quasi-linear or non-linear, parabolic or hyperbolic in nature. Consequently, the simplifications made have a major bearing on numerical techniques that can be employed in the model.

Additionally, simplifications to the governing equations can greatly reduce computer run times, but this might well be at a cost of reduction in the accuracy of the final solution. Some examples of models developed using different simplifying assumptions include:

- Van Deen et al. (1983) in their derivation of the conservation equations ignored terms that account for pipeline inclination and gravitational influence.
- Bisgard et al. (1987) while accounting for pipeline inclination, based their model on isothermal flow conditions. As a result, their model ignores any form of heat transport between the fluid and its surroundings and rests on only the mass and momentum conservation equations.
- Jo et al. (2002) presented a simple model based on steady state isentropic ideal gas flow. The model ignores terms in the conservation equations that account for pipeline inclination and gravitational influence. Above all, the equations fail to account for two-phase flow as it assumes ideal gas behaviour. This approach simplifies terms in the conservation equations that would naturally have been impossible to analytically resolve had two-phase flow been considered.

This chapter will address the first step of the outflow model development. The derivation and formulation of the equations governing the transient flow following pipeline failure are presented. This includes:

- Derivation of the mass, momentum and energy conservation equations for transient fluid flow in including the important assumptions made.
- Selection of an appropriate equation of state (EoS) and the accompanying hydrodynamic correlations.
- The energy balance model employed for estimating transient ambient-pipe wall-fluid heat transfer.
- The isothermal steady state flow model for determining the fluid flow conditions prior to pipeline rupture.

3.2 Model Assumptions

The major assumptions made in the development of the transient outflow model employed in this study are:

- Predominantly one-dimensional flow in the pipeline; that is, the rate of change of fluid properties normal to the streamline direction is negligible compared with the rate of change along the streamline. However, in the region close to the puncture plane where there is fluid flow along and normal to the streamline, a two-dimensional approximation is adopted.
- Homogeneous equilibrium fluid flow (HEM) where the two phases are assumed to travel at the same velocity, and are in thermodynamic and mechanical equilibrium with one another. As such, separate conservation equations for each fluid phase are not considered in this study.
- Isothermal flow conditions exist in the pipeline prior to failure.
- Negligible fluid structure interaction through vibrations.
- Constant cross section area of pipe.

Regarding the HEM assumption, studies by others (see for example Chen et al., 1995; Mahgerefteh et al., 1999) have demonstrated the applicability of this assumption in the case of FBR of pipelines (see section 2.6.3). Furthermore, Chen et al., (1995) show that HEM based models perform similarly or even better than heterogeneous equilibrium and non-equilibrium based models. As such, in the model presented herewith, only one set of mass, momentum, and energy conservation equations will be derived for both single and two-phase flow with two-phase replacing single-phase flow properties where necessary. However, Richardson et al. (2006) highlighted the limitations of using the HEM assumption for modelling the discharge of two-phase mixtures containing > 80% liquid through an orifice (see section 2.7.4). A model addressing this limitation of the HEM is presented later in the study (see section 7.3).

The flowing fluid is assumed to attain isothermal steady state flow conditions prior to failure.

Finally, with respect to fluid-structure interactions and pipeline cross-sectional area, pipelines in a network are assumed to be rigidly clamped, possess inelastic walls, and are time and space invariant with respect to cross-sectional area.

3.2.1 Conservation of Mass

The law of conservation of mass (Welty et al., 2008) states that mass may be neither created nor destroyed. For the control volume shown in figure 3.1, the mass conservation equation can be derived by considering how materials build up within the control volume as fluid passes through the system, i.e.:

Rate of mass flow into control volume	-	Rate of mass efflux from control volume	=	Rate of accumulation of mass within control volume	(3.1)

In figure 3.1, ρ and u represent the fluid density and velocity respectively with Δx representing the length of the pipeline section under consideration. Therefore the mass in the pipeline section can change only due to fluid flowing across the end points x_1 or x_2.

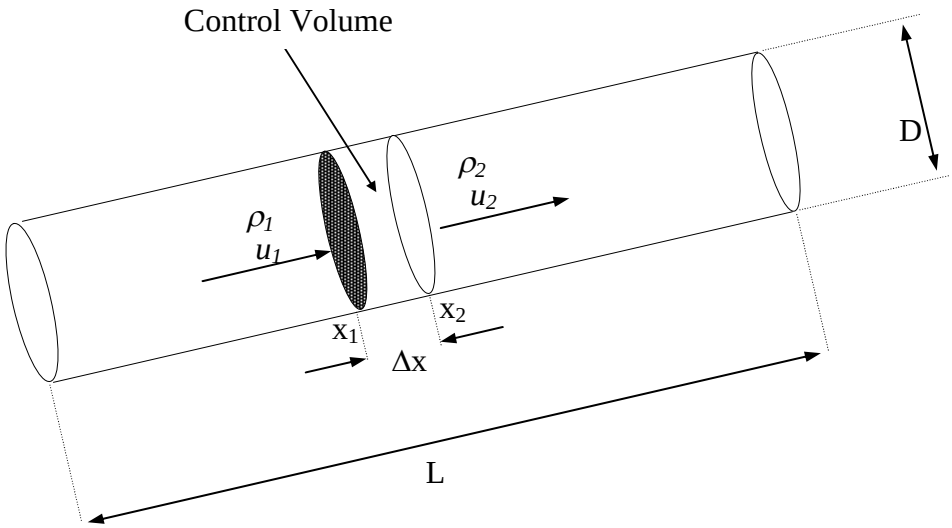

Figure 3.1: Schematic representation of a control volume within a pipe section.

Now, the mass of fluid within the control volume is give by $\rho_{(x,t)}Adx$, and the mass flow rate across x_1 and x_2 is given by $\rho_1 u_1 A$ and $\rho_2 u_2 A$ respectively, the rate of mass change in the control volume (equation (3.1)) can be written as:

$$\frac{\partial}{\partial t}\int_{x_1}^{x_2} \rho(x,t)\,A dx = (\rho u A)_{x_1,t} - (\rho u A)_{x_2,t} \tag{3.2}$$

Where $\rho_{(x,t)}$ is the density of the fluid at any point (x) at any time (t).
Dividing equation (3.2) through by A and rearranging gives:

$$\int_{x_1}^{x_2} \frac{\partial \rho}{\partial t}\,dx = -\int_{x_1}^{x_2} \frac{\partial(\rho u)}{\partial x}\,dx \tag{3.3}$$

Equation (3.3) holds for any section [x_1, x_2] at any time t, and can therefore be written as:

$$\frac{\partial \rho}{\partial t} + \frac{\partial(\rho u)}{\partial x} = 0 \tag{3.4}$$

Expanding equation (3.4) gives:

$$\frac{\partial \rho}{\partial t} + \frac{u \partial \rho}{\partial x} + \frac{\rho \partial u}{\partial x} = 0 \qquad (3.5)$$

Equation (3.5) represents the Euler form of the mass conservation equation. For notational purposes, the total or substantive derivative of a function *f (x, t), f = P, ρ, H, h, u,* is given by:

$$\frac{df}{dt} = \frac{\partial f}{\partial t} + \frac{u \partial f}{\partial x} \qquad (3.6)$$

Where *P, ρ, H, h,* represent the absolute pressure, density, total and specific enthalpies of the fluid respectively.

Applying the above notation to equation (3.5) gives:

$$\frac{d\rho}{dt} + \frac{\rho \partial u}{\partial x} = 0 \qquad (3.7)$$

Oke (2004) showed that the total derivative of density with respect to time can be reformulated and expressed in terms of fluid pressure and enthalpy. Atti (2006) on the other hand showed that this reformulation improves the accuracy of simulated results at reduced computational expense. Hence, the same formulation used by Atti (2006) is employed in this work as derived below.

For any fluid, the fluid pressure can be expressed as a function of density (ρ) and entropy (s) i.e., $P = f(\rho, s)$. Thus, in partial differential form, this relationship can be written as:

$$dP = \left(\frac{\partial P}{\partial \rho}\right)_s d\rho + \left(\frac{\partial P}{\partial s}\right)_\rho ds \qquad (3.8)$$

Where,

$$\left(\frac{\partial P}{\partial \rho}\right)_s = a^2 \qquad a = \text{speed of sound} \qquad (3.9)$$

Assuming:

$$\left(\frac{\partial P}{\partial s}\right)_{\rho} = \varphi \tag{3.10}$$

Hence, by substituting equations (3.9) and (3.10) into equation (3.8), the substantial derivative of pressure with time can be expressed as:

$$\frac{dP}{dt} = a^2 \frac{d\rho}{dt} + \varphi \frac{ds}{dt} \tag{3.11}$$

Rearranging equation (3.11) and making the total derivative of density as the subject gives:

$$\frac{d\rho}{dt} = \frac{1}{a^2}\left(\frac{dP}{dt} - \varphi \frac{ds}{dt}\right) \tag{3.12}$$

For any fluid, the total derivative of enthalpy is given by (Walas, 1987):

$$dh = Tds + \frac{1}{\rho} dP \tag{3.13}$$

Thus, from equation (3.13), the total derivative for enthalpy with respect to time becomes:

$$\frac{dh}{dt} = T\frac{ds}{dt} + \frac{1}{\rho}\frac{dP}{dt} \tag{3.14}$$

Rearranging equation (3.14) gives:

$$\frac{1}{T}\left[\frac{dh}{dt} - \frac{1}{\rho}\frac{dP}{dt}\right] = \frac{ds}{dt} \tag{3.15}$$

Substituting equation (3.15) into equation (3.12) by replacing the total derivative of entropy with time results in:

$$\frac{d\rho}{dt} = \frac{1}{a^2}\left[\frac{dP}{dt}\left(1 + \frac{\varphi}{\rho T}\right) - \frac{\varphi}{T}\frac{dh}{dt}\right] \tag{3.16}$$

Substituting equations (3.16) into equation (3.7) and rearranging yields

$$\left[\rho T+\varphi\right]\frac{dP}{dt}-\rho\varphi\frac{dh}{dt}+\rho^2a^2T\frac{\partial u}{\partial x}=0 \tag{3.17}$$

The above equation can be expressed as

$$\left[\rho T+\varphi\right]\left(\frac{\partial P}{\partial t}+u\frac{\partial P}{\partial x}\right)-\rho\varphi\left(\frac{\partial h}{\partial t}+u\frac{\partial h}{\partial x}\right)+\rho^2a^2T\frac{\partial u}{\partial x}=0 \tag{3.18}$$

Equation (3.18) is the form of the mass conservation equation employed, in which the total derivative of density with time has been expressed in terms of fluid pressure and enthalpy.

3.2.2 Conservation of Momentum

The momentum conservation equation is derived from the application of Newton's second law of motion. Newton's second law of motion (Welty et al., 2008) states that the time rate of change of momentum of a system is equal to the net force acting on the system and takes place in the direction of the net force. For a control volume this law may be expressed as:

Sum of forces	=	Rate of change of momentum within the control volume	+	Net rate of momentum due to fluid flow across the boundary	(3.19)

Figure 3.2 shows the forces acting on the fluid element within the control volume. They include:

1. Gravitational force (F_g)

2. Pressure forces (F_p): This is the force due to the effect of pressure acting on the boundary of the control volume at point x_1 and x_2. At point x_2, the pressure force is negative since it is in the opposite direction of flow.

3. Frictional force (F_f): This is the force that acts in the opposite direction to flow.

In the derivation of the momentum conservation equation, it is assumed that force terms due to tangential and normal viscous stresses, electromagnetic and electrostatic forces are negligible and hence are ignored.

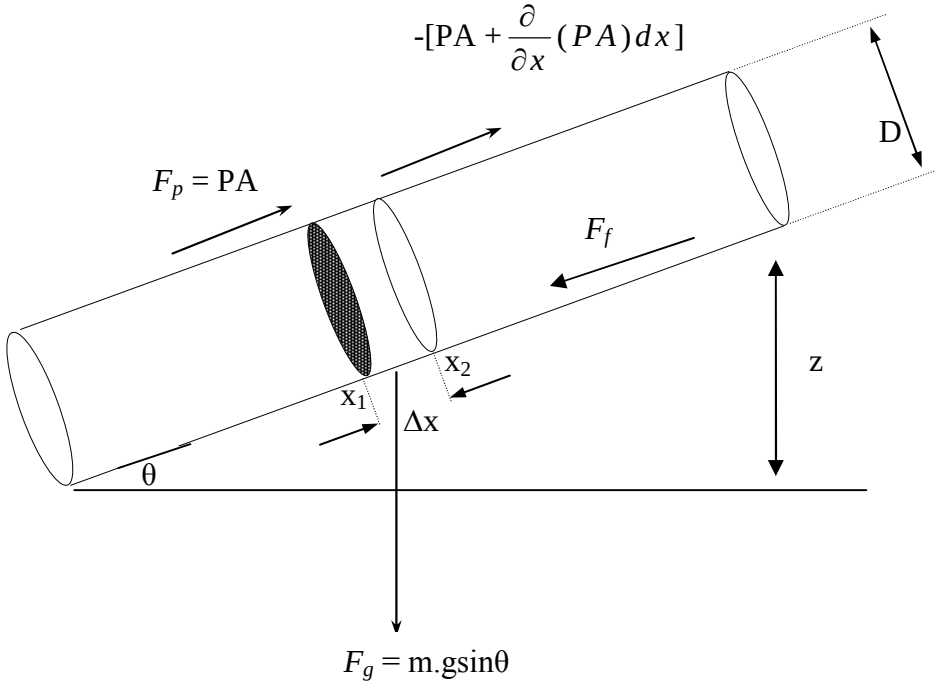

Figure 3.2: Schematic representation of the forces acting on a control volume within a pipeline.

Referring to figure 3.2, equation (3.19) can be mathematically expressed as:

$$\sum F_x = \frac{\partial}{dt}(\rho A u)dx + \frac{\partial}{dx}(\rho A u^2)dx \tag{3.20}$$

Additionally,

$$F_g = \rho A\, dx\, g\, sin\theta \tag{3.21}$$

$$F_p = PA - \left[PA + \frac{\partial(PA)}{\partial x}dx\right] \tag{3.22}$$

$$F_f = -\frac{\rho u^2}{2}\frac{4 f_w}{D} A dx \tag{3.23}$$

Where,

f_w = fanning friction factor

Substituting equations (3.21 - 3.23) into equation (3.20) and dividing through by *Adx* gives:

$$-\frac{2\rho u^2 f_w}{D} - \rho g \sin\theta = \frac{\partial(\rho u)}{\partial t} + \frac{\partial(\rho u^2)}{\partial x} + \frac{\partial P}{\partial x} \tag{3.24}$$

Expanding the terms in the brackets, resolving and rearranging equation (3.24) yields:

$$-\frac{2\rho u^2 f_w}{D} - \rho g \sin\theta = \frac{\partial P}{\partial x} + \rho\frac{\partial u}{\partial t} + \rho u\frac{\partial u}{\partial x} + u\left[\frac{\partial \rho}{\partial t} + u\frac{\partial \rho}{\partial x} + \rho\frac{\partial u}{\partial x}\right] \tag{3.25}$$

The expression in the bracket of equation (3.25) is that of the continuity equation i.e. equation (3.5), which equals zero. Hence, (3.25) becomes:

$$\rho\frac{\partial u}{\partial t} + \rho u\frac{\partial u}{\partial x} = -\frac{\partial P}{\partial x} - \rho g \sin\theta + \beta_x \tag{3.26}$$

This can also be expressed in terms of the total derivatives using equation (3.6):

$$\rho\frac{du}{dt} = -\frac{\partial P}{\partial x} - \rho g \sin\theta + \beta_x \tag{3.27}$$

Where,

$$\beta_x = \frac{2 f_w \rho u|u|}{D} \tag{3.28}$$

The modulus of the velocity, $|u|$ is introduced so that the friction force will change sign with change in flow direction.

Equations (3.26) and (3.27) are the differential forms of the momentum equation employed in this study.

3.2.3 Conservation of Energy

The energy conservation equation is derived from the application of the first law of thermodynamics. The law states that (Welty et al., 1984) if a system is carried through a cycle, the total heat added to the system from its surroundings is proportional to the work done by the system on its surroundings. In relation to a control volume, this can be mathematically expressed as:

$$\frac{\partial(\rho E)}{\partial t}Adx + \frac{\partial(\rho Eu)}{\partial x}Adx = W_{shaft} + W_{shear} + W_n + Q_h \qquad (3.29)$$

Where,

E = Total energy per unit mass of the fluid

Q_h = Rate of heat transfer to the fluid

W_n = Net rate of work done by normal forces (i.e. pressure).

W_{shaft} and W_{shear} are the mechanical work and the shear work respectively.

Based on the assumption of inviscid flow, the shear work done as a result of tangential and normal viscous forces is ignored. Furthermore, the shaft work term in the energy equation is ignored as no external work is done on, or by the flowing fluid.

Equation (3.29) can be reduced to give:

$$\frac{\partial(\rho E)}{\partial t}Adx + \frac{\partial(\rho Eu)}{\partial x}Adx = W_n + Q_h \qquad (3.30)$$

The total energy (E) of the fluid is the sum of its internal (i), kinetic and potential energies per unit mass. It is given by:

$$E = i + \frac{1}{2}u^2 + gz \qquad (3.31)$$

Where, z is the elevation of the fluid element from the horizontal plane and g is the acceleration due to gravity.

On the other hand, the rate of work done by pressure forces on the surface of the control volume is given by *PAu*.

Figure 3.3 gives a schematic representation of the work done on the control volume.

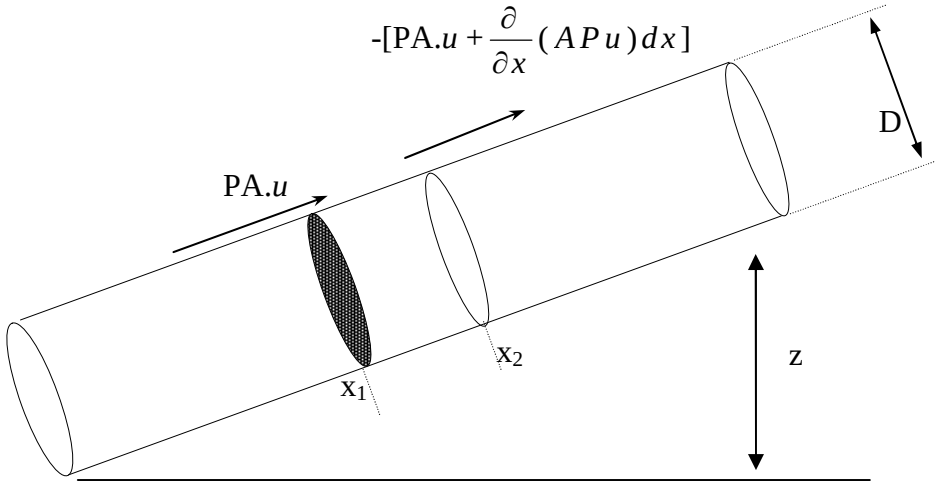

Figure 3.3: Schematic representation showing the work acting on the surfaces of a control volume within a pipeline.

At point x_1:

$$W_{x_1} = A(Pu)_{x_1} \tag{3.32}$$

At point x_2:

$$W_{x_2} = -[A(Pu)_{x_1} + \frac{A\partial(Pu)}{\partial x}dx] \tag{3.33}$$

Hence the net rate of work by pressure forces, W_n acting on the fluid element is give by:

$$W_n = W_{x_2} - W_{x_1} = -A\frac{\partial(Pu)}{\partial x}dx \tag{3.34}$$

Substituting equation (3.34) into equation (3.30), dividing through by *Adx* gives:

$$\frac{\partial(\rho E)}{\partial t}+\frac{\partial(\rho E u)}{\partial x}+\frac{\partial(Pu)}{\partial x}=q_h \tag{3.35}$$

Where, q_h is the heat transferred to the fluid element per unit volume.

However, the internal energy of a fluid is related to its specific enthalpy, *h*, by:

$$i=h-\frac{P}{\rho} \tag{3.36}$$

Thus, substituting for the internal energy term in equation (3.31) and multiplying both sides of the equation by ρ gives:

$$\rho E=\rho H-P+\rho g z \tag{3.37}$$

Where the total enthalpy, *H* is defined as:

$$H=h+\frac{u^2}{2} \tag{3.38}$$

Substituting equation (3.37) into equation (3.35) gives:

$$\frac{\partial(\rho H-P+\rho g z)}{\partial t}+\frac{\partial(\rho H-P+\rho g z+P)u}{\partial x}=q_h \tag{3.39}$$

Expanding equation (3.39) gives:

$$H\frac{\partial\rho}{\partial t}+\rho\frac{\partial H}{\partial t}-\frac{\partial P}{\partial t}+gz\frac{\partial\rho}{\partial t}+\rho g\frac{\partial z}{\partial t}+H\frac{\partial\rho u}{\partial x}+\rho u\frac{\partial H}{\partial x}+gz\frac{\partial\rho u}{\partial x}+g\rho u\frac{\partial z}{\partial x}=q_h \tag{3.40}$$

Collecting like terms and simplifying, equation (3.40) becomes:

$$\rho\frac{\partial H}{\partial t}+\rho g\frac{\partial z}{\partial t}+(H+gz)\left(\frac{\partial\rho}{\partial t}+\frac{\partial\rho u}{\partial x}\right)+\rho u\left(\frac{\partial H}{\partial x}+g\frac{\partial z}{\partial x}\right)-\frac{\partial P}{\partial t}=q_h \tag{3.41}$$

It can be observed that the terms in the second bracket of the above equation make up the mass conservation equation and hence disappear. Also from figure 3.2 it can be seen that:

$$\frac{\partial z}{\partial x}=\sin\theta \tag{3.42}$$

Since the pipeline inclination is time invariant:

$$\frac{\partial z}{\partial t} = 0 \tag{3.43}$$

Substituting equations (3.42) and (3.43) into equation (3.41) and rearranging gives:

$$\rho\left(\frac{\partial H}{\partial t} + u\frac{\partial H}{\partial x}\right) + \rho u g \sin\theta - \frac{\partial P}{\partial t} = q_h \tag{3.44}$$

From equation (3.6), the differential equation above can be written as:

$$\rho\frac{dH}{dt} + \rho u g \sin\theta - \frac{\partial P}{\partial t} = q_h \tag{3.45}$$

Substituting equation (3.38) into equation (3.45) results in:

$$\rho\left[\frac{dh}{dt} + \frac{1}{2}\frac{du^2}{dt}\right] + \rho u g \sin\theta - \frac{\partial P}{\partial t} = q_h \tag{3.46}$$

Simplifying equation (3.46) produces:

$$\rho\left[\frac{dh}{dt} + u\frac{du}{dt}\right] + \rho u g \sin\theta - \frac{\partial P}{\partial t} = q_h \tag{3.47}$$

Multiplying the momentum conservation equation i.e., equation (3.27) by, *u* gives:

$$\rho u\frac{du}{dt} = -u\frac{\partial P}{\partial x} - \rho u g \sin\theta + u\beta_x \tag{3.48}$$

Rearranging equation (3.48) gives

$$\rho u g \sin\theta = -u\frac{\partial P}{\partial x} - \rho u\frac{du}{dt} + u\beta_x \tag{3.49}$$

Substituting equations (3.48) into (3.46) and expanding the terms in the brackets gives:

$$\rho\frac{dh}{dt} + \rho u\frac{du}{dt} - \rho u\frac{du}{dt} - u\frac{\partial P}{\partial x} - \frac{\partial P}{\partial t} + u\beta_x = q_h \tag{3.50}$$

Resolving equation (3.50) results in:

$$\rho \frac{dh}{dt} - \frac{\partial P}{\partial t} - u \frac{\partial P}{\partial x} = q_h - u\beta_x \tag{3.51}$$

By applying the notation expressed in equation (3.6), the differential equation above can be written as:

$$\rho \frac{dh}{dt} - \frac{dP}{dt} = q_h - u\beta_x \tag{3.52}$$

Equations (3.51) and (3.52) are the energy conservation equations expressed in terms of fluid enthalpy.

3.3 Cubic Equation of State (CEoS)

In this study, the Peng-Robinson equation of state (PR-EoS) (Peng et al., 1976) is employed for obtaining the appropriate thermodynamic and phase equilibrium data. This equation has been widely shown (see for example Walas (1987)) to be applicable to high-pressure hydrocarbon mixtures.

The Peng-Robinson equation of state is given by (Walas, 1987):

$$P = \frac{RT}{V - b_V} - \frac{a_V \alpha}{V^2 + 2b_V V - \left(b_V\right)^2} \tag{3.53}$$

Where:

$$a_V = \frac{k_1 R^2 T_c^2}{P_c^2} \tag{3.54}$$

$$b_V = \frac{k_2 R T_c}{P_c} \tag{3.55}$$

For mixtures:

$$a_V \alpha = \sum\sum y_i y_j \left(a_V \alpha\right)_{ij} \tag{3.56}$$

$$\left(a_V \alpha\right)_{ij} = \left(1 - K_{ij}\right)\sqrt{\left(a_V \alpha\right)_i \left(a_V \alpha\right)_j} \tag{3.57}$$

$$b_{V,i} = \sum y_i b_{V,i} \tag{3.58}$$

Where,

P, P_c = The absolute and critical pressures of the fluid respectively (KN/m^2)

T, T_c = The absolute and critical temperatures of the fluid respectively (K)

V = The fluid's molar volume (m^3/Kmol)

R = The universal gas constant (KJ/(Kmol-K))

k_1, k_2 = Constants specific to the respective equations of state

α = The alpha function

K_{ij} = The binary interaction parameter

y_i, y_j = Component mole fractions

Given the fluid molecular weight (M_w) (kg/Kmol), the fluid density (ρ) can be written as:

$$\rho = \frac{M_w}{V} \tag{3.59}$$

Thus substituting equation (3.59) into equation (3.53), the Peng-Robinson equation of state becomes:

$$P = \frac{\rho R' T}{1-\rho b} - \frac{\rho^2 a\alpha}{1+2\rho b - b^2\rho^2} \tag{3.60}$$

Where:

$$R' = \frac{R}{M_w} \tag{3.61}$$

$$a = \frac{k_1 R^2 T_c^2}{P_c^2 M_w^2} \tag{3.62}$$

$$b = \frac{k_2 R T_c}{P_c M_w} \tag{3.63}$$

3.3.1 The generalised alpha function (α) (Oke, 2004)

The alpha function used with the PR-EoS in this study is the Twu-Coon-Cunningham (TCC) generalised alpha function. The TCC alpha function (Twu et al., 1995a, 1995b) is a linear function of the acentric factor at a constant reduced temperature. This

property allows the easy extrapolation of the alpha function to heavy hydrocarbons, petroleum fractions, and gas condensates. The TCC alpha function can be expressed as (Twu et al., 1995a):

$$\alpha = \alpha^{(0)} + \omega\left(\alpha^{(1)} - \alpha^{(0)}\right) \tag{3.64}$$

$$\alpha^{(i)} = T_r^{N_i(M_i-1)} e^{L_i\left(1-T_r^{N_i M_i}\right)} \tag{3.65}$$

Where L, M and N are constants peculiar to the PR-EoS and are given in table 3.1, while (*i*) in equation (3.65) represents (0) or (1) in equation (3.64).

Table 3.1: The values of the L, M, and N for the Peng-Robinson CEoS

Alpha parameter	$T_r \leq 1$		$T_r > 1$	
	$\alpha^{(0)}$	$\alpha^{(1)}$	$\alpha^{(0)}$	$\alpha^{(1)}$
L	0.125283	0.511614	0.401219	0.024955
M	0.911807	0.784054	4.963070	1.248089
N	1.948150	2.812520	-0.20000	-8.00000

3.4 Hydrodynamic and Thermodynamic Relations for the HEM

Atti (2006) and Oke (2004) derived equations for determining two-phase mixture density, the fluid's speed of sound *a*, quantity of heat transferred to the fluid (q_h) and other important hydrodynamic properties. This section presents a summary of these equations implemented in the current work.

3.4.1 Two-phase Mixture Density (Atti, 2006)

In the case of the homogeneous equilibrium model assumption, a pseudo-mixture density, (ρ) based on pure liquid (ρ_l) and gas densities (ρ_g) is calculated using the EoS. This is given by:

$$\rho = \frac{\rho_g \rho_l}{\rho_g (1-\chi) + \rho_l \chi} \tag{3.66}$$

The term, χ refers to the fluid quality, and is the mass of vapour per unit mass of bulk fluid. The values of the respective phase densities can be calculated according to the following equations:

$$\rho_g = \frac{PM_g}{Z_g RT} \tag{3.67}$$

$$\rho_l = \frac{PM_l}{Z_l RT} \tag{3.68}$$

Where,

g and l denote gas and liquid phase respectively.

Z = fluid compressibility

3.4.2 Single and Two-phase Speed of Sound (Atti, 2006)

For single-phase real fluids, the speed of sound through the fluid can be expressed analytically as (Picard et al., 1987):

$$a^2 = \frac{\gamma}{k\rho} \tag{3.69}$$

Where, γ is the ratio of specific heats, and k is the isothermal coefficient of volumetric expansion.

By definition, γ and k can be expressed respectively as (Walas, 1987):

$$\gamma = \frac{C_P}{C_V} \tag{3.70}$$

$$k = -\rho\left(\frac{\partial V}{\partial P}\right)_T \tag{3.71}$$

Where, C_p and C_v are the specific heats at constant pressure and volume respectively, and V is the specific volume of the fluid.

From equation (3.71), the term $\left(\frac{\partial V}{\partial P}\right)_T$ can be obtained analytically by differentiating the Peng-Robinson equation (equation. (3.53)) to give:

$$\left(\frac{\partial V}{\partial P}\right)_T = \left[\frac{-RT}{(V-b_V)^2} - \frac{a_V\alpha.(2V+2b_V)}{[V^2+2b_VV-(b_V)^2]^2}\right]^{-1} \tag{3.72}$$

For two-phase flows, the analytical determination of γ and c_p becomes complex (Mahgerefteh et al., 1999). Hence the speed of sound is evaluated numerically at a given temperature and pressure as (Mahgerefteh et al., 1999):

$$a^2 = \left(\frac{\Delta P}{\rho(T,P) - \rho(T^*, P-\Delta P)}\right)_s \tag{3.73}$$

Where the subscript, s denotes a constant entropy condition and T, P, ΔP and ρ, denote temperature, pressure, infinitesimal change in pressure (ΔP = 1x10^{-6} bar) and density of the fluid respectively. T* represents the corresponding fluid temperature obtained by performing a *(P-ΔP)/s* flash.

3.4.3 Evaluation of the Thermodynamic Function, ▫

For single-phase fluids, the isochoric thermodynamic function φ is given (Picard et al., 1988) as:

$$\varphi = \left(\frac{\partial P}{\partial s}\right)_{\rho} = \frac{\rho \xi T a^2}{C_p} \tag{3.74}$$

Where,

ξ = isobaric coefficients of volumetric expansion, i.e. $\frac{1}{V}\left(\frac{\partial V}{\partial T}\right)_P$

C_p = specific heat capacity at constant pressure.

For two-phase flows, φ is determined numerically in the following manner.

Given that

$$\varphi = \left(\frac{\partial P}{\partial s}\right)_{\rho} \equiv \left(\frac{\partial P}{\partial s}\right)_{V} \tag{3.75}$$

Using Maxwell's relations (Walas, 1987), we get:

$$\left(\frac{\partial P}{\partial s}\right)_{V} = -\left(\frac{\partial T}{\partial V}\right)_{s} \tag{3.76}$$

Since $V = 1/\rho$, hence $dV = -(1/\rho^2)\, d\rho$), equation (3.76) becomes:

$$\left(\frac{\partial T}{\partial V}\right)_{s} = \rho^2 \left(\frac{\partial T}{\partial \rho}\right)_{s} \tag{3.77}$$

Therefore from equation (3.75):

$$\varphi = \rho^2 \left(\frac{\partial T}{\partial \rho} \right)_s = \rho^2 \left(\frac{\Delta T}{\Delta \rho} \right)_s \tag{3.78}$$

Hence, by performing an isentropic flash calculation as given by equation (3.73), the above can be solved numerically.

3.4.4 Fanning Friction Factor (f_w) Determination (Oke, 2004)

The fanning friction factor, f_w is required for calculating the contribution of frictional force to the momentum equation (equation (3.25)). It is a function of the flow Reynolds' number.

In this work, for the calculation of the fanning friction factor for transition and turbulent flows in rough pipes, the Chen (Chen, 1979) correlation is employed. It is given by:

$$\frac{1}{\sqrt{f_w}} = 3.48 - 1.7372 \, ln\left(\frac{\varepsilon}{r_{in}} - \frac{16.2446}{Re} ln A \right) \tag{3.79}$$

Where:

$$A = \frac{\left(\varepsilon / r_{in} \right)^{1.0198}}{6.0983} + \left(\frac{7.149}{Re} \right)^{0.8981} \tag{3.80}$$

ε, is the pipe roughness and r_{in} represents the pipe inner radius

For turbulent flow in smooth pipelines, Rohsenow et al. (1998) recommend the correlation proposed by Techo et al. (1965). The authors assert that the equation gives predictions within ±2 % of extensive experimental measurements (Rohsenow et al., 1998). It is given by:

$$\frac{1}{\sqrt{f_w}} = 1.7372\, ln \frac{Re}{1.964\, ln\, Re - 3.8215} \tag{3.81}$$

In the laminar region, the evaluation of the fanning friction factor is independent of the pipe roughness. Thus in general, the fanning friction factor for laminar fully developed flow is given by (Ouyang et al., 1996; Rohsenow et al., 1998):

$$f_w = \frac{16}{Re} \tag{3.82}$$

3.4.5 Thermal Conductivity and Viscosity Calculations

The vapour thermal conductivity and viscosity used in calculating the Nusselt, Reynolds and Prandtl numbers are determined form the Ely and Hanley's method (Ely et al., 1981, 1983) for non-polar gaseous mixtures. The method is based on the principle of corresponding states with Methane as the reference fluid. Assael et al. (1996) claim that Ely et al.'s (1981) method is one of the few schemes that is able to predict, with reasonable accuracy, the viscosity and thermal conductivity of a large number of non-polar components and their mixtures.

Viscosities and thermal conductivities for liquid mixtures containing alkanes (Methane to n-Dodecane) are determined from a semi-empirical scheme proposed by Assael et al. (1996). The scheme generally applies between temperatures ranging from 280 K to 400 K and pressures from saturation up to 990 atm. and has an uncertainty in predictions not greater than 5 per cent (Assael et al., 1996). The authors employed over 2,000 measurements of viscosity and thermal conductivity to optimise the coefficients used in the scheme.

For mixtures containing different classes of compounds, correlations proposed by DIPPR (Design Institute for Physical Property Data) (Daubert et al., 1990) are employed due to their accuracy and ease of use.

For two-phase fluids, the mixture thermal conductivity and viscosity is employed as given by:

$$\frac{1}{c_m} = \frac{\chi}{c_g} + \frac{1-\chi}{c} \tag{3.83}$$

Where χ and c respectively represent the fluid quality and the property to be determined.

3.4.6 Fluid/Wall Heat Transfer (Atti, 2006)

In the case of flow in pipelines, the pipeline wall constitutes the immediate surrounding of the fluid. However, except in the case of a perfectly insulated pipeline, the overall external heat transferred to the fluid is influenced by wall and ambient properties/conditions.

Newton's cooling law (Picard and Bishnoi, 1989; Chen et al., 1995b; Fairuzov, 1998; Mahgerefteh et al., 1999) is commonly employed for determining the heat transferred to a fluid flowing in a pipe. It is given by:

$$q_h = \frac{4}{D_{in}} U_h \left(T_{amb} - T_f \right) \tag{3.84}$$

Where U_h, is the overall heat transfer coefficient, D_{in}, the pipeline inner diameter, while T_{amb} and T_f denote the ambient and the fluid temperatures respectively.

In order to properly model the transient heat transfer process occurring at the wall-fluid interface, the transient energy balance used by Atti (2006) is employed in this study. The energy balance is carried out across the fluid-wall-ambient surfaces based on a lumped body approach. The method is used to update the wall temperatures after a given time step, thus estimating the heat input to the fluid in the next time interval. Figure 3.4 shows a schematic representation of the important heat transfer parameters.

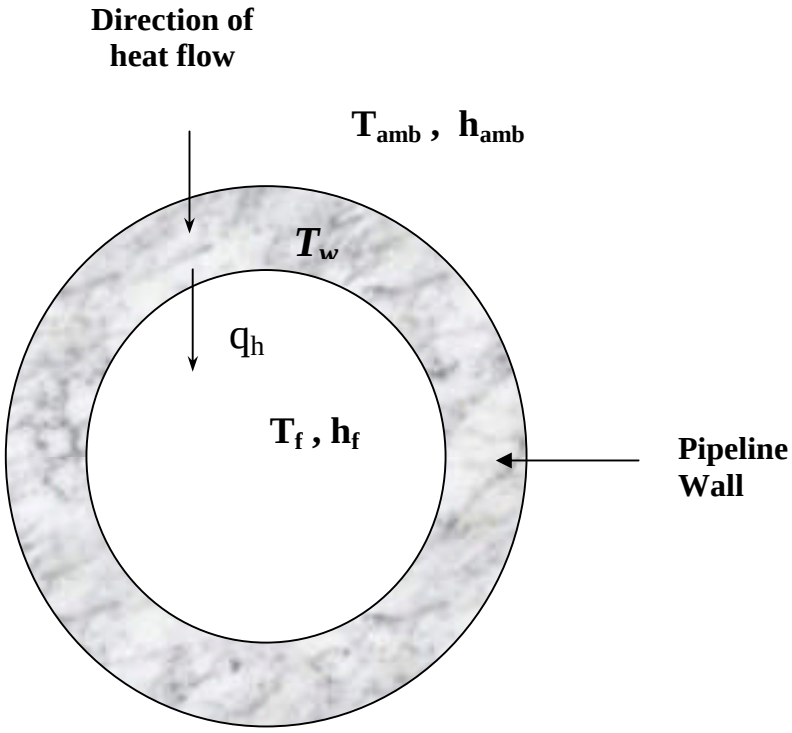

Figure 3.4: Schematic representation of the heat flow across the cross-section of a pipeline wall based on the lumped body approach (Atti, 2006).

Where T_{amb}, h_{amb} and T_w respectively represent the ambient temperature, heat transfer coefficient of the ambient, and wall temperature. T_f, h_f and q_h respectively represent the fluid's temperature, fluid heat transfer coefficient, and the quantity of heat transferred to the fluid.

In the lumped body approach the following assumptions are made:

- The heat transfer coefficient between the pipeline wall and either the ambient (h_{amb}) or the flowing fluid (h_f) is constant within a time step and are determined from flow properties at the beginning of the time step
- The wall density (ρ_w), specific heat capacity (C_{pw}) and thermal conductivity (κ_w) is time and space invariant

- The ambient and fluid temperatures employed in the energy balance are constant within a given time step and are obtained from flow conditions at the beginning of the time step
- Heat transfer occurs predominantly in the radial direction across the pipeline wall, heat flow resulting from tangential and longitudinal conduction inside the pipeline wall is neglected

Thus by applying the Newton's cooling law, the rate of heat transferred to the fluid (q_h) in a given time step can be approximated by (Atti, 2006):

$$q_h = \frac{4}{D_{in}} h_f^{i-1} \left(T_w - T_f \right) \tag{3.85}$$

3.5 The Steady State Isothermal Flow Model (Atti, 2006)

In this section, the steady state isothermal flow model developed by Atti (2006) is presented. The model is for one-dimensional flow based on the continuity and momentum equations presented in section 3.2.1 and 3.2.2 respectively.

From equation (3.4), the steady state expression (i.e. when all fluid properties are time invariant) for continuity in one-dimension can be written as:

$$u \frac{d\rho}{dx} + \rho \frac{du}{dx} = 0 \tag{3.86}$$

Separating variables and integrating equation (3.86), gives (Atti, 2006):

$$\ln\left(\frac{\rho_i}{\rho_{i-1}} \right) = -\ln\left(\frac{u_i}{u_{i-1}} \right) \tag{3.87}$$

Equation (3.87) can be rewritten as:

$$\rho_{i-1} u_{i-1} = \rho_i u_i \quad \text{(i.e. } \rho u = \text{constant)} \tag{3.88}$$

Where the subscripts i-1 and i respectively represents the penultimate and current grid point under consideration.

Equation (3.88) is the governing equation for mass conservation at steady state for flow in a uni-diameter pipeline.

From equation (3.26), the steady state momentum equation in one-dimension can be expressed as:

$$\rho u \frac{du}{dx} = -\frac{dP}{dx} - \rho g \sin\theta + \beta_x \tag{3.89}$$

Where the steady state frictional force term (β_x) is given by:

$$\beta_x = -2\frac{f_w}{D_{in}} \rho u |u| \tag{3.90}$$

The correlations required in calculating the fanning wall friction factor (f_w) have already been discussed in section 3.4.4.

Substituting the expression for β_x in equation (3.89) and rearranging gives (Atti, 2006):

$$\rho dP - (\rho u)^2 \frac{d\rho}{\rho} = -\left(\frac{2f(\rho u)^2}{D_{in}} + \rho^2 g \sin\theta \right) dx \tag{3.91}$$

The above equation can be expressed as

$$\rho dP + K_1 \frac{d\rho}{\rho} = (K_2 + \rho^2 K_3) dx \tag{3.92}$$

Where,

$$-(\rho u)^2 = K_1 \tag{3.93}$$

$$-\frac{2f(\rho u)^2}{D_{in}} = K_2 \tag{3.94}$$

$$-g \sin\theta = K_3 \tag{3.95}$$

Rearranging equation (3.92) and taking the limits results in (Atti, 2006):

$$\int_{P_{i-1}}^{P_i} \frac{\rho}{\left(\rho^2 K_3 + K_2\right)} dP + K_1 \int_{\rho_{i-1}}^{\rho_i} \frac{d\rho}{\rho\left(\rho^2 K_3 + K_2\right)} = \int_{x_{i-1}}^{x_i} dx \qquad (3.96)$$

The final form of equation (3.96) after resolving the integrals on the LHS is given by (Atti, 2006):

$$\frac{1}{2}\left[\left(\frac{\rho}{\rho^2 K_3 + K_2}\right)_{P_i} + \left(\frac{\rho}{\rho^2 K_3 + K_2}\right)_{P_{i-1}}\right]\left(P_i - P_{i-1}\right) + \frac{K_1}{2K_2}\left[2\ln\left(\frac{\rho_i}{\rho_{i-1}}\right) - \ln\frac{\left(\rho_i^2 K_3 + K_2\right)}{\left(\rho_{i-1}^2 K_3 + K_2\right)}\right] = x_i - x_{i-1}$$

(3.97)

The expression derived above is used for calculating the isothermal steady state pressure drop along a pipeline.

The stepwise algorithm below is a summary of the methodology used for calculating the isothermal steady state pressure drop.

1. Collate data at pipeline inlet such as fluid pressure, temperature, velocity, etc.
2. Divide the pipeline into sections (grids) with the distance between the grids being $\Delta_x = x_i - x_{i-1}$.
3. Guess the downstream pressure at the next gird point i.e. P_i.
4. In conjunction with an equation of state, evaluate the expression on the LHS of equation (3.97).
5. If equation (3.97) is satisfied, then the guessed downstream pressure is adopted as the solution. The fluid velocity u_i can then be obtained by applying equation (3.88). If the equation is not satisfied, go back to step 3 and update the guessed P_i.
6. Update the flow properties at this grid point and calculate the pressure drop at the next grid using steps 3-5 until the variables at the final grid is calculated.

3.6 Hyperbolicity of the Conservation Equations

The partial differential equations pertaining to the conservation of mass, momentum and energy together with an equation of state (EoS) constitute a system of equations that are essentially Euler equations with source terms due to the friction term in the momentum equation and the heat transfer term in the energy equation.

In solving these partial differential equations, it is essential to establish their mathematical nature in order to implement the appropriate technique for solving them. It can be shown (see below) that the Euler equations derived on the basis of the inviscid bulk fluid flow assumption can be classified as quasilinear and hyperbolic.

A partial differential equation is said to be quasilinear if all the derivatives of the dependent function *f(x, t)* are linear, while their corresponding coefficients contain at least a term that is either a linear or non-linear function of *f* (Prasad et al., 1985). This is illustrated by equation (3.98) below:

$$a(x,t,f)f_t + b(x,t,f)f_x = c(x,t,f) \qquad (3.98)$$

Where: f_t, f_x are the partial derivatives of the function *f* in terms of *t* and *x* respectively.

Equation (3.98) is quasilinear because its derivative terms (f_t, f_x) are linear while at least one of their corresponding coefficients [*a(x, t, f), b(x, t, f)*] contain terms that are functions of *f.*

The partial derivatives in the system of conservation equations (equations 3.18, 3.26, and 3.50) can be written as:

$$[\rho T + \varphi](P_t + uP_x) - \rho\varphi(h_t + uh_x) + \rho^2 a^2 T(u_x) = 0 \quad \text{(Continuity)} \qquad (3.99)$$

$$\rho(u_t + uu_x) + (P_x) = \alpha \quad \text{(Momentum)} \qquad (3.100)$$

$$\rho(h_t + uh_x) - (P_t + uP_x) = \psi \quad \text{(Energy)} \qquad (3.101)$$

Where:

$$\alpha = -\rho g \sin\theta + \beta_{wx} \tag{3.102}$$

$$\psi = q_h - u\beta_{wx} \tag{3.103}$$

$\beta_{wx} = \beta_x$ (this re-annotation serves to avoid confusing β_x (a non-derivative term) with other derivative terms such as P_x).

u = Fluid velocity in the x- direction (m/s)

θ = Angle the pipeline wall makes with the horizontal plane (^{o})

ρ = Density (kg/m^3)

h = Specific enthalpy (J/kg)

T = Absolute temperature (K)

a = Speed of sound

Based on the definition of quasilinear equations, the conservation equations represented by equations (3.99 – 3.101) can be seen to be quasilinear in structure. This is because all the partial derivative terms are linear. Furthermore, terms that are coefficients of the partial derivatives, such as density [$\rho(P, h)$] or flow velocity (u) are functions of some of the dependent functions (P, h, and u). These attributes render the system of equations quasilinear.

In general, the system of equations (i.e., equations (3.99 – 3.101)) presented above can be broadly expressed as:

$$Am_t + Bm_x = C \tag{3.104}$$

In matrix form, A, m_t, B and m_x, in equation (3.129) are given by:

$$A=\begin{bmatrix}\rho T+\varphi & -\rho\varphi & 0\\ 0 & 0 & \rho\\ -1 & \rho & 0\end{bmatrix}\quad m_t=\begin{bmatrix}P_t\\ h_t\\ u_t\end{bmatrix};\quad B=\begin{bmatrix}(\rho T+\varphi)u & -\rho\varphi u & \rho^2a^2T\\ 1 & 0 & \rho u\\ -u & \rho u & 0\end{bmatrix}\quad m_x=\begin{bmatrix}P_x\\ h_x\\ u_x\end{bmatrix}$$

$$C=\begin{bmatrix}0\\ \alpha\\ \psi\end{bmatrix} \tag{3.105}$$

A quasilinear system of partial differential equations as given by equation (3.105) is said to be hyperbolic if the eigenvalue (λ), satisfying equation (3.106) given below, has real and distinct roots (i.e., λ_1, λ_2, λ_3 are real and distinct) (Prasad et al., 1985):

$$\left|B-\lambda A\right|=0 \tag{3.106}$$

Thus, for the conservation equations, equation (3.106) can be expressed as:

$$\left|B-\lambda A\right|=\begin{vmatrix}(\rho T+\varphi)(u-\lambda) & \rho\varphi(\lambda-u) & \rho^2a^2T\\ 1 & 0 & \rho(u-\lambda)\\ \lambda-u & \rho(u-\lambda) & 0\end{vmatrix}=0 \tag{3.107}$$

Hence:

$$-(\rho T+\varphi)(u-\lambda)\rho^2(u-\lambda)^2+\rho^2\varphi(\lambda-u)(\lambda-u)(u-\lambda)+\rho^3a^2T(u-\lambda)=0 \tag{3.108}$$

Factorising the above equation results in:

$$(u-\lambda)\left[-(\rho T+\varphi)\rho^2(u-\lambda)^2+\rho^2\varphi(u-\lambda)^2+\rho^3a^2T\right]=0 \tag{3.109}$$

Factorising further and resolving yields:

$$(u-\lambda)\left[(-\rho^2(u-\lambda)^2(\rho T)+\rho^3a^2T\right]=0 \tag{3.110}$$

Dividing through by ρ^3T gives:

$$(u-\lambda)\left[a^2-(u-\lambda)^2\right]=0 \tag{3.111}$$

Solving equation (3.111) to obtain the roots of λ gives:

$$\lambda_1 = u \tag{3.112}$$

$$\lambda_2 = u - a \tag{3.113}$$

$$\lambda_3 = u + a \tag{3.114}$$

From equations (3.112-3.114), it can be seen that the eigenvalue (λ) that satisfy equation (3.106) are real and distinct. Thus, the systems of quasilinear partial differential equations for mass, momentum and energy conservation are hyperbolic. This implies that the behaviour and properties of the physical system described by these equations will be dominated by wave-like phenomena (Prasad et al., 1985). Indeed the speed of propagation of these waves, known as Mach lines, are given by the eigenvalues *(u+a)* and *(u-a)*, which correspond to the right running and left running characteristic (Mach) lines respectively.

3.7 Concluding Remarks

In this chapter, the equations describing mass, momentum and energy conservation were derived for transient fluid flow in a pipeline. Of important note is that the mass conservation equation is formulated in terms of pressure, enthalpy and flow velocity as opposed to pressure, density and velocity. The former formulation has the advantage of significantly reducing the computational runtime and improved model accuracy.

The conservation equations together with the Peng-Robinson equation of state constitute the building blocks for modelling the outflow following the rupture or puncture of pipelines.

The various hydrodynamic and thermodynamic expressions for predicting important parameters including the speed of sound in two-phase media, fluid viscosity as well as fluid flow and phase dependent friction coefficient were presented. In addition, the expression for the quantity of heat transferred to the fluid from the ambient based on

the lumped body approach was derived. This approach eliminates the need for assuming a constant overall heat transfer coefficient, and is expected to give predictions that are more reliable.

Furthermore, the steady state isothermal pressure drop model based on a real fluid was presented.

This chapter concluded by showing that the conservation equations derived are quasi-linear and hyperbolic in nature.

In Chapter 4, the different techniques available for solving quasi-linear hyperbolic partial differential equations including the method of characteristics (MOC) which is employed in this study are presented.

CHAPTER 4: APPLICATION OF THE METHOD OF CHARACTERISTICS (MOC)

4.1 Introduction

The Euler equations (continuity, momentum and energy) for unsteady real fluid flow were derived in chapter 3 (equations 3.99-3.101).The systems of equations cannot be solved analytically as they contain terms that are unknown or complex functions of their dependent and independent variables (see Flatt, 1986; Mahgerefteh et al., 1999). In general, two main numerical techniques are commonly employed and have found widespread use in resolving quasilinear hyperbolic partial differential equations. These are:

1. Finite difference methods (explicit and implicit)
2. Method of characteristics (MOC)

The finite difference methods involve system discretisation followed by substitution of derivatives appearing in a differential equation with finite approximations to obtain a system of algebraic relations at all grid points. Either the explicit or the implicit finite difference methods can be employed. The explicit method yields an explicit expression for each value at a new time level t_{n+1} in terms of nearby values at a previous time level t_n. The implicit method couples together values at different grid points at time t_{n+1} leading to an algebraic system of equations, which must be solved simultaneously with the aid of suitable boundary conditions.

Due to problems of convergence, instability and time step limitation commonly associated with explicit methods, implicit methods, which are unconditionally stable and permit the use of large/unrestrained time steps are commonly employed (Swaffield et al., 1993). However, implicit methods may involve the simultaneous solution of a large number of non-linear equations coupled with complex boundary conditions, thus rendering the implementation complicated. Furthermore, the time

step cannot be increased arbitrarily since this will result in a smoothing of the transient pressure peaks. The attributes highlighted above therefore makes the finite difference methods unsuitable for modelling fast transients as encountered in pipeline rupture.

The Method of Characteristics is a general mathematical technique that is particularly suited to the solution of systems of quasi-linear hyperbolic partial differential equations with two independent variables (e.g. distance and time). The method resolves partial differential equations into a system of ordinary differential equations (compatibility equations), which are only valid along that co-ordinate (characteristic line). The compatibility equations may then be solved by standard single step finite-difference methods for ordinary differential equations.

The method is particularly suitable for systems containing complex boundary conditions, as each node point and boundary condition is analysed individually at each time step. However, its primary disadvantage is the need for strict adherence to the time step-distance interval relationship based on the Courant stability criterion (see chapter 8 and section 4.3.2) in its choice of time steps. This handicap has somewhat been compensated for with the advent of cheap and relatively fast computers. Consequently, the MOC has been chosen to resolve the conservative equations in this work.

4.2 The Method of Specified Time

There are two main grid discretisation methods for the MOC. These are the Characteristic Grid method (CG) which is also known as natural method of characteristics, and the Inverse Marching method or the Method of Specified Time Intervals (ST) (Flat, 1986).

In the method of specified time intervals, the location of the solution points in the space-time grid is specified a priori and the characteristic lines are extended backwards in time to intersect a time line on which initial-data points lie (figure 4.1). This necessitates interpolation to locate the intersection of all three characteristic lines on the previous time line.

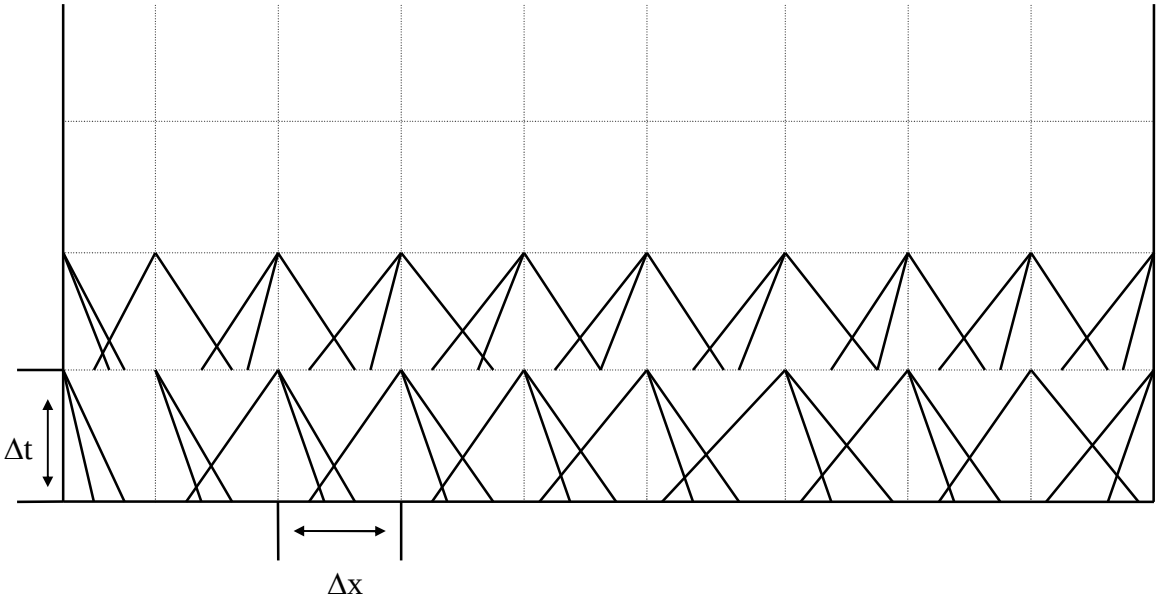

Figure 4.1: The Method of Specified Time

In contrast, the position of the new solution point is not specified a priori in the characteristic grid method, but is determined from the intersection of left and right running characteristics with origins located at known solution points or initial data. Hence, a free-floating grid is developed in the *x-t* plane as shown in figure 4.2. This method of characteristics is particularly accurate since the solution progresses naturally along the characteristic lines. However, when more than two characteristic lines are present, i.e. when an energy equation is solved, in addition to the mass and momentum conservation equations, interpolation is required to locate the path line intersection between known initial points.

Although the CG method may be more accurate than the ST method, its main draw back is that there is no direct control on the time of input variables at boundaries. This is in contrast to the ST approach in which boundary conditions may be introduced at predefined times. This feature makes the CG method quite cumbersome in modelling systems that commonly prevail in reality such as valve closure, or pump shutdown. For this reason, the ST method of discretisation is used throughout this work.

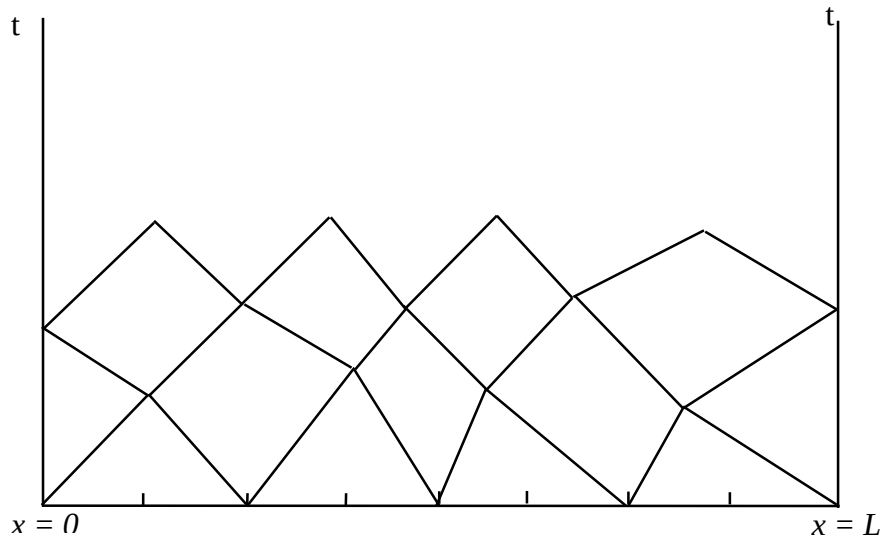

Figure 4.2: The Characteristic Grid Method.

4.3 Numerical Formulation of the Method of Characteristics

The solving of PDEs by the MOC comprises 2 steps:

1. Conversion of the basic partial differential equations of flow into ordinary differential equations (compatibility equations).
2. Solution of the compatibility equations based on the ST method and employing the Euler predictor-corrector technique (Zucrow and Hoffman, 1976) to enhance accuracy of the numerical results.

4.3.1 Step1: Conversion of PDEs to ODEs

The two most common methods of converting the PDEs to ODEs are the matrix transformation method (Tiley, 1989) and multiplying the basic equations by an unknown parameter and subsequent summation. Atti (2006) demonstrated that the latter method was simpler and mathematically rigorous. Consequently, the method employed by Atti (2006) is adapted for use in this study.

The Euler equations (continuity, momentum and energy) for unsteady real fluid flow were derived in Chapter 3. The final forms of the Euler equations are:

$$\left[\rho T+\varphi\right]\left(P_t+uP_x\right)-\rho\varphi\left(h_t+uh_x\right)+\rho^2a^2T\left(u_x\right)=0 \quad \text{(Continuity)} \qquad (3.99)$$

$$\rho\left(u_t+uu_x\right)+\left(P_x\right)=\alpha \quad \text{(Momentum)} \qquad (3.100)$$

$$\rho\left(h_t+uh_x\right)-\left(P_t+uP_x\right)=\psi \quad \text{(Energy)} \qquad (3.101)$$

Where:

$$\alpha=-\rho g\sin\theta+\beta_{wx} \qquad (3.102)$$

$$\psi=q_h-u\beta_{wx} \qquad (3.103)$$

Following Atti (2006), and introducing 1/λ to represent the slope of the characteristic lines, the conservation equations may be replaced by 3 compatibility equations, which are valid along 3 characteristic equations given below:

$$\rho d_0h-d_0P=\psi d_0t \quad \text{along} \quad \frac{d_0t}{d_0x}=\frac{1}{u}=\frac{1}{\lambda_o} \qquad (4.1)$$

(Path line compatibility equation along the Path line characteristic, C_o)

$$d_+P+\left[\rho a\right]d_+u=\left[\frac{\varphi\psi}{\rho T}+a\alpha\right]d_+t \quad \text{along} \quad \frac{d_+t}{d_+x}=\frac{1}{u+a}=\frac{1}{\lambda_+} \qquad (4.2)$$

(Positive Mach line compatibility equation along the Positive Mach line characteristic, C_+)

$$d\_P + [\rho a]\, d\_u = \left[\frac{\varphi\psi}{\rho T} - a\alpha\right] d\_t \quad \text{along} \quad \frac{d\_t}{d\_x} = \frac{1}{u-a} = \frac{1}{\lambda\_} \tag{4.3}$$

(Negative Mach line compatibility equation along the Negative Mach line characteristic, C-)

The positive (C_+) and negative (C-) mach lines respectively govern the speed at which expansion and compression waves propagate from the low and high-pressure ends of the pipeline respectively, while the path line (C_o) dictates the rate of flow through any given point along the pipeline.

4.3.2 Step 2: Solution of the Compatibility Equations

The application of the characteristic and compatibility equations requires the development of a characteristic grid in the space (*x)* - time (t) plane as that shown in figure 4.3.

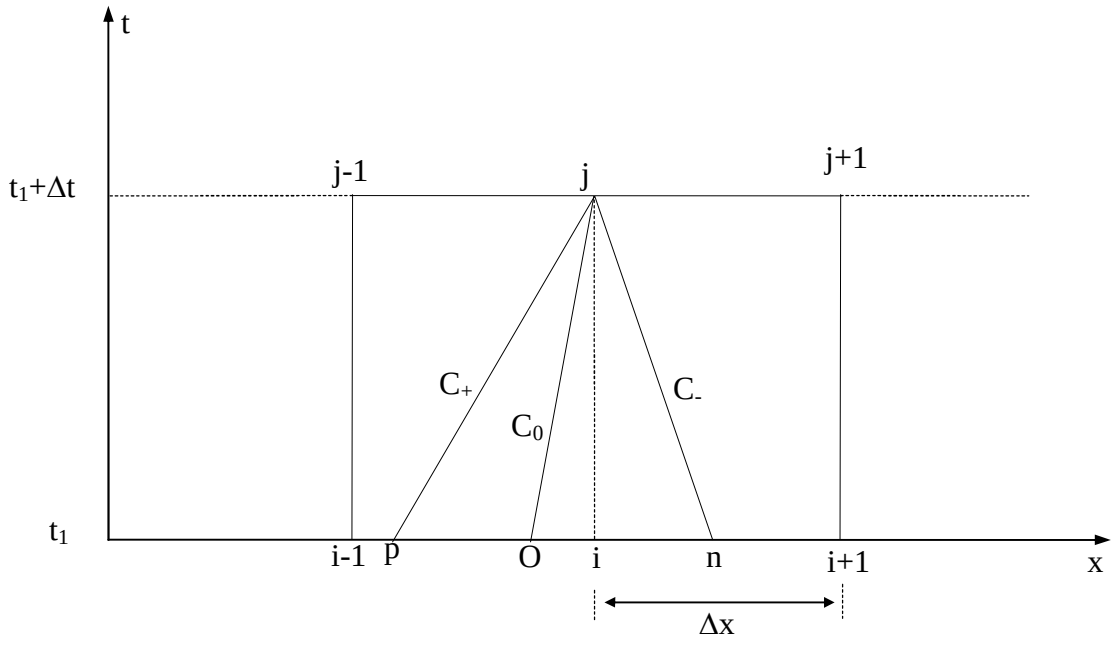

Figure 4.3: A schematic representation of Path line (C_0) and Mach lines (C_+, C-) characteristics at a grid point along the time (t) and space (x) axes.

At time t_1, the fluid properties at the grid points i-1, i and i+1 are known. These initial conditions are used to determine the fluid properties at points p, o and n by linear interpolation. The compatibility equations are solved by the finite difference method to obtain the flow properties (P, h, u) at the intersection point *j* at time $t_1 + \Delta t$.

However, the characteristics lines are curved and not straight, therefore, it is necessary to minimise errors introduced by the first order (linear) approximation. This is achieved by employing the corrector step (the Euler -corrector technique) to update the first order solution (see section 4.4).

The time steps (Δt) employed are pre-specified and are calculated subject to the Courant-Friedrichs-Lewy (CFL) criterion (Courant et al.,1926; Zucrow and Hoffman, 1976). It is given by:

$$\Delta t \leq \frac{\Delta x}{\left(\left|u + a\right|_{\max}\right)} \tag{4.4}$$

Significantly, the CFL criterion is only a necessary condition for stability, but it is not sufficient to ensure it as the flow properties (*u* and *a*) may vary in each time step. This is especially the case during rapid changes in fluid properties such as those encountered near the pipeline rupture plane or when crossing depressurisation induced phase transition boundaries. The effect of the CFL criterion on the simulation results obtained in this work is discussed in chapter 8.

4.4 Finite Difference Solution of the Compatibility and Characteristic Equations

The Euler predictor-corrector algorithm is the finite difference method is used to numerically solve the compatibility and characteristic equations (4.1 - 4.3). The method consists of a predictor step (first order approximation), which is used to estimate the approximate value of the flow properties at the solution point. On the other hand, the corrector step, based on second order approximation improves on the initial approximation of the predictor step.

4.4.1 First Order Approximation: Predictor Step

Following Atti (2006), the compatibility equations given by equations (4.1) to (4.3) can be expressed in finite difference form as:

$$(\rho)_0 (h_j - h_0) - (P_j - P_0) = \psi_0 (t_j - t_0) \tag{4.5}$$

$$(P_j - P_p) + (\rho a)_p (u_j - u_p) = \left(\frac{\varphi\psi}{\rho T} + a\alpha \right)_p (t_j - t_p) \tag{4.6}$$

$$(P_j - P_n) - (\rho a)_n (u_j - u_n) = \left(\frac{\varphi\psi}{\rho T} - a\alpha \right)_n (t_j - t_n) \tag{4.7}$$

The subscripts assigned to the various properties in equations (4.5) to (4.7) denote the location in space and time, as shown in figure 4.3

In order to calculate the fluid properties (P, h, u, ρ, etc) at the solution point j at time $t_1 + \Delta t$, the positions (x_p , x_o and x_n) and fluid properties at the intersection of the characteristic lines at the previous time level (t_1) need to be determined. As mentioned in section 4.3.2, these values are determined from the knowledge of the slope of the characteristics lines and by linear interpolation between points i-1, i and i+1 whose conditions are known at time t_1.

By expressing the characteristic lines in finite difference form, the path line, positive Mach line and negative Mach line can be expressed respectively as:

$$\lambda_0 = u_o = \frac{x_i - x_o}{\Delta t} \Rightarrow x_o = x_i - u_o \Delta t \tag{4.8}$$

$$\lambda_+ = u_p + a_p = \frac{x_i - x_p}{\Delta t} \Rightarrow x_p = x_i - \left(u_p + a_p\right)\Delta t \tag{4.9}$$

$$\lambda_- = u_n - a_n = \frac{x_i - x_n}{\Delta t} \Rightarrow x_n = x_i - \left(u_n - a_n\right)\Delta t \tag{4.10}$$

Also, assuming that flow properties (Z) at the lower time level (t_1) vary linearly in space, linear interpolation formulas that estimate unknown flow variables at points p, o, and n from known variables at points (i), (i-1), and (i+1) can be expressed respectively as:

$$Z_p = Z_{i-1} + \frac{Z_i - Z_{i-1}}{x_i - x_{i-1}}\left(x_p - x_{i-1}\right) \tag{4.11}$$

$$Z_o = \begin{cases} Z_{i-1} + \dfrac{Z_i - Z_{i-1}}{x_i - x_{i-1}}\left(x_o - x_{i-1}\right) & \text{if } \lambda_o > 0 \\ \\ Z_i + \dfrac{Z_{i+1} - Z_i}{x_{i+1} - x_i}\left(x_o - x_i\right) & \text{if } \lambda_o < 0 \end{cases} \tag{4.12}$$

$$Z_n = Z_i + \frac{Z_{i+1} - Z_i}{x_{i+1} - x_i}\left(x_n - x_i\right) \tag{4.13}$$

Where *Z = P, h, u, and a*

Thus the expressions for the velocity (*u*) and speed of sound (*a*) in equations (4.8) - (4.10) can be obtained from linear interpolation formulas. These expressions can then be substituted back into the characteristic equations, (4.8) to (4.10) to give:

$$u_p = u_{i-1} + \frac{u_i - u_{i-1}}{x_i - x_{i-1}}\left[x_i - x_{i-1} - \Delta t\left(u_p + a_p\right)\right] = u_i - \frac{u_i - u_{i-1}}{x_i - x_{i-1}}\Delta t\left(u_p + a_p\right) \tag{4.14}$$

Rearranging equation (4.14) results in:

$$u_p\left(1+\frac{u_i-u_{i-1}}{x_i-x_{i-1}}\Delta t\right)+\frac{u_i-u_{i-1}}{x_i-x_{i-1}}\Delta t a_p=u_i \qquad (4.15)$$

Conducting the same manipulation for a_p, gives:

$$a_p\left(1+\frac{a_i-a_{i-1}}{x_i-x_{i-1}}\Delta t\right)+\frac{a_i-a_{i-1}}{x_i-x_{i-1}}\Delta t u_p=a_i \qquad (4.16)$$

Equations (4.15) and (4.16) can be solved simultaneously for u_p and a_p.

Similarly a 2×2 system of equations can be set up for u_n and a_n by applying the same mathematical manipulation described above.

For u_o, the solution depends on whether the slope of the path line characteristic is positive or negative. The nature of the sign determines which way the fluid is flowing. If it is positive the, flow is travelling towards (i+1), while the converse is true if the sign is negative.

Thus from equations (4.8) and (4.12),

When $\lambda_o > 0$ then,

$$\lambda_0=u_o=u_{i-1}+\frac{u_i-u_{i-1}}{x_i-x_{i-1}}\left(x_i-\Delta t u_o-x_{i-1}\right)=u_{i-1}+u_i-u_{i-1}-\frac{u_i-u_{i-1}}{x_i-x_{i-1}}\Delta t u_o \qquad (4.17)$$

Equation (4.17) on simplifying becomes:

$$u_o=\frac{u_i}{\left(1+\frac{u_i-u_{i-1}}{x_i-x_{i-1}}\Delta t\right)} \qquad (4.18)$$

However, when $\lambda_o < 0$, from equations (4.8) and (4.12), u_o can be similarly derived as:

$$u_o=\frac{u_i}{\left(1+\frac{u_{i+1}-u_i}{x_{i+1}-x_i}\Delta t\right)} \qquad (4.19)$$

Thus, the locations of x_p, x_n, and x_o can be obtained directly from equations (4.8) to (4.10) by substituting the calculated values for u_p, a_p, u_n, a_n, and u_o into their corresponding equations.

Thereafter, the values of P and h at the initial points p, o, and n are calculated from relevant linear interpolation formulas (i.e., equations (4.11), (4.12) and (4.13)). With the aid of these calculated values, other corresponding thermodynamic properties at the initial points such as ρ, T, and φ are determined by performing a P-h flash calculation.

Hence, at this stage all the initial point flow variables available to compute the flow conditions at the solution point (j) in the predictor step.

Manipulating equations (4.6) and (4.7) respectively to solve for P_j gives:

$$P_j = K_1 - (\rho a)_p (u_j - u_p) + P_p \tag{4.20}$$

$$P_j = K_2 + (\rho a)_n (u_j - u_n) + P_n \tag{4.21}$$

Where K_1 and K_2 are given by:

$$K_1 = \left(\frac{\varphi \psi}{\rho T} + a\alpha \right)_p \Delta t \tag{4.22}$$

$$K_2 = \left(\frac{\varphi \psi}{\rho T} - a\alpha \right)_n \Delta t \tag{4.23}$$

Solving the equations (4.20) and (4.21) simultaneously for u_j gives:

$$u_j = \frac{K_1 - K_2 + (\rho a)_p u_p + (\rho a)_n u_n + P_p + P_n}{(\rho a)_n + (\rho a)_p} \tag{4.24}$$

Hence, the pressure at the solution point, P_j can be calculated by the direct substitution of u_j into either equations (4.20) or (4.21).

The enthalpy at the solution point can subsequently be obtained from the path line compatibility (i.e., equation (4.5)) as:

$$h_j = \frac{\psi_0 \Delta t + \left(P_j - P_0\right) + \rho_0 h_0}{\rho_0} \tag{4.25}$$

Once the pressure and enthalpy are determined, other thermodynamic properties at the solution point (e.g. ρ,φ and T) are obtained from a pressure-enthalpy flash calculation.

The procedure in which the tentative values are obtained at the solution point '*j*' constitutes the predictor step.

4.4.2 Second Order Approximation: Corrector Step

To improve on the first order solution, a second order approximation to the compatibility and characteristic is required. The procedure is given below.

The second order finite difference form of the compatibility equations (equations 4.1-4.3) can be expressed as

Path line compatibility:

$$\frac{1}{2}\left[\left(\rho\right)_0 + \left(\rho\right)_j\right]\left(h_j - h_0\right) - \left(P_j - P_0\right) = \frac{1}{2}\left[\psi_0 + \psi_j\right]\left(t_j - t_0\right) \tag{4.26}$$

Positive Mach line compatibility:

$$\left(P_j - P_p\right) + \frac{1}{2}\left[\left(\rho a\right)_p + \left(\rho a\right)_j\right]\left(u_j - u_p\right) = \frac{1}{2}\left[\left(\frac{\varphi\psi}{\rho T} + a\alpha\right)_p + \left(\frac{\varphi\psi}{\rho T} + a\alpha\right)_j\right]\left(t_j - t_p\right) \tag{4.27}$$

Negative Mach line compatibility:

$$\left(P_j - P_n\right) - \frac{1}{2}\left[\left(\rho a\right)_n + \left(\rho a\right)_j\right]\left(u_j - u_n\right) = \frac{1}{2}\left[\left(\frac{\varphi\psi}{\rho T} - a\alpha\right)_n + \left(\frac{\varphi\psi}{\rho T} - a\alpha\right)_j\right]\left(t_j - t_n\right)$$

(4.28)

As with the predictor step, the positions x_p, x_o and x_n, and fluid properties at these corresponding locations need to be determined. This is achieved by expressing the characteristic equations (equations 4.1- 4.3) in second order form and interpolating between points i-1, i and i+1.

The second order approximations to characteristic equation are given by:

Path line characteristic:

$$x_j - x_o = \frac{1}{2}\left(\lambda_0 + \lambda_j\right)\left(t_j - t_o\right) \tag{4.29}$$

Positive Mach line or right running characteristic:

$$x_j - x_p = \frac{1}{2}\left(\lambda_p + \lambda_j\right)\left(t_j - t_p\right) \tag{4.30}$$

Negative Mach line or left running characteristic:

$$x_j - x_n = \frac{1}{2}\left(\lambda_n + \lambda_j\right)\left(t_j - t_n\right) \tag{4.31}$$

From equations (4.29 - 4.31), the corrector step can be expressed as:

$$\frac{1}{2}\left(\lambda_0 + \lambda_j\right) = \frac{1}{2}\left(u_o + u_j^r\right) = \frac{x_i - x_o}{\Delta t} \Rightarrow x_o = x_i - \frac{\Delta t}{2}\left(u_o + u_j^r\right) \tag{4.32}$$

$$\frac{1}{2}\left(\lambda_+ + \lambda_j\right) = \frac{1}{2}\left(u_p + u_j^r\right) + \frac{1}{2}\left(a_p + a_j^r\right) = \frac{x_i - x_p}{\Delta t} \Rightarrow x_p = x_i - \frac{\Delta t}{2}\left(u_p + a_p + u_j^r + a_j^r\right)$$

(4.33)

$$\frac{1}{2}\left(\lambda_- + \lambda_j\right) = \frac{1}{2}\left(u_n + u_j^r\right) - \frac{1}{2}\left(a_n + a_j^r\right) = \frac{x_i - x_n}{\Delta t} \Rightarrow x_n = x_i - \frac{\Delta t}{2}\left(u_n - a_n + u_j^r - a_j^r\right)$$

(4.34)

The subscript *j* together with superscript *r* refer to the solution condition at the previous iteration step, *r*.

From equations (4.32) and (4.12), and following the same approach employed for the predictor step:

If $\lambda_o > 0$ then,

$$u_o = u_{i-1} + \frac{u_i - u_{i-1}}{x_i - x_{i-1}}\left(x_i - \frac{\Delta t}{2}\left(u_o + u_j^r\right) - x_{i-1} \right) \tag{4.35}$$

Rearranging (4.35) yields

$$u_o = \frac{u_i - \frac{u_i - u_{i-1}}{x_i - x_{i-1}}\frac{\Delta t}{2}u_j^r}{\left(1 + \frac{u_i - u_{i-1}}{x_i - x_{i-1}}\frac{\Delta t}{2}\right)} \tag{4.36}$$

If $\lambda_o < 0$, u_o can be obtained from equation (4.32) and (4.12) as:

$$u_o = \frac{u_i - \frac{u_{i+1} - u_i}{x_{i+1} - x_i}\frac{\Delta t}{2}u_j^r}{\left(1 + \frac{u_{i+1} - u_i}{x_{i+1} - x_i}\frac{\Delta t}{2}\right)} \tag{4.37}$$

Thereafter, x_o is obtained by substituting u_o into equation (4.32).

From linear interpolation (equation (4.11)) and equation (4.33) gives:

$$u_p = u_{i-1} + \frac{u_i - u_{i-1}}{x_i - x_{i-1}}\left[x_i - x_{i-1} - \frac{\Delta t}{2}\left(u_p + a_p + u_j^r + a_j^r\right) \right] \tag{4.38}$$

Rearranging equation (4.38) yields:

$$u_p\left(1 + \frac{u_i - u_{i-1}}{x_i - x_{i-1}}\frac{\Delta t}{2}\right) + \frac{u_i - u_{i-1}}{x_i - x_{i-1}}\frac{\Delta t}{2}a_p = u_i - \frac{u_i - u_{i-1}}{x_i - x_{i-1}}\frac{\Delta t}{2}\left(u_j^r + a_j^r\right) \tag{4.39}$$

Performing the same manipulation for a_p, using linear interpolation in conjunction with equation (4.33) yields:

$$a_p\left(1+\frac{a_i-a_{i-1}}{x_i-x_{i-1}}\frac{\Delta t}{2}\right)+\frac{a_i-a_{i-1}}{x_i-x_{i-1}}\frac{\Delta t}{2}u_p=a_i-\frac{a_i-a_{i-1}}{x_i-x_{i-1}}\frac{\Delta t}{2}\left(u_j^r+a_j^r\right) \tag{4.40}$$

As with the predictor step, equations (4.39) and (4.40) can be solved simultaneously for u_p and a_p, and by substituting these values into equation (4.33), x_p is obtained.

A 2×2 system of equations can also be set up for u_n and a_n in the corrector step, and x_n is obtained via equation (4.34).

The dependent flow variables at the solution point can now be calculated at the next iteration (r+1) step.

Manipulating equations (4.27) and (4.28) respectively to solve for P_j gives:

$$P_j^{r+1}=K_1-\frac{1}{2}\left[\left(\rho a\right)_p+\left(\rho a\right)_j^r\right]\left(u_j^{r+1}-u_p\right)+P_p \tag{4.41}$$

$$P_j^{r+1}=K_2+\frac{1}{2}\left[\left(\rho a\right)_n+\left(\rho a\right)_j^r\right]\left(u_j^{r+1}-u_n\right)+P_n \tag{4.42}$$

Where K_1 and K_2 are given by:

$$K_1=\frac{1}{2}\left[\left(\frac{\varphi\psi}{\rho T}+a\alpha\right)_p+\left(\frac{\varphi\psi}{\rho T}+a\alpha\right)_j^r\right]\Delta t \tag{4.43}$$

$$K_2=\frac{1}{2}\left[\left(\frac{\varphi\psi}{\rho T}-a\alpha\right)_n+\left(\frac{\varphi\psi}{\rho T}-a\alpha\right)_j^r\right]\Delta t \tag{4.44}$$

Solving the equations (4.41) and (4.42) simultaneously for yields P_j^{r+1} and u_j^{r+1}

$$u_j^{r+1}=\frac{K_1-K_2+\frac{1}{2}\left[\left(\rho a\right)_p+\left(\rho a\right)_j^r\right]u_p+\frac{1}{2}\left[\left(\rho a\right)_n+\left(\rho a\right)_j^r\right]u_n+P_p-P_n}{\frac{1}{2}\left[\left(\rho a\right)_p+\left(\rho a\right)_j^r\right]+\frac{1}{2}\left[\left(\rho a\right)_n+\left(\rho a\right)_j^r\right]} \tag{4.45}$$

P_j^{r+1} is then obtained from equation (4.41), and the enthalpy at the solution point is obtained from the path line compatibility (i.e., equation (4.26)) as:

$$h_j^{r+1} = \frac{\left[\psi_0 + \psi_j^{\,r}\right]\Delta t + 2\left(P_j^{r+1} - P_0\right)}{\rho_o + \rho_j^{\,r}} + h_o \qquad (4.46)$$

The above second order calculation procedure is repeated until a certain tolerance (*ca* 10^{-5}) is satisfied for the three dependent variables, i.e. *P*, *h* and *u*. Figure 4.4 is the calculation flow chart for the solution of the flow variables at the next time step based on the predictor-corrector procedure, and is given below.

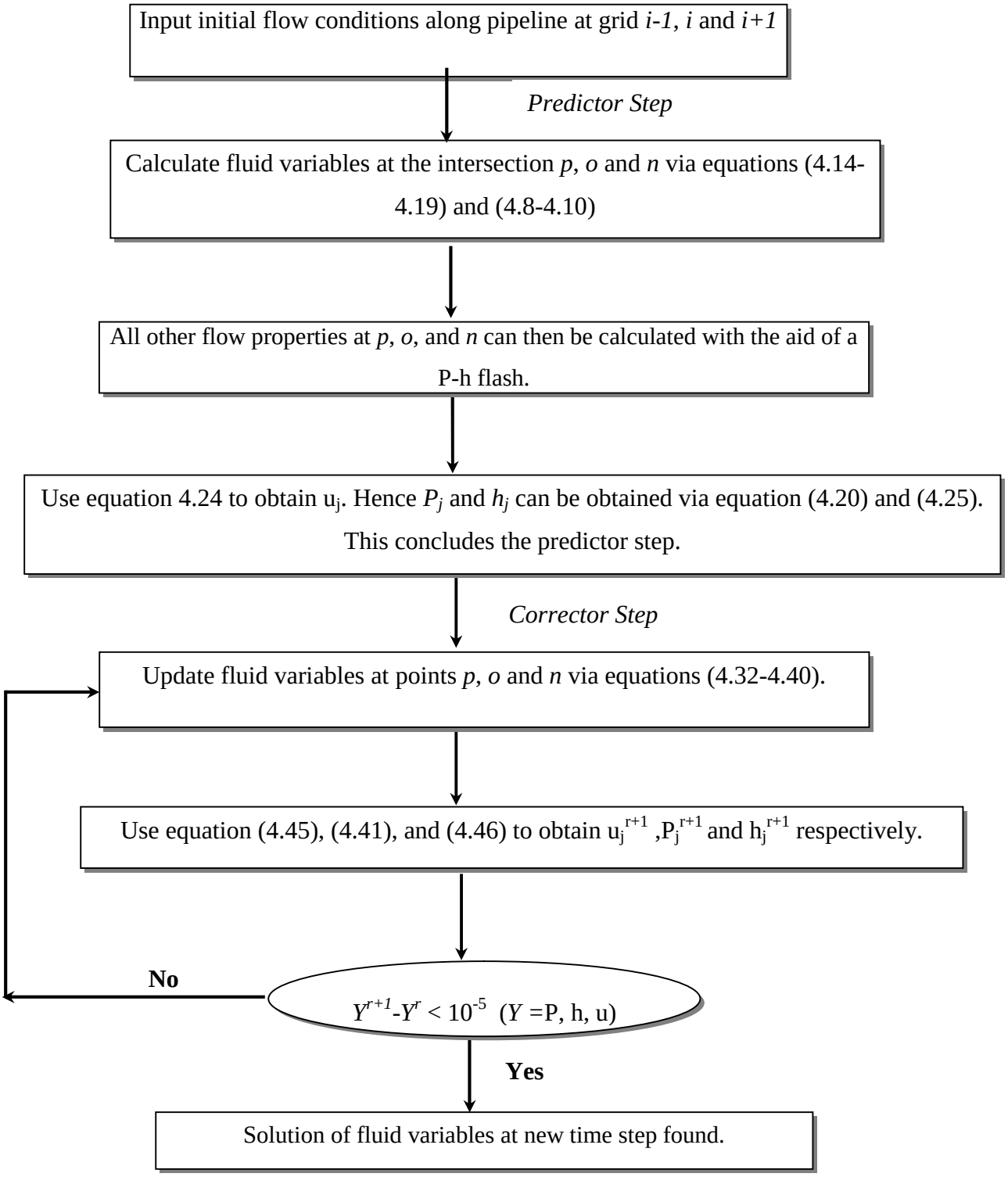

Figure 4.4: Calculation algorithm incorporating the Euler predictor-corrector technique in calculating the flow variables at the next time step.

4.5 Nested Grid System

There are two main types of grid (mesh) discritisation that can be used with the MOC. These are the Simple Grid System (SGS) and the Nested Grid System (NGS). In the normal grid system the pipeline being modelled is divided into equally spaced grids (Δx) as shown in figures 4.1 and 4.3. In the nested grid system, the grids close to the rupture plane are subdivided into smaller meshes to increase the resolution in modelling the fast transients close to the rupture plane as compared to the rest of the pipeline. Clearly the longer the pipeline, the slower the transient within the pipeline, and therefore a comparatively large Δx (fewer grids) may be used to model the flow conditions in this region. The use of fewer grids results in fewer calculations being performed, which in turn reduces CPU run time.

Figure 4.5 gives a schematic representation of the nested grid system employed in this study. As shown in figure 4.5, the 2 normal space-step of length Δx_3 at the pipeline exit are divided into 5×5 cells of length Δx_2. Further refinement is also possible by subdividing the last 2 finer meshes into 5×5 cells of length Δx_1.

Since the smaller cells are geometrically similar, and contained within the large normal mesh (space-step = Δx_3), a consistent Courant number is maintained throughout the discharge process and numerical instability is avoided. Therefore accuracy in the fast transient region near the open end is assured, whilst speeding up the rest of the calculations along the coarser grid where Δx_3 is large.

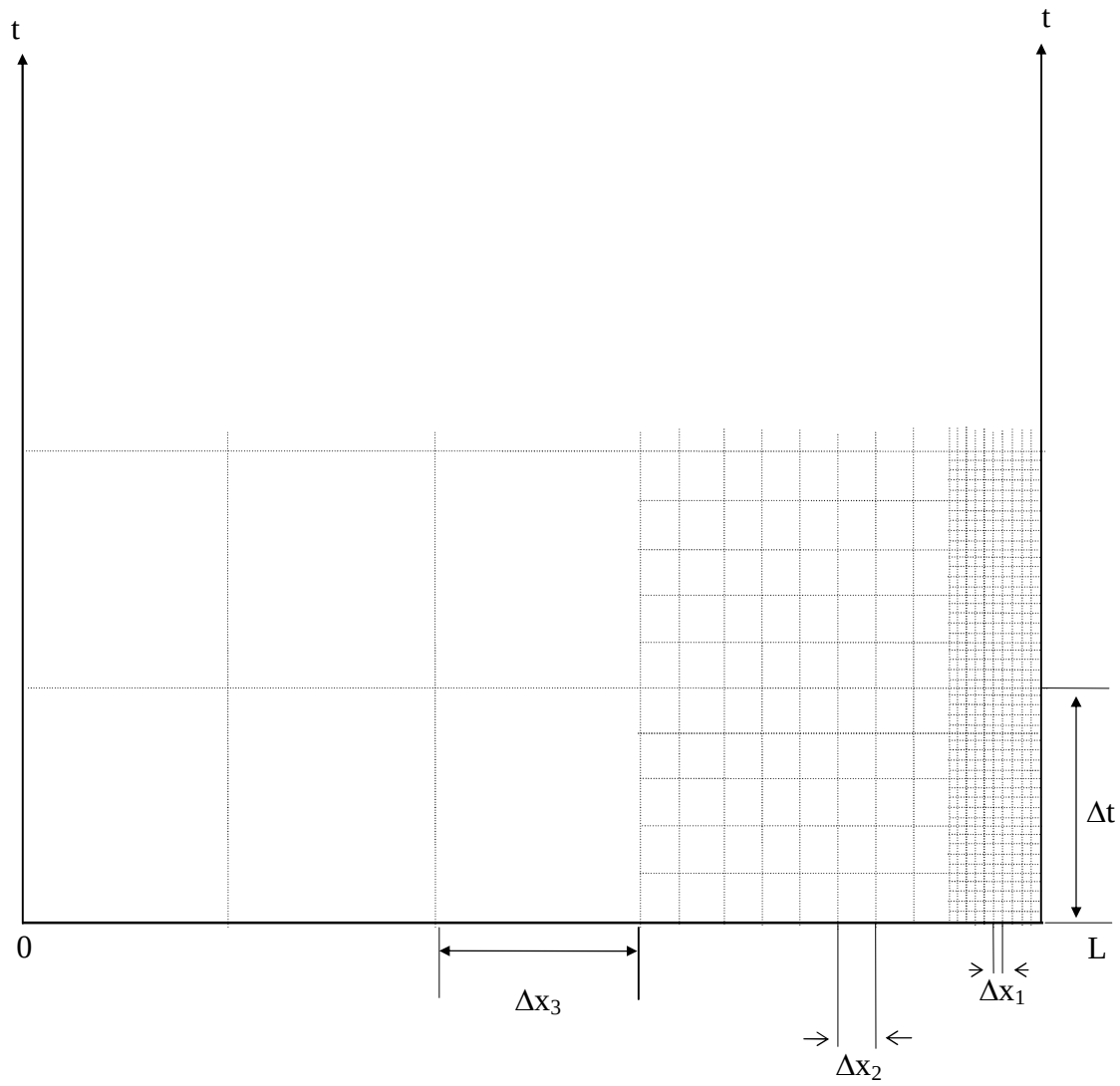

Figure 4.5: Schematic representation of the mesh arrangement in the nested grid system.

For the purposes of terminology, a single refinement to the uniform, simple grid system (i.e., just one 5×5 division over the two Δx's next to the rupture plane) is referred to as 'Nested Grid Scheme (NGS)', whereas the double refinement (say two 5×5 divisions) is denoted as 'Compound Nested Grid Scheme (CNGS)'.

At the junctions of different size meshes, slight modifications to the finite difference form of the compatibility equations presented in section 4.4.1 are required.

4.5.1 Formulation of the NGS

The calculation at solution point j+4 at the boundary between the coarse and fine meshes as shown in figure 4.6 is given as an example.

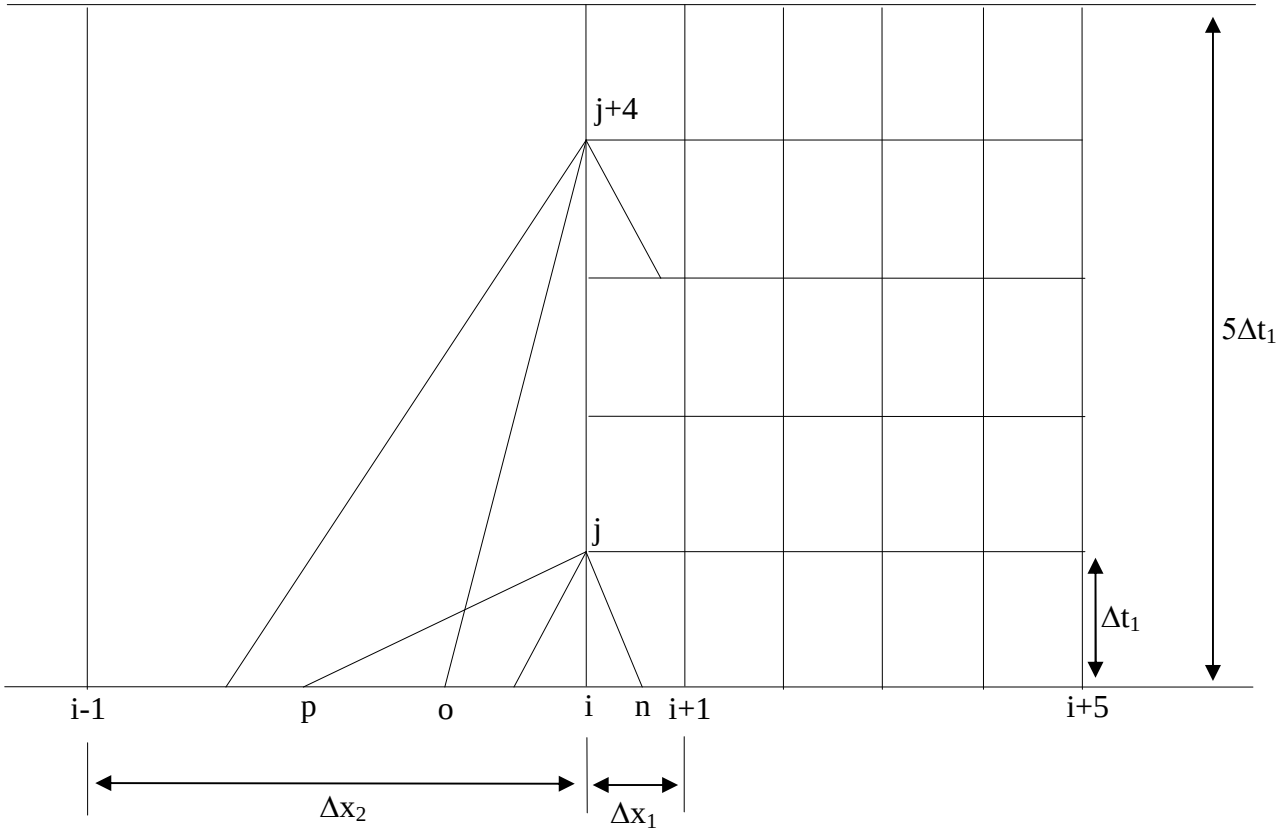

Figure 4.6: Boundary between coarse and fine mesh.

For the predictor step,

$$\lambda_0 = u_o = \frac{x_i - x_o}{4\Delta t_1} \Rightarrow x_o = x_i - 4\Delta t_1 u_o \tag{4.47}$$

$$\lambda_p = u_p + a_p = \frac{x_i - x_p}{4\Delta t_1} \Rightarrow x_p = x_i - \left(u_p + a_p\right) 4\Delta t_1 \tag{4.48}$$

$$\lambda_n = u_n - a_n = \frac{x_i - x_n}{\Delta t_1} \Rightarrow x_n = x_i - \left(u_n - a_n\right)\Delta t_1 \tag{4.49}$$

Following the same mathematical manipulation as that performed in section 4.4.1, the simultaneous equations obtained for the solution of points u_p and a_p are:

$$u_p\left(1+\frac{u_i - u_{i-1}}{\Delta x_2}4\Delta t_1\right)+\frac{u_i - u_{i-1}}{\Delta x_2}4\Delta t_1 a_p = u_i \tag{4.50}$$

$$a_p\left(1+\frac{a_i - a_{i-1}}{\Delta x_2}4\Delta t_1\right)+\frac{a_i - a_{i-1}}{\Delta x_2}4\Delta t_1 u_p = a_i \tag{4.51}$$

Similarly a 2×2 system of equations can be set up for u_n and a_n based on the same mathematical manipulation to yield,

$$u_n\left(1+\frac{u_{i+1} - u_i}{\Delta x_1}\Delta t_1\right)-\frac{u_{i+1} - u_i}{\Delta x_1}\Delta t_1 a_n = u_i \tag{4.52}$$

$$a_n\left(1+\frac{a_{i+1} - a_i}{\Delta x_1}\Delta t_1\right)-\frac{a_{i+1} - a_i}{\Delta x_1}\Delta t_1 u_n = a_i \tag{4.53}$$

The solution for u_o depends on the direction of fluid flow.

If $\lambda_o > 0$ then,

$$u_o = \frac{u_i}{\left(1+\frac{u_i - u_{i-1}}{\Delta x_2}4\Delta t_1\right)} \tag{4.54}$$

If $\lambda_o < 0$,

$$u_o = \frac{u_i}{\left(1+\frac{u_{i+1} - u_i}{\Delta x_1}\Delta t_1\right)} \tag{4.55}$$

The locations of x_p, x_n, and x_o can now be calculated directly from equations (4.47) to (4.49) by substituting the calculated values for u_p, a_p, u_n, a_n, and u_o from the above

equations. The pressure *(P)* and enthalpy *(h)* at the initial points p, o, and n are calculated from relevant linear interpolation formulas (equations (4.11), (4.12) or (4.13)).

All the initial point flow variables are now available to compute the flow conditions at the solution point *j* by employing the predictor-corrector algorithm.

4.6 Concluding Remarks

In this chapter, the formulation of the MOC based on the method of Specified Time (ST) was presented. The compatibility equations obtained from the resolution of conservation equations were discritised using the Euler predictor-corrector technique. By assuming that the fluid properties varied linearly with distance, algebraic expressions for the fluid variables at the next time step along the pipeline length were obtained.

The nested grid system (NGS) of discritisation as an effective means of reducing the computational run time was reviewed. The system employs finer grid discritisation near the rupture plane where greater resolution of the fast transients is required and coarser grids for the remainder of the pipeline. This enables simulation with fewer number of grids and hence a reduction in computation runtime.

In chapter 5, these expressions in conjunction with suitable boundary conditions and solution methodologies are applied to model the fluid dynamics following failure of multi-segment pipelines.

CHAPTER 5: APPLICATION OF MOC FOR SIMULATING PUNCTURE/FULL-BORE RUPTURE OF MULTI-SEGMENT PIPELINE NETWORKS

5.1 Introduction

In the preceding chapter, the formulation and implementation of the Method of Characteristics to solve the conservation equations governing single/two-phase homogenous flow in pipelines was presented. As these equations are in the differential form, their complete solution requires the imposition of appropriate boundary conditions at pertinent nodes situated at the inlet and exit points of the fluid along the pipeline. These boundary conditions enable closure of the governing equations with their solutions establishing the fluid dynamic and thermophysical properties in the time and space grids.

The failure scenario modelled in this study involves the puncture/full-bore rupture of a pipeline at any point along its length. As shown in the review of available outflow models in chapter 2, outflow models have mainly focused on the release from single isolated pipelines. In practice however, long pipelines conveying hydrocarbons over varying topography usually consist of multiple pipeline segments with varying internal diameter and wall thickness. Flanges, bends and elbows are used to connect the pipeline segments, change the direction of flow and the angle of inclination of the pipelines. These fittings introduce losses due to friction or change in direction and need to be accounted for in modelling pipeline failure. Thus, a practical pipeline failure model should account for coupled pipelines, the presence of a flow source and ancillary equipment (e.g., pumps, emergency shutdown valves).

In this chapter, the boundary conditions required to simulate the outflow from a multi-segment pipeline following failure are presented. These boundary conditions represent the source of upstream or downstream disturbance which are propagated along the length of the pipeline. The boundary conditions which constitute the most common components of a pipeline network include:

- Boundary formed by a closed valve or dead-ended pipe (intact end point)
- Full-bore rupture/orifice at pipeline end
- Puncture on the walls of a pipeline
- Junction of two pipelines (bends or connector) in a multiple segment pipeline network
- Pump at pipeline inlet (centrifugal pump with known discharge curve). The formulation and testing of the centrifugal pump boundary condition is presented in chapter 9.

5.2 The Intact End Point Calculation

At the inlet/upstream flow boundary, only the negative mach line (C-) and path line (C_0) characteristics are active. Figure 5.1 shows the grid scheme for the inlet intact end point.

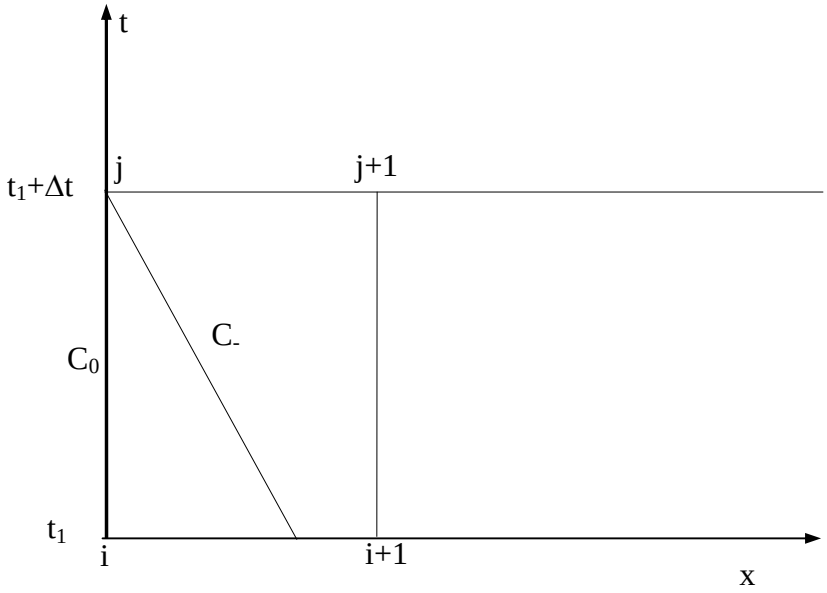

Figure 5.1: Grid scheme showing the active characteristic lines (C_0 and C-) at the inlet intact end point.

From chapter 4, the first order finite difference approximation of the negative characteristic equation, C-, is given by:

$$P_j = K_2 + (\rho a)_n (u_j - u_n) + P_n \qquad (4.21)$$

Where K_2 is defined by equation as:

$$K_2 = \left(\frac{\varphi\psi}{\rho T} - a\alpha \right)_n \Delta t \tag{4.23}$$

Based on equation (4.21), and noting that velocity at the closed end, $u_j = 0$, the negative characteristic can be written as:

$$P_j = K_2 + \left(\rho a\right)_n \left(0 - u_n\right) + P_n \tag{5.1}$$

Solving equation (5.1) yields the pressure at the intact end for the next time step:

$$P_j = K_2 + \left(\rho a u\right)_n + P_n \tag{5.2}$$

The upstream enthalpy (h_j) is obtained via the solution of the path line characteristic (equation (4.5)) and is given as:

$$h_j = \frac{\psi_0 \Delta t + \left(P_j - P_0\right) + \rho_0 h_0}{\rho_0} \tag{5.3}$$

(Where P_j is obtained from equation (5.2))

The corrector step as described in section 4.4.2 is then subsequently employed to yield the flow variables at the intact end.

5.3 Full-bore Rupture/Orifice at Pipeline End

There are two time domains for discharge at the failure/release plane. The first is the choked/critical flow time domain. The duration of the choked/critical flow time domain depends on how quickly the pressure at the failure plane drops to the external pressure. During choked flow, the fluid expands and discharges at a critical pressure higher than the ambient pressure. At this stage the release rate is at a maximum. The release velocity corresponds to the sonic velocity at the prevailing release pressure, and conditions downstream of the release plane have no influence on the discharge process. Thus, during critical flow, no disturbance downstream of the release plane can propagate upstream. However, once the external pressure is reached at the release plane, the second time domain is initiated, and in this period the outflow is subsonic.

For both full-bore rupture and orifice at pipeline end, it is assumed that the fluid approaching the rupture plane (i.e., the solution point fluid with properties P_j, h_j, s_j,ρ_j, u_j) undergo an isentropic expansion on exposure to ambient conditions.

In modelling of the rupture plane conditions only the C_+ and C_0 characteristics are applicable. However, the absence of a simple algebraic relationship expressing the expansion process across the release plane as a function of one or more of the flow variables renders the simultaneous solution of the positive and path line compatibility equations impossible. This necessitates the introduction of a 'ghost' cell adjacent to the boundary cell as depicted in figure 5.2 within which expressions for the negative compatibility can be formulated. The ghost cell is a form of fictitious node with the node (i+1) lying on node (i) as illustrated in figure 5.2 below.

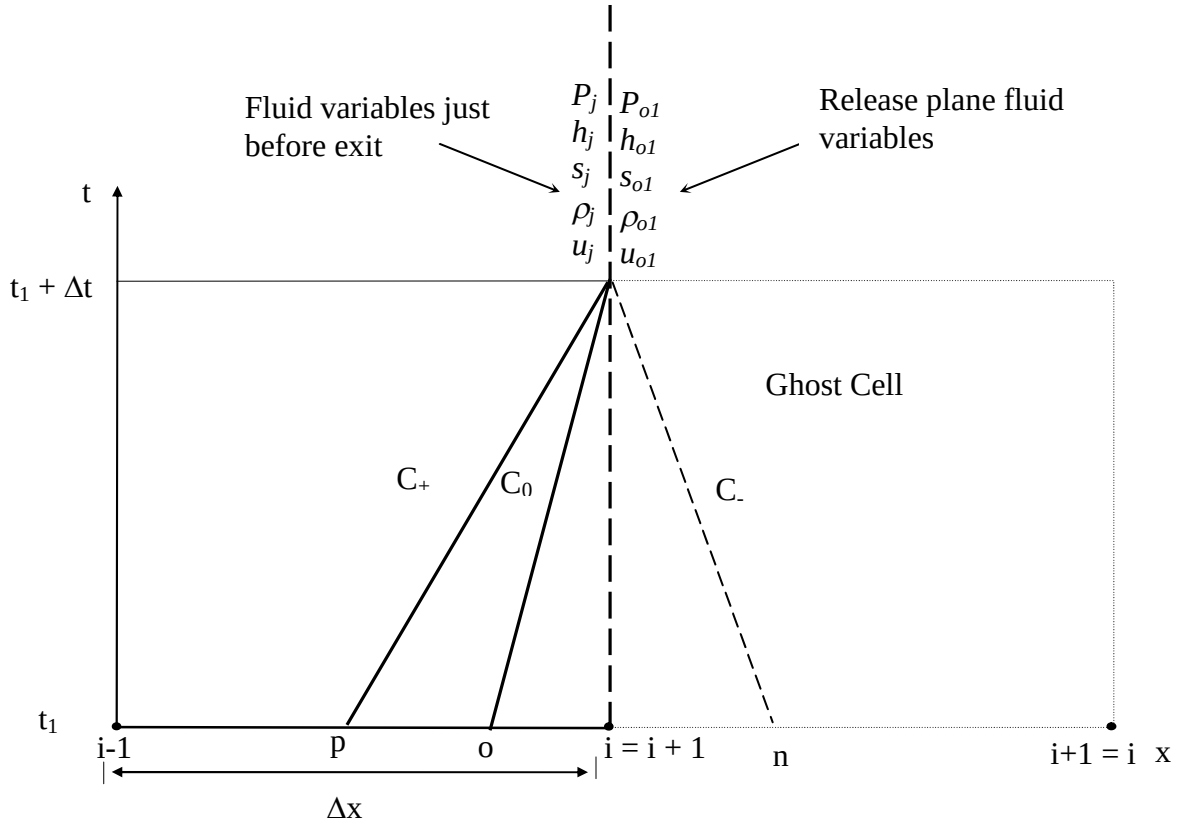

Figure 5.2: Diagram illustrating characteristic lines at the rupture plane based on the concept of a ghost cell.

With the introduction of the negative characteristics, the flow properties at point *j* can be obtained just as it is done for the interior point calculation i.e. with the aid of equations (4.21), (4.24) and (4.25). It should be noted that interpolation is not required within the ghost cell as all the properties within it are space invariant.

The flow variables at the release plane (P_{o1}, h_{o1}, u_{o1}) are calculated using a discharge rate algorithm described later (see section 5.3.1).

For discharge across the release plane, there is no accumulation of mass; thus the mass flow rate across the release plane is conserved. Furthermore, although the expansion process across the release plane is assumed to be isentropic, resistance posed by the release plane to the exiting fluid (as is the case with a puncture at the end of a pipeline) introduces irreversibility and hence non-isentropic conditions.

Accordingly, the actual flow rate of the exiting fluid at the release plane is smaller than the isentropic flow rate and the ratio between both flow rates is given by the discharge coefficient, C_d. Thus, the relationship between the mass flow rate approaching and that leaving the release plane can be expressed as:

$$u_j \times \rho_j \times A_{pipe} = C_d \times \rho_{o1} \times u_{o1} \times A_{o1} \qquad (5.4)$$

Where ρ_{o1}, u_{o1}, A_{o1} and A_{pipe} are the fluid density, fluid velocity, orifice area, and pipe area respectively.

The values of ρ_{o1} and u_{o1} (and all other fluid properties at the release plane) are obtained from the discharge rate calculation algorithm described later.

5.3.1 Discharge Rate Calculation Algorithm

As described in section 5.3, the two time domains for discharge at the failure/release plane are choked/critical flow and non-critical (subsonic) flow. For critical/choked release, the discharge pressure is higher than the downstream pressure. Under such conditions, the discharge rate through the release plane is maximum, and no disturbance can be propagated upstream of the failure plane. However, under non-critical conditions, the fluid discharge pressure is equal to the downstream pressure and the release rate is calculated accordingly.

Figure 5.3 shows the pertinent pressures at the release plane governing the discharge process. P_d, P_{o1}, and P_j represent the downstream or ambient pressure, the discharge pressure and the pressure of the fluid approaching the release plane respectively.

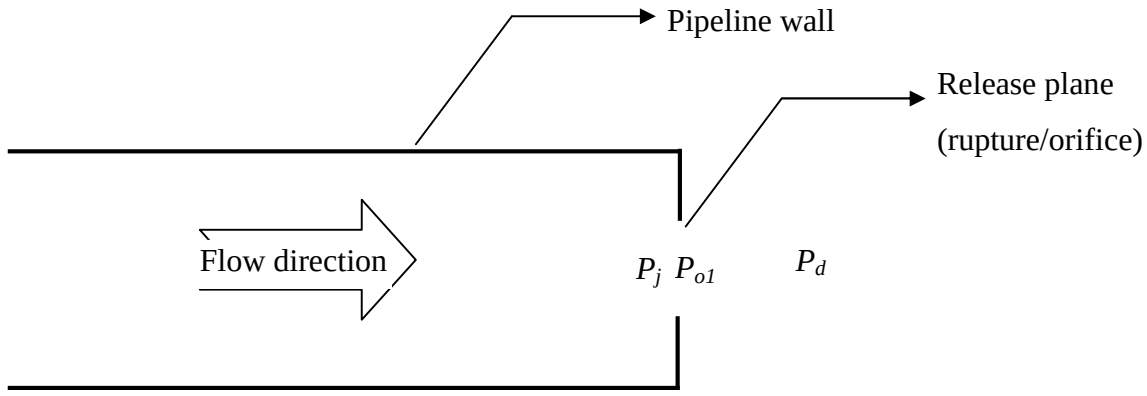

Figure 5.3: A schematic representation of pertinent pressures at the failure plane governing the discharge rate.

The choked and non-choked velocities and hence the discharge rate are calculated by applying an energy balance across the release plane. As mentioned earlier, the expansion process and hence the energy balance written across the release plane is based on an isentropic flow assumption. Non-isentropic effects are accounted for by introducing a discharge coefficient (C_d) in the relationship between the mass flow rate approaching and that leaving the release plane (equation (5.23)). Furthermore, for two-phase release, the homogeneous equilibrium (HEM) assumption is made where

both phases are assumed to be in thermodynamic equilibrium, and travel at the same velocity.

Therefore, at any time (t_j), and ignoring changes in potential energies between the flow approaching and the flow exiting the release plane, the corresponding energy balance across the release plane is given by:

$$H_j = h_{o1} + \frac{1}{2}u_{o1}^2 \tag{5.5}$$

$$H_j = h_j + \frac{1}{2}u_j^2 \tag{5.6}$$

Where, the subscripts j and o1 represent upstream and the release plane conditions respectively.

In the case of choked/critical flow, equation (5.5) is solved iteratively using the Brent iteration method (Press et al., 1992), and the velocity, u_{o1} replaced by the local single/two-phase speed of sound, a_{o1}. The iterative solution of equation (5.5) involves guessing and updating the discharge pressures (P_{o1}) in conjunction with pressure-entropy (isentropic) flash calculations until equation (5.5) is satisfied. Once a solution is obtained, other flow variables at the release plane (ρ_{o1}, T_{o1}, h_{o1}) are determined from a corresponding pressure-entropy (P_{o1}-s_j) flash calculation.

However, Richardson et al. (2006) (see section 2.7.4) showed that the release of two-phase mixtures containing greater than 80% liquid by mass through an orifice gave rise to discharge rates different to those predicted based on the HEM assumption. Consequently, a modified HEM (MHEM) for estimating discharge rates of two-phase mixtures that fall into this category is presented and validated in chapter 7.

On the other hand, for non-critical flow, the release pressure (P_{o1}) is equal to the ambient pressure (P_d). Thus, from a pressure-entropy (P_{o1}-s_j) flash calculation, the release enthalpy (h_{o1}) is determined and substituted in equation (5.5) to obtain the release velocity (u_{o1}). Unlike critical discharge, no iteration is required in determining flow conditions at the release plane.

Following the solution of equation (5.5), u_j is updated using equation (5.4) and employed in the corrector steps (see section 4.3.2) until convergence is observed. The calculation flow logic for calculating the discharge rate is shown in figure 5.4.

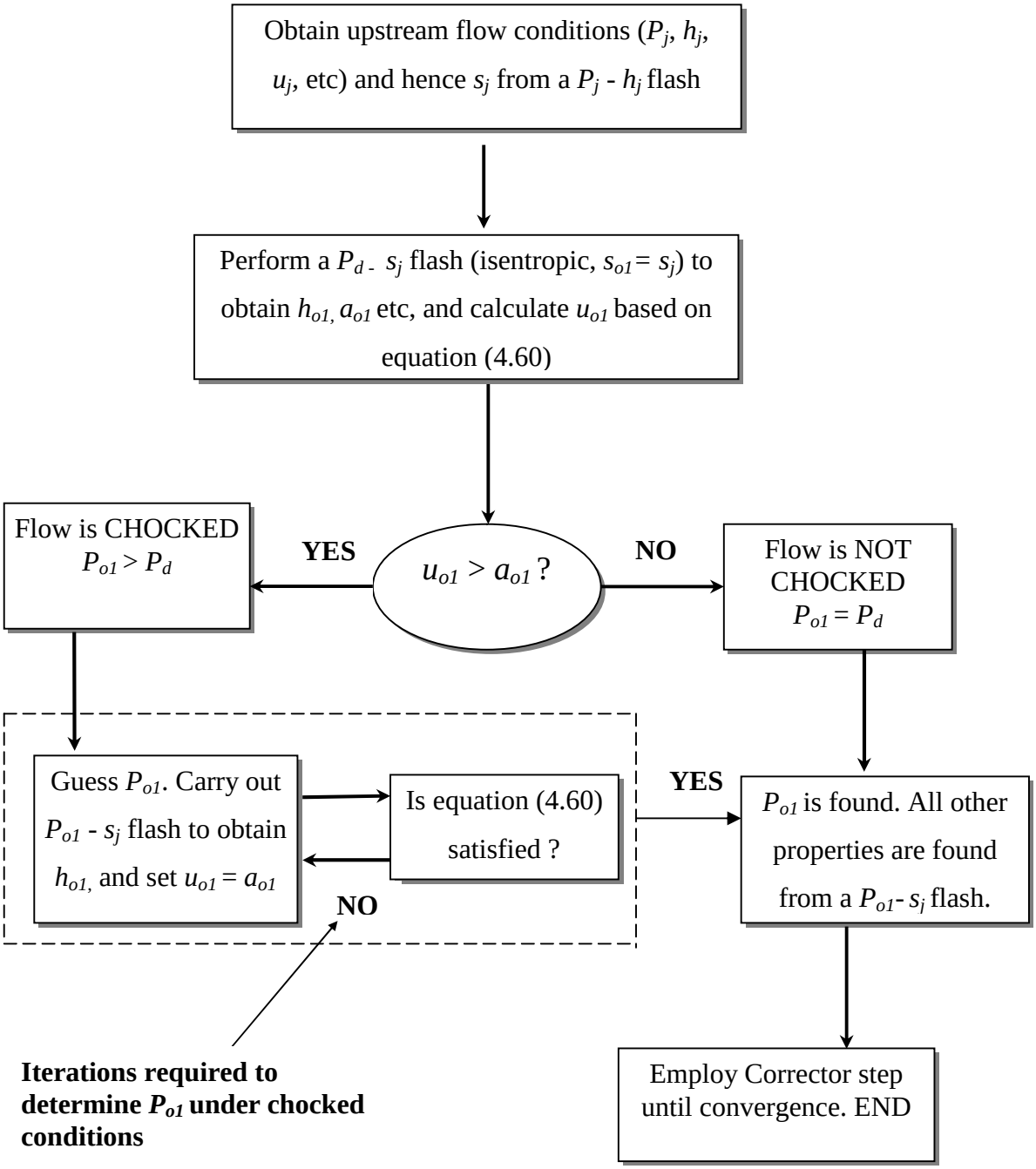

Figure 5.4: Calculation algorithm for obtaining flow variables at the discharge plane.

5.4 Puncture on Pipeline Wall

Atti (2006) highlighted the shortcomings of the puncture model proposed by Oke et al. (2003), in particular its failure to accurately predict the release of compressible or flashing liquids due to the assumption of a constant fluid density across the puncture plane boundaries. Therefore, the model proposed by Atti (2006) as summarised below is implemented in this study.

Figure 5.5 is a schematic representation of the fluid flow process and the active characteristic lines at the boundary following a puncture on the walls of a pipeline.

For ease of analysis, the puncture depicted in figure 5.5 is assumed to split the pipeline under consideration into two sections:

- Upstream pipe section
- Downstream pipe section

The puncture region acts as a common junction between the two pipeline sections with the 2 pipeline sections terminating and emanating from the puncture junction. Consequently, there are three flow boundaries (B_1, B_2, and B_3) at the common junction, each requiring the imposition of appropriate boundary conditions. Additionally, j_1 and j_2 are the fluid properties at the end of a calculation time step, Δt at flow boundaries B_1 and B_2 respectively, while j_{o1} refer to the orifice conditions at boundary, B3.

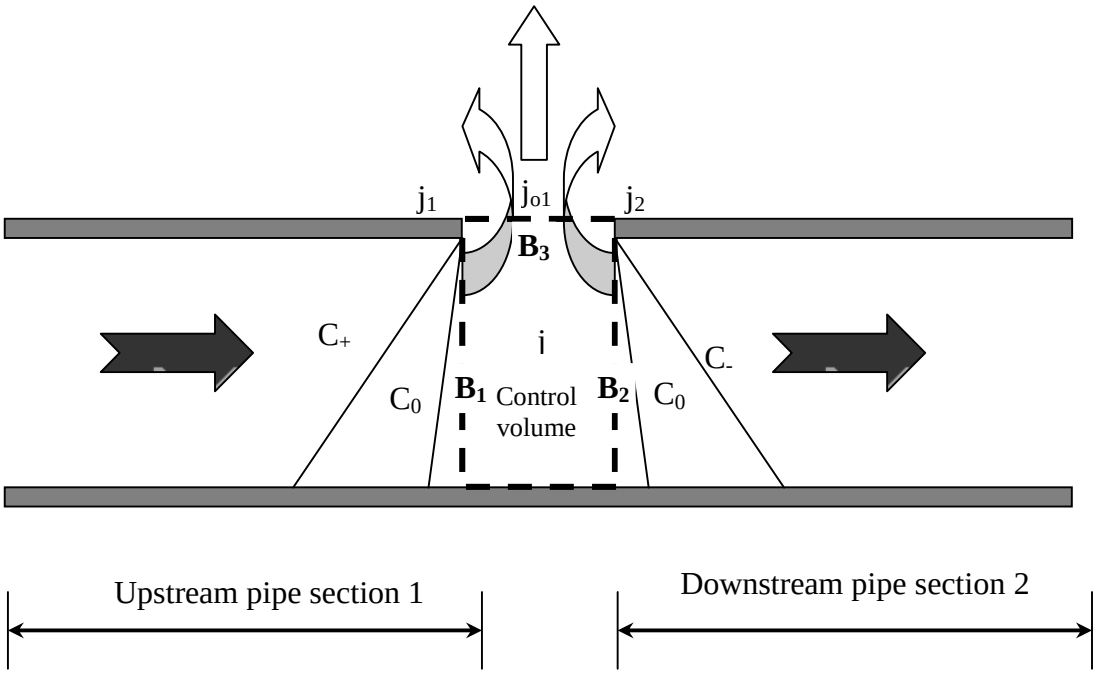

Figure 5.5: Schematic representation of fluid flow analysis following pipeline puncture.

At the upstream boundary (B_1), only the positive and path line compatibility equations are active, while at the downstream boundary (B_2), only the path line and the negative compatibility equations are applicable. A control volume, which bounds boundaries B_1-B_3, and is fixed in space, is employed in the modelling.

The boundary condition imposed when solving for the fluid properties at the current time step is:

$$P_{j1} = P_{j2} = P_j \qquad (5.7)$$

Where,

P_{j1} = pipeline section 1 downstream pressure

P_{j2} = pipeline section 2 upstream pressure

P_j = junction pressure

The fluid properties within the control volume are defined at the centre of the cell such that:

$$s_j = \frac{s_{j1} + s_{j2}}{2} \tag{5.8}$$

The flow through the puncture plane (B_3) is assumed to be isentropic, hence:

$$s_{o1} = s_j \tag{5.9}$$

In order to account for the non- isentropic effects encountered in reality, a discharge coefficient is employed in calculating the mass released from the puncture.

Since the flow at the puncture region is two dimensional, conservation equations to account for radial and axial fluid flow need to be employed.

The mass conservation can thus be written as:

$$V\frac{d\rho}{dt} + A_{pipe}\partial(\rho u) + A_{o1}\partial(\rho v) = 0 \tag{5.10}$$

Where,

V = control cell volume

A_{pipe} = pipeline cross-sectional area

A_{o1} = puncture area

Multiplying equation (5.10) by dt and inserting the limits of integration gives:

$$V\int_{\rho_1}^{\rho_2} d\rho + A_{pipe}\int_{t=t_1}^{t=t_2}\left[(\rho u)_{x_2} - (\rho u)_{x_1}\right]dt + A_{o1}\int_{t=t_1}^{t=t_2}\left[(\rho v)_{y_2} - (\rho v)_{y_1}\right]dt = 0 \tag{5.11}$$

Integrating numerically using the trapezoidal rule and noting that $(\rho v)_{y1} = 0$ gives:

$$V\left(\rho_{j_{|t=t_2}} - \rho_{j_{|t=t_1}}\right) + \left\{A_{pipe}\left[(\rho u)_{j_{|x=x_2}} - (\rho u)_{j_{|x=x_1}}\right]_{ave} + A_{o1}\left(v_{j_{|y=y2}}\right)_{ave}\right\}\Delta t = 0 \tag{5.12}$$

Where,

The subscript *ave* represents the average of the value in the brackets between time, $t = t_1$ and $t = t_2$, such that $t_2 - t_1 = \Delta t$. x_2 and x_1 on the other hand, respectively represent the upper (B_2) and lower (B_1) boundaries along the x-axis of the control volume, V.

As mentioned earlier, to account for non-isentropic effects across the release plane, the release through the orifice is multiplied by a discharge coefficient, C_d. Hence equation (5.12) becomes:

$$V\left(\rho_{j_{|t=t_2}} - \rho_{j_{|t=t_1}}\right) + \left\{A_{pipe}\left[(\rho u)_{j_{|x=x_2}} - (\rho u)_{j_{|x=x_1}}\right]_{ave} + C_d A_{o1}\left(v_{j_{|y=y2}}\right)_{ave}\right\}\Delta t = 0 \quad (5.13)$$

Equation (5.13) represents the boundary equation based on a 2-D continuity balance, which couples together the flow behaviour at planes B_1-B_3. Hence, the solution at the common junction must satisfy the above equation.

The corresponding algorithm employed involves guessing a junction pressure P_j = P_{j1} = P_{j2}, and using the Euler predictor-corrector algorithm to obtain u_{j1}, and h_{j1} from active compatibility equations at plane B_1 (i.e., equations (4.20) and (4.25)). From a pressure-enthalpy (P_{j1} - h_{j1}) flash calculation, s_{j1}, the fluid entropy at $B_1$is determined.

Similarly, by employing equations (4.21) and (4.25), u_{j2}, and h_{j2} can be obtained at plane B_2 with a P_{j2} - h_{j2} flash calculation, yielding $s_{j2.}$ The representative fluid entropy within the control volume is then taken as the average entropies at plane B_1 and B_2.

The discharge rate algorithm described in section 5.3.1 is employed for determining flow conditions at the puncture plane. The flow transport properties obtained from the solution of characteristic/boundary equations at planes B_1, B_2, and B_3, are substituted into equation (5.13). If equation (5.13) is satisfied, the flow transport properties obtained at the corresponding iteration step are adopted as the required solution. Otherwise, a new junction pressure is guessed and the iteration process repeated until a satisfactory solution is found. The Brent iteration algorithm (Press et al., 1992) is employed in updating guessed junction pressures until equation (5.13) is satisfied.

Figure 5.6 is the calculation algorithm for determining fluid flow transport properties at the puncture plane during the release process.

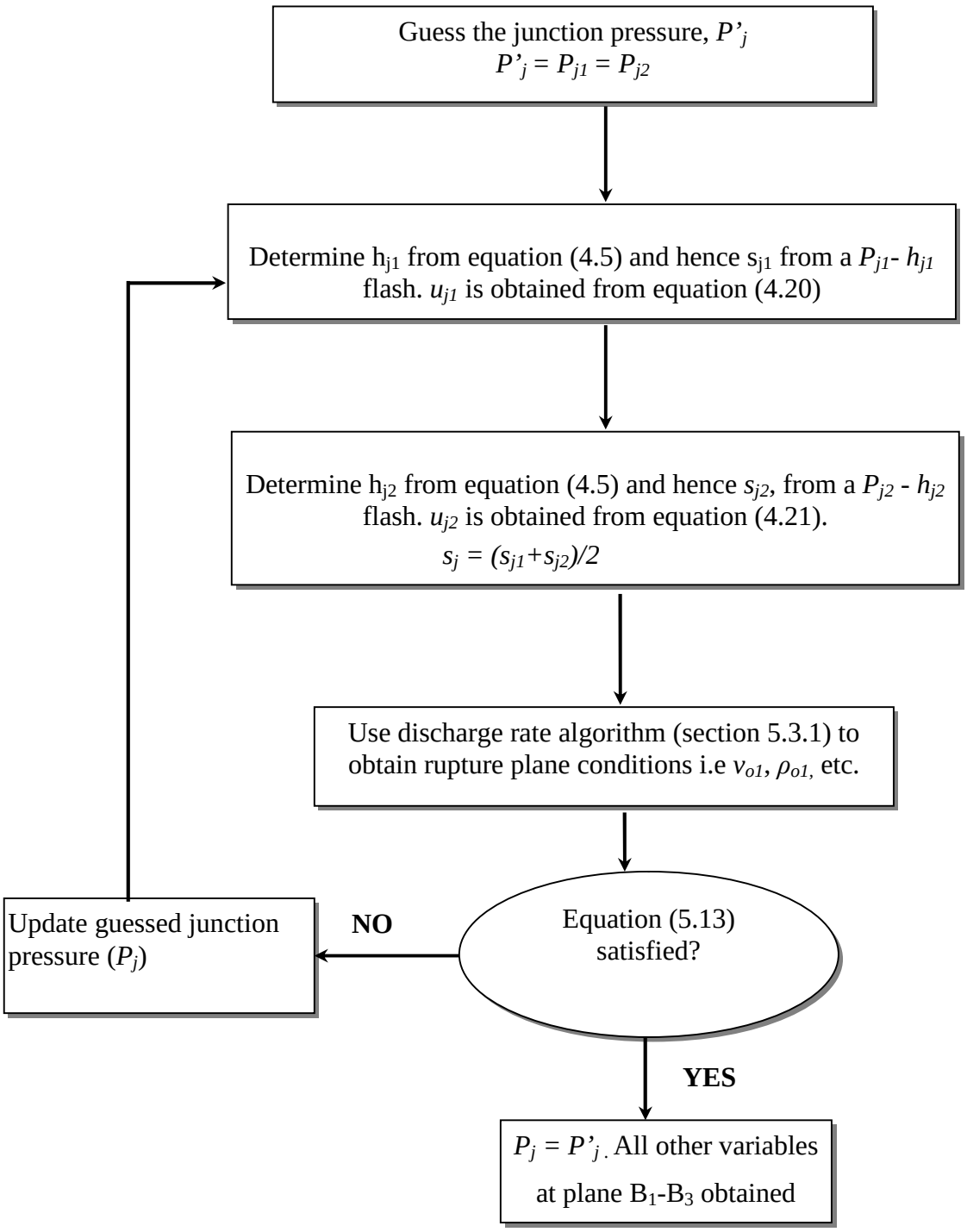

Figure 5.6: Calculation algorithm for obtaining flow variables at puncture located along the major axis of a pipeline.

5.5 Junction of Two Pipelines in a Multi-Segment Pipeline Network

Publications dealing with the problem of pipeline rupture have been almost entirely limited to those involving straight pipelines. In practice however, long pipelines conveying hydrocarbons over a varying topography usually consist of multiple pipeline segments with varying internal diameter and wall thickness. Flanges, bends and elbows are used to connect the pipeline segments, change the direction of flow and the angle of inclination of the pipelines. These fittings introduce losses due to friction or change in direction and need to be accounted for in modelling pipeline failure.

The model presented in this work takes into account effect of the above losses when calculating the release rate following the accidental failure of a pipeline transporting hydrocarbons over varying terrains. Figure 5.7 is a schematic representation of characteristic lines at a typical bend or connector. B_1 and B_2 represent the flow boundaries at the common junction associated with pipeline 1 and 2 respectively.

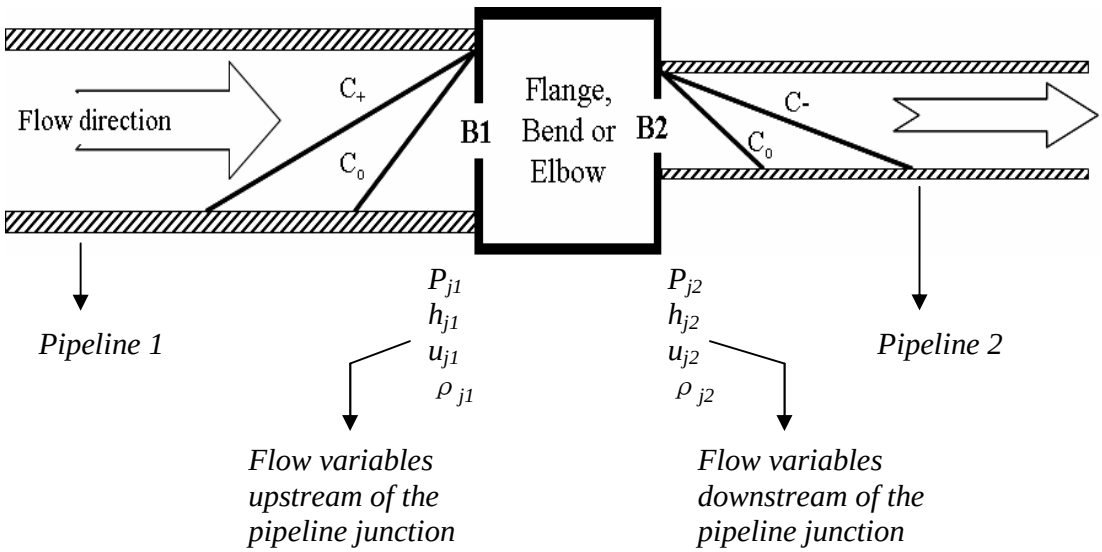

Figure 5.7: Schematic representation of characteristic lines upstream and downstream of a 2-way junction.

For the pipeline terminating at the junction (pipeline 1), only the positive (C_+) and path line (C_0) compatibility equations are active, while for pipeline 2, only the negative (C_-) and path line (C_0) compatibility equations are applicable. In modelling the boundary variables resulting from the junction of two pipelines, losses due to friction or changes in flow direction across a fitting are accounted for using a loss coefficient (K_{loss}) (Swaffield and Boldy, 1993). This coefficient is determined empirically for different types of fittings, and is employed in calculating the pressure drop resulting from flow across a given fitting (Perry and Green, 1997).

Apart from the compatibility equations presented in chapter 4, two other boundary equations are employed in defining flow behaviour through a pipeline junction (Swaffield and Boldy, 1993). The first represents the effect of separation losses, K_{pl} due to flow across the junction as given by:

$$P_{j2} = P_{j1} + K_{pl} \tag{5.14}$$

Where,

$$K_{pl} = 0.5\left(\rho_{j1} u_{j1} \left|u_{j1}\right| - \rho_{j2}\left(1 + K_{loss}\right) u_{j2} \left|u_{j2}\right|\right) \tag{5.15}$$

P_j = pressure at junction j

ρ_j = density at junction j

h_j = enthalpy at junction j

u_j = velocity at junction j

The subscript, j_1 and j_2 represent the solution variables at boundary planes B_1 and B_2 for pipelines 1 and 2 respectively.

The loss coefficient, K_{loss} accounts for the pressure drop due to friction or changes in flow direction across a fitting at the pipeline junction, and its values are obtained from the literature (Perry and Green, 1997). Experimental data (Perry and Green, 1997)

indicate that these loss-coefficients are Reynolds number (Re) insensitive for Re ≥ 500. During pipeline rupture, turbulent flow (Re ≥ 20,000) will most likely prevail at pipeline junctions for the duration of the depressurisation process. Hence, constant loss coefficients are employed in this study. Table 5.1 gives a summary of the K_{loss} values used for valves and fittings in this study.

Table 5.1: K_{loss} for turbulent flow through fittings and valves (Perry and Green, 1997)

Type of fitting or valve	K_{loss}
45^o elbow (standard)	0.35
90^o elbow (standard)	0.75
Coupling/Union	0.04
Tee (standard, branch blanked off)	0.40
Gate valve (open)	0.17
Angle valve (open)	2

The second, boundary equation ensures flow continuity between the two pipeline sections. Taking the junction as a control volume with no accumulation such that flows into it are positive, and flows away are negative; the continuity equation is given by:

$$\rho_{j1} u_{j1} A_{j1} + \rho_{j2} u_{j2} A_{j2} = 0 \qquad (5.16)$$

Where,

A_j = cross section area of the pipeline.

If continuity is satisfied across the boundaries, the flow transport properties obtained are adopted as the required solution.

Figure 5.8 shows the calculation algorithm for determining the fluid condition at the junction of a multi-segment pipeline network.

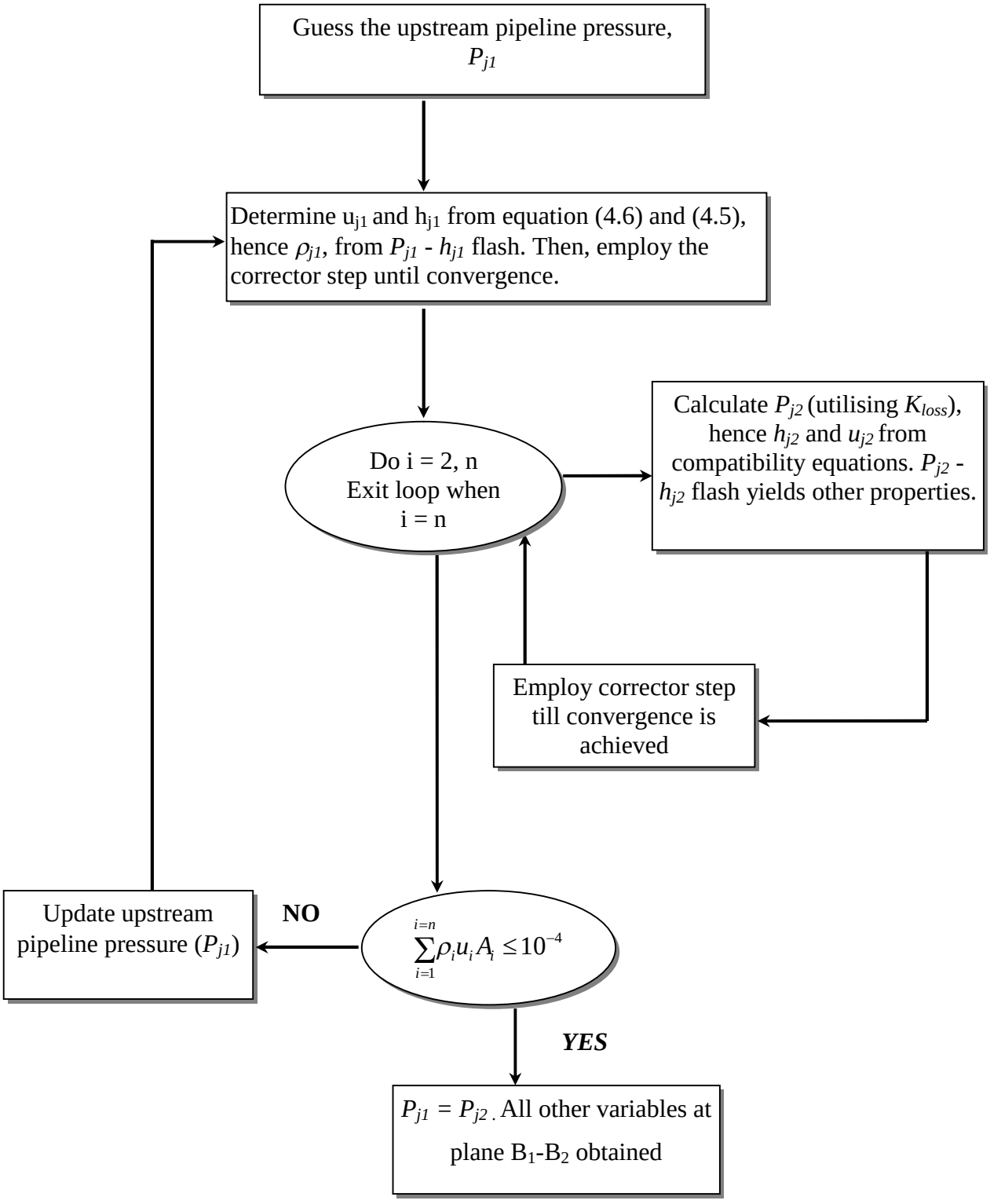

Figure 5.8: Calculation algorithm for obtaining the flow variables at the boundaries of a multi-segment pipeline

5.6 Concluding Remarks

In this chapter, the compatibility equations formulated in chapter 4 were combined with appropriate boundary conditions to model the fluid dynamics following the failure of multi-segment pipeline networks. The frictional losses due to valves, fittings, changes in pipeline diameter and changes in elevation were accounted for by the introduction of a loss coefficient, K_{loss}.

Chapter 6 will present results relating to the testing and where possible validation of the above model. In addition, the outflow characteristics such as variations of discharge rate, pressure and temperature following pipeline failure are presented and discussed. In all cases, a mass conservation index is used to judge the accuracy of results. This is particularly useful for cases where experimental data for model validation are not available.

CHAPTER 6: VALIDATION OF THE MULTI-SEGMENT PIPELINE OUTFLOW MODEL

6.1 Introduction

In chapters 3 - 5, the governing theory, solution methodology and the relevant boundary conditions describing the numerical model for simulating the failure of a multi-segment pipeline were described. In contrast to the pipeline models presented in chapter 2, the multi-segment outflow model takes into account the losses due to changes in elevation, flanges and bends in long pipeline networks.

In this chapter, in the absence of available experimental data, the efficacy of the multi-segment outflow model presented earlier is evaluated based on the determination of a 'mass conservation index'. This is then followed by a more detailed analysis of the effect of bends and branches on the depressurisation process following the full bore rupture of a hypothetical multi-segment pipeline network. In order to highlight the impact of pipeline complexity such as the inclusion of branches or bends on outflow, the above results are compared against those generated from the single pipeline model of the same equivalent length.

6.2 Mass Conservation Index

In developing pipeline rupture mathematical models, it is always desirable to validate the simulated results against experimental data in order to ascertain the robustness and accuracy of their predictions. However, it is impracticable to conduct experiments or field tests to validate the model predictions under a full range of conditions due to cost and/or safety implications. As such, only a handful of published experimental data for pipeline ruptures are available.

In view of the above, it is therefore desirable that some methodology be available to check the efficacy of the numerical model. In this study, a measure of the numerical accuracy or the robustness of the simulated data is obtained by evaluating the mass

conservation index as proposed by Flatt (1986). This in essence checks how well the global conservation of mass is satisfied.

The mass conservation index, ε, is calculated as follows:

$$\varepsilon = \frac{M - M^*}{\Delta M} \tag{6.1}$$

Where,

M = the mass of gas contained in the entire pipeline at time t.

M^* = the mass in the pipeline at time $t + \Delta t$

ΔM = the total mass discharged from the pipeline at the rupture end (or both ends if the rupture is along the length of the pipeline) during Δt.

M and M^* are computed by integrating the density-distance profile at time t and $t + \Delta t$ along the length of the pipeline, while ΔM is computed by integrating the discharge rate-time profile. In this study, the integrals of M, M^* and ΔM are evaluated using the trapezoidal rule.

The calculation converges if, as the number of grid discretisation, N increases, ε tends towards unity. A value of $\varepsilon = 1$ indicates 'perfect' mass conservation. $\varepsilon > 1$ or $\varepsilon < 1$ respectively indicate if the mass released given by M – M* is overestimated or underestimated. Figure 6.1 show the impact of overestimating or underestimating M – M* on ε for the hypothetical full bore rupture (FBR) of a 100 m, 300 internal diameter pipeline transporting 100% Methane at 21.6 bara and 300 K. Curve A shows the variation of the actual value of ε with time. Curves B and C on the other hand respectively show the impact of + 2% or - 2% error in the calculation of the mass within the pipeline on ε. Such errors in the prediction of mass within the pipeline may easily arise from inaccuracies associated with the vapour equilibrium data obtained from the equation of state.

Returning to figure 6.1, it can be seen that a 2% change in M – M* is equivalent to a 2% change in ε. In this study, an error of $\pm$ 2% in the mass conservation index (i.e $0.98 \leq \varepsilon \leq 1.02$) is considered tolerable.

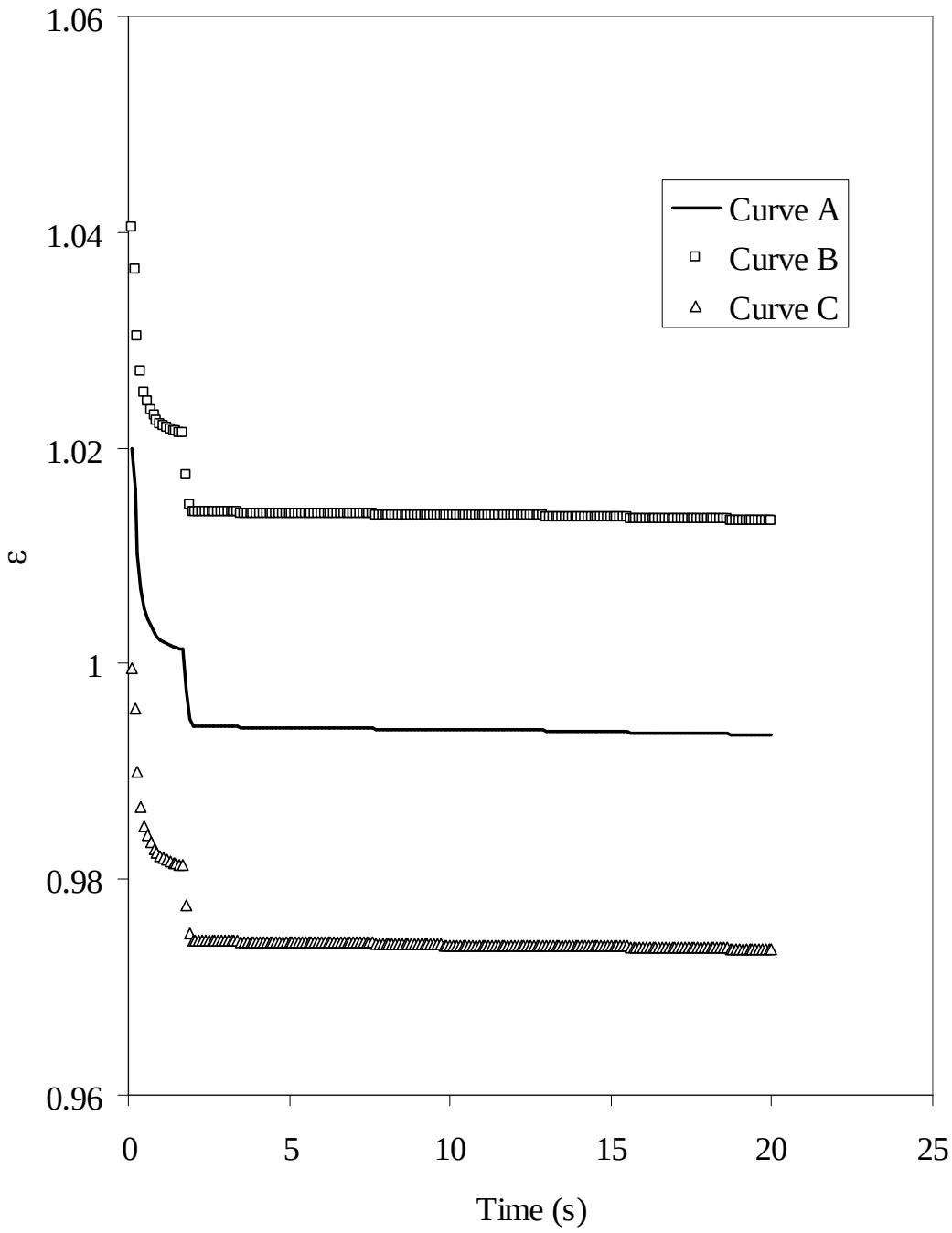

Figure 6.1: Variation of ε with time for the hypothetical FBR of a 100 m, 300 i.d. pipeline transporting 100% Methane at 21.6 bara and 300 K.

Curve A – Actual ε

Curve B – ε for + 2% overestimation of M – M*

Curve C – ε for - 2% overestimation of M – M*

6.3 Results and Discussion

In order to carry out comparisons between the single pipeline model (Atti, 2006) and the multi-segment pipeline model, an equivalent single pipeline containing the same initial inventory is used to approximate the multi-segment pipeline. The internal diameter of the equivalent single pipeline is determined using the initial total inventory, fluid density and length of the multi-segment pipeline. The pipe wall thickness is chosen as the average of the wall thickness of the individual pipeline segments. This is based on the observation of Atti (2006) that the thickness of the pipeline wall has a negligible impact on heat transfer during the full bore depressurisation of long pipelines. For consistency, the overall angle of inclination of the multi-segment pipeline is assumed to be the same as that for the single pipeline.

In the first instance, both models are employed for simulating the failure of a hypothetical 10 km pipeline transporting various inventories including gas, liquid and two–phase mixtures following FBR 6 km from the high pressure end. Figures 6.2 and 6.3 are schematics of the two pipelines modelled. Figure 6.2 shows the multi-segment pipeline consisting of four pipeline segments connected with three elbows (see section 5.5 for the values of K_{loss} used in this study). From the flow source (A) the pipeline goes through two changes in inclination resulting in a total downward slope of 23^{o}. Figure 6.3 shows the equivalent single pipeline.

The initial conditions prior to rupture and pipeline dimensions for the multi-segment and the single pipelines are given in tables 6.1 and 6.2 respectively.

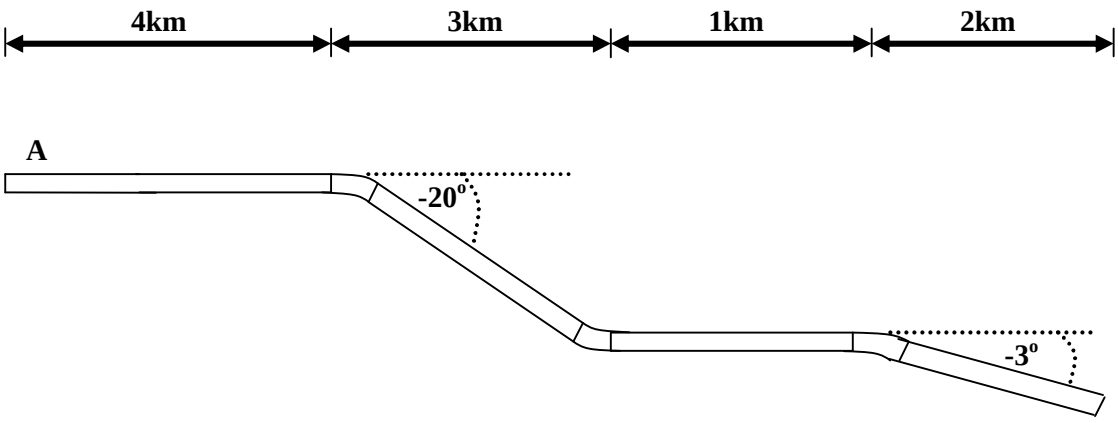

Figure 6.2: Schematic representation of the 10 km multi-segment pipeline.

A – high pressure end of the pipeline

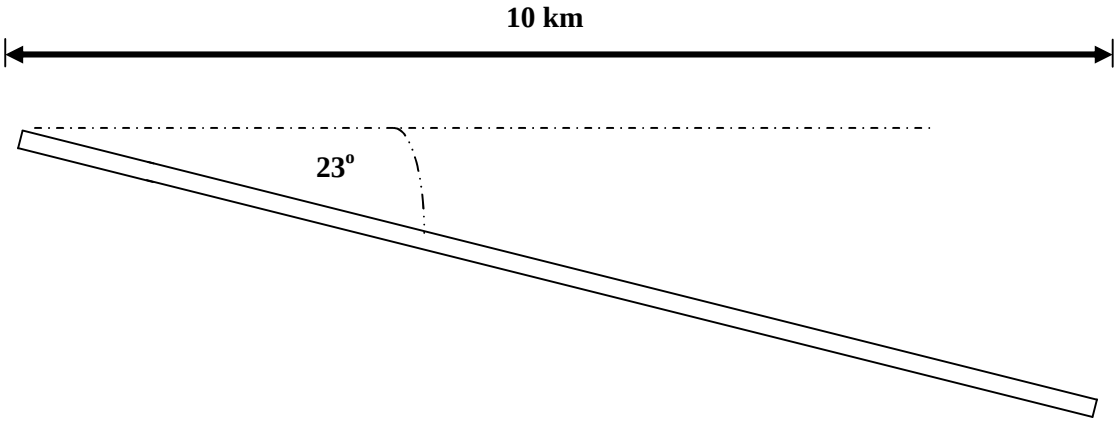

Figure 6.3: Schematic representation of the equivalent (see figure 6.1) 10 km single pipeline.

Table 6.1: Initial conditions prior to FBR of the 10km multi-segment pipeline (figure 6.2)

Pipeline Segment 1 :	
Length (m)	4000
Pipe Internal Diameter (mm)	180
Pipe Wall Thickness (mm)	10
Number of Grids	500
Pipe Orientation Relative to Horizontal (degrees)	0
Pipeline Segment 2 :	
Length (m)	3000
Pipe Internal Diameter (mm)	260
Pipe Wall Thickness (mm)	20
Number of Grids	500
Pipe Orientation Relative to Horizontal (degrees)	-20
Pipeline Segment 3 :	
Length (m)	1000
Pipe Internal Diameter (mm)	388
Pipe Wall Thickness (mm)	6
Number of Grids	250
Pipe Orientation Relative to Horizontal (degrees)	0
Pipeline Segment 4 :	
Length (m)	2000
Pipe Internal Diameter (mm)	180
Pipe Wall Thickness (mm)	10
Number of Grids	250
Pipe Orientation Relative to Horizontal (degrees)	-3
Pipe roughness (m)	0.0005
Initial Pressure (bara)	40
Initial Temperature (K)	293.15
Ambient Temperature (K)	292.25
Ambient Pressure (K)	1.01

Table 6.2: Initial conditions prior to FBR of the equivalent 10km single pipeline.

Length (m)	10000
Pipe Internal Diameter (mm)	221
Pipe Wall Thickness (mm)	11.5
Number of Grids	1000
Pipe Orientation Relative to Horizontal (degrees)	-23
Pipe roughness (m)	0.0005
Initial Pressure (bara)	40
Initial Temperature (K)	293.15
Ambient Temperature (K)	292.25
Ambient Pressure (K)	1.01

6.3.1 Liquid release –100% Hexane

Figure 6.4 shows the simulated pressure profiles along the pipeline length for the multi-segment pipeline model (curve A) and the single pipeline model (curve B) prior to FBR. The figure shows that the pressure profile along the length of the multi-segment pipeline (curve A) remains constant along the horizontal segments of the pipeline (segments 1 and 3) and increases in the inclined segments (segments 2 and 4) due to hydrostatic head. In contrast, the pressure along the length of the single pipeline (curve B) increases linearly due to hydrostatic head. Consequently, there is a significant difference in the initial release pressure predicted by each outflow model. The single pipeline model (curve B) predicts an initial discharge pressure of 196.9 bara while the multi-segment model (curve A) produces a discharge pressure of only 85.4 bara.

Figure 6.5 shows the corresponding variation of release rate with time. As it may be observed, the initial discharge rate predicted using the single pipeline model (curve B) is 6005.8 kg/s. This compares with the much lower flow rate of 3951.4 kg/s as predicted from the multi-segment model.

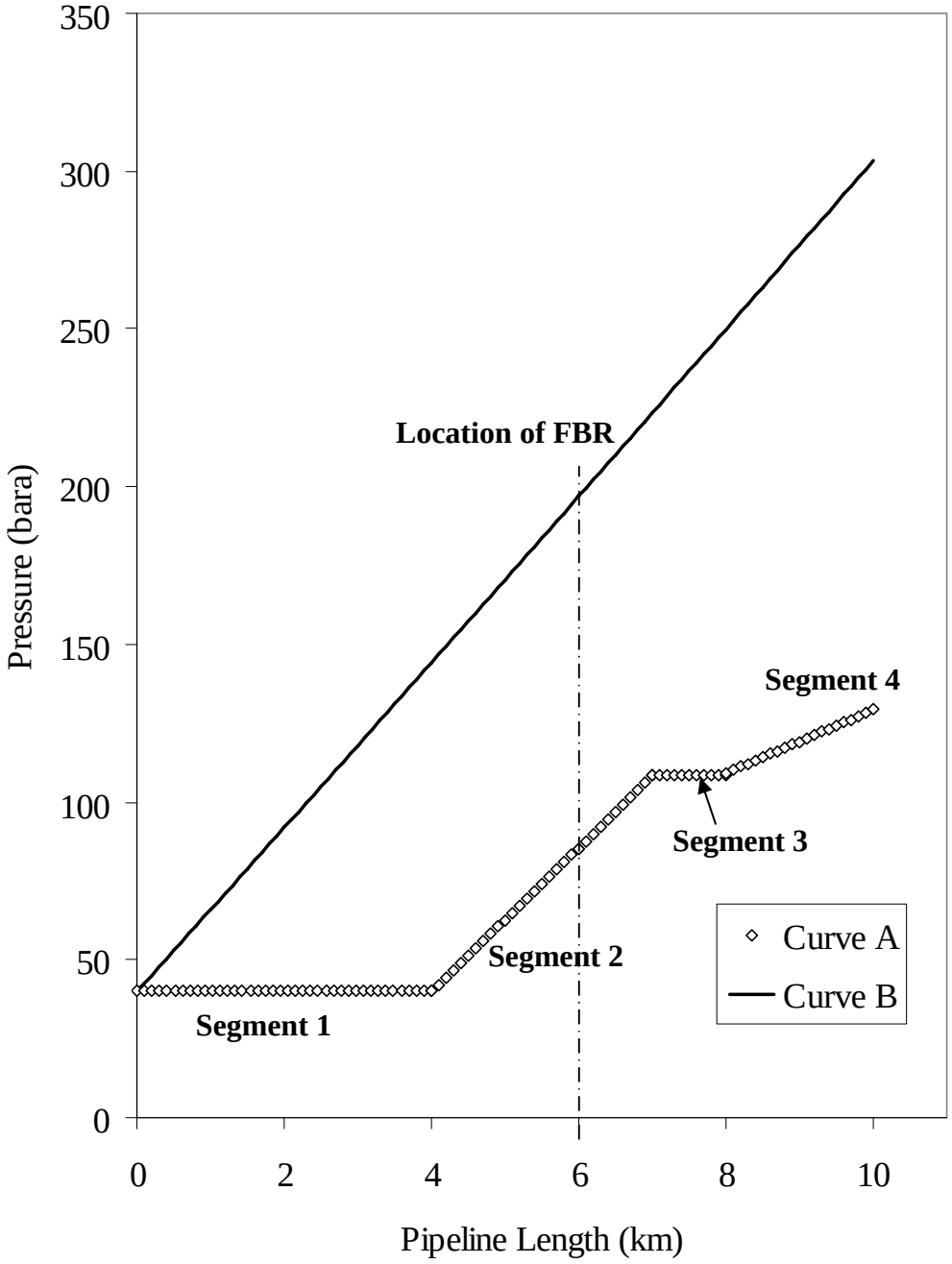

Figure 6.4: Variation of Hexane pressure along the length of the 10km pipeline transporting 100% Hexane prior to FBR.

Curve A – Multi-segment pipeline model

Curve B – Single pipeline model (Atti, 2006)

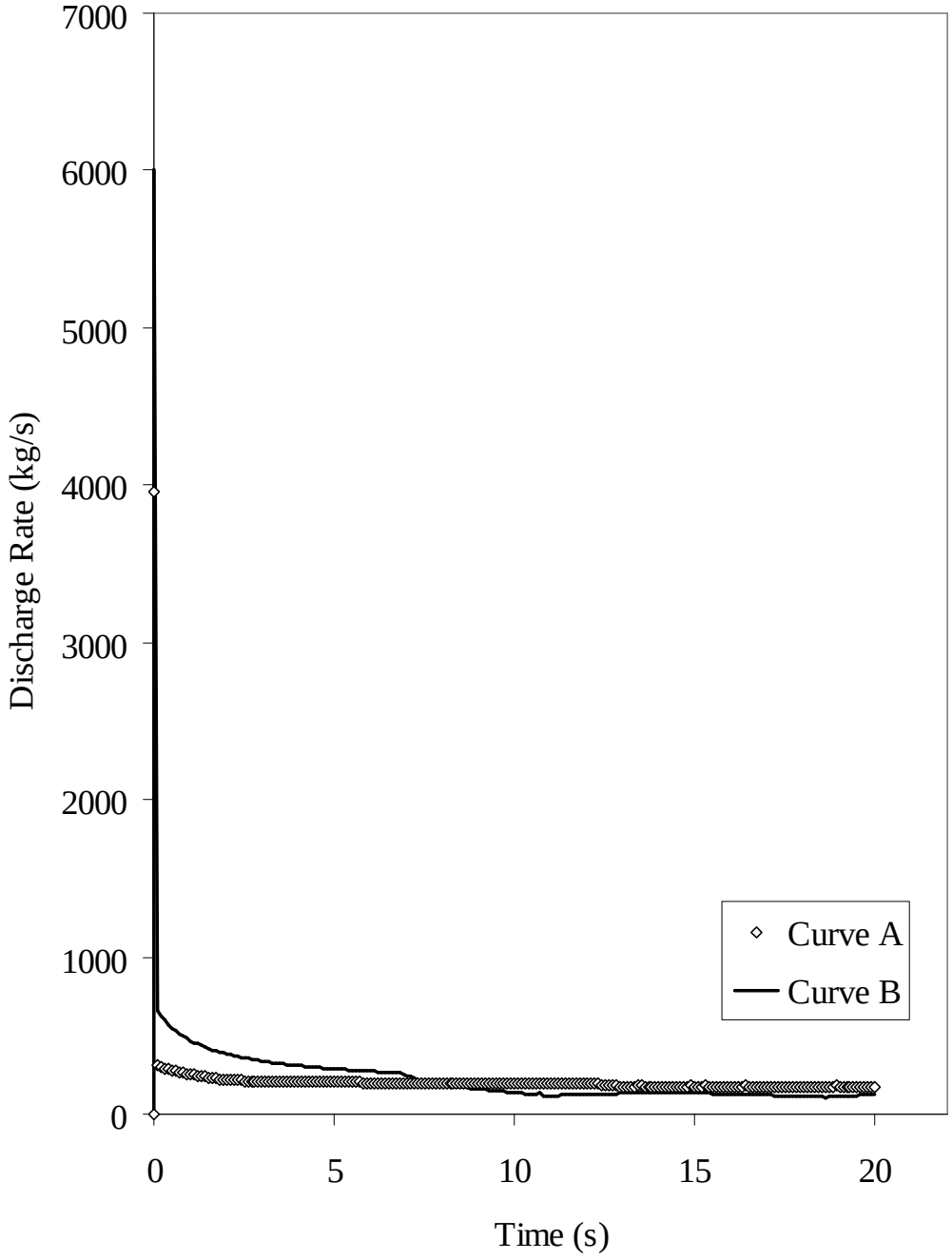

Figure 6.5: Variation of release rate with time following FBR of the 10km pipeline transporting 100% Hexane using the 2 pipeline models.

Curve A – Multi segment pipeline model

Curve B – Single pipeline model (Atti, 2006)

Returning to figure 6.5, it can be seen that both models predict the expected rapid initial release of inventory from the pipeline which quickly dissipates. As liquid inventory pipelines rapidly depressurise following FBR, the post 10 s discharge is gravity induced.

Figure 6.6 shows the simulated cumulative mass discharge with time using both outflow models. From the figure it can be seen that the single pipeline model (curve B) significantly over predicts the inventory loss from the pipeline following failure. After 20 s the single pipeline model (curve B) and the multi-segment pipeline models predict losses of 4286 kg and 3973 kg respectively from an initial inventory of 12600 kg.

The mass conservation index obtained using the single and multi-segment models were 0.99 and 1.01 respectively which also falls within the 2% error range established in section 6.2.

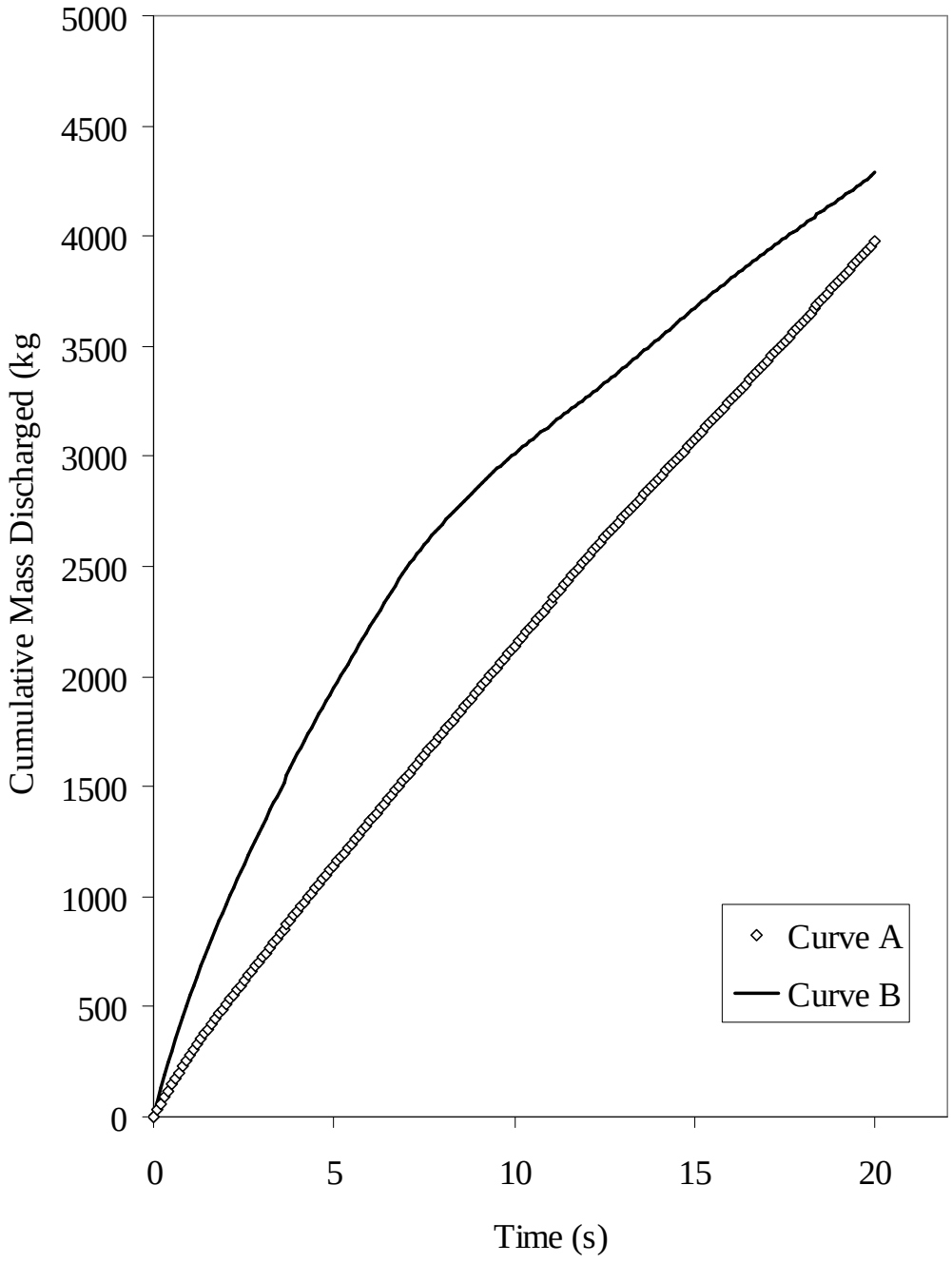

Figure 6.6: Variation of cumulative mass discharged with time following FBR of the 10km pipeline transporting 100% Hexane.

Curve A – Multi segment pipeline model

Curve B – Single pipeline model (Atti, 2006)

6.3.2 Vapour and Two-Phase release

Figure 6.7 shows the variation of release pressure with time following failure of the 10 km pipeline transporting 100% gaseous Methane. From the figure it can be seen that the single pipeline model (curve B) has a higher initial discharge pressure (~ 47 bara) due to the greater head at the failure location.

In comparison to liquid inventories (figure 6.4) which have a higher density, the difference in initial pressure predicted from both models is not significant (~ 5 bara for vapour inventory and ~ 110 bar for liquid inventory). As a consequence, the predicted discharge rate (figure 6.8) and the cumulative mass (figure 6.9) predicted from both models are very similar after 20 seconds following pipeline failure.

The mass conservation index obtained using the single and multi-segment models are 0.98 and 0.99 respectively.

Figures 6.10 to 6.12 respectively show the variations of release pressure, discharge rate and cumulative mass with time following the FBR of a 10 km pipeline transporting a two-phase mixture of 50% Methane and 50% Hexane at 293.15 K and 40 bara. From the figure, it can be seen that both the single pipeline model and the multi-segment pipeline model produce very similar results. This can be attributed to the dominance of pressure forces over hydraulic forces during two-phase discharge.

Both outflow models produce the same mass conservation index of 1.01 for the two-phase simulations.

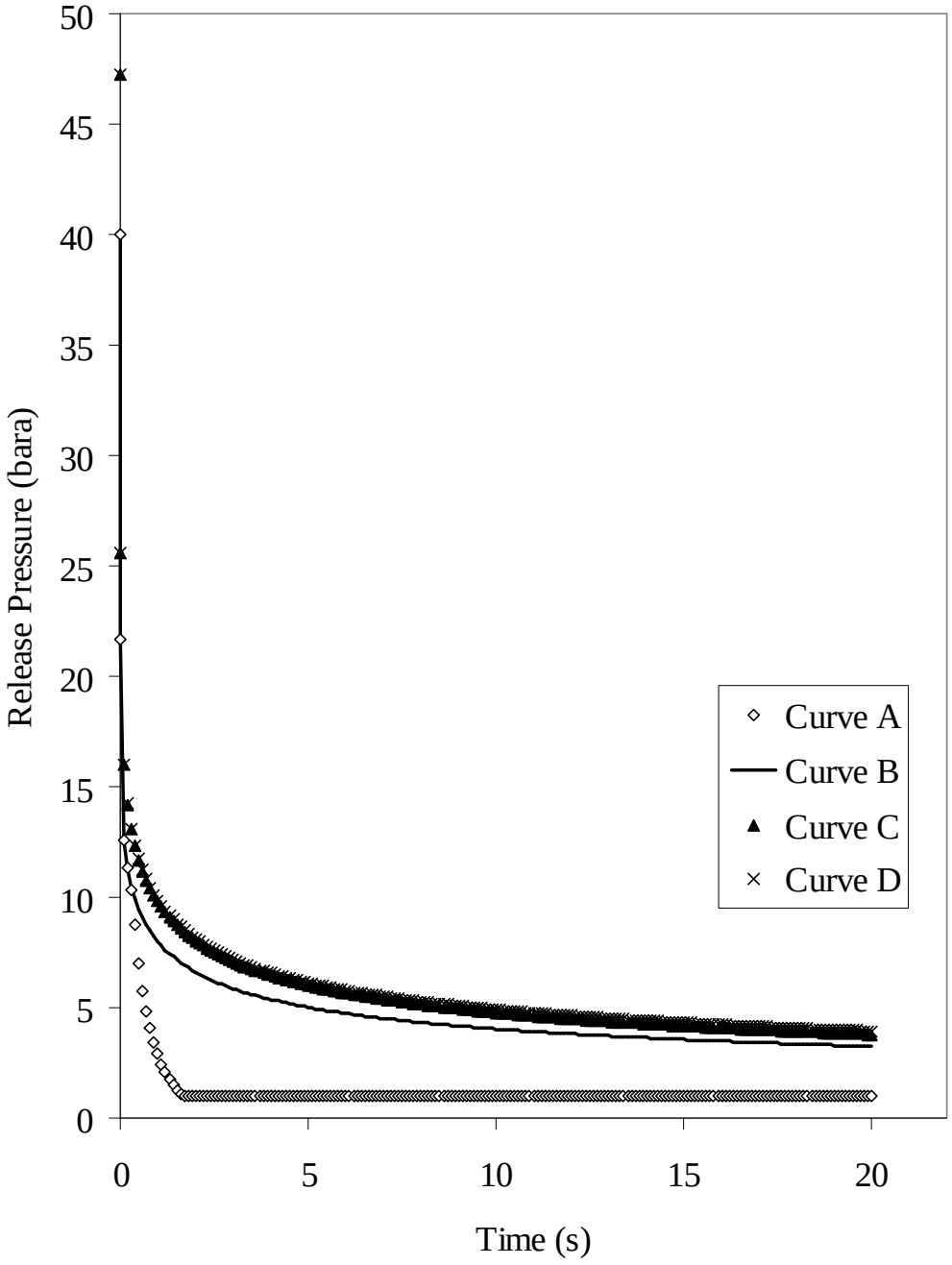

Figure 6.7: Variation of release pressure with time following FBR of the 10km pipeline transporting 100% Methane.

Curve A – Upstream of failure - Multi segment pipeline model

Curve B – Downstream of failure - Multi segment pipeline model

Curve C – Upstream of failure - Single pipeline model (Atti, 2006)

Curve D – Downstream of failure - Single pipeline model (Atti, 2006)

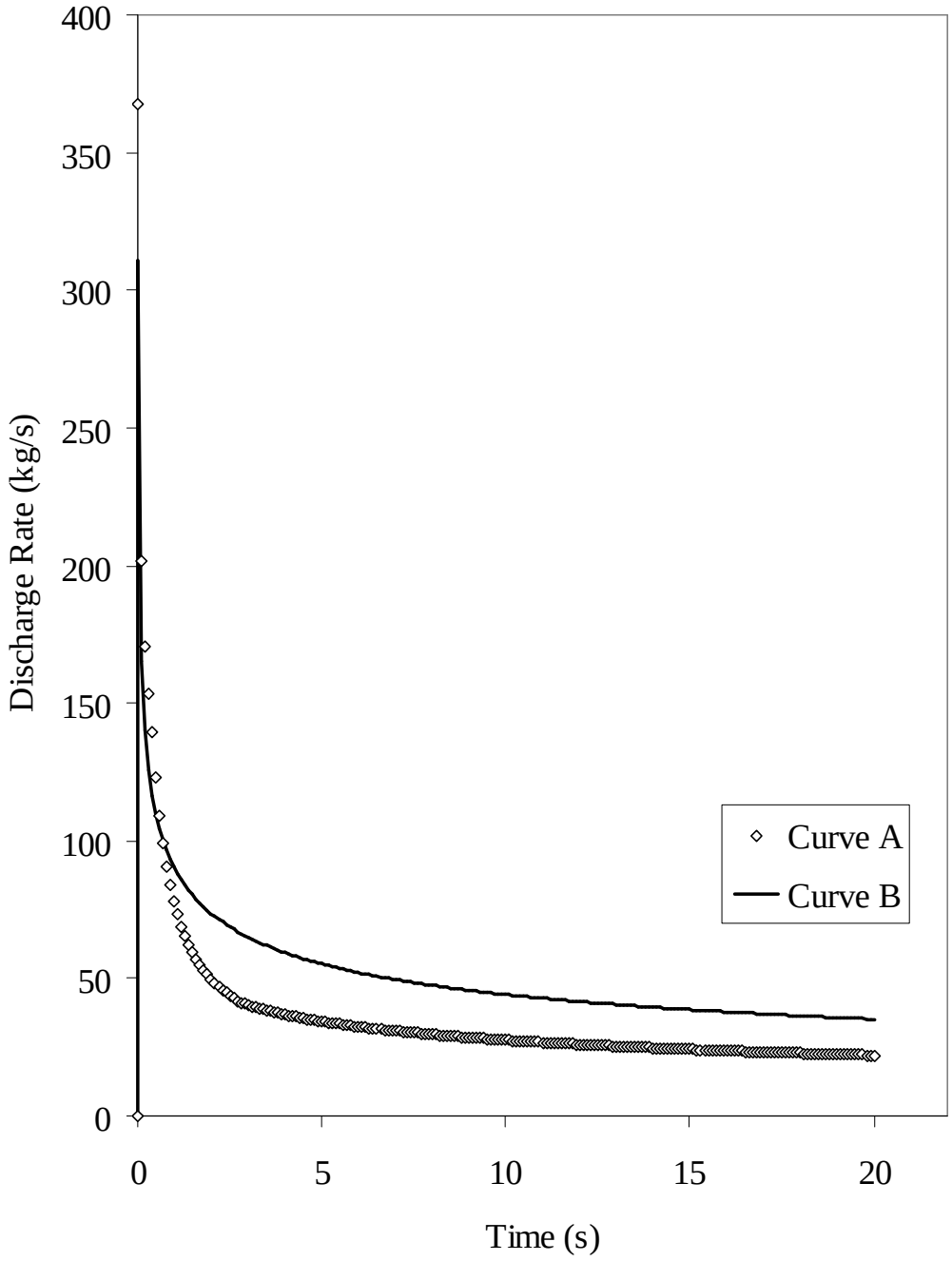

Figure 6.8: Variation of release rate with time following FBR of the 10km pipeline transporting 100% Methane using the 2 pipeline models.

Curve A – Multi segment pipeline model

Curve B – Single pipeline model

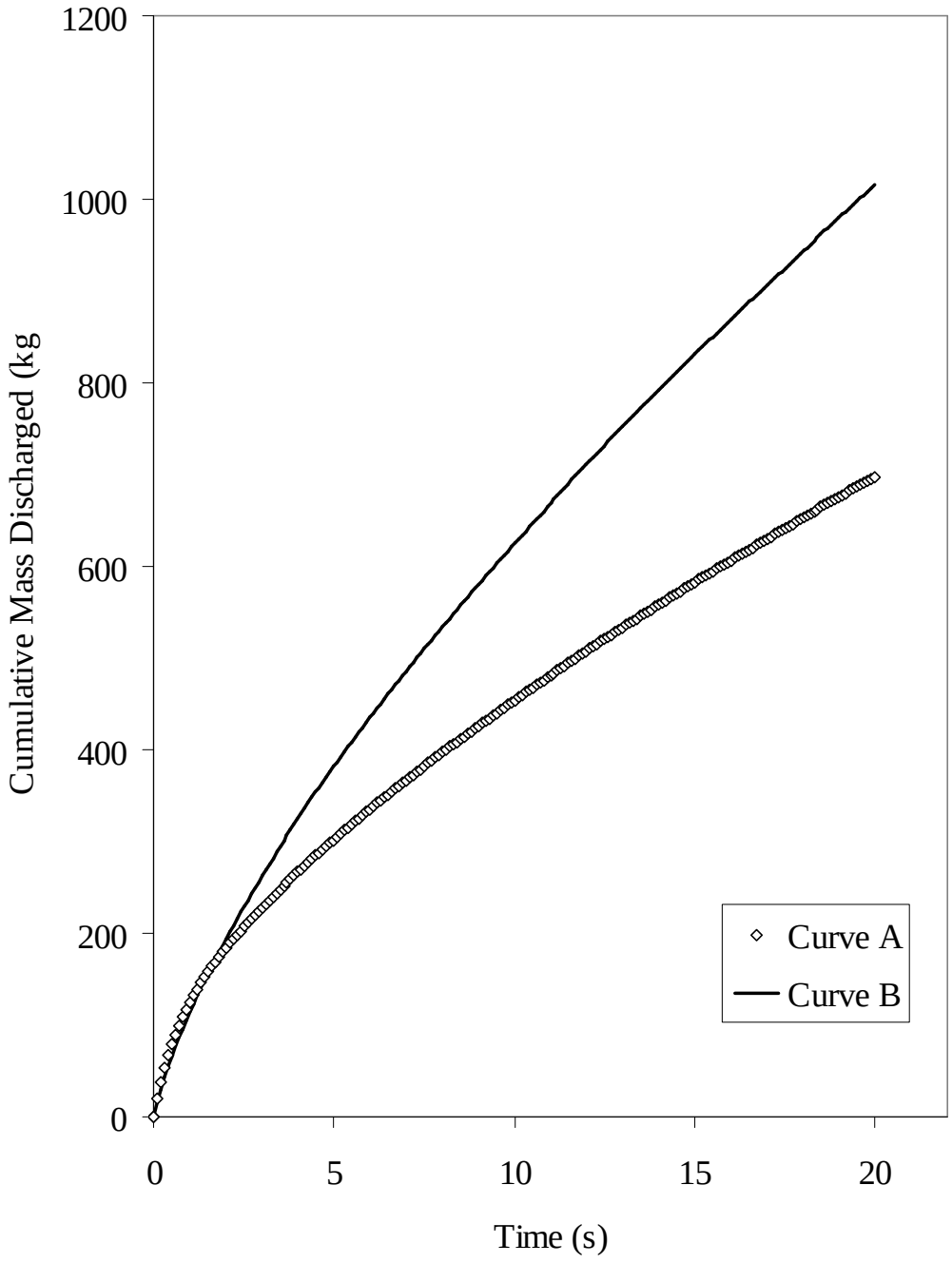

Figure 6.9: Variation of cumulative mass discharged with time following FBR of the 10km pipeline transporting 100% Methane.

Curve A – Multi diameter model

Curve B – Single pipeline model (Atti, 2006)

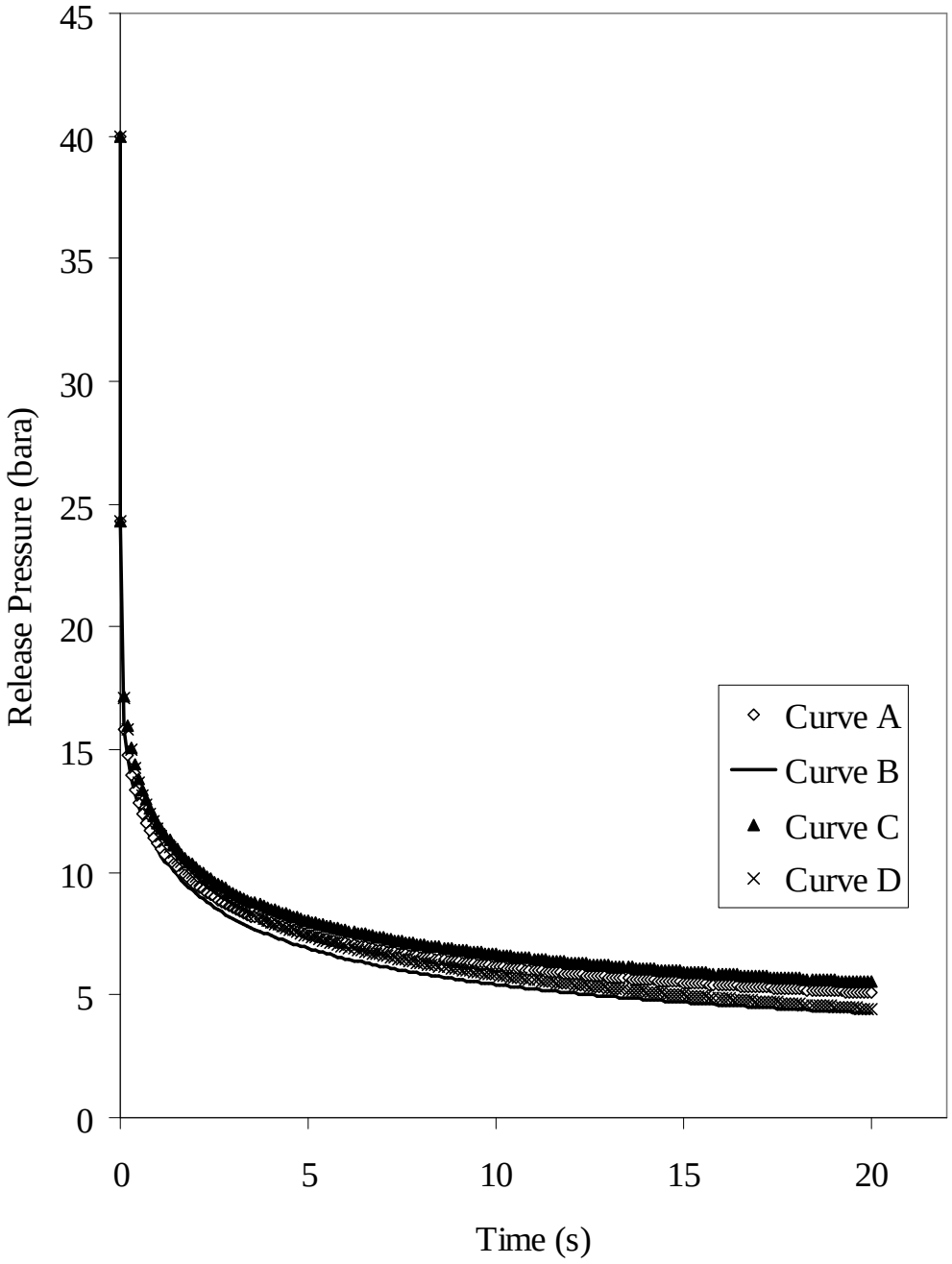

Figure 6.10: Variation of release pressure with time from upstream and downstream at the failure location following FBR of the 10km pipeline transporting 50% Methane and 50% Hexane.

Curve A – Upstream of failure - Multi segment pipeline model

Curve B – Downstream of failure - Multi segment pipeline model

Curve C – Upstream of failure - Single pipeline model

Curve D – Downstream of failure - Single pipeline model

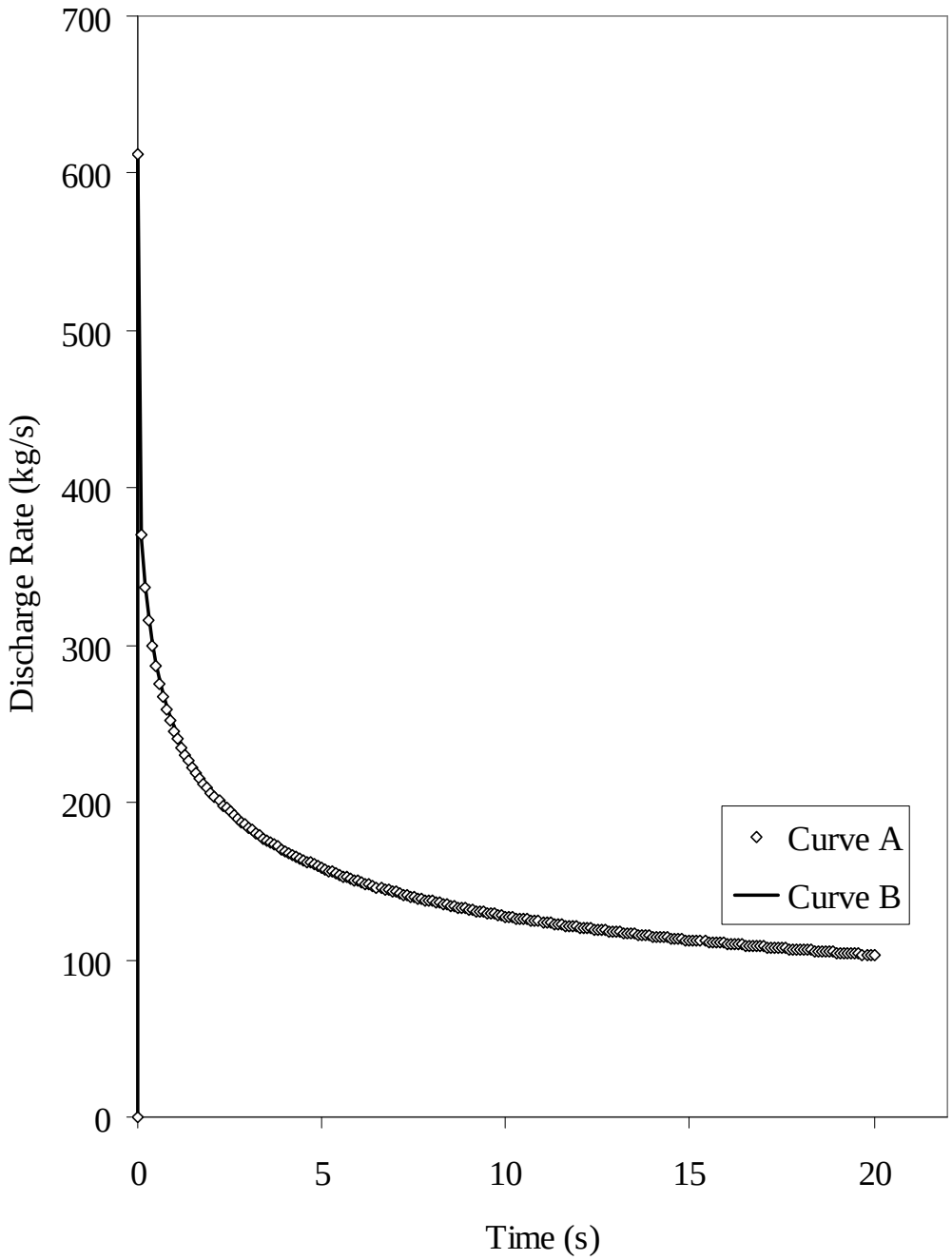

Figure 6.11: Variation of release rate with time following FBR of the 10km pipeline transporting 50% Methane and 50% Hexane using the 2 pipeline models.

Curve A – Multi segment pipeline model

Curve B – Single pipeline model

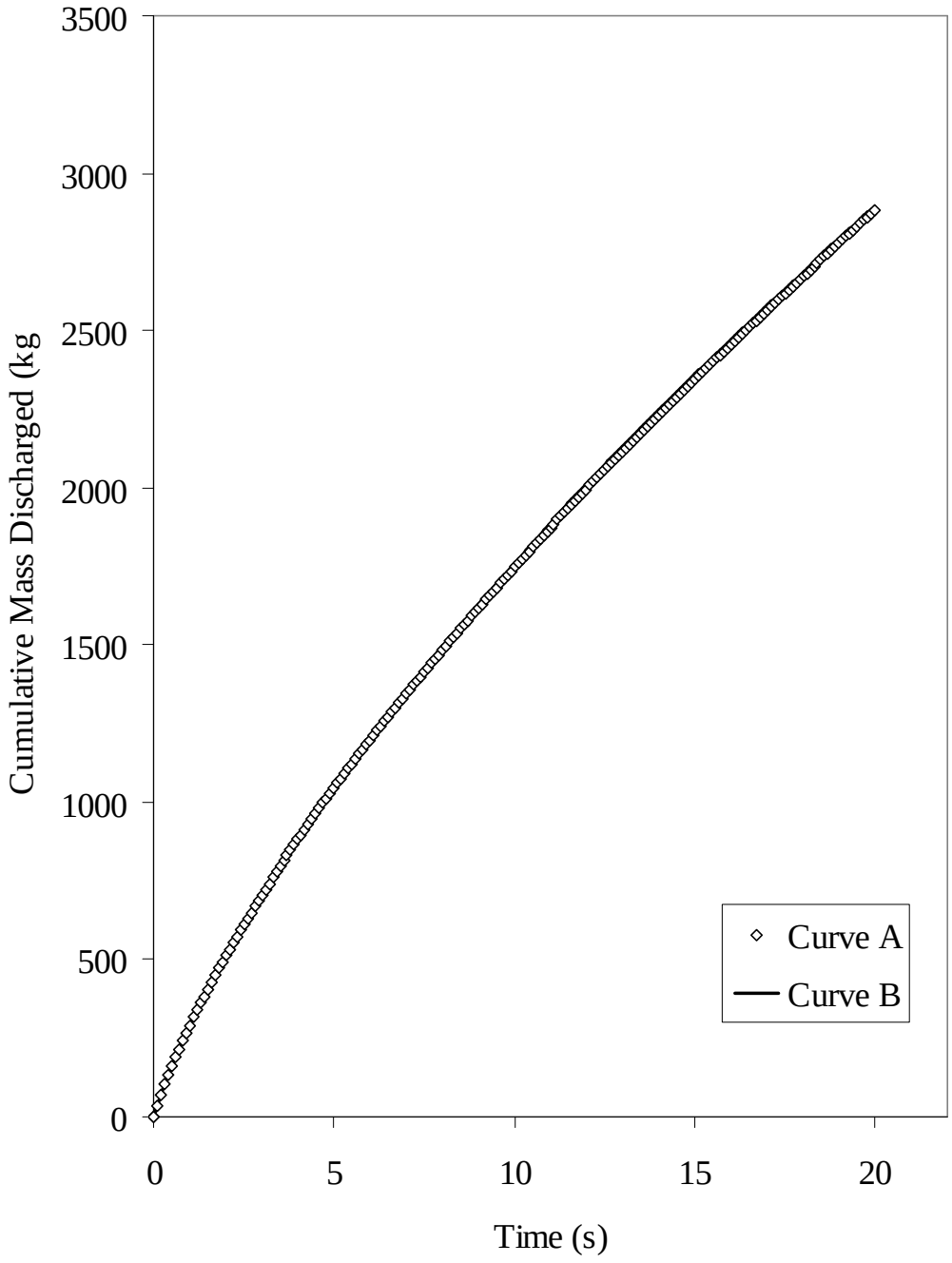

Figure 6.12: Variation of cumulative mass discharged with time following FBR of the 10km pipeline transporting 50% Methane and 50% Hexane.

Curve A – Multi diameter model

Curve B – Single pipeline model

6.4 Concluding Remarks

In this chapter the efficacy of the outflow model for simulating release from a multi-segment pipeline following failure presented in chapters 3 - 5 was investigated. This task involved a comparative study of the simulation results produced by the multi-segment model against the single pipeline model developed by Atti (2006). Additionally, in the absence of experimental data, the numerical accuracy of the model was evaluated based on the calculation of a mass conservation index, ε. An error of $\pm$ 2% in the mass conservation index (i.e. $0.98 \leq \varepsilon \leq 1.02$) corresponding to a % mass error of $\pm$ 2% was considered tolerable in the evaluation.

The comparative investigation carried out involved the full bore rupture of a hypothetical 10 km pipeline consisting of four pipeline segments against an equivalent single pipeline of equal length. Various pressurised inventories including vapour, liquid and two-phase mixtures were considered.

In the case of pipelines transporting a liquid inventory such as 100% Hexane for example, the pressure losses due to fittings and changes of elevation were most significant due to the greater hydrostatic head as compared to vapour inventory.

However, in the case of pipelines transporting two-phase inventories, the presence of fittings in the pipeline had minimal impact on the pressure profile and on the rate of depressurisation of the pipeline. This can be attributed to the dominance of pressure forces over hydraulic forces during two-phase discharge.

In conclusion a multi-inclined pipeline cannot be modelled as a straight pipeline inclined at an ‘equivalent’ angle because neglecting the losses due to fittings and changes in elevation result in significant over predictions in the single pipeline model results. Such over-prediction will be manifested in significantly increased costs due to the extra provisions required to reduce the subsequent hazard associated with pipeline failure to as low as reasonably practicable.

CHAPTER 7: LIMITATIONS OF THE HOMOGENEOUS EQUILIBRIUM MODEL

7.1 Introduction

This chapter presents the development and testing of two models designed to address the limitations of the Homogeneous Equilibrium Model (HEM) for predicting outflow following the failure of pressurised pipelines. These include a post-depressurisation hydraulic discharge model (termed the Hybrid Model) that deals with the failure of the HEM in predicting post depressurisation outflow following the rupture of a declined pipeline.

The other, a Modified Homogeneous Equilibrium Model (MHEM) is developed to address the breakdown of HEM in predicting pressurised orifice discharge for various composition hydrocarbons in the light of the experimental evidence produced by Richardson et al. (2006).

7.2 Post Depressurisation Hydrostatic Discharge from Declined Pipelines (Hybrid Model)

In practice long pipelines often pass through various topographies. This poses an immediate problem in the case of modelling of rupture of downward sloped or 'declining' pipelines since the MOC based simulation terminates once the line pressure reaches the ambient pressure. As such the gravity induced discharge of any remaining inventory in the pipeline is not accounted for. This is particularly relevant for pipelines containing non-flashing liquids.

In this section, the development of a Hybrid Model (HM) for predicting outflow following the rupture of downward sloped pressurised hydrocarbon pipelines is described. The model addresses the failure of the MOC based numerical solution technique in predicting post depressurisation outflow through coupling it with a hydraulic flow model.

In essence the model involves the application of the MOC for determining outflow until complete depressurisation of the pipeline. The outflow of any remaining liquid in the pipeline is then determined using the hydraulic model described below. In the case of two-phase mixtures, the quantity of liquid in the pipeline is determined using an isothermal flash and assuming its immediate disengagement from the vapour towards the open end of the pipeline. It is further assumed that during the post depressurisation liquid outflow, the space vacated by the liquid in the pipeline is displaced by ingress of the ambient air passing through the rupture plane thus maintaining the intact end pressure at the ambient pressure.

7.2.1 Model Formulation

There are two main driving forces that affect the discharge rate from declining pipelines:

1. Pressure forces due to the presence of a pressure gradient inside the pipeline
2. Gravitational forces due to the weight of inventory inside the pipeline

Following failure, the discharge rate is primarily determined by pressure forces until complete depressurisation of the pipeline to ambient conditions. At this point the fluid discharge is totally governed by gravitational force with the effect of this force increasing with an increase in the angle of inclination.

The declining pipeline model is developed from the energy balance equation for incompressible turbulent flow taking into account the kinetic, potential and frictional losses within the pipeline. Figure 7.1 is a schematic representation of the system under consideration.

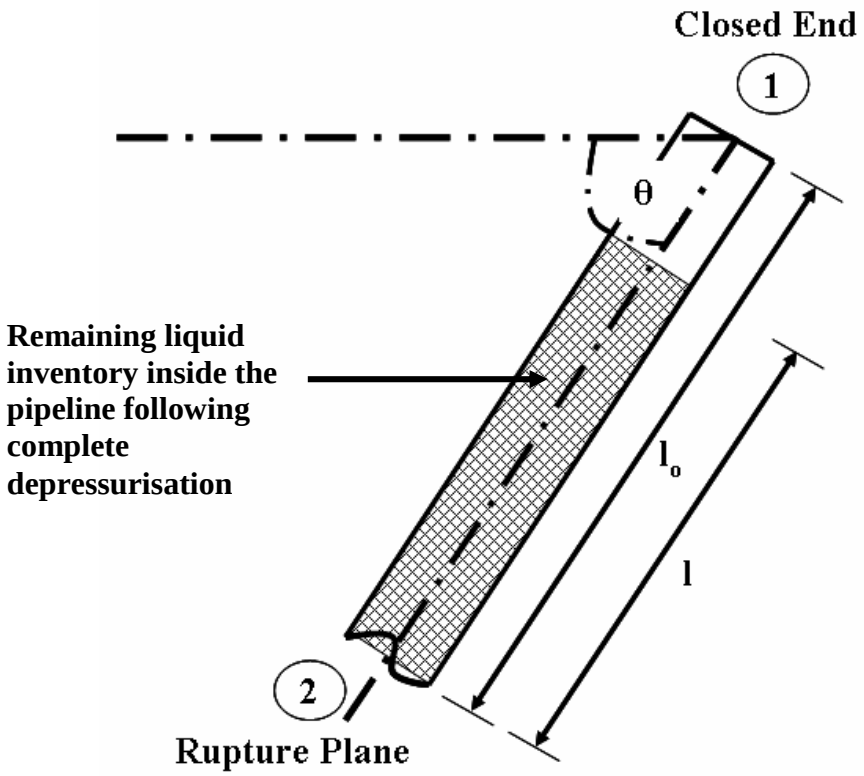

Figure 7.1: Schematic representation of a pipeline declined at an angle θ

Applying the energy balance equation for turbulent flow (Coulson and Richardson (1998)) gives:

$$\frac{v_1^{\,2}}{2} + gl_0 \sin\theta + v(P_2 - P_1) = gl\sin\theta + \frac{v_2^{\,2}}{2} + F \qquad (7.1)$$

Where,

Subscripts 1 and 2 denote closed and open end conditions respectively.

v_1 = the velocity at closed end of the pipeline; $v_1 = 0$

v_2 = the velocity at rupture plane

θ = angle of elevation with horizontal as origin these angles are taken as negative.

F = energy dissipated per unit mass due to friction.

l_0 = initial height of fluid in the pipeline.

l = height of fluid at anytime, t

P_1 and P_2 = pressure at the closed and rupture plane respectively.

Since both ends of the pipeline are at ambient pressure (pipeline is completely depressurised) we get:

$$P_1 = P_2 \tag{7.2}$$

Now, Coulson and Richardson (1998) give the energy dissipated per unit mass due to friction as:

$$F = 4\frac{R}{\rho u^2}\frac{l_0}{d}v_2^2 \tag{7.3}$$

Where, d is the internal diameter of the pipeline.

The fanning friction factor, f_w (Coulson and Richardson, 1998), is given by:

$$f_w = \frac{2R}{\rho u^2} \tag{7.4}$$

Substituting f_w into equation (7.3) gives:

$$F = 2f_w\frac{l_0}{d}v_2^2 \tag{7.5}$$

Substituting F in equation (7.1):

$$\frac{v_2^2}{2} = g\sin\theta(l_0 - l) - 2f_w\frac{l_0}{d}v_2^2 \tag{7.6}$$

Rearranging equation (7.6) gives:

$$v_2^2 = \frac{g\sin\theta(l_0 - l)}{\left[0.5 + 2f_w\frac{l_0}{d}\right]} \tag{7.7}$$

$$v_2 = \left[\frac{Lg\sin\theta}{0.5 + 2f_w\frac{l_0}{d}}\right]^{1/2}, \tag{7.8}$$

Where,

$$L = l_0 - l \tag{7.9}$$

The fanning friction factor is calculated using the Chen correlation (Chen, 1979) for transition and turbulent flow through rough pipes:

$$\frac{1}{\sqrt{f_w}} = 3.48 - 1.7372 \times \ln\left[\frac{\varepsilon}{r_{in}} - \frac{16.2446}{\mathrm{Re}} \times \ln A\right] \tag{7.10}$$

Where,

$$A = \frac{\left(\frac{\varepsilon}{r_{in}}\right)^{1.0198}}{6.0983} + \left(\frac{7.149}{\mathrm{Re}}\right)^{0.8981} \tag{7.11}$$

ε = the pipeline roughness

r_{in} = the pipeline inner radius

Re = the Reynold's number;

$$\mathrm{Re} = \frac{\rho d v_2}{\mu} \tag{7.12}$$

Since v_2 is unknown (and hence Re) the following procedure is used to calculate, v_2 and f_w:

1) Guess an initial value for f_w
2) Calculate the value of v_2 using equation (7.8)
3) Calculate the value of Re using equation (7.12)
4) Use the value of Re calculated in step 3 to determine f_w using equation (7.10)
5) If the initial guess is within an acceptable range of the calculated value of f_w (range used in model is $1x10^{-3}$), then calculated value of is used f_w, else
6) Calculated f_w is used as the new guess; go to step 2.

Assuming f_w is constant for the change a liquid level, L:

$$v_2 = \left[\frac{Lg\sin\theta}{0.5 + 2f_w\frac{l_0}{d}}\right]^{1/2} \tag{7.13}$$

Substituting $B = \dfrac{g\sin\theta}{0.5 + 2f_w\frac{l_o}{d}}$ into equation (7.13) gives:

$$v_2 = [BL]^{1/2} \tag{7.14}$$

Assuming that v_2 remains constant during the time taken for the liquid height to change by ΔL, and that all the liquid inside the pipeline is moving at v_2, the time taken for liquid height to change by ΔL is given by:

$$t = \frac{\Delta L}{v_2} \tag{7.15}$$

Figure 7.2 shows Hybrid Model outflow calculation algorithm for declining pipelines.

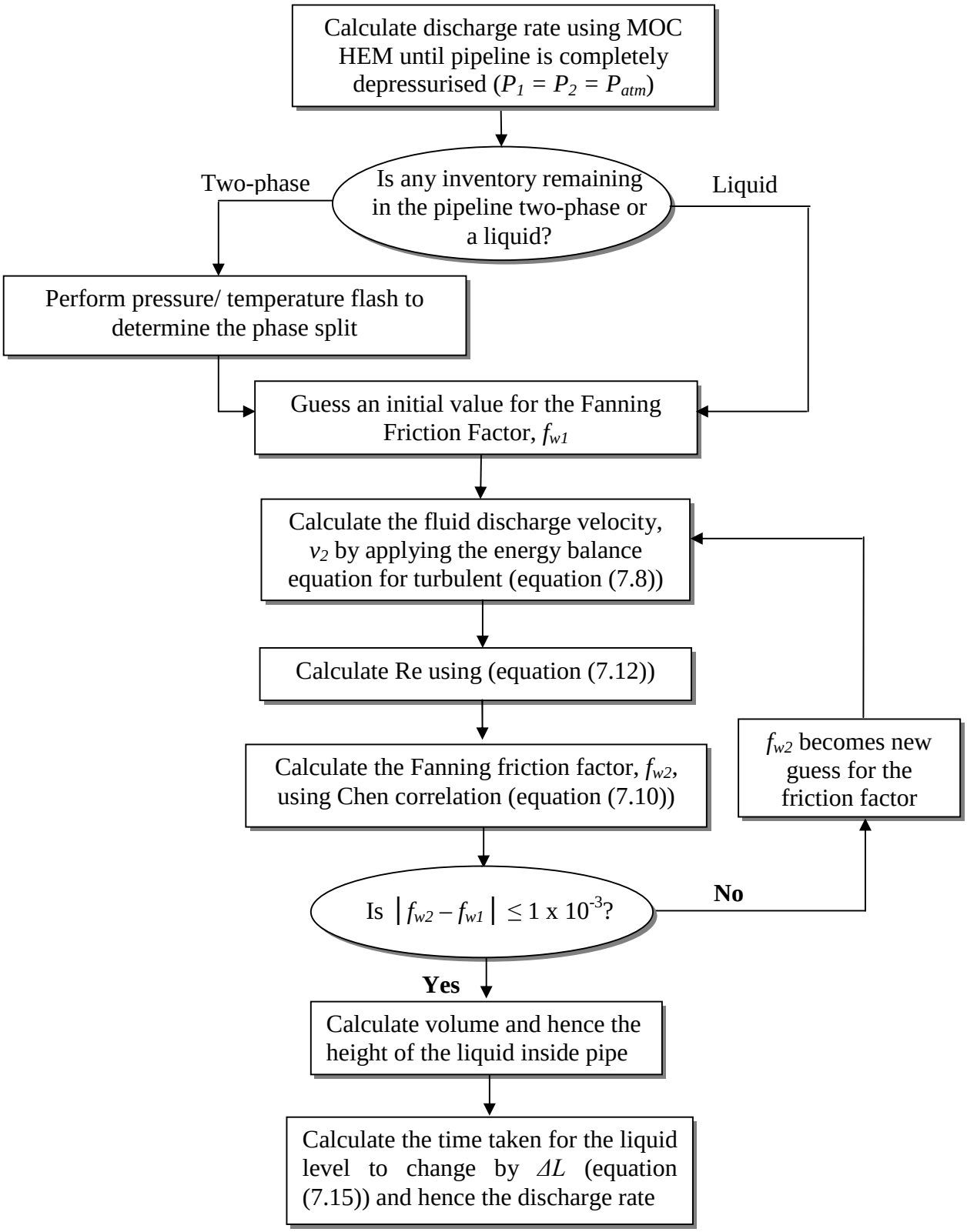

Figure 7.2: Hybrid Model outflow calculation algorithm

7.2.2 Results and Discussion

The following presents the results of the application of the Hybrid Model described above for the full bore rupture of a 100m long 0.154m i.d. pipeline containing different classes of fluids including flashing liquid, permanent liquid, two-phase mixture and a permanent gas at 21.6 bara. The overall pipeline dimensions including the prevailing conditions prior to failure are given in table 7.1. Apart from discussing the salient features in the data, the results are compared against those generated based on the HEM based outflow model which ignores post depressurisation discharge in order to highlight any of its limitations.

Table 7.1: Pipeline characteristics and prevailing conditions prior to full bore rupture of the pipeline for Hybrid Model investigation.

Length (m)	100
Internal diameter (mm)	154
Wall thickness (mm)	7.3
Roughness (m)	0.0005
Initial line pressure (bara)	21.6
Initial line temperature (K)	293.15
Ambient temperature (K)	292.25
Ambient pressure (bara)	1.01

7.2.2.1 Flashing liquid

Figure 7.3 shows the variation of the % cumulative mass discharge with time following the FBR of the 100 m pipeline containing 100% liquid Butane at an angle of decline of -10^{o}. Curve A shows the simulated data based on HEM. Curve B on the other hand shows the outflow data predicted using the Hybrid Model (HM).

As it may be observed from figure 7.3, HEM simulated data (curve A) significantly under predict the mass of fluid released from the pipeline following its full bore rupture as it ignores the post depressurisation hydraulic discharge of the remaining inventory. In contrast, HM successfully predicts the complete discharge of the entire inventory (1133.5 kg) which is released in 39s. The corresponding mass conservations, ε, based on the HEM and HM are 0.6 and 1 respectively.

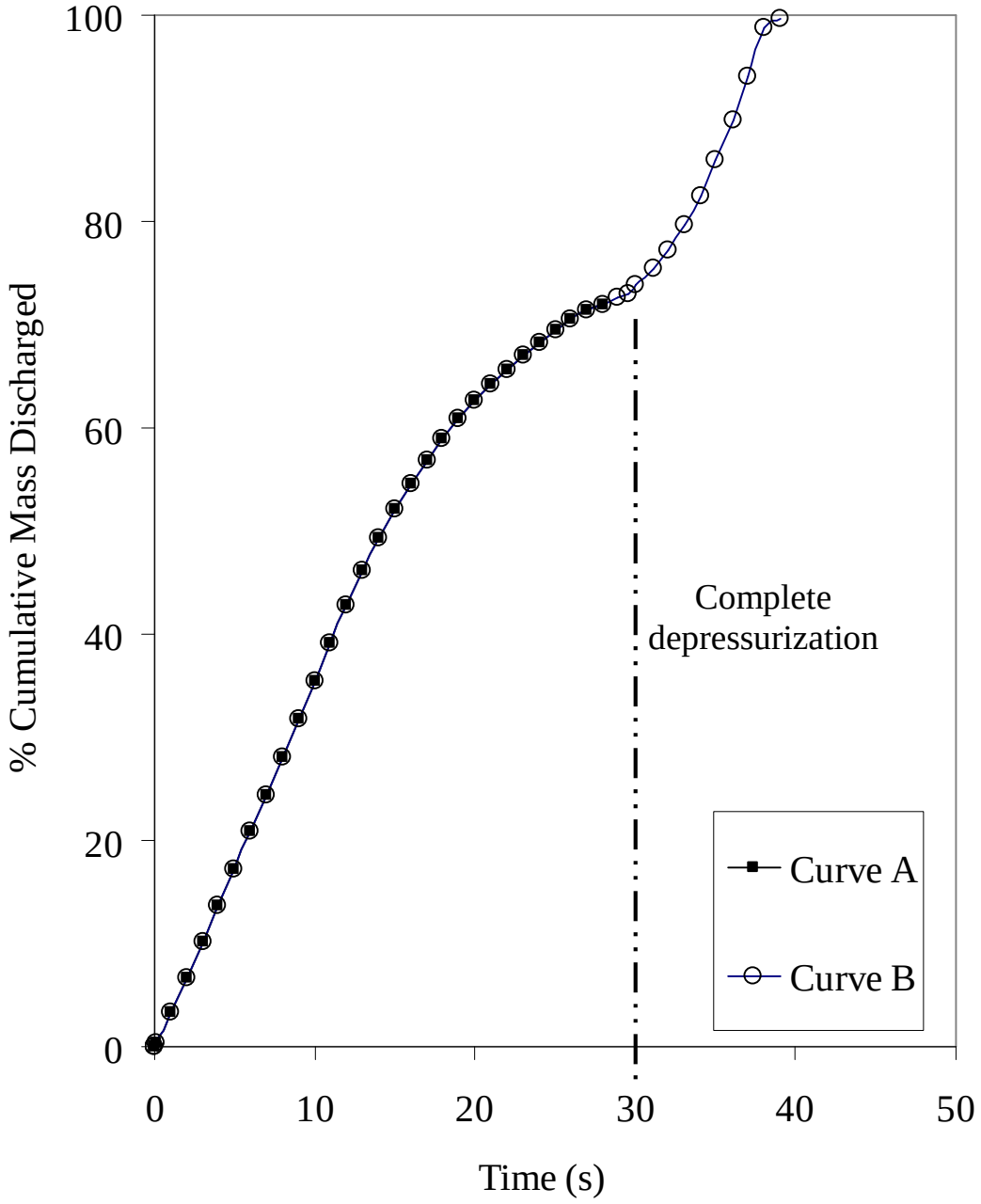

Figure 7.3: Variation of % cumulative mass discharged with time for the pipeline transporting 100% Butane at a decline angle of -10^{o} following FBR

Curve A: HEM (mass conservation index, ε = 0.6)

Curve B: Hybrid Model (mass conservation index, ε = 1)

Figure 7.4 shows the corresponding variation of % cumulative mass discharged with time at different angles of decline following the FBR of the 100m pipeline transporting 100% Butane. The approximate time corresponding to the complete depressurisation of the pipeline to 1 bara at each angle of decline is indicated on the same figure using the dashed lines. Several important trends may be observed in the data:

i) During the initial pressure equilibration period, the rate of cumulative mass loss remains, for the most part, independent of the angle of decline. This is consistent with the pressure forces being the dominant factor in driving out the inventory.

ii) The post depressurisation discharge rate increases with the angle of decline consistent with the increasing influence of the gravitational field effect.

iii) All the curves indicate an apparent discontinuity marked by the slowing down of the discharge rate around 1 bara followed by a rapid recovery. This is due to the assumption that the transition between the HEM and hydrodynamic flow occurs after the complete depressurisation of the pipeline. In practice this may happen earlier thus resulting in a higher discharge rate than that predicted. Interestingly, the extent of this transition, where the outflow remains relatively unchanged, decreases with increase in the angle of decline.

iv) As expected the total evacuation time decreases with increase in the angle of decline.

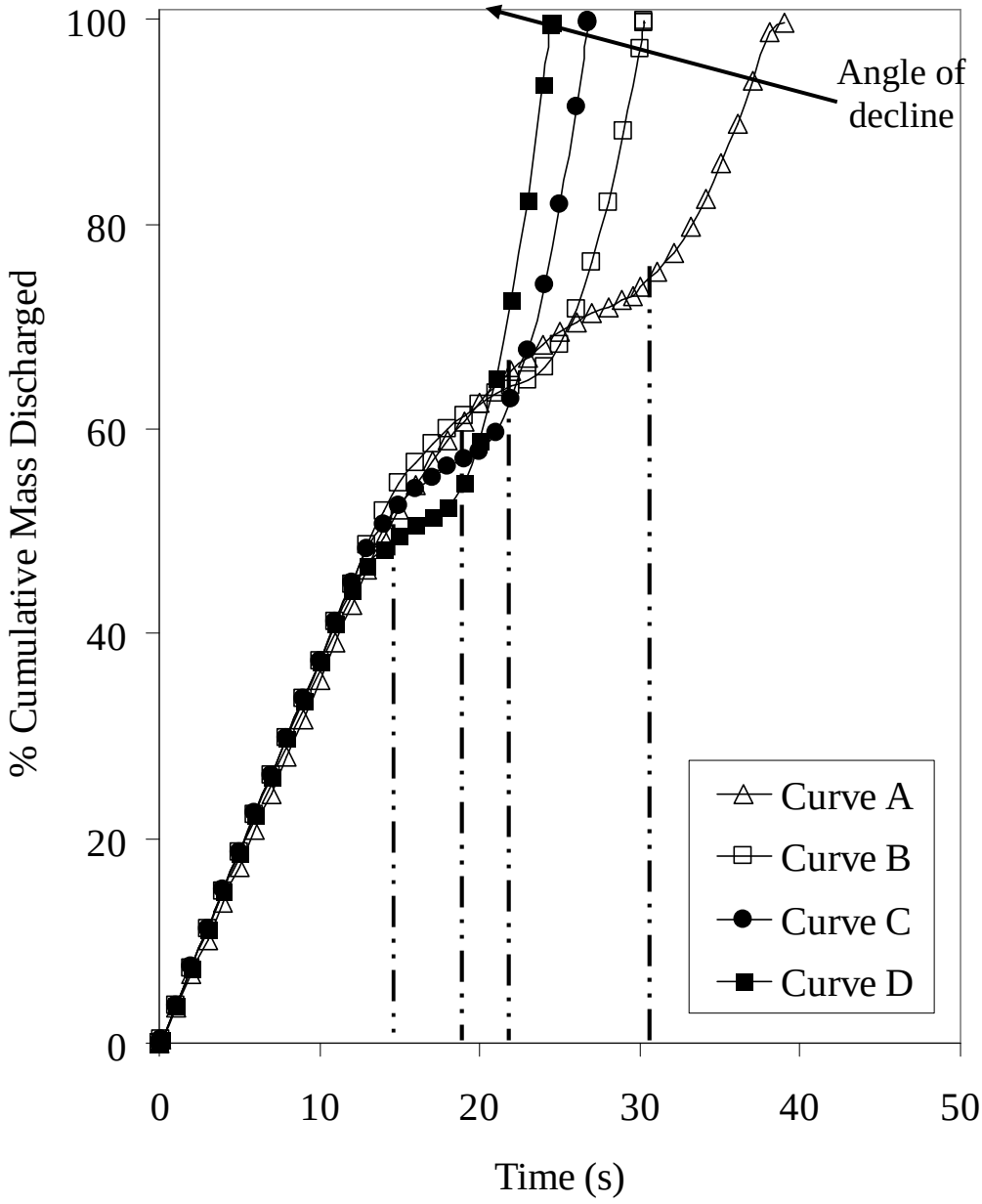

Figure 7.4: Variation of % cumulative mass discharged with time for a 100 m pipeline transporting 100% Butane at different angles of decline following FBR. The dashed lines show the depressurization time to 1 bara.

Curve A: -10^{o} Curve B: -30^{o}

Curve C: -50^{o} Curve D: -90^{o}

7.2.2.2 Permanent liquid

Figure 7.5 presents the variation of % cumulative discharge mass with time for the 100 m pipeline containing liquid Hexane following its full bore rupture at an angle decline of -10^{o}. Curve A shows the data based on HEM whereas curve B shows the corresponding data using HM.

As it may be observed from figure 7.5, once again, HEM (curve A) significantly under predicts the inventory released from the pipeline following its full bore rupture. Of the total 1242 kg initial inventory, only 0.7% (8.6 kg) corresponding to its expansion from 21.6 bara to atmospheric pressure is released in the first 0.2s following pipeline failure. In contrast, HM successfully predicts the complete discharge of the entire inventory (1242 kg) which is released in 36s.

Figure 7.6 is a plot of the % cumulative mass discharged with time at different angles of decline in the range 10 – 90^{o} for the 100m pipeline transporting 100% Hexane following its FBR. As expected the time to completely discharge the pipeline contents dramatically decreases with increasing the angle of decline due to the increased influence of gravity.

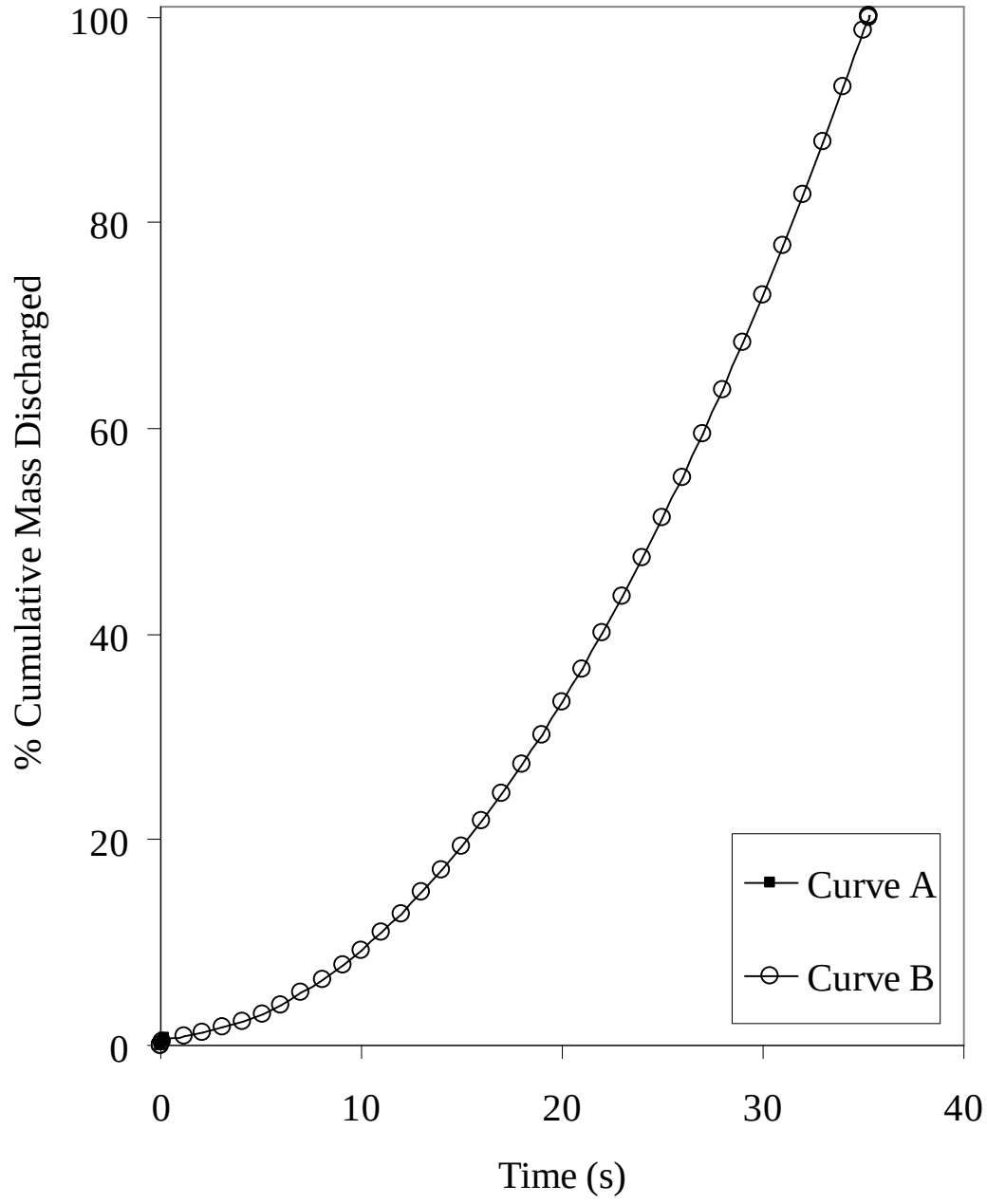

Figure 7.5: Variation of % cumulative mass discharged with time for the pipeline transporting 100% Hexane at a decline angle of -10^{o} following FBR

Curve A: HEM (mass conservation index, $\varepsilon = 0.5$)

Curve B: HM (mass conservation index, $\varepsilon = 1$)

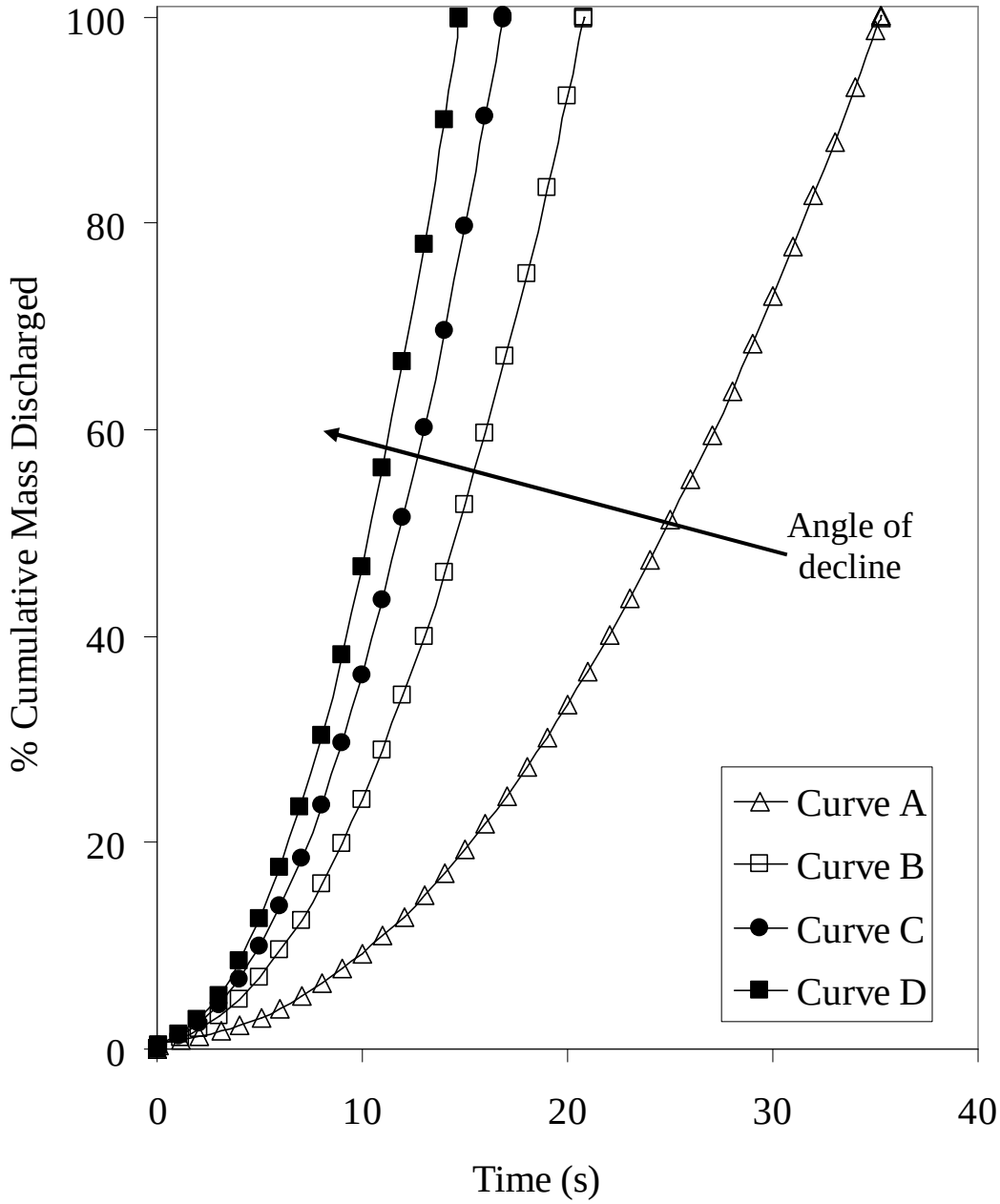

Figure 7.6: Variation of % cumulative mass discharged with time for a 100 m pipeline transporting 100% Hexane at different angles of decline following FBR

Curve A: -10^o Curve B: -30^o

Curve C: -50^o Curve D: -90^o

7.2.2.3 Two-phase Mixture and Permanent Gas

Figure 7.7 shows the variation of the % cumulative mass discharged with time for the 100 m pipeline containing a two-phase mixture of 80% Hexane and 20% Methane following its FBR at different angles of decline. On this occasion, both the HEM and the HM produce very similar results. This is consistent with the entire liquid content of the pipeline being discharged by the pressurised Methane by the time the pipeline reaches 1 bara. Also, the rate of depletion of the inventory during pressure equilibration is independent of the angle of decline, once again, indicating the dominant influence of the pressure forces due to the presence of the gas in the mixture. The same observation may be made in the case of the pipeline containing only Methane following its FBR. As indicated in figure 7.8, in this case, the discharge rate is relatively independent of the angle of decline.

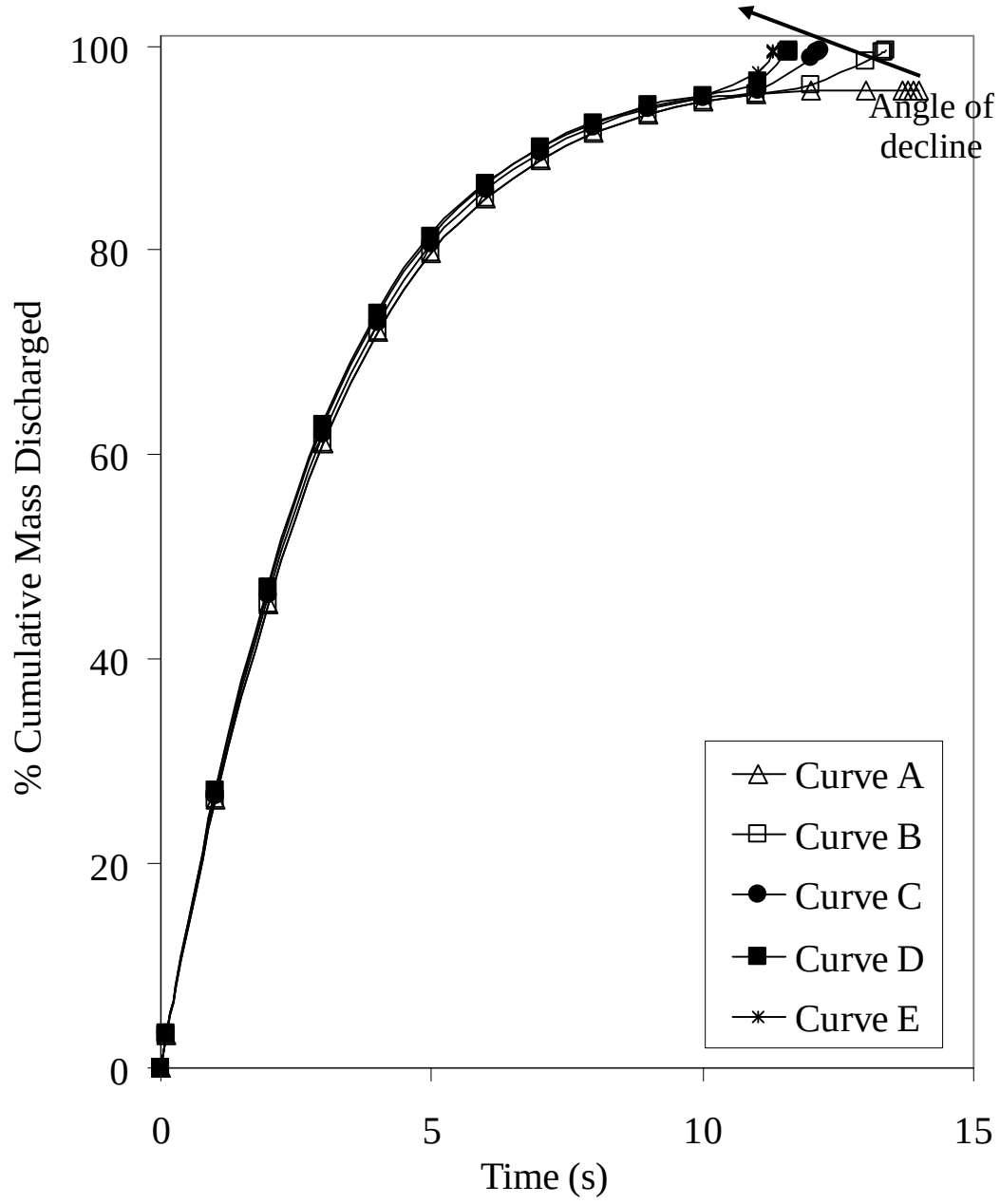

Figure 7.7: Variation of % cumulative mass discharged with time for a 100 m pipeline transporting 80% Hexane and 20% Methane at different angles of decline following FBR

Curve A: -10^{o} (HEM) Curve B: -10^{o} (HM)

Curve C: -30^{o} (HM) Curve D: -50^{o} (HM)

Curve E: -90^{o} (HM)

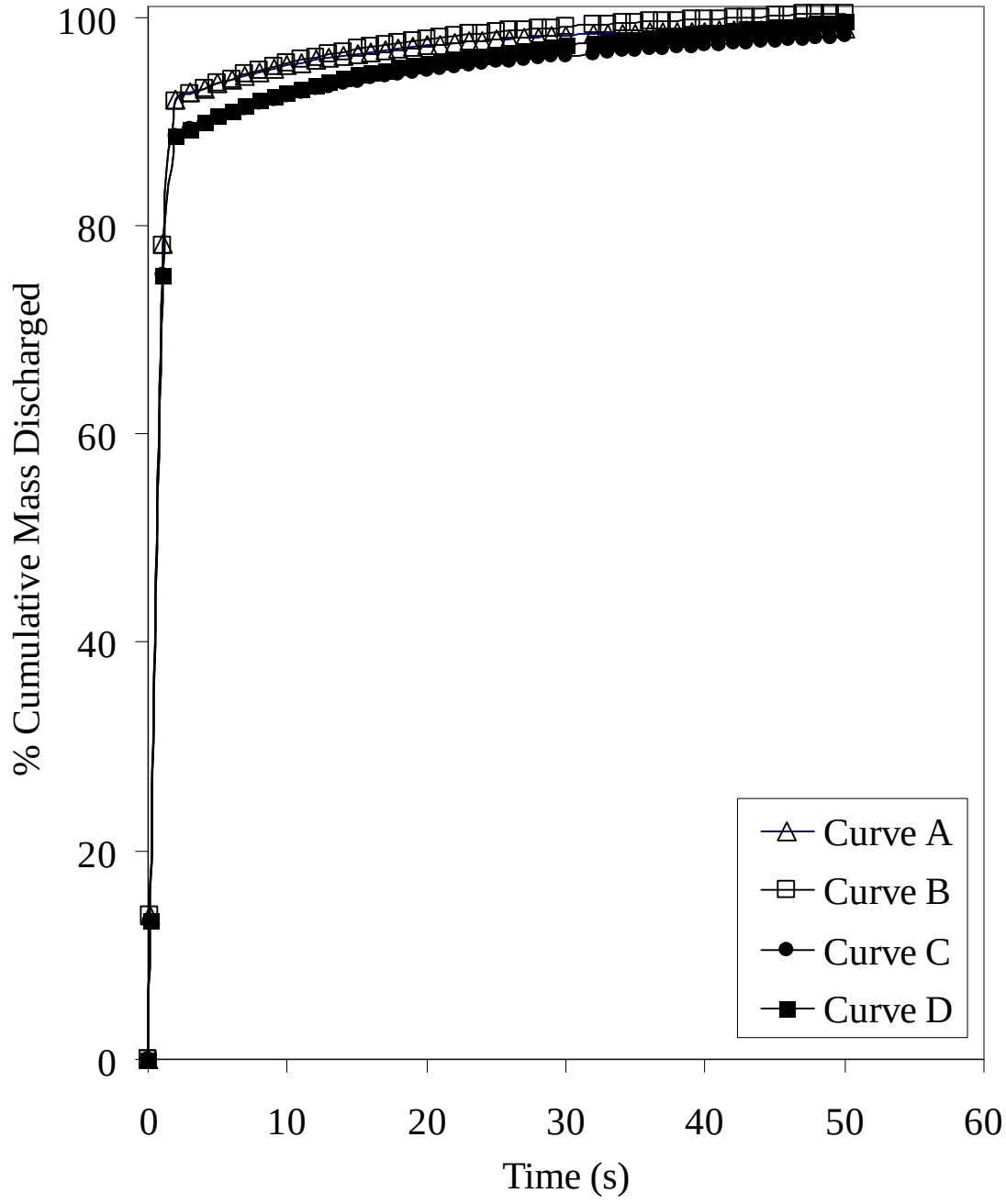

Figure 7.8: Variation of % cumulative mass discharged with time for a 100 m pipeline transporting 100% Methane at different angles of decline following FBR.

Curve A: -10^{o} Curve B: -30^{o}

Curve C: -50^{o} Curve D: -90^{o}

7.3 Modified Homogeneous Equilibrium Model (MHEM)

The HEM assumes that the constituent phases in a two-phase mixture are in thermal and mechanical equilibrium with one another. This assumption simplifies the analysis of two-phase discharge from a pipeline as a single set of conservation equations can be used to describe the behaviour of the fluid. As indicated in chapter 2, this assumption has been found to be generally valid in the case of full bore pipeline rupture for the types of inventories tested.

However, in the case of flashing liquids containing small quantities of dissolved vapour, the rapid transients occurring at the failure plane may limit the time for dissolution of the dissolved vapour as the fluid expands into the surrounding environment. Consequently, calculating the release rate based on the HEM which assumes instantaneous flash or equilibration to two-phase conditions gives erroneous results.

In this section, a Modified HEM (MHEM) is developed to address the failure of the HEM to accurately predict the discharge rate of two phase mixtures containing low quantities of vapour through an orifice. The model is based on the experimental results presented by Richardson et al. (2006) which showed that the applicability of HEM following rapid depressurisation is governed by proportion of dissolved vapour present in the mixture.

The investigation begins with a comparison of measured discharge data through an office reported by Richardson et al. (2006) for a variety of hydrocarbon mixtures against those predicted using HEM. The formulation of the MHEM to address the limitations highlighted by the above comparisons is then presented. The section concludes with a comparison of the results obtained using the HEM and MHEM for the release of two-phase mixtures containing different quantities of dissolved vapour.

7.3.1 Applicability of the HEM

Table 7.2 gives the compositions of the natural gas, propane and condensate used in the experiments conducted by Richardson et al. (2006) to test the applicability of the HEM for simulating the release of two phase mixtures through an orifice.

Table 7.2: Compositions (mole %) of natural gas, propane and condensate used in the experiments conducted by Richardson et al. (2006).

Component	Natural Gas	Propane	Condensate
C_1	94.489	0	0
C_2	5.002	0.567	0
C_3	0.422	97.112	0.446
C_4	0.087	2.269	4.908
C_5	0	0.052	14.178
C_6	0	0	22.029
C_7	0	0	25.718
C_8	0	0	19.116

Tables 7.3 - 7.6 show the comparison of the discharge coefficients obtained using the HEM developed by Richardson et al. (2006) (PREPROP), HEM presented in this work (UCLM) and the American Petroleum Institute (API) recommended discharge coefficients. The latter, presented in the tables is defined as:

$$Discharge\ Coefficient = \frac{Experimental\ Flow\ Rate}{Theoretical\ Flow\ Rate} \qquad (7.16)$$

Table 7.3: Comparison of the discharge coefficient required by UCLM and PREPROP to match experimental data: Natural gas through an orifice.

Diameter (mm)	Pressure (bara)	Temperature (K)	Discharge Coefficient (C_d)	
			PREPROP	UCLM
15	10.0	254.35	0.90	0.89
15	9.9	243.55	0.91	0.93
15	10.5	268.85	0.92	0.93
15	10.7	257.95	0.89	0.90
15	10.2	244.15	0.93	0.93
15	10.3	240.25	0.92	0.92
10	24.6	252.65	0.88	0.87
15	12.0	266.55	0.89	0.90
10	28.9	278.85	0.87	0.87
10	31.9	283.45	0.88	0.87
10	30.6	274.85	0.91	0.92
10	30.9	271.95	0.90	0.90
10	31.5	266.15	0.89	0.89
10	30.4	256.85	0.90	0.90
10	36.8	283.55	0.89	0.88
10	38.7	282.25	0.88	0.87
10	37.9	281.65	0.90	0.89
15	15.6	241.55	0.92	0.91
15	15.8	247.85	0.93	0.93
15	17.0	250.65	0.90	0.90
10	42.1	277.05	0.88	0.87
10	43.2	279.95	0.89	0.89
10	41.6	257.25	0.89	0.88
10	45.8	286.15	0.90	0.89
15	21.1	243.85	0.92	0.92
10	49.0	259.85	0.90	0.89
10	50.6	269.15	0.90	0.90

Table 7.3 contd.:

Diameter (mm)	Pressure (bara)	Temperature (K)	Discharge Coefficient (C_d)	
			PREPROP	UCLM
15	22.9	248.95	0.90	0.90
10	50.9	261.75	0.89	0.88
15	23.4	254.75	0.93	0.92
8	79.8	273.75	0.90	0.90
10	57.1	279.35	0.88	0.87
10	55.1	262.05	0.89	0.88
10	59.8	280.55	0.88	0.87
15	25.7	246.55	0.91	0.92
15	29.5	250.55	0.91	0.90
15	31.0	268.85	0.92	0.91
15	30.0	249.45	0.91	0.91
10	74.7	281.45	0.90	0.89
15	32.4	249.95	0.91	0.91
10	74.2	280.55	0.93	0.91
10	79.7	271.75	0.91	0.90
10	79.9	270.75	0.92	0.91
15	50.8	258.95	0.90	0.89
15	53.1	259.75	0.90	0.90
15	78.1	270.65	0.91	0.90
15	82.0	271.45	0.91	0.90
15	78.4	271.15	0.91	0.90
15	80.2	270.15	0.91	0.91
15	78.8	271.05	0.90	0.89
15	80.1	272.15	0.90	0.89

Table 7.4: Comparison of the discharge coefficient required by UCLM, API and PREPROP to match experimental data: Natural gas and Propane through an orifice.

Diameter (mm)	Pressure (bara)	Temperature (K)	Propane (mass fraction)	Discharge Coefficient (C_d)		
				PREPROP	UCLM	API
10	39.6	258.65	0.43	0.95	0.96	0.96
10	44.2	263.25	0.50	0.94	0.95	0.95
10	47.0	267.05	0.56	0.95	0.95	0.96
10	48.0	270.05	0.61	0.96	0.96	0.97
10	50.3	272.45	0.63	0.98	0.97	0.98
10	52.1	276.95	0.70	1.00	1.00	1.01
10	36.1	254.15	0.29	0.92	0.92	0.93
10	53.6	256.55	0.22	0.93	0.94	0.94
10	57.1	262.25	0.35	0.94	0.95	0.95
10	59.1	265.75	0.43	0.94	0.94	0.95
10	60.5	268.85	0.49	0.94	0.95	0.95
10	61.0	271.75	0.55	0.96	0.96	0.97
10	62.3	273.85	0.58	0.97	0.97	0.97
10	63.7	275.55	0.61	0.97	0.97	0.98
10	64.5	277.25	0.63	0.99	0.98	0.99
10	65.4	278.85	0.66	0.98	0.98	0.99
10	79.6	268.15	0.08	0.92	0.94	0.91
10	80.6	266.45	0.14	0.93	0.91	0.88
10	81.4	265.95	0.18	0.93	0.92	0.86
10	81.9	265.95	0.22	0.93	0.93	0.93
10	83.3	267.25	0.25	0.93	0.93	0.94
10	83.9	270.15	0.32	0.94	0.95	0.95
10	84.0	270.75	0.33	0.94	0.94	0.94
10	84.3	272.45	0.37	0.95	0.95	0.95
10	84.4	275.15	0.44	0.97	0.97	0.97
10	85.8	276.95	0.47	0.95	0.96	0.96
10	84.7	277.75	0.49	0.95	0.95	0.96
15	81.3	266.55	0.14	0.92	0.91	0.87
15	81.3	266.05	0.18	0.92	0.91	0.85
15	81.3	265.85	0.23	0.92	0.92	0.93

Table 7.4 contd.:

Diameter (mm)	Pressure (bara)	Temperature (K)	Propane (mass fraction)	Discharge Coefficient (C_d)		
				PREPROP	UCLM	API
15	81.4	267.75	0.28	0.93	0.93	0.93
15	81.6	269.25	0.31	0.93	0.94	0.94
15	51.6	252.15	0.09	0.91	0.90	0.89
15	53.2	251.35	0.16	0.91	0.92	0.92
15	55.4	256.45	0.27	0.92	0.92	0.93
15	56.3	258.45	0.30	0.93	0.93	0.93
15	57.5	260.55	0.34	0.93	0.93	0.94
15	58.2	262.05	0.37	0.93	0.94	0.94
15	58.7	263.75	0.40	0.93	0.93	0.93
15	33.4	240.65	0.14	0.93	0.94	0.94
15	35.6	245.35	0.24	0.94	0.95	0.95
15	37.4	249.55	0.32	0.95	0.96	0.96
15	41.2	256.55	0.44	0.96	0.96	0.97
8	81.5	264.55	0.19	0.93	0.92	0.88
8	85.9	272.15	0.42	0.94	0.94	0.94
8	88.1	276.65	0.52	0.93	0.93	0.94
8	90.6	280.85	0.60	0.94	0.93	0.94
10	52.9	276.75	0.75	0.98	0.95	0.98
10	65.9	282.85	0.64	1.00	0.98	1.00
10	67.4	281.65	0.79	1.00	0.96	1.00
10	67.3	284.05	0.81	1.04	0.99	1.00
10	87.8	280.55	0.56	0.96	0.94	0.96
10	88.3	272.55	0.64	0.90	0.88	0.88
10	66.1	276.85	0.49	0.96	0.94	0.96
10	64.3	271.55	0.44	0.93	0.92	0.94
10	61.6	266.25	0.36	0.92	0.91	0.93
10	57.8	260.45	0.23	0.91	0.91	0.92
10	68.3	281.85	0.66	0.99	0.96	0.99
10	65.7	281.75	0.61	0.99	0.97	0.99

Table 7.5: Comparison of the discharge coefficient required by UCLM, API and PREPROP to match experimental data: Natural gas, Condensate and Propane.

Diameter (mm)	Pressure (bara)	Temperature (K)	Mass Fraction		Discharge Coefficient (C_d)		
			Propane	Condensate	PREPROP	UCLM	API
10	85.4	264.45	0.21	0.00	0.93	0.91	0.85
10	85.4	264.35	0.26	0.00	0.92	0.91	0.93
10	89.3	272.75	0.47	0.00	0.92	0.90	0.92
10	90.2	276.75	0.56	0.00	0.92	0.90	0.92
10	90.1	278.35	0.59	0.00	0.92	0.89	0.92
10	90.0	278.95	0.61	0.00	0.92	0.89	0.92
10	47.2	264.75	0.33	0.00	0.95	0.94	0.96
10	51.3	272.85	0.47	0.00	0.99	0.97	1.00
10	57.0	277.25	0.57	0.00	1.01	0.98	1.02
10	61.5	270.25	0.63	0.00	0.96	0.92	0.96
10	64.0	266.55	0.68	0.00	0.91	0.87	0.92
10	61.9	274.75	0.70	0.00	0.98	0.93	0.98
10	66.1	276.15	0.72	0.00	0.95	0.91	0.95
10	70.7	282.15	0.78	0.00	1.00	0.95	1.00
10	72.3	284.15	0.81	0.00	1.08	0.98	0.62
10	40.7	282.85	0.12	0.42	0.99	0.98	0.99
10	39.3	276.55	0.27	0.23	0.97	0.95	0.98
10	39.9	277.15	0.21	0.34	0.98	0.97	0.98
10	54.0	271.25	0.40	0.03	0.88	0.84	0.89
10	50.7	268.35	0.38	0.03	0.91	0.89	0.91
10	49.6	266.85	0.35	0.04	0.93	0.91	0.94
10	57.4	280.85	0.18	0.43	0.92	0.88	0.92
10	58.4	284.35	0.14	0.53	0.97	0.96	0.97
10	57.4	285.45	0.14	0.52	0.96	0.95	0.96
10	65.9	284.45	0.38	0.36	0.95	0.92	0.95

Table 7.5 contd.:

Diameter (mm)	Pressure (bara)	Temperature (K)	Mass Fraction		Discharge Coefficient (C_d)		
			Propane	Condensate	PREPROP	UCLM	API
10	68.9	284.15	0.49	0.29	0.91	0.87	0.91
10	71.6	283.35	0.33	0.49	0.93	0.89	0.92
15	66.6	273.15	0.49	0.03	0.97	0.95	0.98
15	67.4	275.75	0.42	0.15	0.97	0.94	0.97
15	67.8	278.75	0.34	0.30	1.00	0.97	1.00
15	66.3	271.05	0.52	0.01	0.94	0.90	0.94
10	48.7	265.85	0.50	0.09	0.95	0.92	0.95
10	45.4	262.25	0.48	0.09	0.94	0.91	0.94
10	41.2	260.05	0.45	0.08	0.94	0.92	0.95
10	36.1	263.15	0.37	0.07	0.96	0.94	0.97
15	43.3	262.35	0.31	0.06	0.95	0.93	0.96
15	44.1	259.75	0.37	0.07	0.97	0.95	0.98
15	42.6	256.85	0.34	0.06	0.94	0.92	0.95
15	44.2	257.05	0.37	0.07	0.94	0.92	0.95
15	36.8	251.35	0.22	0.04	0.92	0.91	0.93
15	37.3	250.85	0.23	0.04	0.93	0.91	0.94
15	35.8	249.45	0.22	0.04	0.93	0.91	0.93
15	34.9	248.45	0.21	0.04	0.93	0.91	0.93
10	47.9	277.65	0.00	0.21	0.92	0.92	0.94
10	50.6	278.65	0.00	0.36	0.95	0.95	0.96
10	52.6	280.15	0.00	0.49	0.99	0.99	1.00
10	83.3	278.35	0.00	0.67	1.02	1.01	1.01
10	81.7	281.05	0.00	0.62	1.01	1.01	1.01
10	80.2	282.65	0.00	0.56	1.01	1.00	1.01

Table 7.6: Comparison of the discharge coefficient required by UCLM, API and PREPROP to match experimental data: Natural gas and Propane – compressed volatile liquid.

Diameter (mm)	Pressure (bara)	Temperature (K)	Mass Fraction		Discharge Coefficient (C_d)	
			Propane	Natural Gas	PREPROP	UCLM
5	11.8	280.05	1.00	0.00	0.59	0.58
5	38.2	280.25	1.00	0.00	0.60	0.58
5	48.4	280.55	1.00	0.00	0.60	0.58
5	55.6	280.85	1.00	0.00	0.60	0.59
5	25.0	281.25	1.00	0.00	0.59	0.58
5	33.0	281.45	1.00	0.00	0.59	0.58
5	61.1	281.15	1.00	0.00	0.60	0.58
5	9.0	281.05	1.00	0.00	0.59	0.57
5	21.0	281.35	1.00	0.00	0.59	0.57
5	34.3	281.55	1.00	0.00	0.60	0.57
5	9.4	281.35	1.00	0.00	0.59	0.53
5	22.7	281.45	1.00	0.00	0.59	0.54
5	34.9	281.55	1.00	0.00	0.60	0.55
5	45.1	281.65	1.00	0.00	0.60	0.56
7	6.3	282.25	1.00	0.00	0.57	0.79
7	8.7	282.85	1.00	0.00	0.59	0.57
7	11.7	283.05	1.00	0.00	0.59	0.57
7	14.5	283.45	1.00	0.00	0.59	0.57
7	19.9	283.85	1.00	0.00	0.59	0.57
10	6.5	283.45	1.00	0.00	0.58	0.80
10	6.4	282.85	1.00	0.00	0.57	0.78
10	6.6	283.65	1.00	0.00	0.59	0.76
7	40.9	281.95	1.00	0.00	0.61	0.59
7	17.3	282.25	1.00	0.00	0.60	0.59
7	35.8	282.45	1.00	0.00	0.61	0.59
7	68.6	281.35	1.00	0.00	0.61	0.59

Table 7.6 contd.:

Diameter (mm)	Pressure (bara)	Temperature (K)	Mass Fraction		Discharge Coefficient (C_d)	
			Propane	Natural Gas	PREPROP	UCLM
5	27.1	278.75	0.96	0.04	0.60	0.58
5	36.6	278.85	0.96	0.04	0.60	0.58
5	44.9	278.95	0.96	0.04	0.61	0.59
5	52.0	278.95	0.96	0.04	0.61	0.59
5	78.1	280.05	0.96	0.04	0.58	0.56
7	41.1	277.35	0.95	0.05	0.58	0.55
7	53.9	278.05	0.95	0.05	0.59	0.57
7	61.9	278.65	0.95	0.05	0.60	0.57
7	63.4	279.05	0.95	0.05	0.60	0.57
7	26.1	276.85	0.95	0.05	0.60	0.57
7	40.3	283.85	0.94	0.06	0.60	0.58
7	75.1	283.55	0.94	0.06	0.61	0.59

From the results shown in tables 7.3 - 7.6, the following conclusions can be made:

- The UCLM and PREPROP are in good agreement with the maximum difference in the discharge coefficient required by both models being < 5%.
- For mixtures containing less than 0.8 liquid mass fraction, the HEM provides a good approximation. The discharge coefficient needed to match the predicted and experimental data varies from 0.90 for pure single-phase gas flow to about 0.98 when the upstream liquid fraction is 0.8.
- The incompressible-flow (non-choked) model performs fairly accurately for flows of compressed volatile liquids (liquid mass fractions > 0.97) with a discharge coefficient of about 0.60.

No results were presented by Richardson el al. (2006) for two-phase mixtures with upstream liquid mass fraction between 0.8 – 0.97. However, Richardson et al. (2006) pointed out that neither the HEM nor the incompressible flow model was applicable for predicting the release rate of two-phase mixtures falling into this region termed the ‘grey area’.

Figure 7.9 is a summary of the findings of the investigation highlighting the 'grey area' where neither outflow model holds.

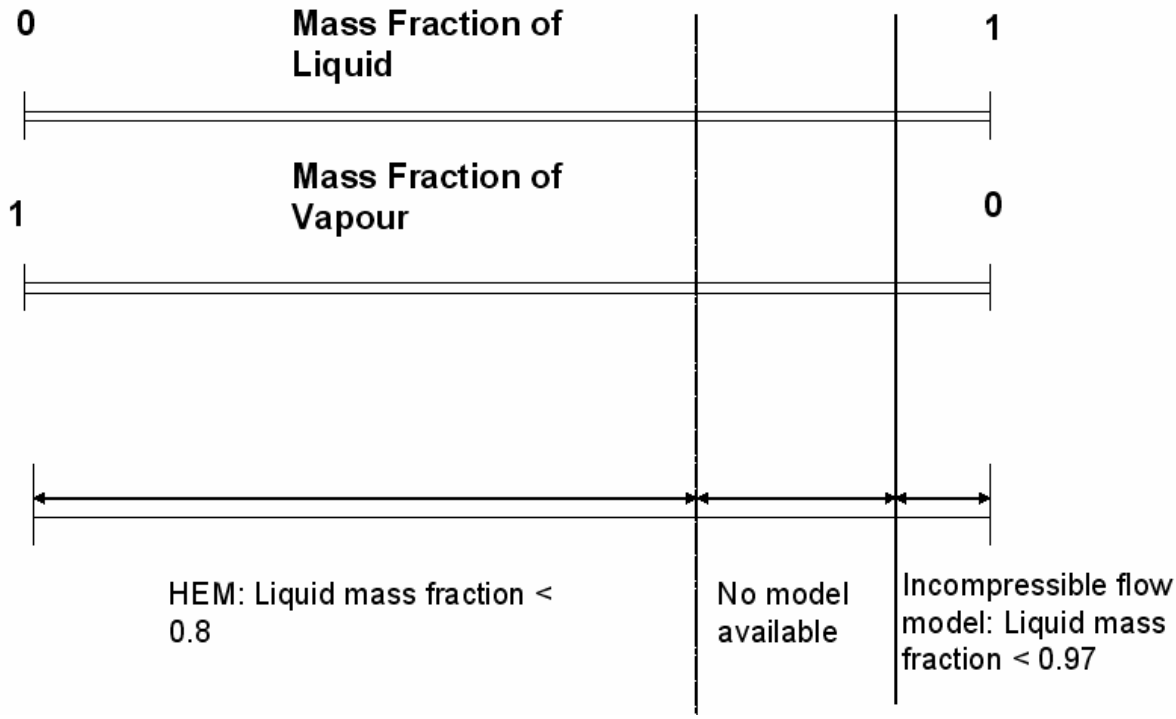

Figure 7.9: Limitations of the Homogeneous Equilibrium Model (HEM).

7.3.2 Model Formulation

Based on the above findings, to address the limitation of the HEM, the following amendments to the discharge rate algorithm presented in section 5.3.1 are made:

- Perform an isothermal flash ($P_j - T_j$) flash to determine the phase split of the fluid entering the orifice.
- Calculate the properties of the fluid at the orifice (P_{o1}, ρ_{o1}, etc.) as described in section 5.3.1 (see figure 5.8).
- If the liquid mass fraction is < 0.8 or equal to 1, the discharge rate is calculated normally using the discharge rate algorithm presented in section 5.3.1.

- If the liquid mass fraction > 0.97 upstream of the orifice, the discharge velocity is calculated using the incompressible flow model. Subsequently, the discharge rate is calculated and the mass balance around the orifice is updated.
- If the liquid mass fraction is > 0.8 but < 0.97, until an appropriate model is developed (heterogeneous flow model) the discharge rate is calculated using the HEM. In section 7.3.4, the justification for choosing the HEM over the incompressible flow model is discussed.

7.3.3 Comparison of the MHEM and HEM

The following presents the comparisons between the MHEM and HEM predictions by simulating the puncture at the end of a 100 m pipeline transporting inventories with upstream liquid mass fractions of 0.95 (termed as the 'grey area' where neither the HEM nor the incompressible model is applicable) and 0.99 (incompressible region). The initial conditions in the pipeline prior to failure are given in table 7.7.

Table 7.7: Pipeline characteristics and prevailing conditions prior to failure of the pipeline.

Length (m)	100
Pipe External Diameter (mm)	168.6
Pipe Wall Thickness (mm)	7.3
Number of Grids	50
Pipe roughness (m)	0.0005
Initial Pressure (bara)	21.6
Initial Temperature (K)	293.15
Ambient Temperature (K)	292.25
Ambient Pressure (K)	1.01

7.3.4 Grey area: Liquid Mass Fraction = 0.95

Figures 7.10 - 7.12 show the results of comparisons between the MHEM and the HEM outflow predictions following the puncture of a 100 m pipeline transporting 25% Methane and 75% Hexane corresponding to a liquid mass fraction of 0.95. The 100 mm puncture diameter is placed at the end of the pipeline. From figure 7.10 it may be observed that the MHEM (curve A) indicates the release pressure instantaneously reaches the ambient pressure (non-choked flow) while the HEM (curve B) produces a gradual depressurisation of the pipeline. Consequently the predicted discharge rate as indicated in figure 7.11 using the MHEM is significantly lower than that predicted using the HEM.

Since neither the HEM nor the MHEM are applicable for such fluids, the HEM is recommended to simulate the outflow from pipelines transporting fluids falling into this category. This is based on the fact that the HEM predicts the 'worst case scenario' corresponding to the highest initial discharge and total mass released.

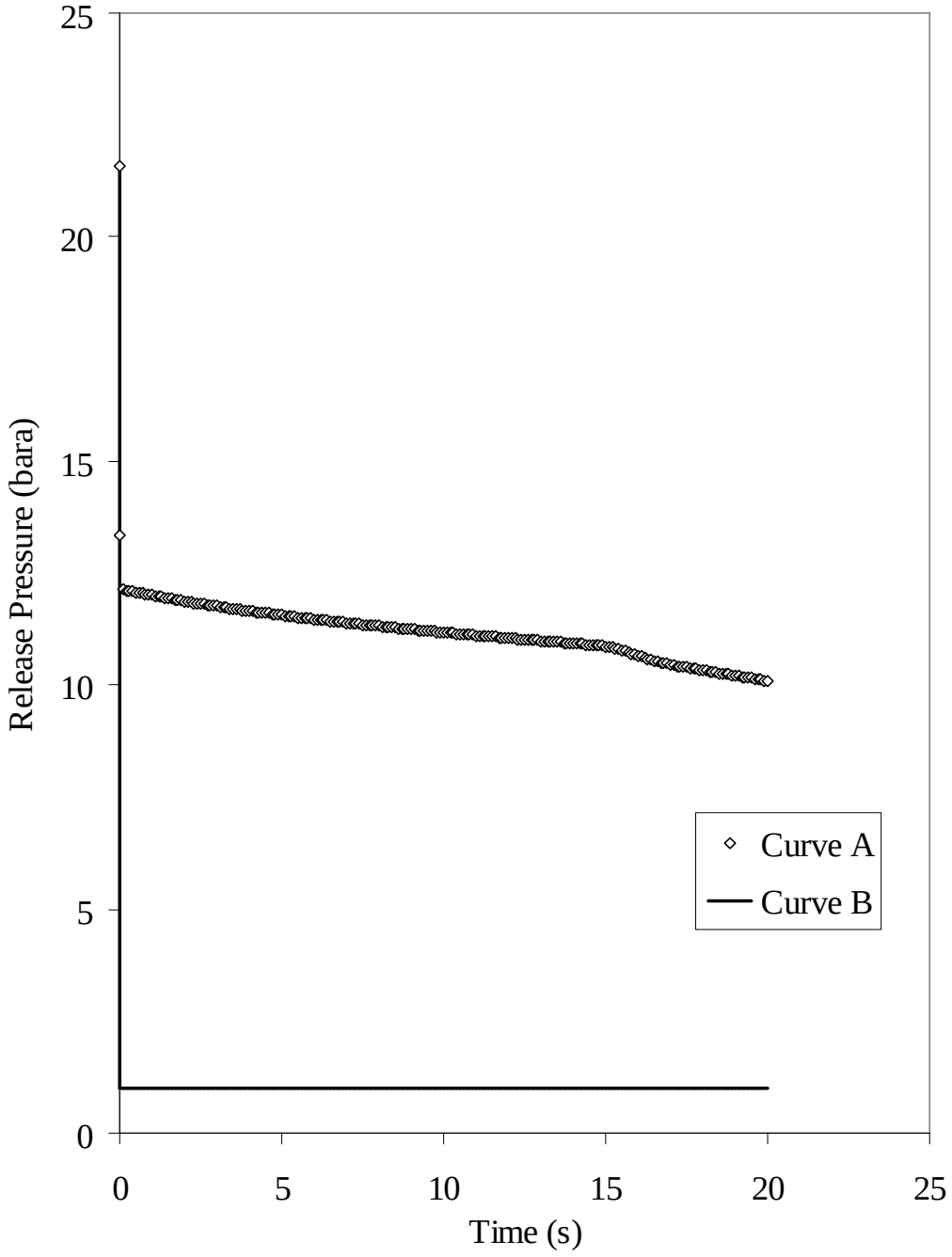

Figure 7.10: Variation of release plane pressure with time for a 100 m pipeline transporting 25% Methane and 75% Hexane with a 100 mm puncture at the end of the pipeline for the Grey area (upstream liquid mass fraction = 0.95).

Curve A – HEM (mass conservation index, ε = 1.01)

Curve B – MHEM (mass conservation index, ε = 0.99)

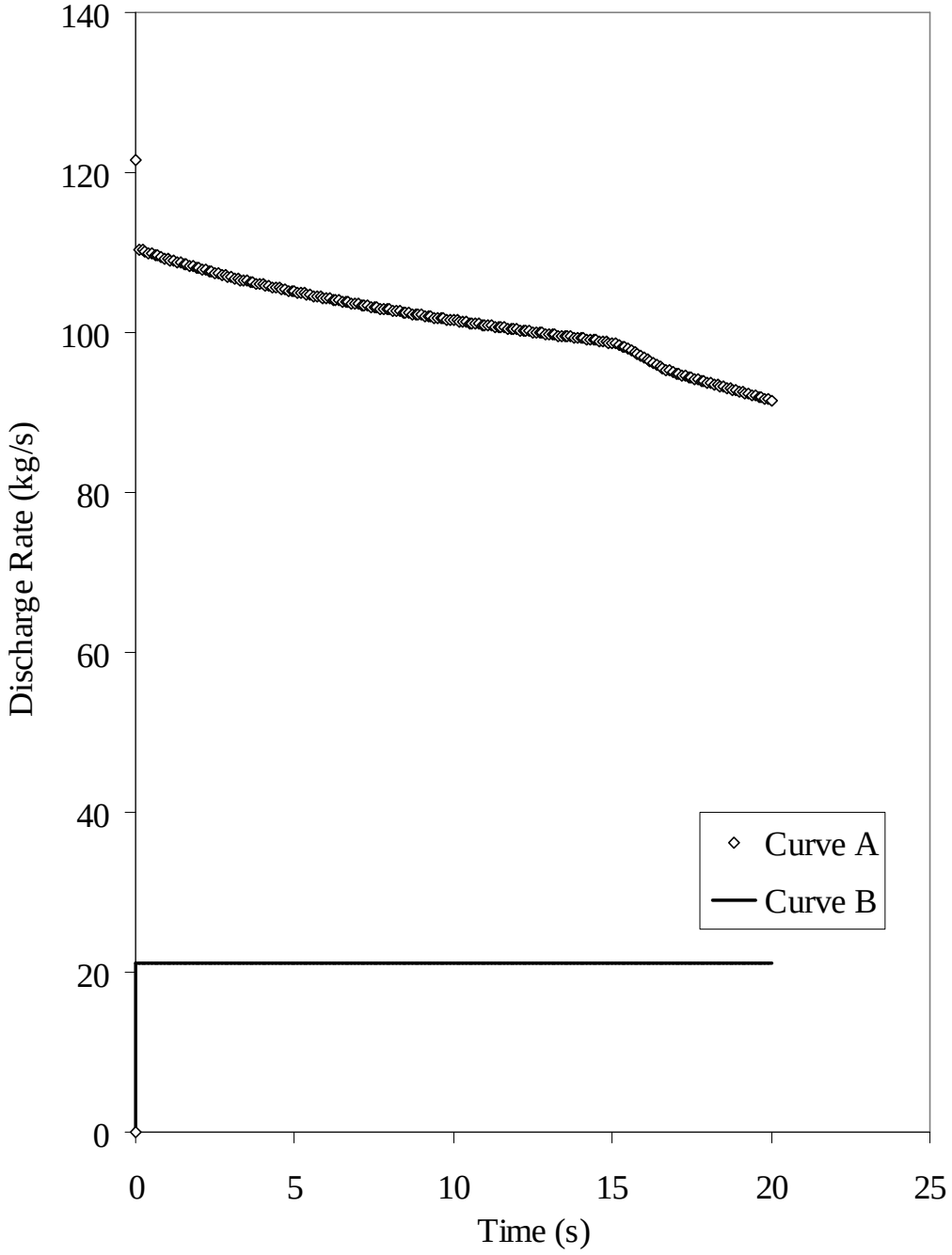

Figure 7.11: Variation of discharge rate with time for a 100 m pipeline transporting 25% Methane and 75% Hexane with a 100 mm puncture at the end of the pipeline for the Grey area (upstream liquid mass fraction = 0.95).

Curve A – HEM (mass conservation index, ε = 1.01)

Curve B – MHEM (mass conservation index, ε = 0.99)

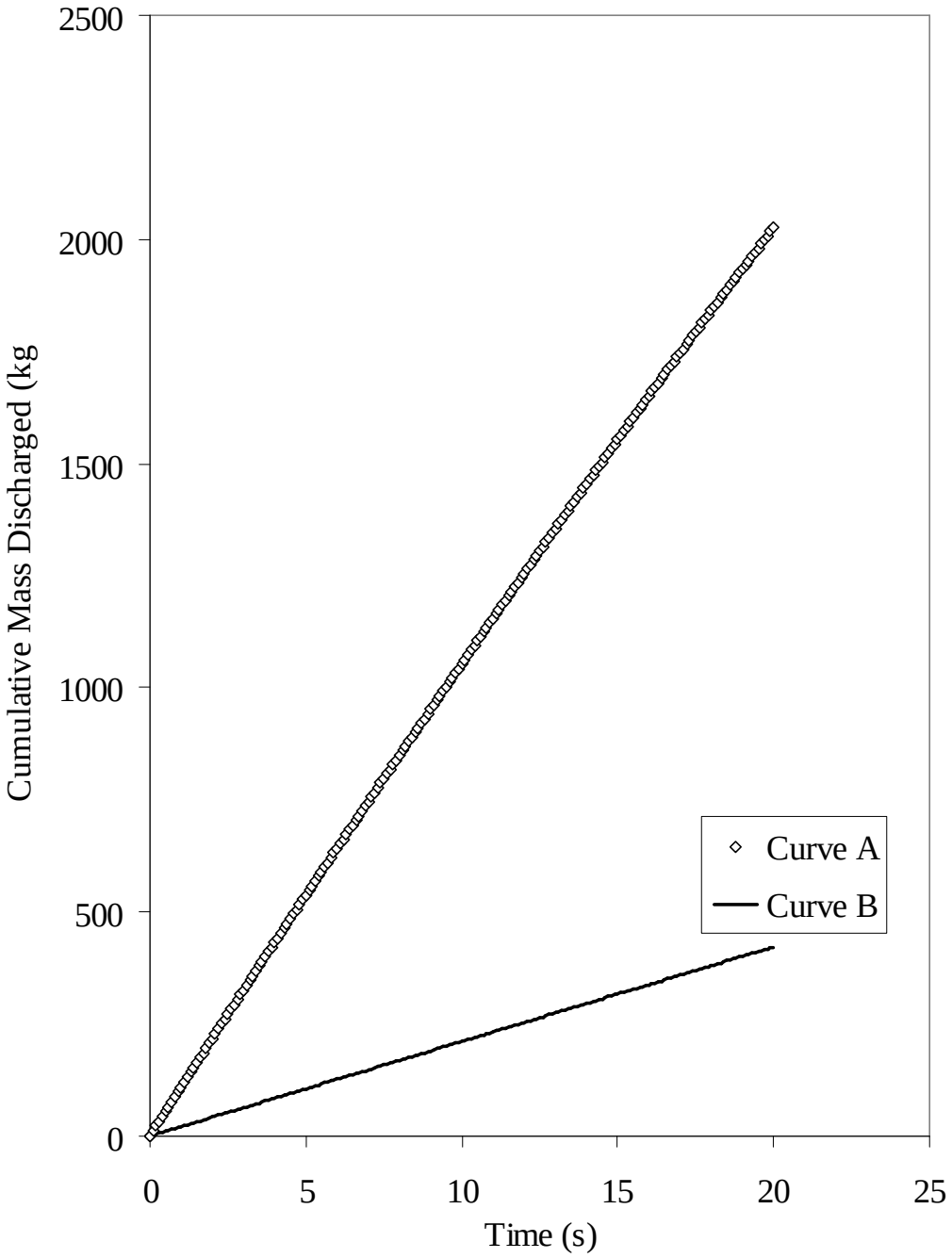

Figure 7.12: Variation of cumulative mass discharged with time for a 100 m pipeline transporting 25% Methane and 75% Hexane with a 100 mm puncture at the end of the pipeline (upstream liquid mass fraction = 0.95).

Curve A – HEM (mass conservation index, ε = 1.01)

Curve B – MHEM (mass conservation index, ε = 0.99)

7.3.5 Incompressible Flow: Liquid Mass Fraction = 0.99

Figures 7.13 - 7.15 show the results of orifice outflow comparisons between the Modified MHEM and the HEM predictions for a 100 m pipeline transporting 1% Methane and 99% Hexane corresponding to an upstream liquid mass fraction of 0.99. Referring to figure 7.13, since the inventory in the pipeline is initially liquid both the HEM (curve A) and the MHEM (curve B) produce the expected instantaneous significant initial drop in pressure. However, the HEM (curve A) predicts a choke pressure of 1.89 bara following which the fluid flashes to a two-phase mixture manifested in the step change in pressure. Consequently, the corresponding discharge rate as indicated in figure 7.14 and the cumulative mass discharged; figure 7.15, as predicted form both models are significantly different. MHEM (curve B) predicts a higher initial flow rate as compared with HEM (c.f 152 kg/s with 62 kg/s). However the trend is reversed in the subsequent time domain.

Additionally, the MHEM (curve B) predicts no further loss of inventory after complete depressurisation of the pipeline after 4s. In comparison, due to choked conditions existing at the failure plane, the HEM continues to predict loss of inventory as the pipeline is still pressurised. This leads to significant over prediction of the total mass released as indicated in figure 7.15. After 20s the HEM predicts 780 kg of inventory released as compared to 190 kg based on MHEM.

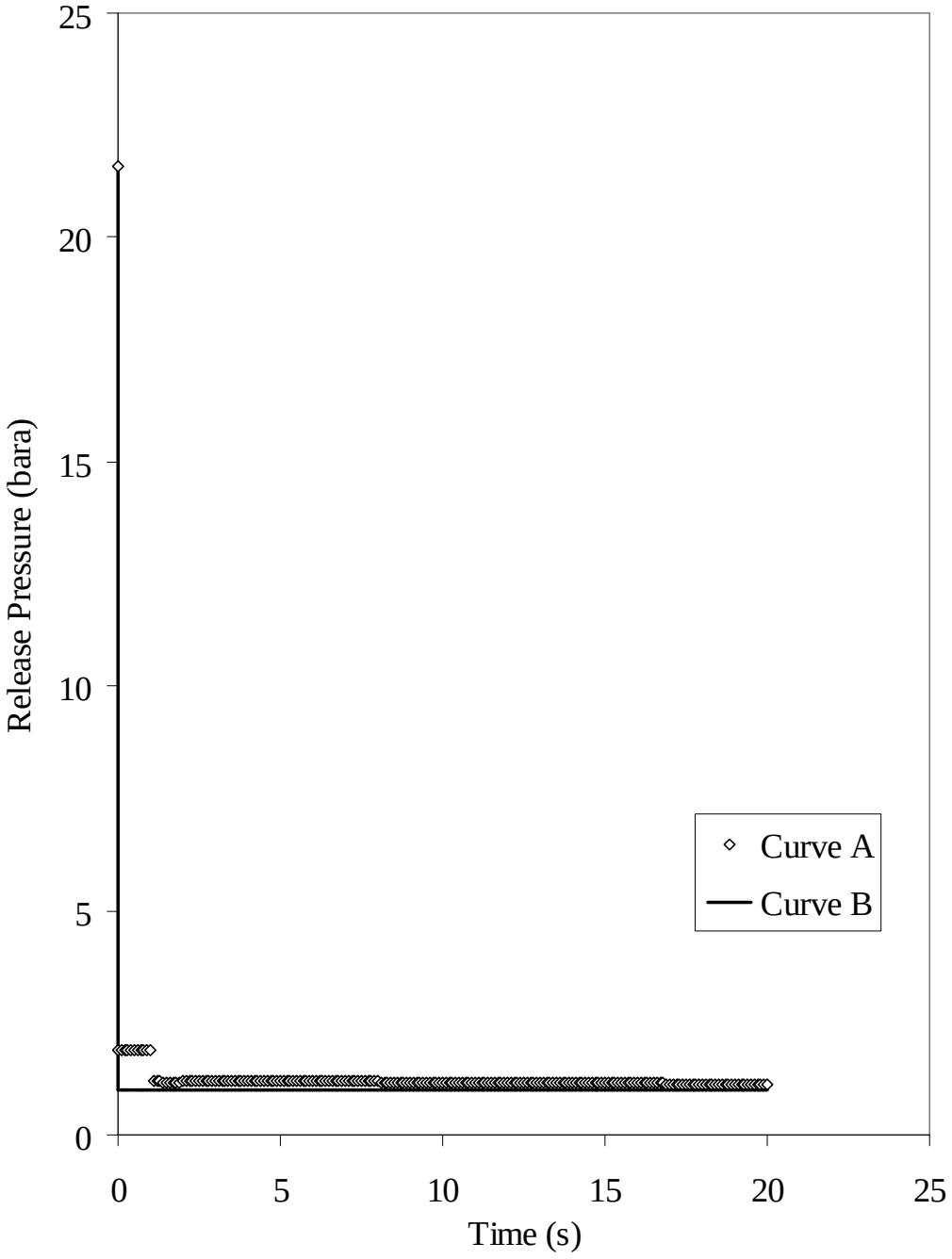

Figure 7.13: Variation of release plane pressure with time for a 100 m pipeline transporting 1% Methane and 99% Hexane with a 100 mm puncture at the end of the pipeline (upstream liquid mass fraction = 0.99).

Curve A – HEM (mass conservation index, $\varepsilon = 0.98$)

Curve B – MHEM (mass conservation index, $\varepsilon = 0.98$)

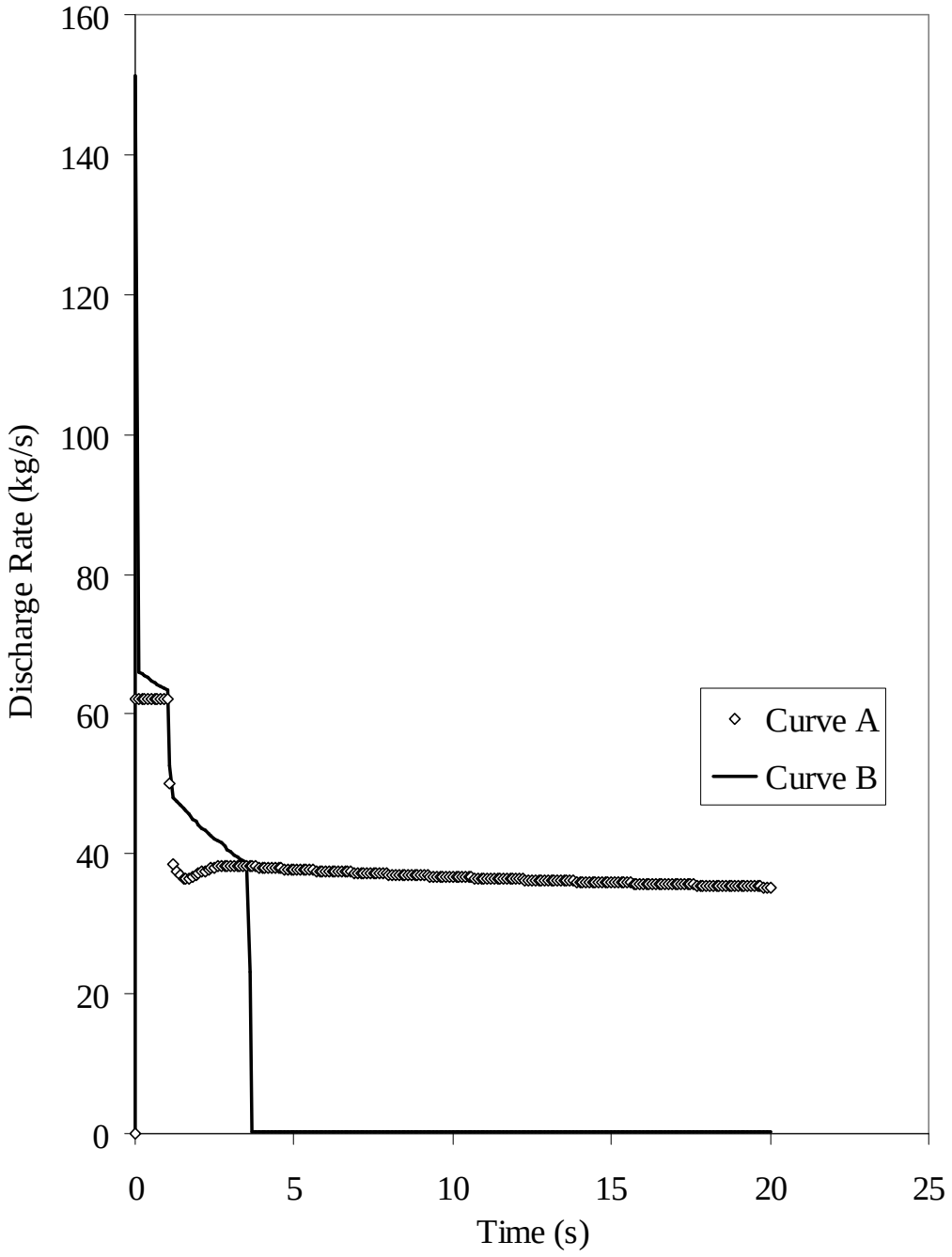

Figure 7.14: Variation of discharge rate with time for a 100 m pipeline transporting 1% Methane and 99% Hexane with a 100 mm puncture at the end of the pipeline (upstream liquid mass fraction = 0.99).

Curve A – HEM (mass conservation index, $\varepsilon = 0.98$)

Curve B – MHEM (mass conservation index, $\varepsilon = 0.98$)

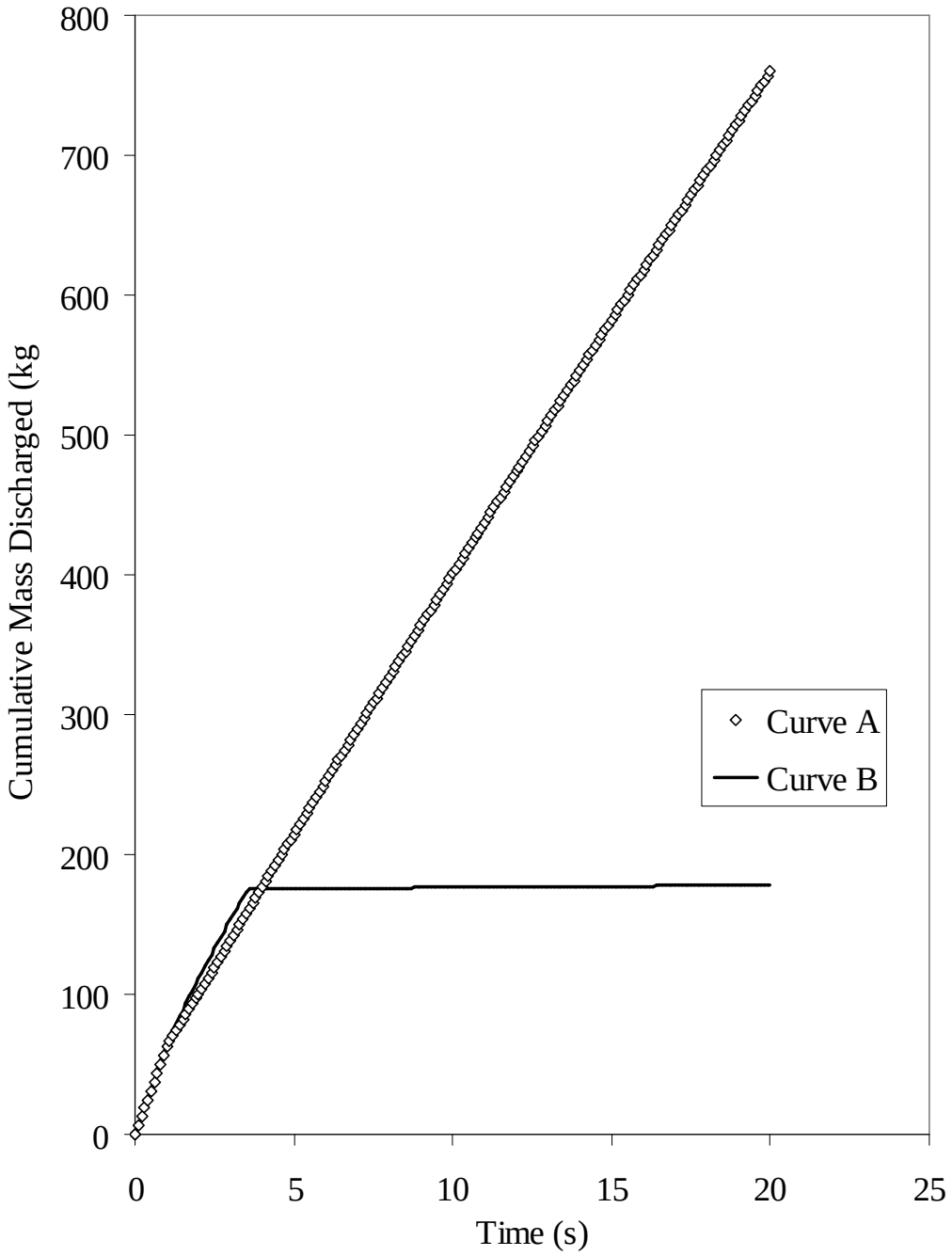

Figure 7.15: Variation of cumulative mass discharged with time for a 100 m pipeline transporting 1% Methane and 99% Hexane with a 100 mm puncture at the end of the pipeline (upstream liquid mass fraction = 0.99).

Curve A – HEM (mass conservation index, $\varepsilon = 0.98$)

Curve B – MHEM (mass conservation index, $\varepsilon = 0.98$)

7.4 Concluding Remarks

This chapter presented the formulation and validation of the Hybrid Model and the MHEM developed to address limitations in the HEM.

The Hybrid Model, based on coupling the HEM with a hydraulic model was shown to addresses a principal limitation of the HEM model by accounting for the post depressurisation hydrodynamic discharge from inclined pipelines.

The Hybrid Model takes account of the fact that during the early stages of blowdown, the pressure forces are dominant and hence the HEM model is applicable. Once the line pressure reaches atmospheric pressure, the remaining outflow will be primarily due to the hydrodynamic head at which point a hydraulic outflow model is employed.

Outflow simulation results following the full bore rupture of a 100 m long 0.154 m diameter pipeline containing various classes of hydrocarbons at different angles of decline were presented and discussed.

In the case of flashing liquid inventories in declining pipelines, the HEM model under predicts the amount of inventory loss as compared to the Hybrid model as it fails to account for the discharge of the remaining liquid in the pipeline following its depressurisation to 1 bara. Also, the rate of discharge prior to the pressure equilibration of the pipeline does not depend on the angle of decline. This is consistent with pressure forces as opposed to the gravitational field effect being the dominant driving force in discharging the inventory during this initial period. The post depressurisation discharge rate is however markedly affected by the angle of decline.

Similar trends are also observed for compressed liquids with the exception of the differences between the predictions between the two models being much more pronounced than those for the compressed volatile liquid. HEM only accounts for the loss of liquid due to its finite and very rapid expansion from the line pressure to 1bara.

In contrast, the presence of a relatively small proportion of gas in the liquid resulted in a dramatic change in behaviour with the rate of loss of inventory no longer being dependent on the angle of decline. The results of the investigations indicate that the entire liquid inventory is discharged by the gas by the time the line is depressurised to 1 bara.

In the second part of the study, the limitations of the homogenous equilibrium model with respect to the blowdown of pipelines conveying flashing/ two-phase fluids discharging through a small orifice were highlighted. The results of the MHEM developed to address this limitation were presented and discussed.

Comparison of the discharge rates predicted by the outflow model and the experimental data presented by Richardson et al. (2006) show that:

- UCLM is in good agreement with PREPROP for all mixtures with the maximum difference being < 5%.
- For mixtures containing less than 0.8 liquid mass fraction, the HEM provides a good approximation. The discharge coefficient needed to match the predicted and experimental data varies from 0.90 for pure single-phase gas flow to about 0.98 when the upstream liquid fraction is 0.8.
- The incompressible-flow (non-choked) model performs fairly accurately for flows of compressed volatile liquids (liquid mass fractions > 0.97) with a discharge coefficient of about 0.60.

Comparisons of the MHEM and the HEM outflow prediction following the puncture of a 100 m pipeline transporting 25% Methane and 75% Hexane corresponding to a liquid mass fraction of 0.95 (‘grey area’) were made. The results showed that HEM predicts the ‘worst case scenario’ corresponding to the highest initial discharge and total mass released. Consequently, the HEM is recommended to simulate the outflow from pipelines transporting fluids falling into this category, as neither the HEM nor the MHEM are applicable for such fluids.

Similar comparisons were performed between the MHEM and the HEM predictions for a 100 m pipeline transporting 1% Methane and 99% Hexane corresponding to a

liquid mass fraction of 0.99 (incompressible region). The results indicated that the HEM significantly over predicted the total mass released from the pipeline. This was due to the HEM treating the fluid as a two-phase mixture undergoing choked flow with a sustained discharge from the pipeline.

CHAPTER 8: CFL IMPACT ON NUMERICAL CONVERGENCE

8.1 Introduction

The numerical instabilities when simulating outflow are generally avoided by ensuring the Courant, Friedrichs and Lewy (CFL) condition (Courant et al.,1926; Zucrow and Hoffman, 1976) which limits the maximum allowable discretisation time steps. From section 4.2.2, the corresponding time step (Δt) is given by:

$$\Delta t = \frac{\Delta x}{(|u+a|_{\max})_{t=0}} \qquad (4.4)$$

Where, Δx is the discretisation distance.

u and *a* are the maximum values of the velocity and speed of sound along the length of the pipeline respectively.

Significantly, the CFL limitation is only a necessary condition for stability, but it is not sufficient to ensure it (Leveque, 2002). This is especially the case during rapid changes in fluid properties such as those encountered near the pipeline rupture plane or when crossing depressurisation induced phase transition boundaries.

To address this limitation, CFL factors (C_f) varying in the range $0 < C_f \leq 1$ are used to multiply the maximum time step, Δt. However, this is at the cost of increasing the computational run time. A deceptively logical assumption is that the use of the smaller discretisation time steps will necessarily increase the accuracy and convergence of the numerical solution scheme. In this section, the impact of the CFL factor (C_f) on the numerical convergence and stability of the pipeline rupture outflow simulation results based on a case example is investigated.

8.2 Results and Discussion

Table 8.1 presents the pipeline characteristics and the prevailing conditions used for investigating the impact of the CFL factor on discharge predictions.

Table 8.1: Pipeline characteristics and prevailing conditions prior to failure of the pipeline.

Pipe length (m)	100
Pipe internal diameter (mm)	154
Pipe wall thickness (mm)	7.3
Pipe wall roughness (m)	0.0005
Initial line pressure (bara)	21.6
Initial line temperature (K)	293.15
Ambient temperature (K)	292.25
Ambient pressure (bara)	1.01

The CFL factors investigated are in the range 0.2 - 0.9 at 0.1 intervals. Failure is assumed to be in the form of a 50 mm puncture midway along the 100 m long 0.154m i.d. pipeline. Different classes of inventories are considered including a permanent gas, two-phase mixtures and a permanent liquid.

8.2.1 Permanent Gas

Figure 8.1 shows the variation of computational runtime against CFL factor for the complete depressurisation of the 100 m pipeline containing 100% Methane. For the conditions tested, Methane remains in the gaseous phase throughout depressurisation. As it may be observed, the variation between the two parameters is hyperbolic with

computational run time increasing rapidly for CFL factors below 0.5. The trends for CFL factors of less than 0.2 were not investigated due to the long computational run times. The observed hyperbolic behaviour in the computational run time is characteristic of all the subsequent mixtures investigated.

Figures 8.2 and 8.3 respectively show the corresponding variations of release pressure and cumulative mass discharged with time using different values of CFL factors. As it may be observed, a reduction in the CFL factor has no impact on the data obtained. As such there is no incentive in using CFL factors of less than 0.9 as this will only lead to a significant increase in the computational run time with no impact on the data.

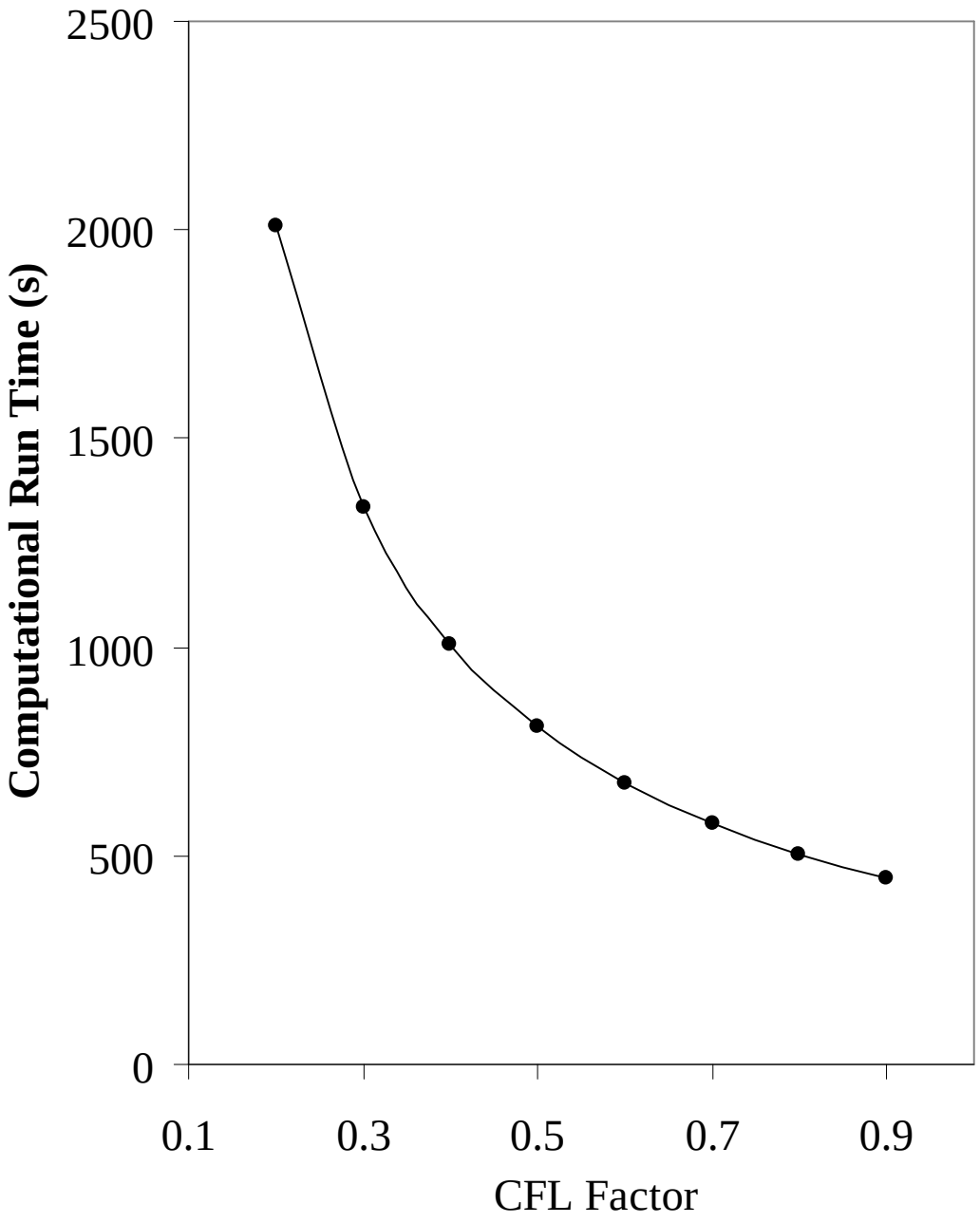

Figure 8.1: Variation of computational runtime with CFL factor for a permanent gas, Methane (mass conservation index, ε = 0.99).

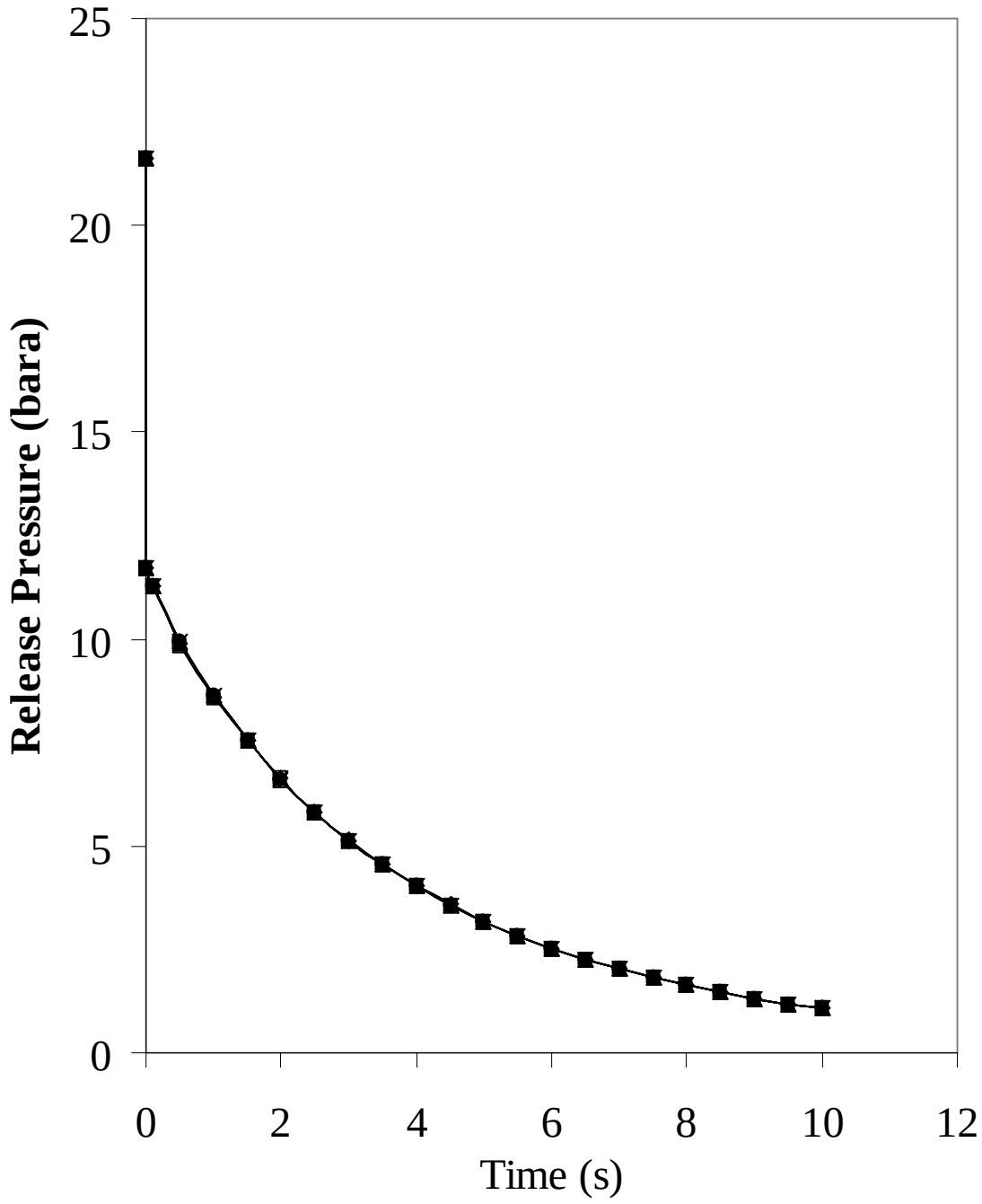

Figure 8.2: Variation of release pressure with time for the permanent gas inventory, Methane following puncture at various CFL factors in the range 0.2 – 0.9 at 0.1 intervals.

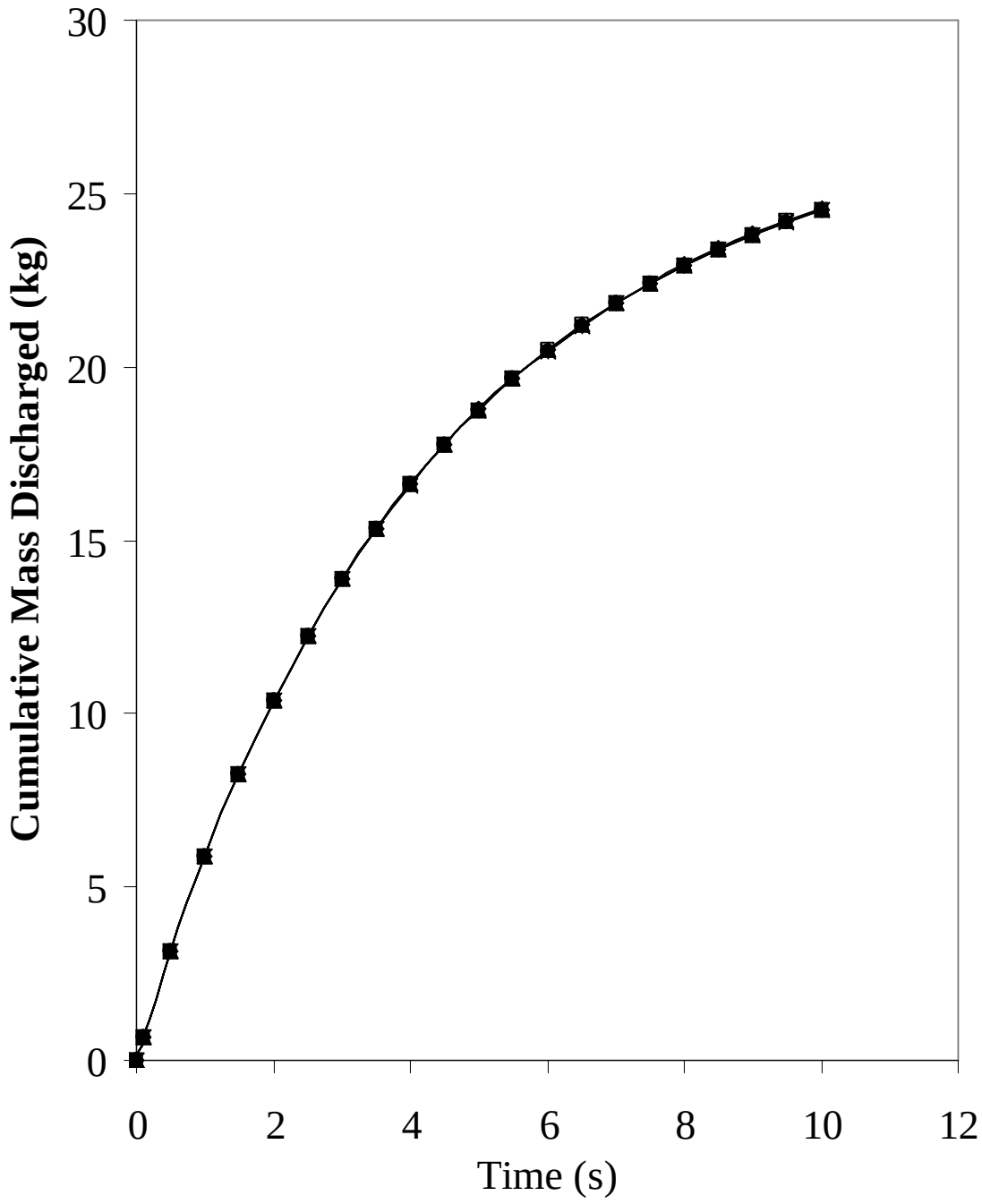

Figure 8.3: Variation of cumulative mass discharged with time for the permanent gas inventory, Methane following puncture at various CFL factors in the range 0.2 – 0.9 at 0.1 intervals.

8.2.2 Two-Phase Mixtures and Permanent Liquids

The CFL sensitivity analysis for pipelines transporting two-phase mixtures is divided into the following categories of inventories:

i) Flashing liquid mixture and pure flashing liquid
ii) Equi-molar liquid/gas mixture; 50% n-Pentane and 50% Methane
iii) Gas rich mixture; 5% n-Pentane and 95% Methane

Figure 8.4 shows the variation in release pressure with time following puncture at various CFL factors for a flashing liquid mixture comprising 95% Hexane and 5% Methane. Figure 8.5 shows the corresponding variations of the cumulative mass discharged against time.

Figures respectively show 8.6 and 8.7 the pressure and mass release data for the pure flashing liquid, Propane.

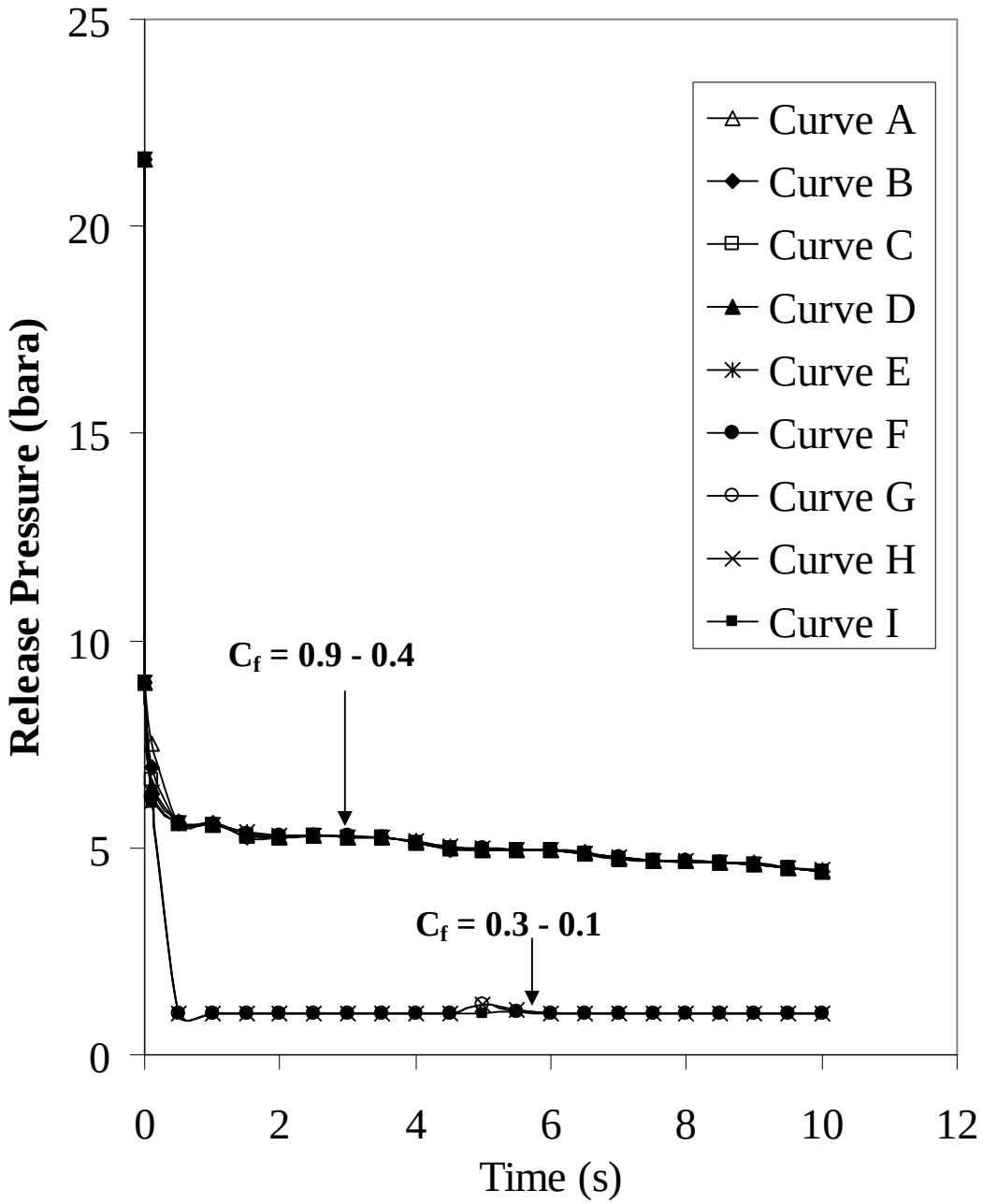

Figure 8.4: Variation of release pressure with time for 95% Hexane and 5% Methane following puncture at various CFL factors in the range 0.2 – 0.9 at 0.1 intervals.

Curve A: C_f = 0.9 Curve D: C_f = 0.6 Curve G: C_f = 0.3

Curve B: C_f = 0.8 Curve E: C_f = 0.5 Curve H: C_f = 0.2

Curve C: C_f = 0.7 Curve F: C_f = 0.4

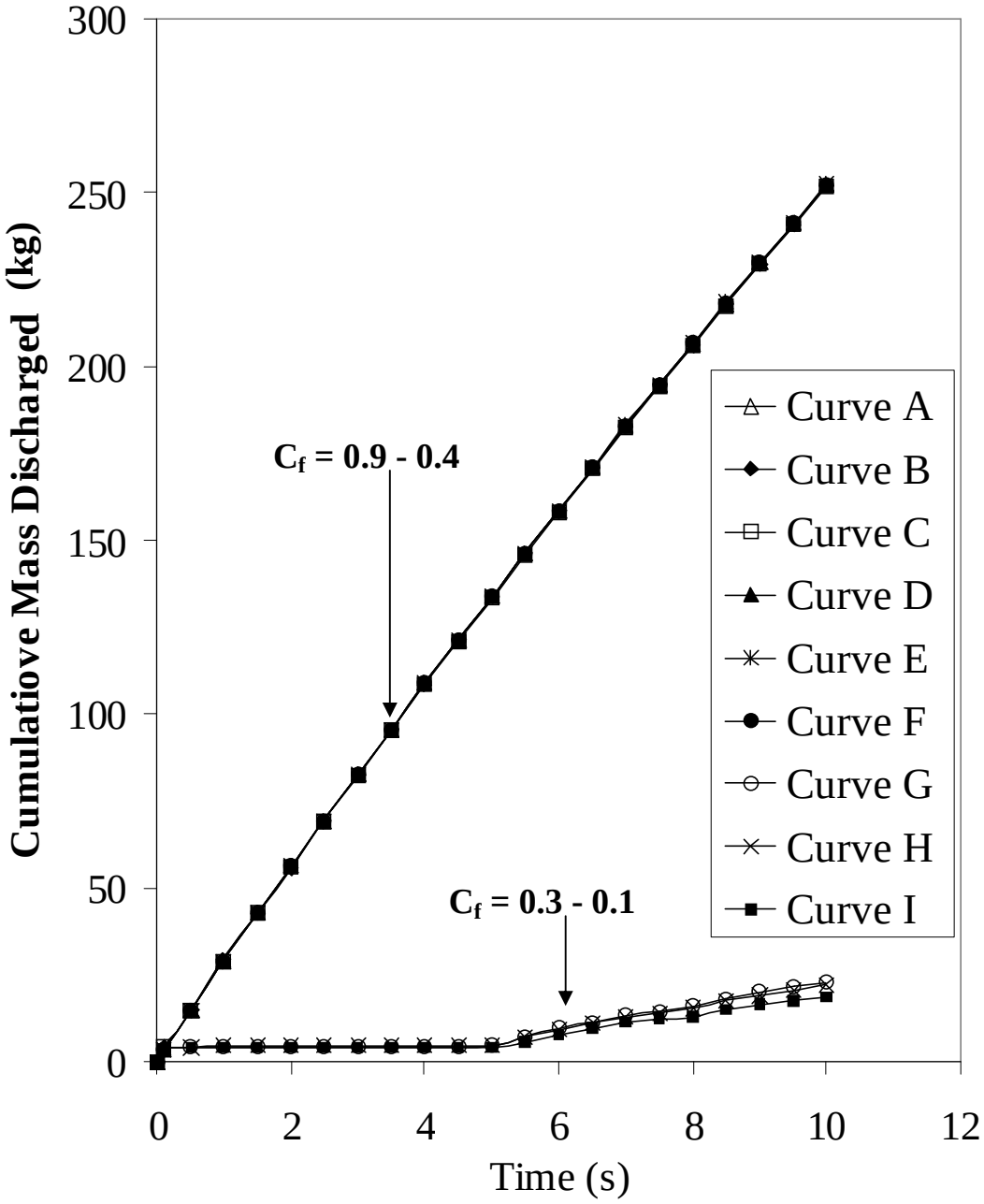

Figure 8.5: Variation of cumulative mass with time for 95% Hexane and 5% Methane following puncture at various CFL factors in the range 0.2 – 0.9 at 0.1 intervals.

Curve A: C_f = 0.9 Curve D: C_f = 0.6 Curve G: C_f = 0.3

Curve B: C_f = 0.8 Curve E: C_f = 0.5 Curve H: C_f = 0.2

Curve C: C_f = 0.7 Curve F: C_f = 0.4

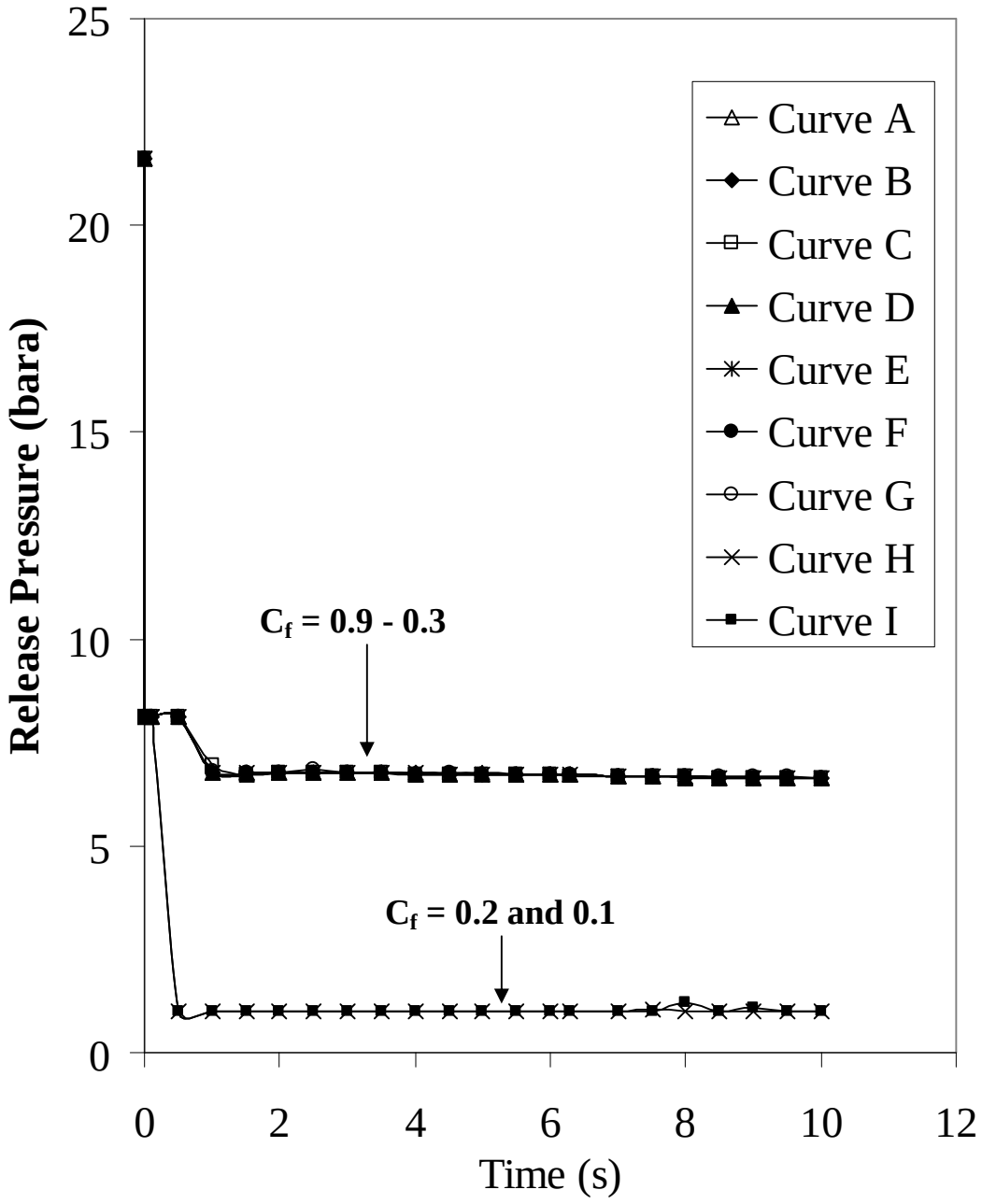

Figure 8.6: Variation of release pressure with time for the flashing liquid, 100% Propane following puncture at various CFL factors in the range 0.2 – 0.9 at 0.1 intervals.

Curve A: C_f = 0.9
Curve B: C_f = 0.8
Curve C: C_f = 0.7
Curve D: C_f = 0.6
Curve E: C_f = 0.5
Curve F: C_f = 0.4
Curve G: C_f = 0.3
Curve H: C_f = 0.2

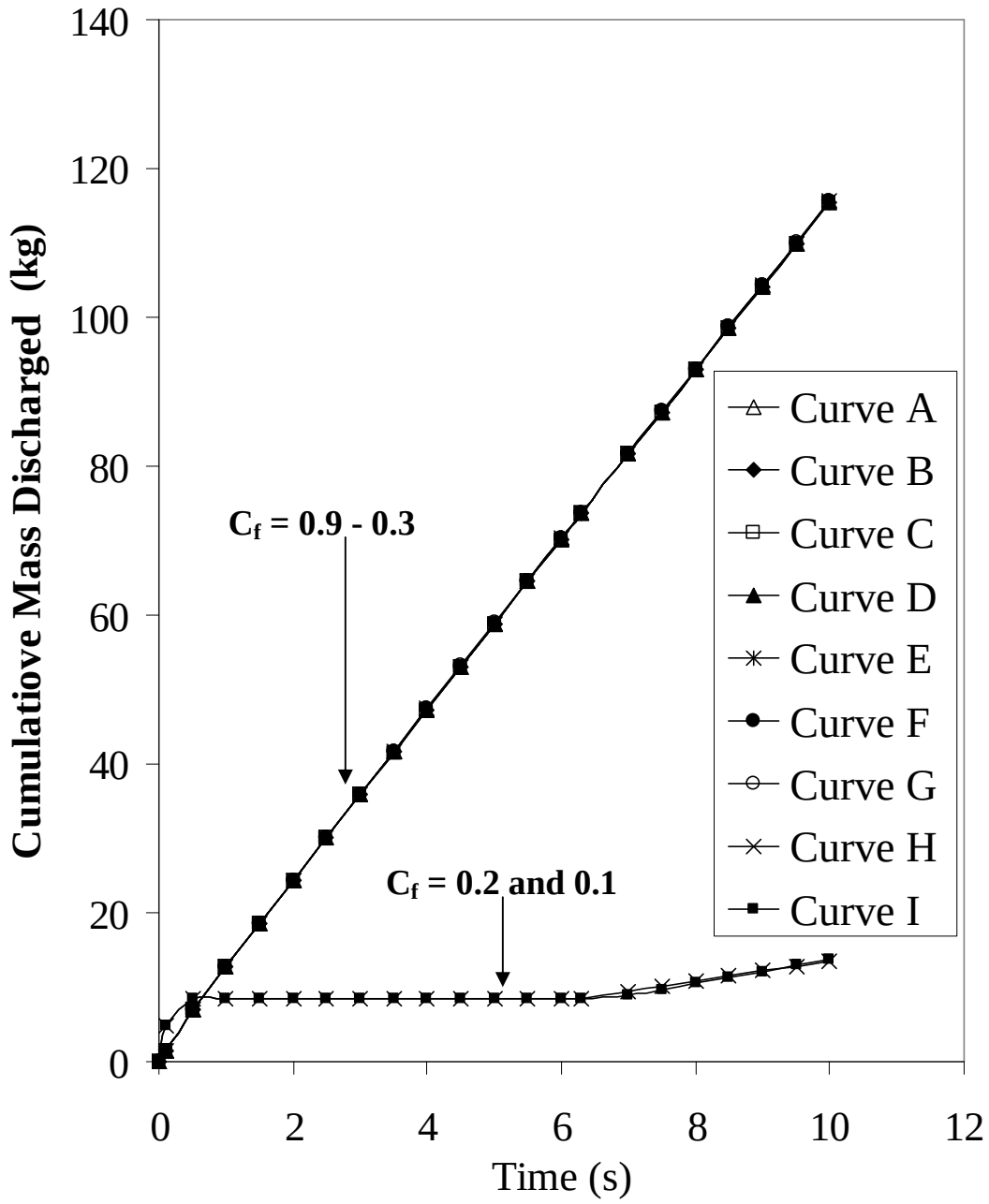

Figure 8.7: Variation of cumulative mass with time for the flashing liquid, 100% Propane following puncture at various CFL factors in the range 0.2 – 0.9 at 0.1 intervals.

Curve A: C_f = 0.9 Curve D: C_f = 0.6 Curve G: C_f = 0.3

Curve B: C_f = 0.8 Curve E: C_f = 0.5 Curve H: C_f = 0.2

Curve C: C_f = 0.7 Curve F: C_f = 0.4

As it may be observed, for both flashing inventories, during the first ca 0.25 s following failure, the pressure and the discharge data are independent of the CFL factor. However the data at the subsequent time interval are strongly dependent on the CFL factor converging into two distinct bands. Identical behaviours were observed for other flashing liquid mixtures (e.g 95% Octane and 5% Methane) and pure flashing liquids (e.g Ethylene).

An examination of the fluid phases reveals that the onset of CFL dependency in the data coincides with the transition of the liquid inventory into a two-phase mixture. This results in a liquid/two-phase boundary (boiling boundary) propagating from the orifice location towards the intact end of the pipeline.

The substantial difference in acoustic velocities across the moving interface (c.f 840 m/s in liquid (Hexane); 39 m/s in vapour (Methane) at 21.6 bara and 20 ^{o}C (Huber, 1999) results in significant refraction in the characteristic lines as schematically represented in figure 8.8 for a left travelling interface. Consequently, the propagation velocity of the positive characteristic and hence its gradient ($\Delta t/\Delta x$) will be significantly greater in the two-phase mixture as compared to the liquid. As such the assumption that the fluid properties vary linearly within a grid leads to significant errors as schematically represented by, $\Delta\xi$ in figure 8.8. Clearly, $\Delta\xi$ will be a function of the discretisation time step, Δt and hence C_f.

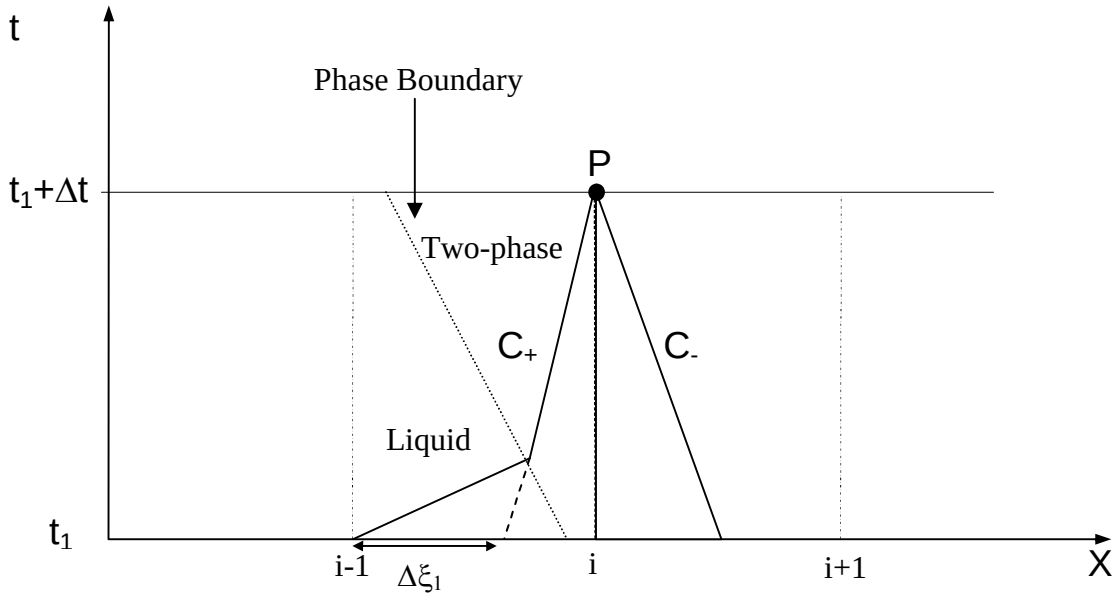

Figure 8.8: Refraction of the characteristic lines at a liquid/2-phase interface for a two component flashing liquid.

Despite satisfying the CFL criterion, it is clear that the constant marginal cumulative mass release data presented (e.g figures 8.5 and 8.7) for C_f in the range 0.1 – 0.3 are unrealistic and may therefore be ignored.

Figures 8.9 and 8.10 show the variations of release pressure and cumulative mass discharged with time using different values of C_f for equi-molar liquid/gas mixture comprising 50% n-Pentane and 50% Methane. Figures 8.11 – 8.14 show the corresponding data for the gas rich mixture comprising 5% n-Pentane and 95% Methane and a permanent liquid, n-Hexane. It is clear that for all above cases tested, reducing C_f has no impact on the results obtained. Given the significant increase in the computational run time with a reduction in C_f, there is no incentive in using C_f values of less than 0.9 for such inventories. In the case of the permanent liquid inventory, the almost instantaneous drop in the line pressure (figure 8.13) following pipeline failure is characteristic of liquids due to their negligible compressibility.

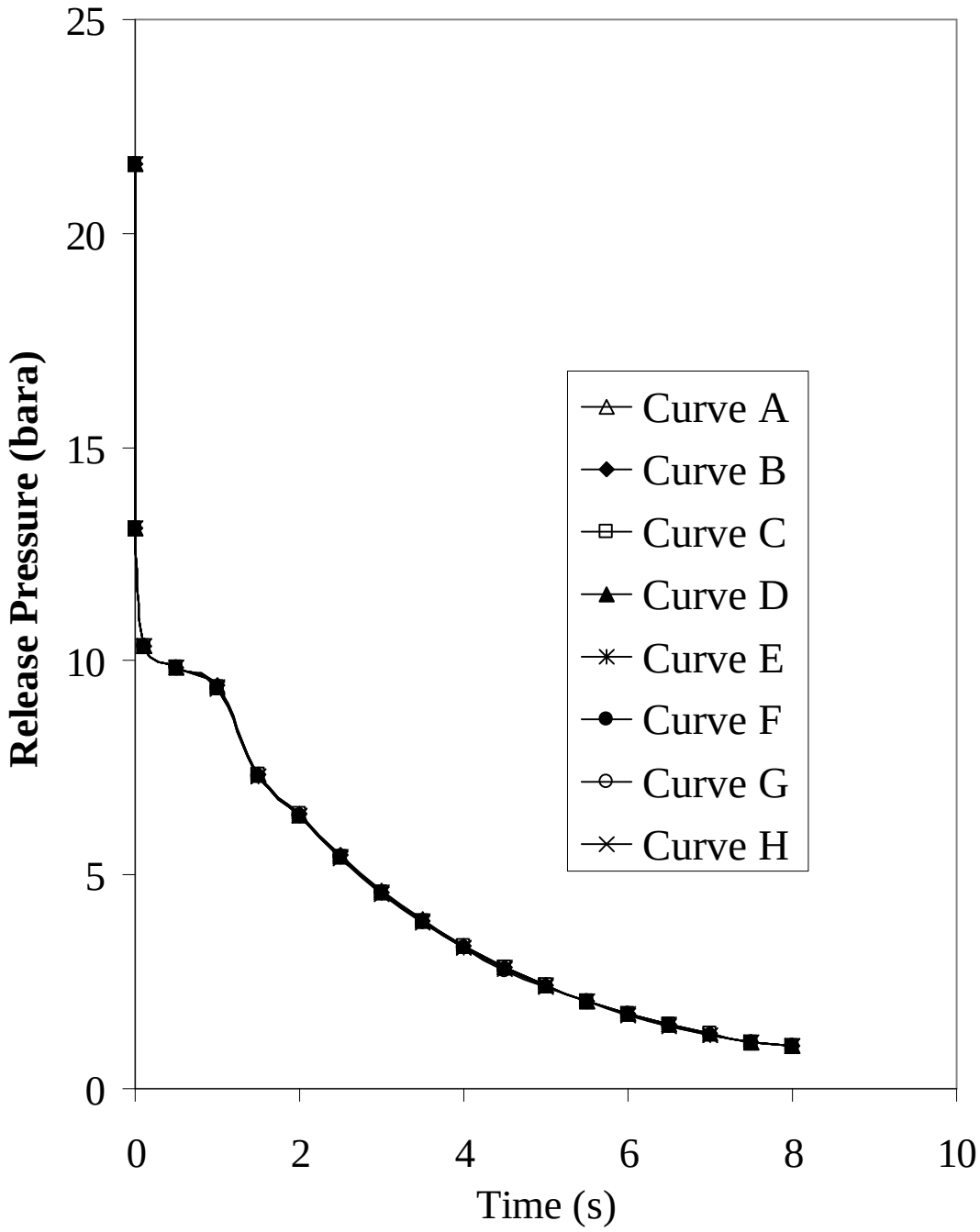

Figure 8.9: Variation of release pressure with time for 50% Methane and 50% n-Pentane following puncture at various CFL factors in the range 0.2 – 0.9 at 0.1 intervals.

Curve A: $C_f = 0.9$ Curve D: $C_f = 0.6$ Curve G: $C_f = 0.3$

Curve B: $C_f = 0.8$ Curve E: $C_f = 0.5$ Curve H: $C_f = 0.2$

Curve C: $C_f = 0.7$ Curve F: $C_f = 0.4$

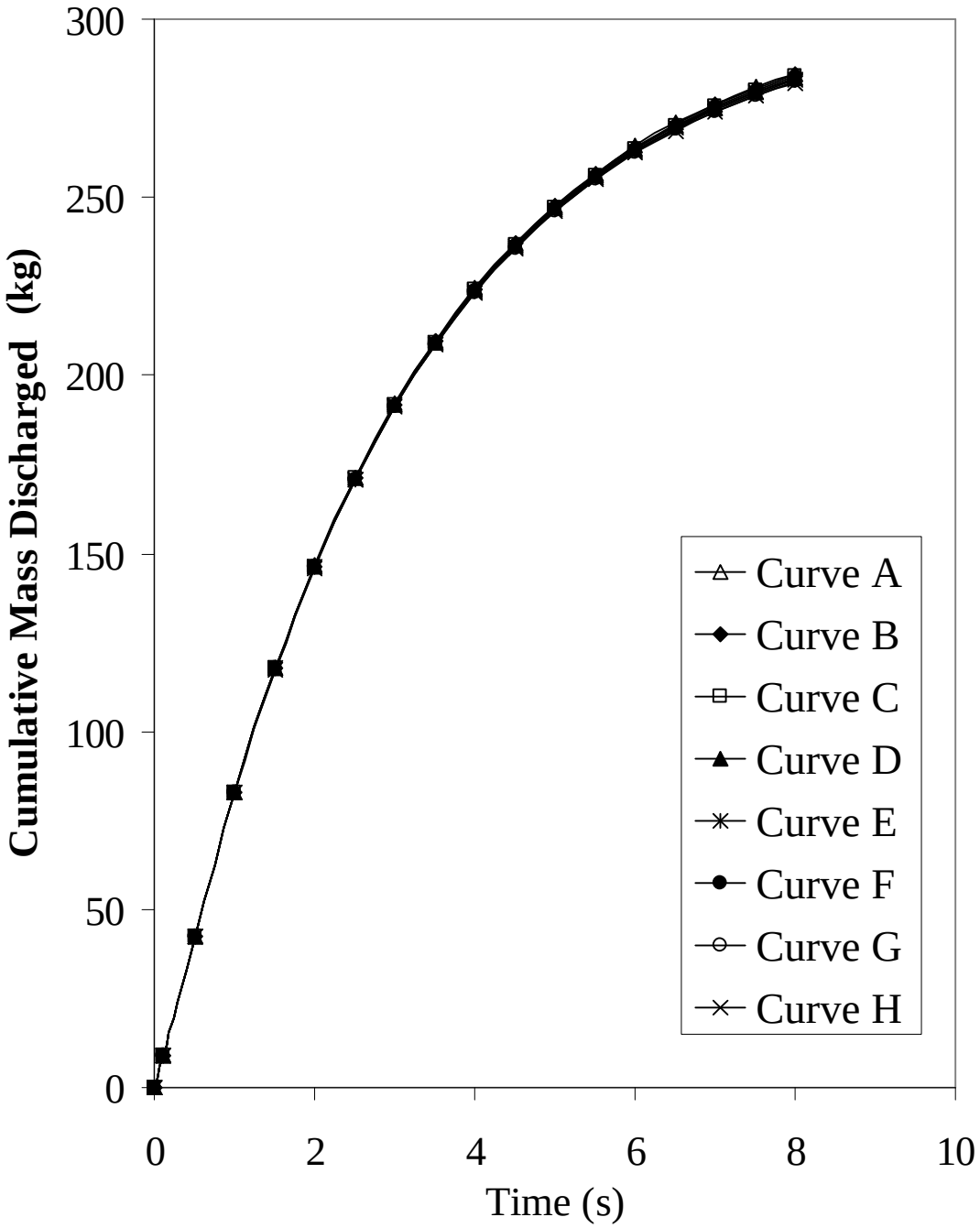

Figure 8.10: Variation of cumulative mass with time for 50% Methane and 50% n-Pentane following puncture at various CFL factors in the range 0.2 – 0.9 at 0.1 intervals.

Curve A: $C_f = 0.9$ Curve D: $C_f = 0.6$ Curve G: $C_f = 0.3$

Curve B: $C_f = 0.8$ Curve E: $C_f = 0.5$ Curve H: $C_f = 0.2$

Curve C: $C_f = 0.7$ Curve F: $C_f = 0.4$

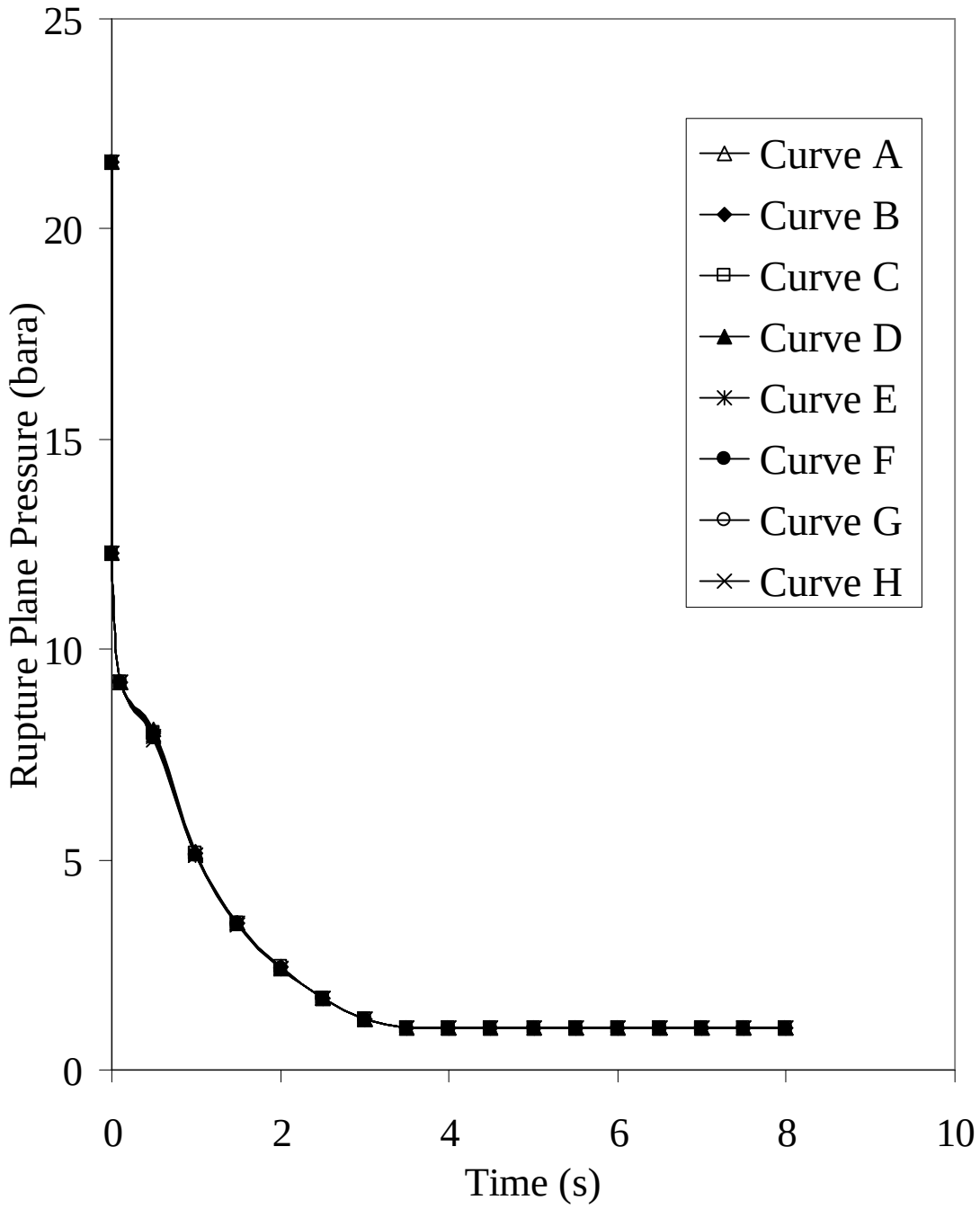

Figure 8.11: 100m pipeline transporting 95% Methane and 5% n-Pentane following puncture at various CFL factors in the range 0.2 – 0.9 at 0.1 intervals.

Curve A: $C_f = 0.9$ Curve D: $C_f = 0.6$ Curve G: $C_f = 0.3$

Curve B: $C_f = 0.8$ Curve E: $C_f = 0.5$ Curve H: $C_f = 0.2$

Curve C: $C_f = 0.7$ Curve F: $C_f = 0.4$

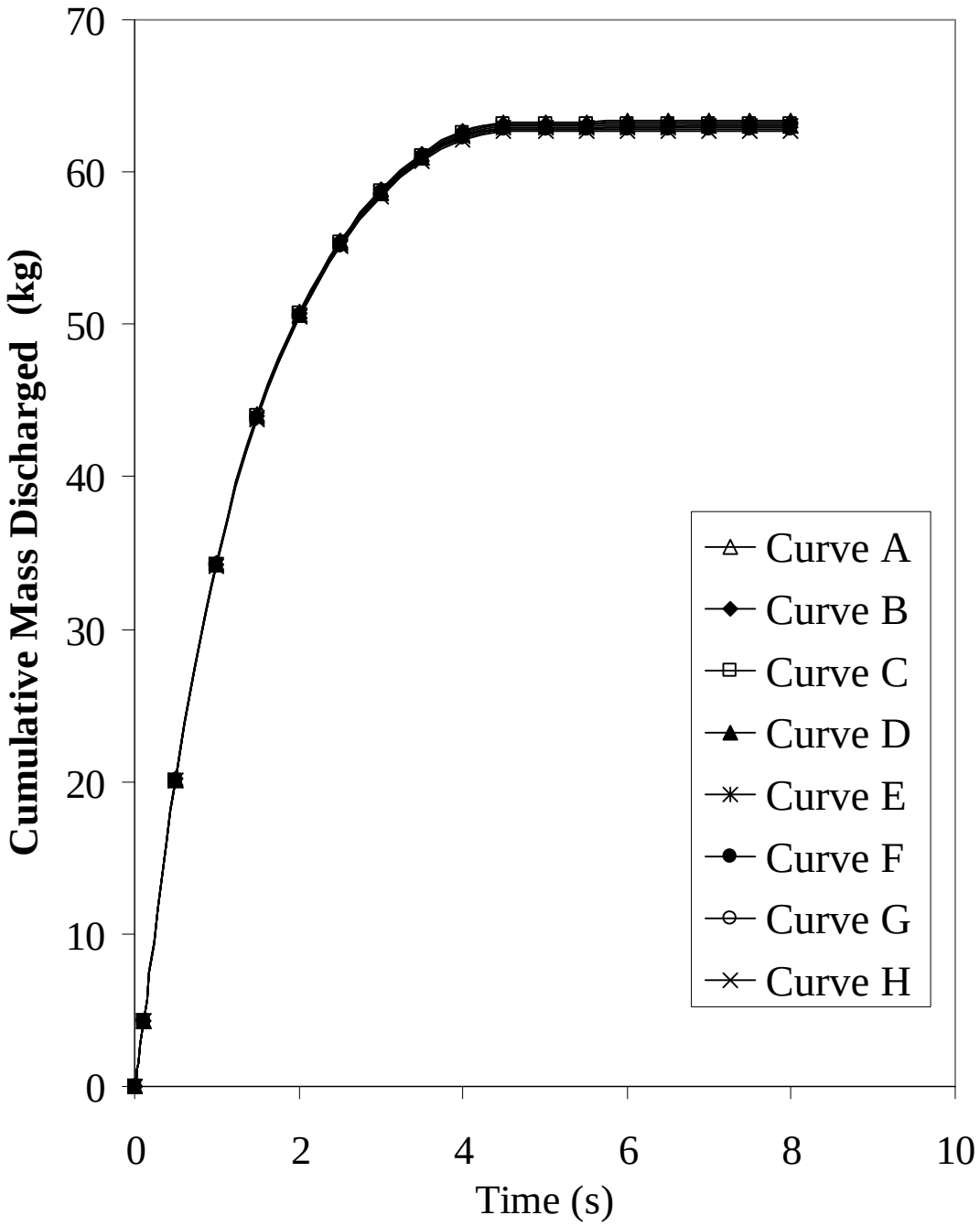

Figure 8.12: Variation of cumulative mass with time for 95% Methane and 5% n-Pentane following puncture at various CFL factors in the range 0.2 – 0.9 at 0.1 intervals.

Curve A: $C_f = 0.9$ Curve D: $C_f = 0.6$ Curve G: $C_f = 0.3$

Curve B: $C_f = 0.8$ Curve E: $C_f = 0.5$ Curve H: $C_f = 0.2$

Curve C: $C_f = 0.7$ Curve F: $C_f = 0.4$

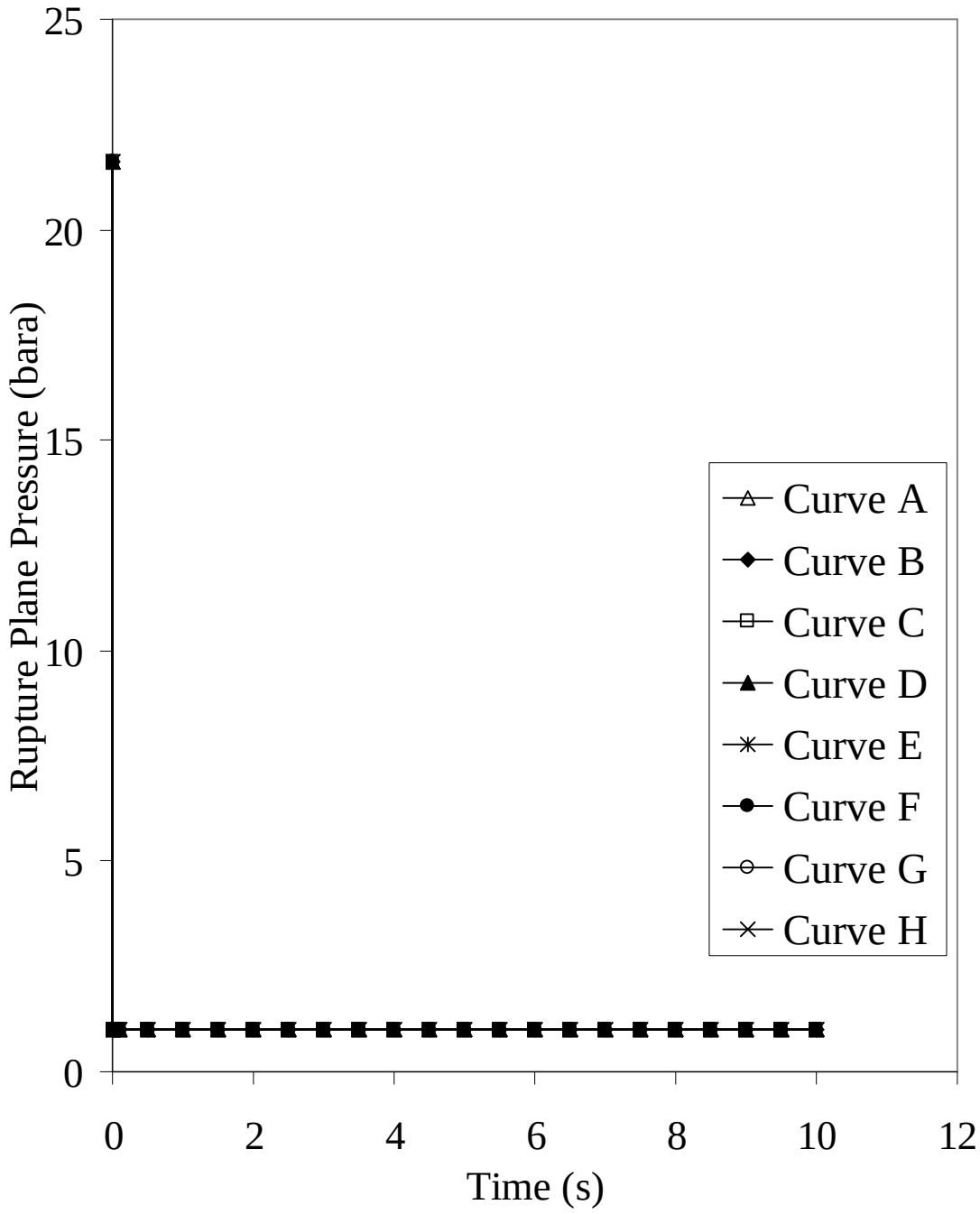

Figure 8.13: Variation of release pressure with time for 100% n-Hexane following puncture at various CFL factors in the range 0.2 – 0.9 at 0.1 intervals.

Curve A: $C_f = 0.9$ Curve D: $C_f = 0.6$ Curve G: $C_f = 0.3$

Curve B: $C_f = 0.8$ Curve E: $C_f = 0.5$ Curve H: $C_f = 0.2$

Curve C: $C_f = 0.7$ Curve F: $C_f = 0.4$

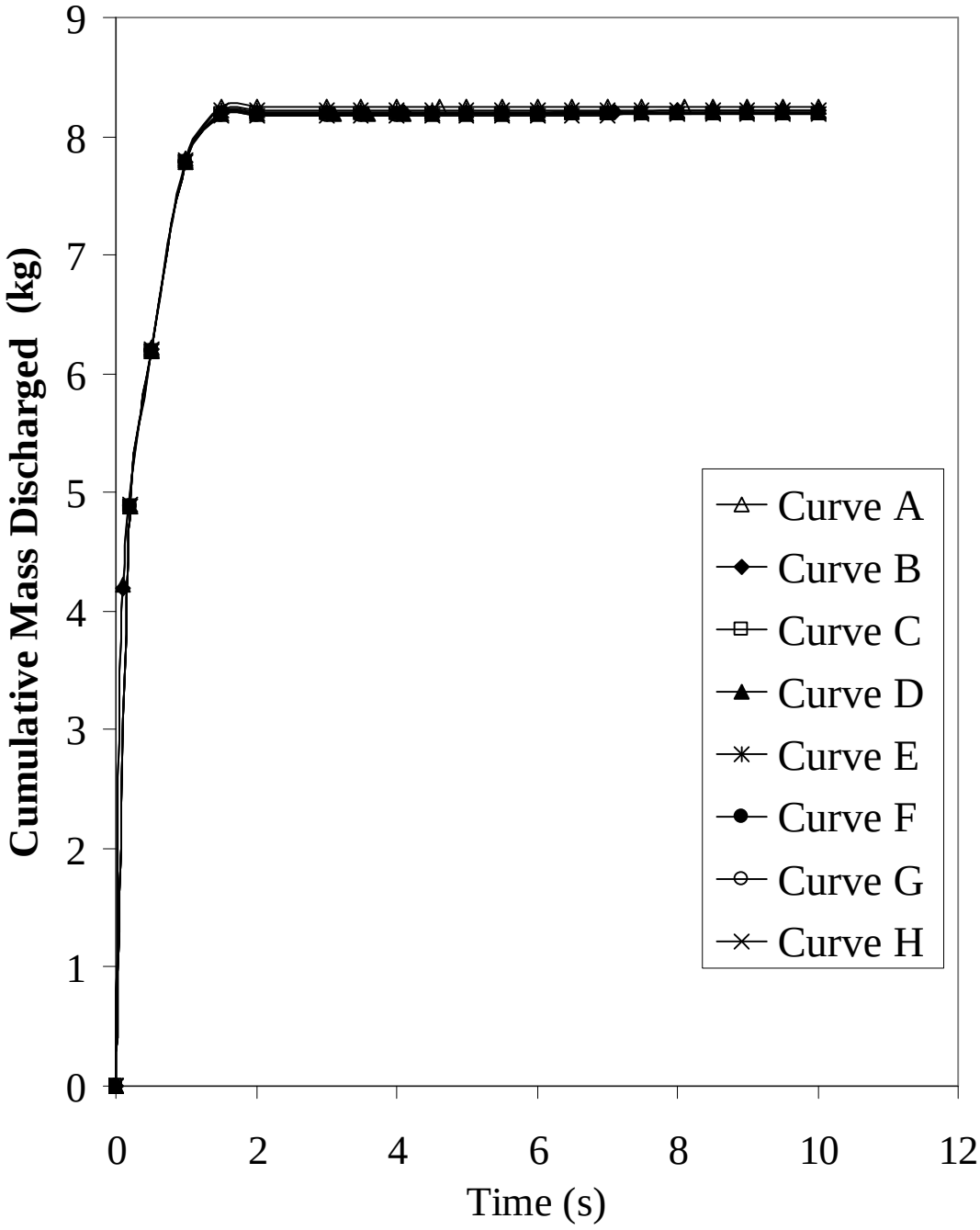

Figure 8.14: Variation of cumulative mass with time for 100% Hexane following puncture at various CFL factors in the range 0.2 – 0.9 at 0.1 intervals.

Curve A: $C_f = 0.9$ Curve D: $C_f = 0.6$ Curve G: $C_f = 0.3$

Curve B: $C_f = 0.8$ Curve E: $C_f = 0.5$ Curve H: $C_f = 0.2$

Curve C: $C_f = 0.7$ Curve F: $C_f = 0.4$

8.3 Concluding Remarks

The impact of the application of the CFL criterion on the numerical stability of the pipeline outflow model was investigated for the discharge of various classes of fluids through an orifice. In the case of permanent gas, liquid and two-phase mixtures it was found that the reduction in the size of the discretisation elements as expressed in terms of the CFL factor varying in the range 0.9 – 0.1 resulted in a significant disproportionate increase in the computational run time. There was no impact on the simulated outflow data. As such there is no incentive in using CFL factors of less than 0.9 for such inventories.

Although the same observation was made in terms of computational run times for the flashing hydrocarbons, the outflow predictions were found to become unreliable for CFL factors of less than 0.4. This is due to the significant difference in the acoustic velocities across the flashing interface propagating from the puncture plane towards the intact ends of the pipeline. Here, the approximation of linear variation in the fluid properties within the numerical cell encapsulating the moving boundary breaks down giving rise to ‘instability’. This was manifested in the observed premature termination of outflow despite the significant downstream line pressure. It is clear that in the case of simulating outflow for pipelines containing flashing hydrocarbons, the application of CFL condition limiting the minimum discretisation elements does not necessarily ensure numerical simulation stability.

CHAPTER 9: CENTRIFUGAL PUMP MODELLING

9.1 Introduction

In this chapter the effect of a feed pump on outflow following the rupture of a pressurised pipeline is presented through the formulation of the appropriate boundary conditions. The model is the applied to the hypothetical failure of a 100 m pipeline transporting 100 % Hexane connected to a Grundfos centrifugal pump (model CR-4-120, vertical, 12 stage, nonself-priming, fitted with a Grundfos standard motor) (Al-Khomairi, 2003).

9.2 Formulation of the Pump Boundary Condition

The pump head-discharge curve is an experimentally derived curve that reflects the performance of a pump at different operating conditions. For steady-state flow conditions, the pump head-discharge curve can be used to accurately predict the pump head from the pump discharge rate and vice versa. The pump curve can also be used for unsteady pipe flow applications where the flow transient conditions are very mild. However, large errors in the predicted data are possible for severe transient operations such as the sudden closing or opening of a valve downstream of the pump (Al-Khomairi, 2003).

In this study, the equation for centrifugal pumps given by Wylie (1993) is employed to describe the behaviour of the pump discharge pressure as a function of its discharge rate or velocity:

$$P_j = P_{SH} + u_j \left(K_{p1} + K_{p2} u_j \right) \tag{9.1}$$

Where, P_{SH} is the pump shut-off head and it represents the maximum discharge pressure of the pump. The pump ceases to operate once this value is reached. K_{p1} and K_{p2} are negative constants whose magnitudes depend on the type of pump used.

P_j = the pump discharge pressure

u_j = the pump discharge velocity

Expanding equation (9.1) gives:

$$P_j = P_{SH} + K_{p1}u_j + K_{p2}u_j^2 \qquad (9.2)$$

To determine the constants K_{p1}, K_{p2} and P_{SH}, the steady-state pump head-discharge curve data related to the pump being modelled is first fitted. The curve fitting is done using the NAG routine nag_ cheb_1d_fit (Numerical Algorithms Group, 2000) which computes the weighted least-squares polynomial approximations of the Chebyshev-series.

The Chebyshev polynomial approximation of degree *i* (Numerical Algorithms Group, 2000) is given by:

$$P_i(x) = 0.5a_0T_0(\bar{x}) + a_1T_1(\bar{x}) + a_2T_2(\bar{x}) + ... + a_nT_n(\bar{x}) \qquad (9.3)$$

for i = 0, 1, ….. n

Where,

a_i = fitted polynomial constants

$T_j(\bar{x})$ = Chebyshev polynomial of the first kind of degree j with normalised argument $\bar{x}$. This argument lies in the range -1 to +1 and is related to the original variable x by the linear transformation:

$$\bar{x} = \frac{\left(2x - \left(x_{max} + x_{min}\right)\right)}{x_{max} - x_{min}} \qquad (9.4)$$

Where, x_{max} and x_{min} are the largest and smallest values of x respectively.

The Chebyshev quadratic approximation of equation (9.2) is:

$$P(x) = 0.5a_0T_0(\bar{x}) + a_1T_1(\bar{x}) + a_2T_2(\bar{x}) \qquad (9.5)$$

Where,

$$T_0(\bar{x}) = 1 \tag{9.6}$$

$$T_1(\bar{x}) = \bar{x} \tag{9.7}$$

$$T_2(\bar{x}) = 2(\bar{x})^2 - 1 \tag{9.8}$$

Substituting equations (9.6) - (9.8) into equation (9.5) gives:

$$P(x) = 0.5a_0 + a_1\bar{x} + 2a_2(\bar{x})^2 - 1 \tag{9.9}$$

Substituting for $\bar{x}$ gives:

$$P(x) = 0.5a_0 + a_1\left[\frac{(2x - (x_{max} + x_{min}))}{x_{max} - x_{min}}\right] + 2a_2\left[\frac{(2x - (x_{max} + x_{min}))}{x_{max} - x_{min}}\right]^2 - a_2 \tag{9.10}$$

Substituting $B = x_{max} + x_{min}$ and $C = x_{max} - x_{min}$:

$$P(x) = 0.5a_0 + \frac{2a_1x}{C} - \frac{a_1B}{C} + 2a_2\left[\frac{2x - B}{C}\right]^2 - a_2 \tag{9.11}$$

The pump constants K_{p1}, K_{p2} and P_{SH} are determined by simplifying equation (9.11) and comparing its coefficients with equation (9.2). The pump constants are given by:

$$P_{SH} = \frac{2a_2B^2}{C^2} - \frac{a_1B}{C} + \frac{a_0}{2} - a_2 \tag{9.12}$$

$$K_{p1} = \frac{2a_1}{C} - \frac{8a_1B}{C^2} \tag{9.13}$$

$$K_{p2} = \frac{8a_2}{C^2} \tag{9.14}$$

Similar to the intact end boundary condition (section 5.2), only the path and negative mach line compatibility equations are active at the pump boundary. The first order finite difference approximation of the negative characteristic equation, C-, is given by:

$$P_j = K_2 + (\rho a)_n (u_j - u_n) + P_n \tag{4.21}$$

Rearranging equation (4.21) to make u_j the subject of the equation gives:

$$u_j = \frac{P_j}{(\rho a)_n} - \frac{P_n}{(\rho a)_n} - \frac{K_2}{(\rho a)_n} + u_n \tag{9.15}$$

Simplifying equation (9.15) gives:

$$u_j = K_{nu1} P_j - K_{nu2} \tag{9.16}$$

Where,

$$K_{nu1} = \frac{1}{(\rho a)_n} \tag{9.17}$$

$$K_{nu2} = \left(\frac{P_n + K_2}{(\rho a)_n} \right) - u_n \tag{9.18}$$

Substituting equation (9.2) into equation (9.16) gives:

$$K_{nu1} K_{p2} u_j^2 + \left(K_{nu1} K_{p1} - 1 \right) u_j + K_{nu1} P_{SH} - K_{nu2} = 0 \tag{9.19}$$

The positive root of equation (9.19) corresponds to u_j. Hence, by substituting the value of u_j obtained from the solution of equation (9.19) in equation (9.2), the corresponding value of P_j can be obtained.

9.3 Results and Discussion

In this section, the centrifugal pump boundary condition is validated using the pump curve for a Grundfos, model CR-4-120, vertical, 12 stage, nonself-priming, centrifugal pump fitted with a Grundfos standard motor (Al-Khomairi, 2003). The simulation of outflow following the FBR at the end of a 100 m pipeline at 21.6 bara and 20^{o}C transporting 100% Hexane is used as a hypothetical pipeline failure.

The initial conditions prior to failure of the pipeline with Grundfos centrifugal pump as the flow source are given in table 9.1. The centrifugal pump is assumed to operate throughout the depressurisation.

Table 9.1: Pipeline characteristics and prevailing conditions prior to failure of the pipeline.

Length (m)	100
Pipe External Diameter (mm)	300
Pipe Wall Thickness (mm)	10
Number of Grids	50
Initial Pressure (bara)	10.2
Initial Temperature (K)	300
Ambient Temperature (K)	293.15
Ambient Pressure (K)	1.01
Initial Flow Rate (kg/s)	0.56

Figure 9.1 shows the pump curve for the centrifugal pump. The figure shows the variation of total head (m) developed by the pump versus the discharge rate (l/min) as supplied by the manufactures.

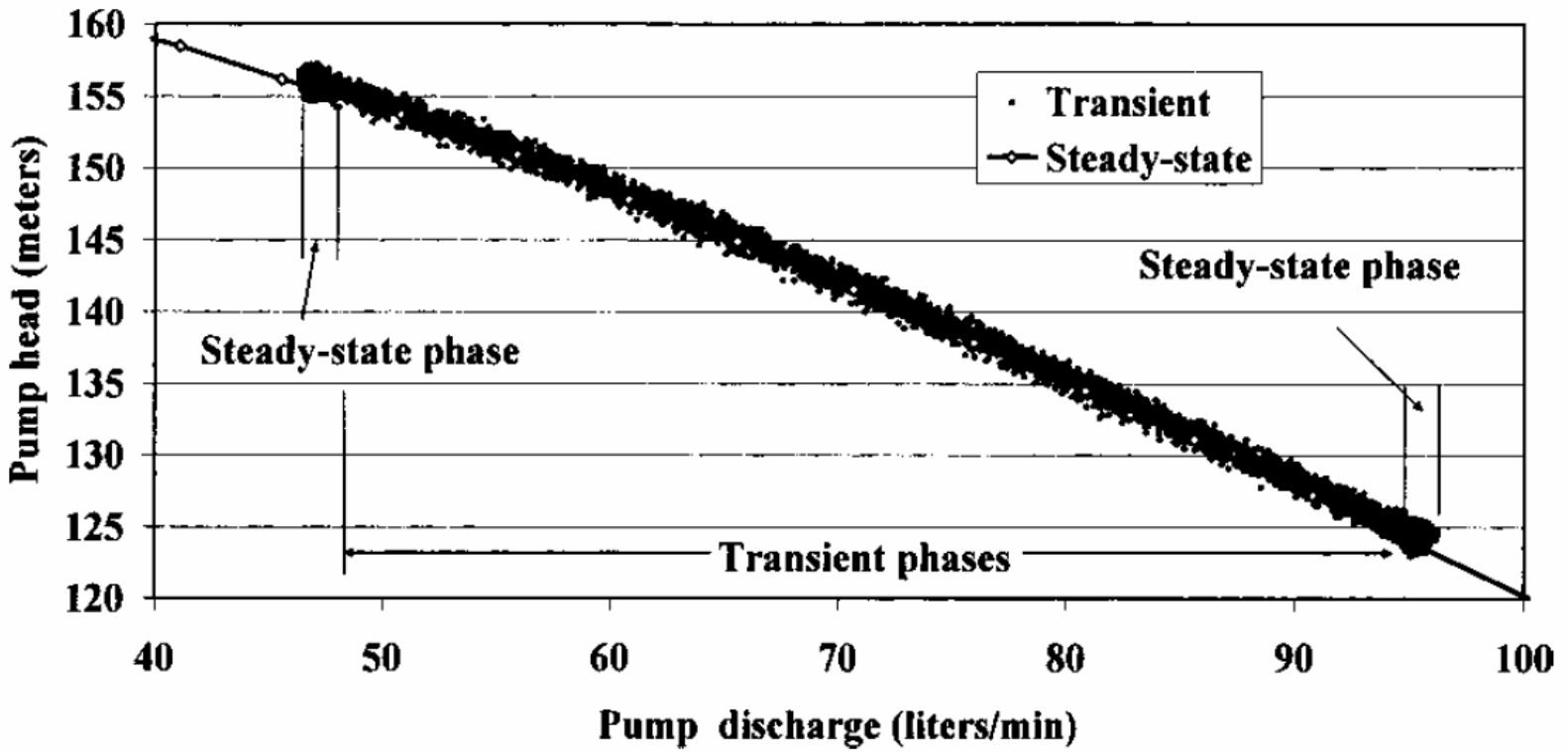

Figure 9.1: Pump curve for a Grundfos, model CR-4-120, vertical, 12 stage, nonself-priming, centrifugal pump fitted with a Grundfos standard motor (Al-Khomairi, 2003).

However, the outflow model requires the pump curve data to be input with discharge pressure in bar and discharge velocity with units of m/s. Figure 9.2 shows the pump curve using the required units based on an inlet Hexane density of 665 kg/m^3. The inlet density was determined using an isothermal flash at the initial feed conditions of 10.2 bar and 300 K. Table 9.2 gives tabulated data used to incorporate the pump curve into the outflow model.

Table 9.2: Data used to input the pump curve into the outflow model.

Pump Head		Pump Discharge Rate		Pump Discharge Velocity
m	bar	L/min	Kg/s	m/s
155	10.2	50	0.56	0.014
150	9.9	57	0.64	0.015
145	9.5	67	0.75	0.018
140	9.2	73	0.82	0.020
135	8.9	81	0.90	0.022
130	8.5	88	0.98	0.024
125	8.2	95	1.06	0.026

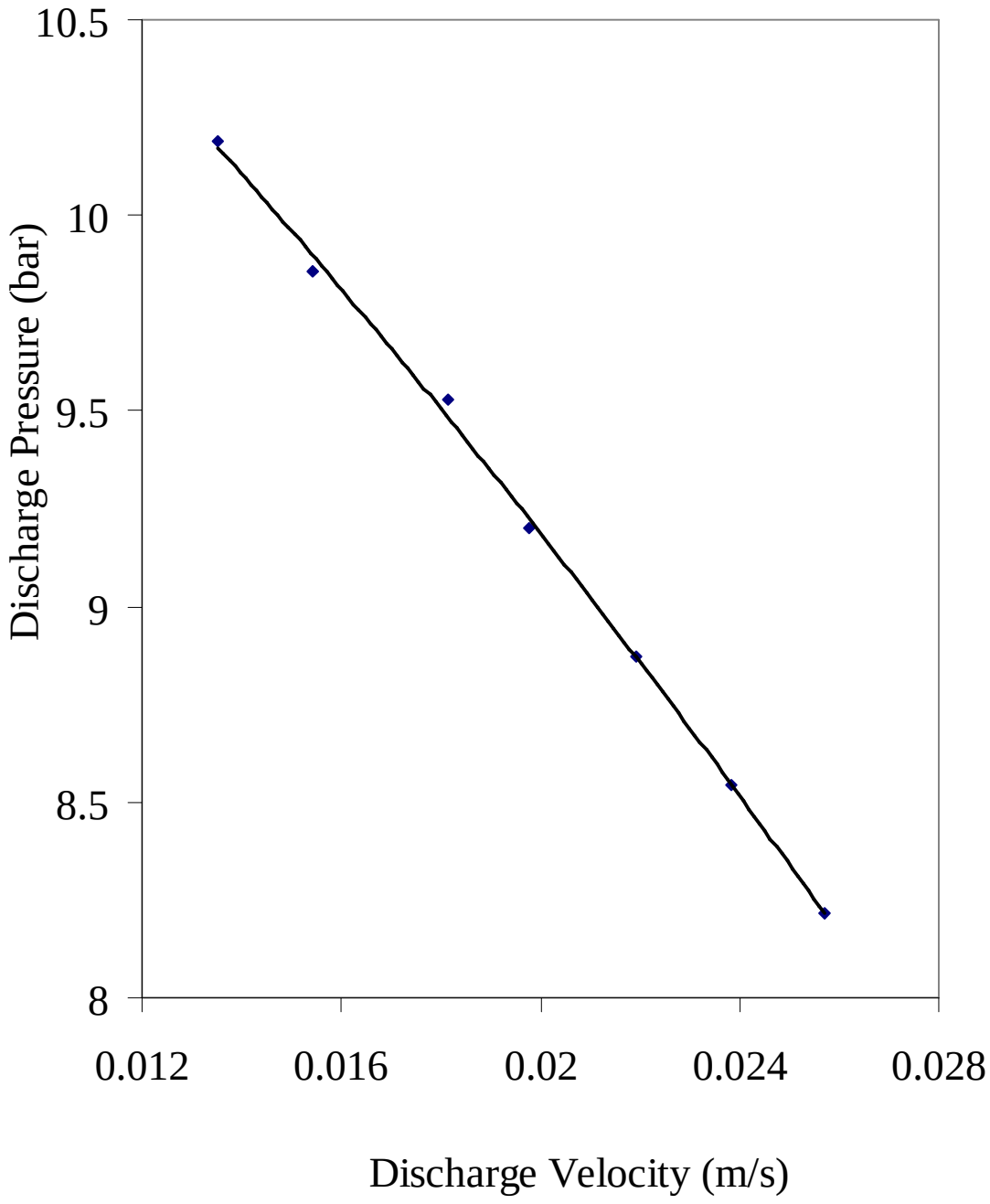

Figure 9.2: Variation of discharge pressure (bar) with discharge velocity (m/s) for the Grundfos centrifugal pump.

The pump curve constants determined using the NAG routine nag_ cheb_1d_fit (Numerical Algorithms Group, 2000) as described in section 9.2 are summarised below:

k_{p1} = -103.28

k_{p2} = -1465.8

P_{SH} = 11.839 bar

Figure 9.3 shows the semi log plot of the variation of discharge rate with time at the rupture plane (curve A) and the centrifugal pump outlet (curve B). As the pipeline contains a non-flashing liquid, a large initial discharge of inventory (curve A) from the pipeline is observed upon FBR. As the depressurisation induced expansion wave propagates along the length of the pipeline from the rupture plane towards the centrifugal pump, there is a corresponding increase in the discharge rate from the centrifugal pump (curve B) from its initial discharge rate of 0.56 kg/s. The discharge rate continues to increases until the pressure at the centrifugal pump reaches the ambient pressure (1.01 bara), 0.2 seconds after pipeline failure. At this point, the discharge rate from the pump attains a final discharge rate of 2.36 kg/s (0.058 m/s) which is equal to the discharge rate predicted by extrapolating the pump curve to 1.01 bara as shown in figure 9.4.

Consequently, the step change in the discharge rate from the rupture plane after 0.1 seconds (curve A) in figure 9.3 is due to the increase in pump discharge. From the figure it can be seen that the discharge rate from the rupture plane continues to fall rapidly until it reaches a steady state discharge rate equal to the final pump discharge rate.

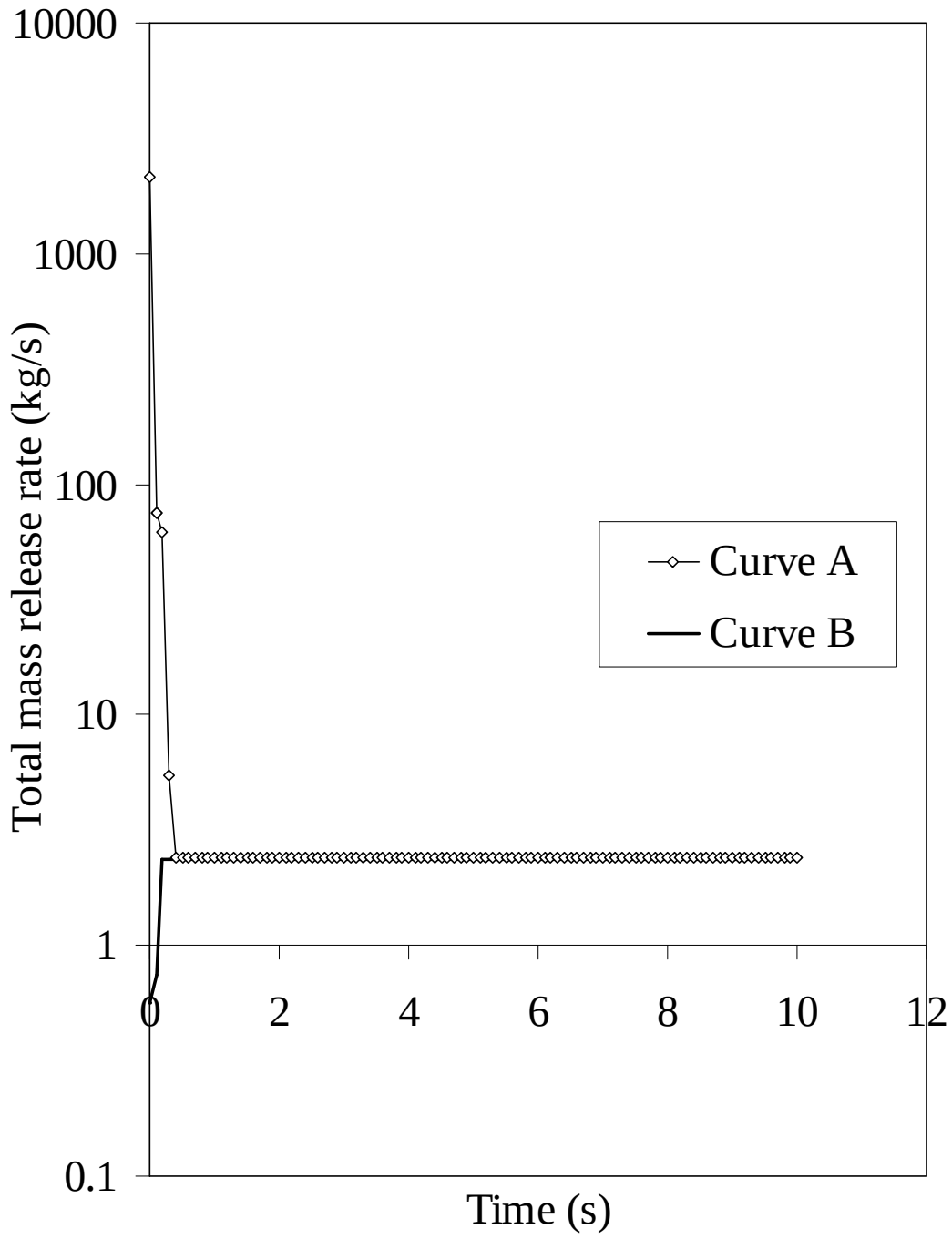

Figure 9.3: Variation of discharge rate with time for a 100 m pipeline transporting 100% Hexane following FBR at the end of the pipeline.

Curve A – Rupture plane

Curve B – Centrifugal pump

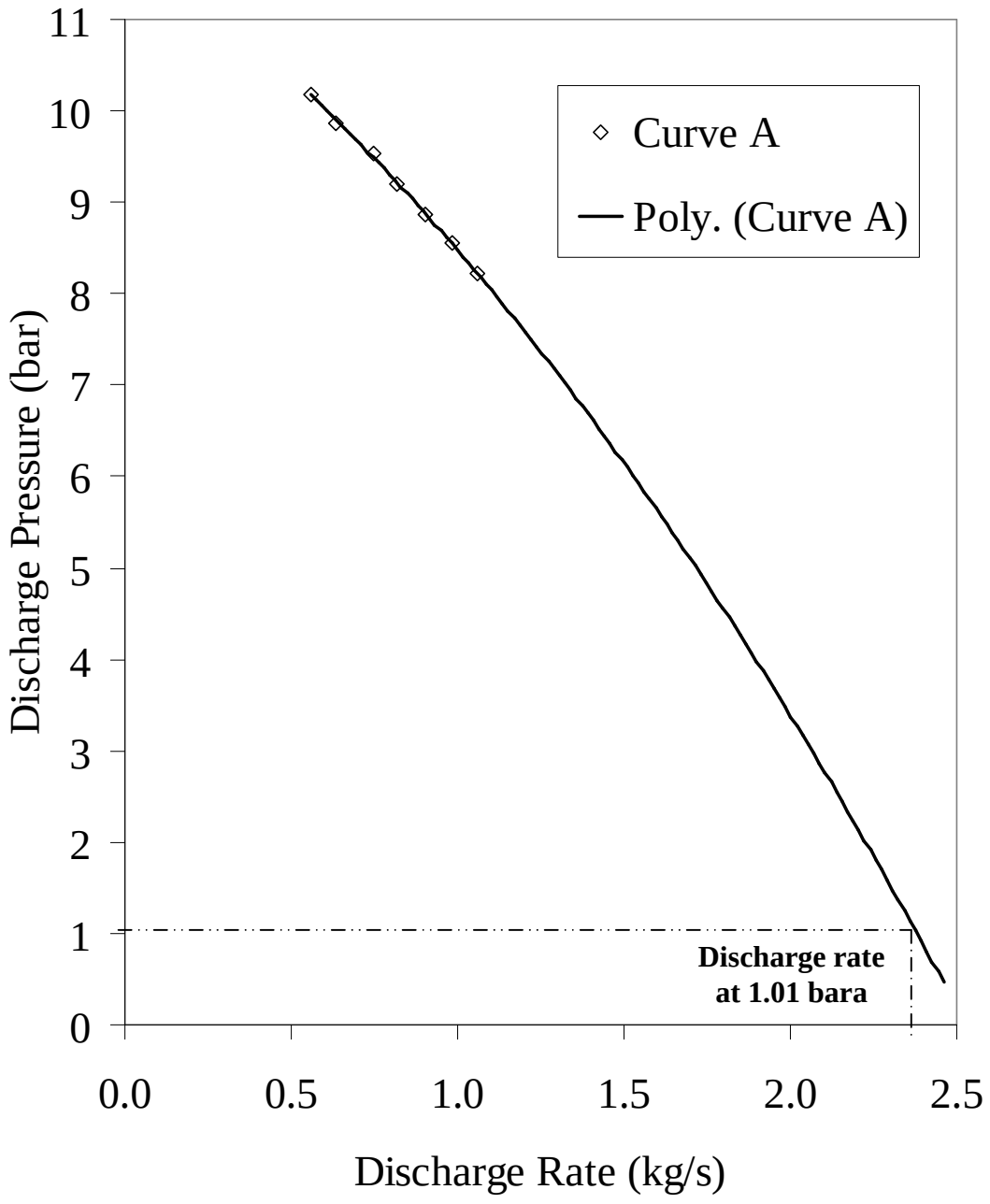

Figure 9.4: Variation of discharge pressure with discharge rate for the Grundfos centrifugal pump.

Curve A – Pump curve

Poly. (Curve A) – Extrapolated pump curve

9.4 Concluding Remarks

The centrifugal pump boundary condition was validated using the pump curve for a Grundfos, model CR-4-120, vertical, 12 stage, nonself-priming, centrifugal pump fitted with a Grundfos standard motor. The simulation of outflow following the FBR at the end of a 100 m pipeline at 21.6 bara and 20 ^{o}C transporting 100% Hexane was used as a case example in the validation. The fitted pump constants obtained for the centrifugal pump were as follows:

k_{p1} = -103.28

k_{p2} = -1465.8

P_{SH} = 11.839 bar

The simulation results showed that upon complete depressurisation of the pipeline, both the centrifugal pump and the release from the pipeline maintains a final steady discharge rate of 2.36 kg/s (0.058 m/s) which is equal to the discharge rate predicted by extrapolating the pump curve to 1.01 bara.

CHAPTER 10: CONCLUSION AND FUTURE WORK

10.1 Conclusion

This thesis described the fundamental extension and extensive testing of a robust CFD model for predicting transient fluid flow following the failure of pressurised pipelines. The main thrust of the study involved extension of the basic model to account for complex pipeline systems and improvements of the theoretical basis and the numerical stability.

In chapter 2 a detailed review of the outflow models designed to simulate pipeline failure was conducted. This highlighted the varying degree of rigour of the models developed. For example, several of the models reviewed are unrealistic due to the assumption of perfect gas behaviour, or ignore depressurisation induced wave propagation phenomena. Others employ incorrect boundary conditions, simulate multi-segment pipelines as an 'equivalent' single pipeline, or ignore frictional and heat transfer effects. These limitations inevitability undermine the efficacy of the simulated data.

The homogenous equilibrium based models by Mahgerefteh et al. (1999), Chen et al. (1995a, b) and Atti (2006) were found to be the most robust with the latter performing best in terms of accuracy and computational run time. Nonetheless, when simulating the complete blowdown of long pipelines (>100 km), the computational run times associated with all of these models still remain rather long.

In chapter 3, the equations describing mass, momentum and energy conservation were presented. These were shown to be quasi-linear and hyperbolic in nature. The MOC was chosen to solve these, as it is well suited to handling the fast transients at the rupture plane.

The various hydrodynamic and thermodynamic expressions for predicting important parameters including the speed of sound in two-phase media, fluid viscosity as well as

fluid flow and phase dependent friction coefficient were presented. In addition, the mathematical expression for the quantity of heat transferred to the fluid from the ambient based on the lumped body approach was derived. This approach eliminated the need for assuming a constant overall heat transfer coefficient.

In chapter 4, the formulation of the MOC based on the method of Specified Time (ST) was presented. The compatibility equations obtained from the resolution of conservation equations were discritised using the Euler predictor-corrector technique (a finite difference scheme). By assuming that the fluid properties varied linearly with distance, algebraic expressions for the fluid variables at the next time step along the pipeline length were obtained. The chapter concluded with the formulation of the nested grid system (NGS) of discritisation. The system employs finer grid discritisation near the rupture plane where greater resolution of the fast transients is required and coarser grids for the remainder of the pipeline. This enables simulation with fewer number of grids and hence a reduction in computation runtime.

In chapter 5, the compatibility equations formulated in chapter 4 in conjunction with suitable boundary conditions and solution methodologies were applied to model the fluid dynamics following failure of multiple segment pipelines. The frictional losses due to valves, fittings, changes in pipeline diameter and changes in elevation were accounted for by the introduction of a loss coefficient, K_{loss}.

In chapter 6, the problems associated with the simplification of a multi-segment pipeline with that of an equivalent single pipeline with the same overall length were highlighted based on a case study. In the absence of experimental data for validation purposes, the efficacy of the multi-segment pipeline model was evaluated based on the calculation of a mass conservation index. In the case of liquid and vapour inventories, the outflow models produced significant differences in the predicted pressure profile, discharge rate and cumulative mass released due to the over-prediction of the hydrostatic head in the single pipeline model. However, despite the higher mixture density for the two-phase mixture as compared to vapour inventory, only minor differences were observed in the results produced by both models. This was attributed to the independence of the rate of depletion of the two-phase inventory

during pressure equilibration on the angle of decline of the pipeline due to the dominant influence of the pressure forces over hydraulic forces.

The development of two models, namely the Hybrid Model and the Modified Homogeneous Equilibrium Model (MHEM) each addressing a principal limitation of the HEM was presented in chapter 7. The Hybrid Model accounted for the post depressurisation hydrodynamic discharge following the rupture of angled pipelines, ignored by HEM. The MHEM on the other hand addressed the limitations of the HEM highlighted by Richardson et al. (2006) for simulating blowdown of pipelines conveying flashing/ two-phase fluids discharging through an orifice.

The Hybrid model takes account of the fact that during the early stages of blowdown, the pressure forces are dominant. In this region, the HEM remains applicable due to the absence of gravity induced phase separation. However, once the line pressure reaches atmospheric pressure, the remaining outflow will be primarily due to the hydrodynamic head at which point the HEM fails. The Hybrid Model addresses this limitation through the coupling of the HEM with a hydraulic flow model. Case studies involving the FBR of various angles of decline pipelines containing gas, liquid and two-phase mixtures were used to demonstrate the efficacy of the Hybrid Model.

These investigations revealed that in the case of flashing liquid inventories in declining pipelines, the HEM model under predicted the amount of inventory loss as compared to the Hybrid Model as it failed to account for the discharge of the remaining liquid in the pipeline following its depressurisation to 1 bara. Additionally, the post-depressurisation discharge rate was strongly affected by the angle of decline. Similar trends were also observed for compressed liquids with the exception of the differences between the predictions being much more pronounced than those for the compressed volatile liquid. HEM only accounted for the loss of liquid due to its finite and very rapid expansion from the line pressure to 1 bara. In contrast, the presence of a relatively small proportion of gas in the liquid resulted in a dramatic change in behaviour with the rate of loss of inventory no longer being dependent on the angle of decline. The results indicated that the entire liquid inventory was discharged by the gas by the time the line was depressurised to 1 bara.

The MHEM was developed by taking into account the results of the extensive experimental investigations conducted by Richardson et al. (2006) involving the flow of different types of pressurised hydrocarbons through various diameter orifices in order to highlight the limitations of HEM. This in essence involved the approximation of liquid rich two-phase mixtures containing less than 3% vapour where the HEM failed with an incompressible liquid. In the grey area corresponding to mixtures containing 80 – 97 % liquid, despite its inapplicability, the HEM was chosen as it produced the worse case scenario prediction in terms of the maximum discharge.

Chapter 8 presented the results of a sensitivity analysis to determine the impact of the application of the Courant-Friedrichs-Lewy (CFL) criterion (Courant et al.,1926; Zucrow and Hoffman, 1976) on outflow prediction and computational run time following the failure of a pressurised pipeline. In the case of permanent gas, liquid and two-phase mixtures it was found that the reduction in the size of the discretisation elements as expressed in terms of the CFL factor varying in the range 0.9 – 0.1 resulted in a significant disproportionate increase in the computational run time. There was no impact on the simulated outflow data. As such there is no incentive in using CFL factors of less than 0.9 for such inventories. Although the same observation was made in terms of computational run times for the flashing hydrocarbons, the outflow predictions were found to become unreliable for CFL factors of less than 0.4. This was attributed to the significant difference in the acoustic velocities across the flashing interface propagating from the puncture plane towards the intact ends of the pipeline. Here, the approximation of linear variation in the fluid properties within the numerical cell encapsulating the moving boundary broke down giving rise to numerical instability. It was concluded that when simulating outflow for pipelines containing flashing hydrocarbons, the application of CFL condition limiting the minimum discretisation elements did not necessarily ensure numerical stability.

Chapter 9 presented the formulation of the pump boundary condition followed by its validation. The simulation of outflow following the FBR at the end of a 100 m pipeline at 21.6 bara and 20 ^{o}C transporting 100% Hexane was used as a case example in the validation.

In conclusion, the work presented in this study provides the mathematical and computational basis for the accurate assessment of the consequences associated with the rupture of pressurised pipelines. It goes beyond the current state of the art by allowing the analysis of the failure of complex pipeline systems whilst at the same time addressing some of the critical drawbacks of the established theory. The work presented is also applicable to pipe work attached to vessels in process units.

Since the release rates act as the source terms for subsequent dispersion, fire and explosion, the results of this work will help to define the hazardous effects with greater certainty. Not only will this help to identify physical effects but will also yield cost benefits in terms of targeted control, protection and mitigation systems designed to combat these effects.

Thus the fundamental nature of this work will benefit process safety in the longer term by protecting life, property and the environment.

10.2 Suggestions for Future Work

Incorporation of heterogeneous equilibrium

Despite the success of the method of characteristics (MOC) based model in predicting outflow, the technique is based on a homogeneous equilibrium model in which the constituent phases are assumed to be in thermal and mechanical equilibrium with one another. In practice the general validity of such an assumption especially in the case of release from a small puncture for flashing liquids or release from inclined pipelines is in doubt due to the possibility of stratified flows.

A heterogeneous equilibrium model ascribing separate conservation equations to each constituent phase and accounting for cross-phase concentration changes is expected to address the above limitation.

Reduction in computational run time

The following investigations and models are recommended to reduce the computational workload in the model:

1. An implicit scheme for modelling the fluid dynamics in regions far from the rupture plane where the Mach number is less than 0.5 will be developed. This has the advantage that discretisation time steps are no longer restricted by the CFL stability criteria, thus allowing the use of larger time steps. In addition, by extending the characteristic lines into adjacent nodes, the maximum allowable time step may be further increased, while still satisfying the CFL stability criteria.
2. The use of a dynamic grid system, in which the number of grids is continually updated based on the upstream flow conditions will be investigated. This would allow the use of the optimum number of grid numbers thereby reducing computational runtime and improving accuracy.

Effect of fluid structure interaction

In the present study, pipelines have been assumed to be rigid. Often the risers linking sub sea wellhead clusters to semi-submersibles or sometimes floating production storage and off-loading systems (FPSO's) are flexible pipes and as a result are prone to the phenomenon of fluid structure interaction. The effect of this with regards to transient fluid flow predictions in flexible pipes needs to be studied.

Hybrid Model

At present, the Hybrid Model is limited to single pipelines with a FBR at the low pressure end of the pipeline. Its extension to multiple-segment pipelines undergoing failure at any location along the length of the pipeline would be desirable.

Modelling other transient flow scenarios

The present model can easily be extended to deal with other transient fluid flow scenarios in pipeline networks such as the effect of operating in line valves and pumps during failure. In addition, in the case of the ignition of the released inventory, a useful extension would be to determine if the resulting thermal stress coupled with the

mechanical weakening of the pipeline might lead to its secondary catastrophic failure during the discharge process. The model may also be usefully modified in order to account for fire impingement on the pipeline from a secondary source.

Modelling the dynamics of the above processes can help pipeline safety engineers to determine the likelihood of accident escalation.

REFERENCES

Al-Khomairi, A. M., "Use of steady-state pump head-discharge curve for unsteady pipe flow applications", *Journal of Hydraulic Engineering*, Vol. 129, No. 12 (2003).

American Petroleum Institute, "Recommended Practice 520, Sizing, Selection and Installation of Pressure-Relieving Devices in Refineries: Part 1—Sizing and Selection", 6th edition (1993).

American Petroleum Institute, "Recommended Practice 520, Sizing, Selection and Installation of Pressure-Relieving Devices in Refineries: Part 1—Sizing and Selection", 7th edition (2000).

Andritsos, N., "Effect of pipe diameter and liquid viscosity on horizontal stratified flow (two-phase, wave generation)," Ph.D. Thesis, University of Illinois at Urbana-Champaign (1986).

APIGEC: Alberta Petroleum Industry Government Environmental Committee, "Hydrogen sulphide isopleth prediction-phase I: model sensitivity study," (1978).

APIGEC: Alberta Petroleum Industry Government Environmental Committee, "Hydrogen sulphide isopleth prediction-phase II: pipe burst study," (1979).

Assael, M. J., J. P. M., Trusler, and T. F., Tsolakis, *Thermophysical properties of fluids: an introduction to their prediction*, Imperial College Press, London (1996).

Atti, O., "Modelling outflow and low temperature induced crack propagation in pressurised pipelines," Ph.D. Thesis, University College London (2006).

Bendiksen, K. H., I. Brandt, P. Fuchs, H. Linga, D. Malnes, and R. Moe, "Two-phase flow research at SINTEF and IFE. Some experimental results and a demonstration of the dynamic two-phase flow simulator OLGA." *The Offshore Northern Seas Conference*, Stavanger (1986).

Bendiksen, K. H., D. Malnes, R. Moe, and S. Nuland, "The dynamic two-fluid model OLGA: theory and applications," *SPE Production Eng.*, **6**, 171 (1991).

Bisgaard, C., H. H. Sorensen, and S. Spangenberg, "A finite element method for transient compressible flow in pipelines," *Int. J. Num. Meth. Fluids*, 7, 291 (1987).

Chen, J. R., S. M. Richardson, and G. Saville, "Numerical simulation of full-bore ruptures of pipelines containing perfect gases," *Trans. Inst. Chem. Eng. Part B*, **70**, 59 (1992).

Chen, J. R., "Modelling of transient flow in pipeline blowdown problems," PhD Thesis, University of London, 81 (1993).

Chen, J. R., S. M. Richardson, and G. Saville, "A simplified numerical method for transient two-phase pipe flow," *Trans IChemE*, **71A**, 304 (1993).

Chen, J. R., S. M. Richardson, and G. Saville, "Modelling of two-phase blowdown from pipelines – I. A hyperbolic model based on variational principles," *Chem. Eng. Sci.*, **50**, 695 (1995a).

Chen, J. R., S. M. Richardson, and G. Saville, "Modelling of two-phase blowdown from pipelines – II. A simplified numerical method for multi-component mixtures," *Chem. Eng. Sci.*, **50**, 2173 (1995b).

Chen, N. H., "An explicit equation for friction factor in pipes," *Ind. Eng. Chem. Fundam.*, **18**, No. 3, 296 (1979).

Coulson, J. M., and J. F. Richardson. "Chemical Engineering – Fluid Flow, Heat Transfer and Mass Transfer," Volume 1, Fifth Edition, Butterworth-Heinemann, Linacre House, Oxford (1998).

Courant, R., E. Isaacson, and M. Reeves, "On the solution of non-linear hyperbolic differential equations by finite differences," *Comm. On Pure and Applied Mathematics*, **5**, 243 (1952).

Cunliffe, R. S., "Condensate flow in a wet-gas line can be predicted." *Oil and Gas Journal.*, Oct 30 (1978).

Daubert, T. E., and R. P. Danner, "Tables of physical and thermodynamic properties of pure compounds," DIPPR Project 801 Data Compilation (1990).

Ely, J. F., and H. J. M. Hanley, "Prediction of transport properties. 1. Viscosity of fluids and mixtures," *Ind. Eng. Chem. Fundam.*, **20**, 323 (1981).

Ely, J. F., and H. J. M. Hanley, "Prediction of transport properties. 2. Thermal conductivity of pure fluids and mixtures," *Ind. Eng. Chem. Fundam.*, **22**, 90 (1983).

Fairuzov, Y. V., "Blowdown of pipelines carrying flashing liquids," *AIChE J.*, **44,** No. 5, 245 (1998).

Flatt, R., "Unsteady compressible flow in long pipelines following a rupture," *Int. J. Num. Meth. Fluids*, **6**, 83 (1986).

Hall, A. R. W., E. R. Butcher, and C. E. Teh, "Transient simulation o two-phase hydrocarbon flows in pipelines," *Proceedings of the European Two-Phase Flow Group Meeting*, Hannover (1993).

Harlow, F. H., and A. A. Amsden, "A numerical fluid dynamics calculation method for all flow speeds," *J. Comput. Phys.*, **8**, 197 (1971).

Health and Safety Executive - Offshore,
"http://www.hse.gov.uk/offshore/fireexp/riskasse.htm", (2009).

Huber, M. L., NIST thermophysical properties of hydrocarbon mixtures, NIST Standard Reference Database 4, 1999.

Hyprotech, *PROFES-Transient user manual*, Aspentech, Houston (2001).

International Energy Agency, http://www.iea.org/, (2009).

Ishii, M., and N. Zuber, "Drag coefficient and relative velocity in bubbly, droplet or particulate flow," *AIChE J.*, **25**, 843 (1979).

Ishii, M., and K. Mishima, "Two-fluid model and hydrodynamic constitutive relations," *Nucl. Eng. Des.*, **82**, 107 (1984).

Joukowsky, N., "Über den hydraulischen Stoss in Wasserleitungsröhren ("On the hydraulic hammer in water supply pipes."),"* Mémoires de l'Académie Impériale des Sciences de St.-Pétersbourg* , Series 8, 9(5), 1-71 (1900).

Jones, D. G., and D. W. Gough, "Rich gas decompression behaviour in pipelines," *AGA-EPRG Pipeline Research Seminar IV*, Duisburg, British Gas, Report No. ERSE 293, (1981).

Kimambo, C. Z., and A. Thorley, "Computer modelling of transients ruptured high-pressure natural gas pipelines: a review of experimental and numerical studies," *IMechE*, C502/003, 55 (1995).

Leveque, R. J., "Cambridge Texts in Applied Mathematics: Finite Volume Methods for Hyperbolic Problems", Cambridge University Press, New York (2002).

Mahgerefteh, H., P. Saha, and I. G. Economou, "A study of the dynamic response of emergency shutdown valves following full-bore rupture of gas pipelines," *Trans. Inst. Chem. Eng.*, Part B, **75**, 201 (1997).

Mahgerefteh, H., P. Saha, and I. G. Economou, "Fast numerical simulation for full-bore rupture of pressurized pipelines," *AIChE J.*, **45**, No. 6, 1191 (1999).

Mahgerefteh, H., P. Saha, and I. G. Economou, "Modelling fluid phase transition effects on dynamic behaviour of ESDV," *AIChE J.*, **46**, No. 5, 997 (2000).

Mahgerefteh, H., and S. M. a. Wong, "A numerical blowdown simulation incorporating cubic equations of state," *Computers in Chemical Engineering*, **23(9)**, 1309 (1999).

Mahgerefteh, H., G. Denton, and Y. Rykov, "A hybrid multiphase flow model," *AIChE Journal*. 54(9)**:** 2261-2268 (2008)**.**

Necmi, S., and W. T. Hancox, "An experimental and theoretical investigation of blowdown from a horizontal pipe," *Proceedings of the 6th International Heat Transfer Conference*, Toronto, Canada (1978).

Numerical Algorithms Group, NAG Fortran 90 Library, The Numerical Algorithms Group Ltd, Oxford UK, (2000).

Nordsveen, M., and A. Haerdig, "Simulation of severe slugging during depressurisation of an oil/gas pipeline, modelling, identification and control," **18(1)**, 61 (1997).

Offshore Technology Report, OTO 98 162, *Subsea hydrocarbon pipeline failure: survey of available prediction schemes*, HSE, (1998).

Ouyang, L., and K. Aziz, "Steady-state gas flow in pipes," *J. Pet. Sci. Eng.*, **14**, 137 (1996).

Peng, D. Y., and D. B. Robinson, "A new two-constant equation of state," *Ind. Eng. Chem. Fund.*, **15**, 59 (1976).

Perry, R. H., and D. W. Green, *Perry's chemical engineers' handbook*, 7th Ed., McGraw Hill, London (1997).

Peterson, C.E., V. K. Chexal, and T. B. Clements, "Analysis of a hot-leg small break LOCA in a three loop Westinghouse PWR plant," *Nuc. Tech*., 70, No.1, 104 (1985).

Philbin, M. T., and A. H. Govan, "Pipeline analysis code," UKAEA Report AEA-APS-0031 (1990).

Philbin, M. T., "The simulation of transient phenomena in multiphase production systems," AEA Harwell Report AEA-APS-0177 (1991).

Picard, D. J., and P. R. Bishnoi, "Calculation of the thermodynamic sound velocity in two-phase multi-component fluids," *Int. J. Multiphase Flow*, **13(3)**, 295 (1987).

Picard, D. J., and P. R. Bishnoi, "The importance of real-fluid behaviour and non-isentropic effects in modelling compression characteristics of pipeline fluids for application in ductile fracture propagation analysis," *Can. J. Chem. Eng.*, **66**, 3 (1988).

Picard, D. J., and P. R. Bishnoi, "The importance of real-fluid behaviour in predicting release rates resulting from high pressure sour-gas pipeline ruptures," *Can. J. Chem. Eng.*, **67**, 3 (1989).

Prasad, P., and R. Ravindran, *Partial differential equations*, Wiley Eastern Limited, New Delhi (1985).

Press, W. H., S. A. Teukolsky, W. T. Vetterling, and B. P. Flannery, *Numerical recipes in FORTRAN 77: the art of scientific computing*, 2nd ed., Cambridge University Press, Cambridge, U.K. (1992).

Richardson, S. M., and G. Saville, "Blowdown of pipelines," *Society of Petroleum Engineers Europe 91*, Paper SPE 23070, Aberdeen, UK, 369 (1991).

Richardson, S. M., and G. Saville, "Isle of Grain pipeline depressurisation tests," HSE OTH 94441, HSE Books, HSE, Bootle, U.K. (1996a).

Richardson, S. M., and G. Saville, "Blowdown of LPG pipelines," *Trans. IChemE*, 74B, 236 (1996b).

Richardson, S. M., G. Saville, A. Fisher, A. J. Meredith, and M. J. Dix, "Experimental Determination of Two-Phase Flow Rates of Hydrocarbons Through Restrictions," *Trans IChemE, Part B: Process Safety and Environmental Protection*, **84 (B1)**, 40, (2006).

Rohsenow, W. M., J. P. Hartnett, and Y. I. Cho, eds., *Handbook of heat transfer*, 3rd ed., McGraw-Hill, New York (1998).

Saville, G., and R. Szczepanski, "Methane-based equations of states for a corresponding states reference substance," *Chem. Eng. Sci.*, **37**, 719 (1982).

Schwellnus, C. F., and M. Shoukri, "A two-fluid model for non-equilibrium two-phase flow," *Can. J. Chem. Eng.*, **69**, 188 (1991).

Shoup, G., J. J. Xiao, and J. O. Romma, "Multiphase pipeline blowdown simulation and comparison to field data," *1st North American Conference on Multiphase Technology*, BHR Group Conference Series No. 31, Banff, Canada, **3**, June 10 – 11 (1998).

Swaffield, J. A., and A. P. Boldy, *Pressure surge in pipe and duct systems*, Ashgate Publishing Limited, Vermont, USA, (1993).

Tam, V. H. Y., and L. T. Cowley, "Consequences of pressurised LPG releases: the Isle of Grain full scale experiments," *Proceedings of GASTECH 88 (13th Int. LNG/LPG Conf.)* Kuala Lumpur, 2 (1988).

Techo, R., R. R. Tickner, and R. E. James, "An accurate equation for the computation of the friction factor for smooth pipes from the Reynolds number," *J. Appl. Mech.*, **32**, 443 (1965).

Tiley, C. H., "Pressure transient in a ruptured gas pipeline with friction and thermal effects included," PhD Thesis, City University, London (1989).

Twu, C. H., D. Bluck, J. R. Cunningham, and J. E. Coon, “A cubic equation of state with a new alpha function and a new mixing rule”, Fluid Phase Equilibria, **69**, 33 (1991).

Twu, C. H., J. E. Coon and J. R. Cunnigham "A new generalised alpha function for a cubic equation of state part 1. Peng-Robinson equation", *Fluid Phase Equilibria*, **105**, 49 (1995a).

Twu, C. H., J. E. Coon and J. R. Cunnigham "A new generalised alpha function for a cubic equation of state part 2. Redlich-Kwong equation", *Fluid Phase Equilibria*, **105**, 61 (1995b).

US Department of Transportation - Office of Pipeline Safety, “http://ops.dot.gov/stats/stats.htm”, (2009).

Vahedi, S., “Modelling the effects of inclination and pipeline enlargement on outflow following pipeline rupture,” PhD Thesis, University College London (2003).

Van Deen, J. K., and S. R. Reintsema, “Modelling of high pressure gas transmission lines,” *App. Math. Modelling*, 7, No. 4, 268 (1983).

Walas, S. M., *Phase equilibrium in Chemical Engineering*, Butterworth Publisher, Boston, 15 (1987)

Wallis, G. B., “One –dimensional two-phase flow”, McGraw – Hill Co., New York (1969).

Welty, J., C. E. Wicks, G. L. Rorrer, and R. E. Wilson, *Fundamentals of Momentum, Heat and Mass Transfer*, 5th Edition, John Wiley & Sons (2008).

Zucrow, M. J., and J. D. Hoffman, *Gas Dynamics*, Volume I and II, Wiley, New York, 297 (1976).